RATIONAL ENGINEERING OF POROUS MATERIALS FOR BIFUNCTIONAL CATALYSIS: PROBING THE STRUCTURE-ACTIVITY RELATIONSHIPS

WUN CHING KIT

PhD

The Hong Kong Polytechnic University

2025

The Hong Kong Polytechnic University

Department of Applied Biology and Chemical Technology

Rational Engineering of Porous Materials for Bifunctional Catalysis: Probing the Structure-Activity Relationships

Wun Ching Kit

A thesis submitted in fulfilment of the requirements for the degree of Doctor of Philosophy

Aug 2024

CERTIFICATE OF ORIGINALITY

I hereby declare that this thesis is my own work and that, to the best of my knowledge and belief, it reproduces no material previously published or written, nor material that has been accepted for the award of any other degree or diploma, except where due acknowledgment has been made in the text.

_____ (signed)

Wun Ching Kit (Name of Student)

Dedication

To my parents

Abstract

The rational design of metal-doped bifunctional porous materials has emerged as a prominent subject in heterogeneous catalysis due to their potential for synergistic cooperativity and scalability in tandem or cascade reactions. Various metal catalysts, such as isolated single atoms, clusters, and nanoparticles supported on different matrices, have been developed. By employing the aforementioned catalyst strategies, it is possible to create tailor-made bifunctional catalysts suitable for diverse applications. This thesis aims to concentrate on the precise synthesis of bifunctional catalysts falling into two primary categories: (1) **bimetallic catalysts** and (2) **dual active site catalysts** incorporated within the porous supports of **zeolites** and **metal-organic frameworks (MOFs)**. The preparation of desirable bifunctional catalysts will involve employing diverse synthesis and modification strategies for the porous materials. By utilizing cutting-edge techniques for structural elucidation, the electronic and geometric structure of the active species confined within the porous materials can be unveiled, facilitating a comprehensive discussion on the atomic-level structure-activity relationship. **Chapter 1** will introduce the strategies for the synthesis and modification of metal-doped catalysts, as well as the recent advances in bifunctional catalysts. In **Chapter 2**, the raw materials, catalyst preparation strategies, and characterization techniques employed in this thesis will be provided. **Chapter 3** presents the preparation of atomic dispersed 3d metal bimetallic dual-atom catalysts. By utilizing a di-basic imidazole linker, a linker-bridged 3d bimetallic dual atom can be assembled within the zeolite support. Three distinct synergistic advantages have been revealed in a probe superoxide dismutation reaction: (1) neighboring bimetallic active motifs, (2) tertiary structure around the zeolite support, and (3) the local coordination environment. These findings unravel a reliable approach for the precise engineering of novel bimetallic catalysts. In **Chapter 4**, the preparation of Cu-Fe dual-atom catalysts (DACs) on the Zr_6O_4 secondary building unit (SBU) of UiO-66-NH_2 is presented. The Cu-Fe DACs are initially positioned on the framework linker using the strategies mentioned in Chapter 3, and further immobilized on the SBU through O_2 activation. The peroxyl group bridged Cu-Fe DACs facilitate the selective oxidation of styrene, achieving a selectivity of higher than 92% towards benzaldehyde, based on the well-balanced synergy between the electronic and steric characteristics. **Chapter 5** reports the preparation of a bifunctional metal/Brønsted acid zeolite catalyst through one-pot hydrothermal synthesis. By performing systematic investigations of the strength of the active species (Lewis acidity of metal species and Brønsted acidity) using two probe reactions, namely styrene oxidation and GVL decarboxylation, the synergistic cooperativity between the two active species is revealed.

List of Publications

(1) **Wun, C. K. T.**; Wang, Z.; Kawaguchi, S.; Kobayashi, S.; Wu, T. S.; Chen, T.; Lin, C.; Tang, C. C.; Yin, J.; Lo, T. W. B.Investigating Synergistic Cooperativity of Metal-Brønsted Acid Site Pair in MFI-Type Zeolites by Synchrotron X-Ray Powder Diffraction. *J. Mater. Chem. A* **2024**, 25442–25448. https://doi.org/10.1039/d4ta04737k.

(2) Xue, Q.; **Wun, C. K. T.**; Chen, T.; Kawaguchi, S.; Day, S.; Tang, C.; Wu, T.-S.; Soo, Y.-L.; Lin, C.; Peng, Y.-K.Controlled Synthesis of Cu, Fe Dual-Atom Catalysts Restrained on Metal–Organic Frameworks for Efficient O 2 Activation. *J. Mater. Chem. A* **2023**, *11* (26), 14204–14212.

(3) **Wun, C. K. T.**; Mok, H. K.; Chen, T.; Wu, T. S.; Taniya, K.; Nakagawa, K.; Day, S.; Tang, C. C.; Huang, Z.; Su, H.; Yu, W. Y.; Lee, T. K. W.; Lo, T. W. B.Atomically Dispersed 3d Metal Bimetallic Dual-Atom Catalysts and Classification of the Structural Descriptors. *Chem Catal.* **2022**, *2* (9), 2346–2363. https://doi.org/10.1016/j.checat.2022.07.027.

(4) Xie, F.; Jia, H.; **Wun, C. K. T.**; Huang, X.; Chai, Y.; Tsoi, C. C.; Pan, Z.; Zhu, S.; Ren, K.; Lo, T. W. B.Dual-Defect Abundant Graphitic Carbon Nitride for Efficient Photocatalytic Nicotinamide Cofactor Regeneration. *ACS Sustain. Chem. Eng.* **2023**, *11* (30), 11002–11011.

(5) Zhou, R.; Hou, Z.; Fan, K.; **Wun, C. K.**; Liu, Q.; Lo, T. W. B.; Huang, H.; Zhang, B.An Advanced Organic Cathode for Non-Aqueous and Aqueous Calcium-Based Dual Ion Batteries. *J. Power Sources* **2023**, *569*, 232995.

(6) Chen, T.; Yu, W.; **Wun, C. K. T.**; Wu, T.-S.; Sun, M.; Day, S. J.; Li, Z.; Yuan, B.; Wang, Y.; Li, M.Cu–Co Dual-Atom Catalysts Supported on Hierarchical USY Zeolites for an Efficient Cross-Dehydrogenative C (Sp2)–N Coupling Reaction. *J. Am. Chem. Soc.* **2023**, *145* (15), 8464–8473.

(7) Chen, T.; Wang, Y.; Xue, Q.; **Wun, C. K. T.**; So, P. K.; Yung, K. F.; Wu, T.-S.; Soo, Y.-L.; Taniya, K.; Day, S.Atomically Precise Bimetallic Metal Ensembles with Tailorable Synergistic Effects. *Cell Reports Phys. Sci.* **2022**, *3* (4).

(8) Chen, T.; **Wun, C. K. T.**; Day, S. J.; Tang, C. C.; Lo, T. W. B.Enantiospecificity in Achiral Zeolites for Asymmetric Catalysis. *Phys. Chem. Chem. Phys.* **2020**, *22* (34), 18757–18764.

Acknowledgments

First, I would like to express my deepest gratitude to Dr. Benedict Lo for offering me the opportunity to join his research group and for his unwavering support, guidance, and encouragement throughout my FYP and PhD studies spanning over four years. His invaluable expertise in material science, synchrotron techniques, and innovative ideas served as a profound source of inspiration, laying a robust groundwork for my academic pursuits.

I wish to express my heartfelt appreciation to all members of the Lo and Wong groups whose boundless kindness and camaraderie fostered a welcoming environment in the laboratory. I deeply thank Dr. Chen Tianxiang for his mentorship and counsel during my FYP and PhD journey. Special acknowledgments go to Dr. Xue Qi and Mr. Zhang Hao for their guidance on XAFS analysis, contribution to "Cu, Fe" project, and advice on my work. I extend special thanks to Prof. Terence Lee and Dr. Ho Kit Mok for their steadfast support of the "SOD" project. To the others of the group, Lin Biyun, Li Yunong, Dr Alan Wong, Dr Wang Zi, Winky Lui, Keira Lo, Ball Kong, Felix Hung, and every member of the group, thank you for the help and for all the time we spent together. My gratitude extends to my friends from other research groups at PolyU, including Billy, Michael, Aries, Dr. Matthew Lam, Marcus, Marco, Vincent, Carlos, Daniel, and David, for their invaluable feedback, suggestions, and assistance during my doctoral studies.

Lastly, I would like to express my deepest appreciation to my family for their enduring love and unwavering support.

Table of Contents

Abstract	III
List of publications	IV
Acknowledgment	V
Table of contents	VI
List of abbreviation	VIII
Chapter 1 Introduction	**1**
1.0 The importance of studying bifunctional catalysts	1
1.1 Support for bifunctional catalyst	3
1.2 Metal introduction approach in zeolites	13
1.3 Metal introduction approach in MOFs	17
1.4 Bifunctional catalyst utilizing two metal active species	20
1.5 Bifunctional catalyst integrating metal active species and support active site	23
1.6 Aim and Objective	27
1.7 Thesis overview	28
1.8 Reference	29
Chapter 2 Material and Methodology	**36**
2.1 Materials	36
2.2 Synthesis of catalyst	37
2.3 Characterisation techniques	39
2.4 Characterisation experiment details	43
2.5 Reference	46
Chapter 3 Atomically dispersed 3d metal bimetallic dual atom catalysts and classification of the structural descriptors	**49**
3.1 Introduction	50
3.2 Experimental procedure	52
3.3 Results and Discussion	54
3.4 Conclusion	83
3.5 Reference	84
3.6 Supplementary information for Chapter 3	90
Chapter 4 Controlled synthesis of Cu, Fe dual atom catalysts restrained on metal-organic frameworks for efficient O_2 activation	**101**
4.1 Introduction	102
4.2 Experimental procedure	104
4.3 Results and Discussion	106

4.4. Conclusion 127
4.5 Reference 128
4.6 Supplementary information for Chapter 4 132
Chapter 5 Investigating Synergistic Cooperativity of Metal-Bronsted Acid site Pair in MFI type Zeolites by Synchrotron X-ray Powder Diffraction **137**
5.1 Introduction 138
5.2 Experimental procedure 141
5.3 Results and Discussion 143
5.4 Conclusion 166
5.5 Reference 167
5.6 Supplementary information for Chapter 5 171
Chapter 6 Conclusion and Outlook **194**

List of abbreviations

Abbreviation	Definition
Al	Aluminum
Al_2O_3	Aluminum oxide
Ar	Argon
ATA	2-Aminoterephthalic acid
ATR	Attenuated total reflection
B	Boron
BAS	Brσnsted acid site
BDC	Terephthalic Acid
BE	Binding energy
Br	Bromine
CBUs	Cage-building units
CcO	Cytochrome c oxidase
CeO_2	Cerium (IV) oxide
$CHCl_3$	Chloroform
CMA	CoMnAl oxide
CMR	Catalytic membrane reactor
CN	Coordination number
Co	Cobalt
CO	Carbon monoxide
CO_2	Carbon dioxide
CO-IR	Carbon monoxide adsorbed FT-IR
Cu	Copper
$Cu(NO_3)_2{\cdot}2.5H_2O$	Copper(II) nitrate hemi(pentahydrate)
CUS	Coordination unsaturated sites
CVD	Chemical vapor deposition
DACs	Dual-atom catalysts
DCM	Double crystal monochromator
DFT	Density functional theory
DI water	Deionized water
DMEM	Dulbecco's Modified Eagle Medium
DMF	Dimethylformamide
DMF	2,5-dimethylfuran
DMTHF	2,5-dimethyltetrahydrofuran
DSC	Differential Scanning Calorimeter
DTGS	Deuterated triglycine sulfate

EDX	Energy-dispersive X-ray spectroscopy
eV	Electron volt
EXAFS	Extended X-ray absorption fine structure
F-	Fluorine
FAU	Faujasites
FBS	Fetal bovine serum
Fe	Iron
$Fe(NO_3)_3$	Iron(III) nitrate
Fe_2O_3	Iron (III) oxide
FT-IR	Fourier-transform infrared spectroscopy
FTO	Fischer-Tropsch to olefins
Ga	Gallium
GC-MS	Gas chromatography-mass spectrometry
Ge	Germanium
GVL	Gamma-valerolactone
H^+	Hydrogen
H_2DPT	4′-(4-(3,5-dicarboxylphenoxy) phenyl)-4,2′:6′,4″-terpyridine
H_2O	Water
H_2O_2	Hydrogen peroxide
HCC	Human hepatocellular carcinoma
Hg	Mercury
HMF	5-hydroxymethylfurfural
HOMO	Highest Occupied Molecular Orbital
HT	high temperature
IC_{50}	Half maximal inhibitory concentration
Im	Imidazole
IUPAC	International Union of Pure and Applied Chemistry
IZA	International Zeolite Association
k_{cat}	Constant that describes the turnover rate of an enzyme-substrate complex to product
LAS	Lewis acid site
LED	Light-emitting diode
LMCT	Ligand to metal charge transfer
LMMEs	Ligand-mediated metal ensembles
LT	Low temperature
LUMO	Lowest Unoccupied Molecular Orbital
MAC	Multi-analyzer crystal
MALDI	Matrix-assisted laser desorption/ionization
MALDI-TOF-TOF MS	Matrix-assisted laser desorption/ionization time-of-flight/time-of-flight mass spectroscopy

MeOH	Methanol
Mn	Manganese
MOFs	Metal organic frameworks
MOR	Mordenite
MS	Mass spectroscopy
MYTHEN	Microstrip sYstem for Time rEsolved experimeNts
N	Nitrogen
Na	Sodium
NaOH	Sodium hydroxide
NBT	Nitro blue tetrazolium chloride
NH_2	Amine group
NH_2-BDC	2-aminoterephthalic Acid
NH_3-TPD	Ammonia temperature programmed desorption
NH_4	Ammonium
Ni	Nickel
NOx	Nitrogen oxides
O	Oxygen
O_2	Dioxygen
OH	Hydroxide
P	Phosphorus
PBUs	Primary buliding units
PCNs	Porous coordination networks
PCPs	Porous coordination polymers
PDOS	Projected density of states
PSE	Post-synthetic exchange
PSM	Post-synthetic modification
Pt	Platinum
PXRD	Powder x-ray diffraction
Py-FTIR	Pyridine-assisted Fourier-transform infrared spectroscopy
Py-IR	Pyridine-adsorbed FT-IR
ROS	Reactive oxygen species
RXRD	Resonant X-ray diffraction
S	Sulfur
SALE	Solvent-assisted linker exchange
SBUs	Secondary building units
SDA	Structure-directing agent
SEM	Scanning electron microscopy
SH	Thiol group

Si	Silicon
SiO_2	Silicon oxide
Sm	Samarium
Sn	Tin
SO_3H	Sulfonic acid
SOD	Super oxide dismutase
SOFs	Site occupancy factors
STA	Syngas to aromatic
STEM	Scanning transmission electron microscopy
SXRD	Synchrotron X-ray diffraction
TEOS	Tetraethyl orthosilicate
TGA	Thermogravimetric analysis
TPAOH	Tetrapropylammonium Hydroxide
UiO	Universitetet i Oslo
USALE	Ultrasonic-assisted linker exchange
USY	Ultra-stable Y zeolite
UV	Ultraviolet
UV-Vis	Ultraviolet–visible spectroscopy
UV-Vis-NIR DRS	Ultraviolet-visible-Near-Infrared Diffuse Reflection Spectroscopy
WT	Wavelet transform
XAFS	X-ray absorption fine structure
XANES	Near-Edge X-ray Absorption Fine Structure
XPS	X-ray photoelectron spectroscopy
XRD	X-ray diffraction
XRF	X-ray fluorescence spectroscopy
Zn	Zinc
Zn(NO3)2.6H2O	Zinc nitrate hexahydrate
ZnO	Zinc oxide
ZrO_2	Zirconium oxide

Chapter 1 Introduction

1.0. The importance of studying bifunctional catalysts

The investigation of bifunctional catalysts holds significant importance in the field of catalysis. Crystalline porous materials like zeolites and metal-organic frameworks (MOFs) find widespread application in gas adsorption, separation, and catalysis due to their consistent pore size distribution, diverse framework structures, and chemical adaptability [1–4]. These materials, with their uniform framework structure and high surface area, not only serve as catalysts based on their functionality but also as carriers for catalytic species [5–12]. When combined with doped active sites, crystalline porous materials offer abundant active sites that enhance catalytic reactions.

Porous materials, recognized for their exceptional stability and high surface area, act as supports that create a secure environment for immobilizing active species on their surfaces or within their pores. This immobilization prevents the loss or undesirable aggregation of active species, thereby enhancing stability, resistance to poisoning, and prolonging the lifespan of the catalyst. The unique channel and adjustable pore structures enable favorable reaction kinetics and selectivity. Modifying the channel and pore structures of porous materials allows for selective adsorption of substrate molecules and spatial confinement of catalytic reactions, ultimately improving catalytic efficiency and selectivity.

Active species anchored on porous materials play a pivotal role in catalytic processes, encompassing a diverse array of entities such as metal nanoparticles, organic molecules, solid acids, and other catalysts. The integration of active species not only enhances catalytic performance based on their individual properties but also introduces additional functionality in catalysis. This includes the modulation of intermediate formation, activation of molecules, and the selection of reaction pathways based on the interaction between the supported active species and the electrons or spatial structures of the porous support, culminating in heightened catalytic efficiency and selectivity. A bifunctional catalyst can be prepared by combining the porous support and active species.

The coexistence of two active species in bifunctional catalysts engenders a unique synergistic interaction that imparts distinctive catalytic reactivity. This interaction facilitates substrate co-activation and the progression of tandem or cascade steps within catalysis. Furthermore, the carrier's distinctive properties and pore structures establish an environment conducive to optimal performance by the supported catalytic species, thereby enabling the observation of a synergistic effect in active species-doped supports. Leveraging these benefits, the utilization of bifunctional catalysts enhances catalytic

performance through functional regulation, thereby yielding augmented catalytic efficiency and selectivity.

In catalytic processes, the synergistic interplay between carrier materials and supported catalytic species is pivotal for enhancing catalytic performance. Bimetallic synergistic catalytic systems, wherein two metal species immobilized through different strategies interact, represent a prevalent form of synergistic catalytic system. This interaction engenders various forms of synergistic effects. Initially, the metal species on the carrier furnish abundant active sites, heightening reactivity and selectivity in reactions. Additionally, the two metal species can interact to form alloys or cooperative catalysts that govern the reaction pathway and intermediate generation in catalytic reactions. Secondly, the distinct electronic properties and catalytic activities of the two metal species in bimetallic synergistic catalytic systems foster electron transfer and redistribution, thereby amplifying the efficiency and selectivity of catalytic reactions. Furthermore, bimetallic synergistic catalytic systems bolster the stability and resistance to poisoning of catalysts through the synergistic effect, thereby prolonging the catalyst's functional lifespan.

Beyond bimetallic synergistic catalytic systems, various other types of synergistic catalytic systems have been extensively explored. For instance, supported metal species can interact with non-metal species on the carrier, culminating in dual active site synergistic catalytic systems. The non-metal species can provide ancillary sites or electron transfer pathways to modulate the catalytic activity and selectivity of the metal species. Moreover, metal-functionalized group synergistic catalytic systems can be established through the interaction between supported metal species and functional groups on the porous support. These functional groups can furnish additional reaction sites or the specialized environment essential for substrate adsorption and activation, thereby augmenting the efficiency and selectivity of catalytic reactions.

In essence, crystalline porous materials stand as pivotal carriers in catalytic processes. Their interaction with supported active species not only furnishes a stable environment and regulates reaction dynamics and selectivity but also engenders synergistic effects to enhance catalytic performance. While bimetallic synergistic catalytic systems remain a focal point of the study, the exploration and application of other forms of dual active site synergistic catalytic systems present promising avenues. These investigations hold substantial importance in shaping the design and advancement of efficient catalysts, propelling the evolution of catalytic science.

1.1. Support for bifunctional catalyst

Porous materials serve as excellent raw materials for crafting bifunctional catalysts, acting not only as the catalyst itself but also as a supportive structure for other doped active species. Among the array of materials available, zeolites and metal-organic frameworks (MOFs) stand out as popular examples due to their attributes such as high surface area, remarkable stability, and versatile applications. This section delves into the exploration of bifunctional catalyst preparation using zeolites and MOFs, shedding light on the background information and strategies for synthesizing and modifying these materials.

Zeolite

Zeolites, being crystalline materials primarily comprised of interconnected silica and alumina tetrahedra bridged by oxygen atoms, form the backbone of bifunctional catalysts [13]. These tetrahedra, made up of silicon (Si^{4+}) and aluminum (Al^{3+}) ions, act as the primary building units (PBUs) within the zeolite's unit cell. Represented as TO_4 units, where T signifies the silicon or aluminum ions and O_4 denotes the bridging oxygen connecting two T atoms [14]. A general equation is employed to represent the crystalline unit cell of zeolite:

$$M_{\frac{y}{a}}[Al_y Si_{x-y} O_{2x}] \cdot bH_2O$$

Here, '**M**' represents the cation, encompassing protons, alkali metal cations, or alkali earth metal cations. The variables '**a**' and '**b**' denote the oxidation state of these cations and the quantity of water molecules within a unit cell, respectively. Additionally, '**x**' and '**y**' correspond to the total number of T atoms and the number of Al atoms.

Incorporating heteroatoms and diverse combinations of primary components not only enhances the catalytic activity but also introduces shape selectivity within the zeolite structure. This customization allows for the tailored design of zeolite catalysts for bifunctional catalyst synthesis. To lay the groundwork for the synthesis of a desired zeolite support for bifunctional catalyst production, the subsequent paragraph will delve into the background and critical factors involved in zeolite synthesis.

As mentioned above, the Si/Al ratio in zeolites can vary from 10 to 50 or even higher. However, managing the abundance of Al is crucial to prevent excessive defects within the zeolite framework, which can compromise its crystallinity. Zeolite frameworks consist of infinite unit cells, each constructed from secondary building units (SBUs) composed of TO_4 tetrahedra. These SBUs typically assemble into cage-like structures known as cage-building units (CBUs), which give rise to diverse morphologies such as cubic, tetrahedral, hexagonal, and other complex structures, depending on the

configuration of the TO_4 tetrahedra [14]. An example of a cage-building unit is depicted in **Figure 1.1**. By combining different CBUs, channels of various shapes and pore sizes are created, influencing the adsorption properties of the zeolite. Each zeolite framework is identified by a three-letter code determined by the Si/Al ratio and the basic unit's morphology, with notable examples being MFI (e.g., ZSM-5) and FAU (e.g., zeolite Y). The International Zeolite Association (IZA) has classified over 250 framework types, each designated by a unique code [15].

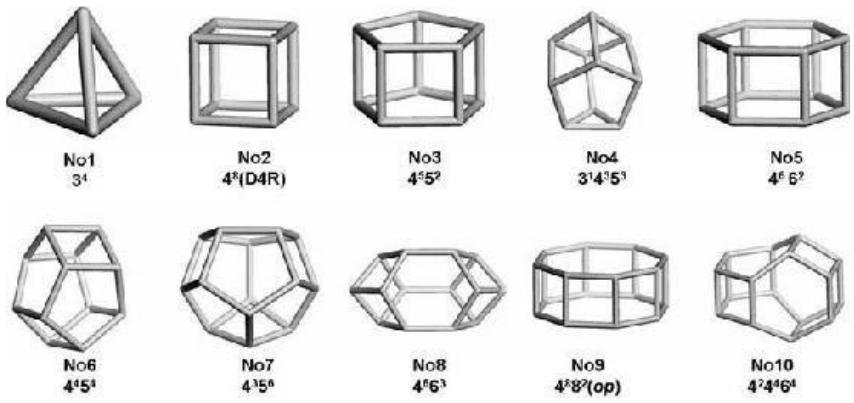

Figure 1.1. Example of the cage building units in zeolites. Reprinted with permission from ref. [14]. Copyright (2017) Int. Res. J. Environmental Sci.

To attain the desired morphology or framework type of zeolite, meticulous control over various parameters during the synthesis process is essential. These parameters include the component ratio, pH value, reaction temperature, and the addition of substances like mineralizers, templates, and structure-directing agents [16,17].

Most zeolites are synthesized using a hydrothermal method within a temperature range of 333 K to 473 K. The crystallization rate, particle size, and morphology of zeolites are significantly influenced by the chosen crystallization temperature and time. Higher temperatures expedite crystallization, reducing the time needed for nucleation and crystal growth. For instance, in ZSM-5 synthesis, lowering the crystallization temperature from 180 °C to 150 °C extends the crystallization time from around 12 hours to approximately 28 hours [18]. The reaction temperature also dictates the particle size of the zeolite, with lower temperatures favoring nucleus formation and smaller crystal production. For instance, zeolite A crystals have a diameter of about 2 μm at 333 K, but at 473 K, the diameter increases to around 4 μm with a wider size distribution [19]. Similarly, for ZSM-5, the particle size grows from 10-20 nm to 40-60 nm as the temperature increases from 363 K to 443 K [20].

In the realm of zeolite synthesis, achieving high-quality crystallization is contingent upon various factors such as temperature, duration, and notably, the pH of the precursor solution. The pH of the solution plays a pivotal role in determining the successful crystallization of zeolites, alongside temperature and duration. The synthesis process typically begins with an amorphous gel, the solubility of which is directly influenced by the alkalinity of the solution. Lechert's findings underscore the critical nature of maintaining a specific pH range for the successful preparation of zeolites with distinct framework types [21]. For instance, faujasites (FAU) crystallize optimally within a pH range of 12.3 to 13.8, mordenite (MOR) thrives between 11.3 and 12.7, and a lower pH is necessary for the synthesis of ZSM-5. Moreover, variations in pH within the precursor solution significantly impact the coordination species of the T atom. Elevated pH values, particularly above 12, lead to the generation of more condensed silicate species, while reduced pH levels increase dimer and four-membered ring species. This pH dependency extends to zeolites containing other T atoms like P, Ge, and Sn. The adjustment of the pH environment is crucial for preparing bifunctional catalysts as it influences the successful introduction of active species, with the heteroatom typically requiring a specific pH for dissolution in the precursor solution.

In the intricate design of zeolite frameworks, additives play a pivotal role, with mineralizers and structure-directing agents standing out as crucial factors. Mineralizers, instrumental in controlling the solubility and mobility of framework-forming atoms, establish an optimal pH environment for crystallization while structure-directing agents dictate the zeolite's structure and pore dimensions. This includes managing the distribution of framework atoms like Al, Zn, and Ge [22,23]. Mineralizers, like hydroxide (OH^-) and fluoride ions (F^-), modulate solubility during crystallization, affecting dissolution rates and the final composition of the zeolite by altering the concentration of framework species.

Hydroxide ions (OH^-) are instrumental in enhancing the dissolution of essential framework constituents such as aluminum and silicon, leading to their presence as silicate and aluminosilicate anions in alkaline solutions. The behavior of silicate and alumina differs in the presence of OH^- ions. OH^- ions ionize the silanol groups and cleave the siloxane bonds, which increases the solubility of silicate species. In contrast, OH^- ions solubilize alumina by forming $Al(OH)_4^-$ anions, without inducing further ionization or oligomerization. Given these characteristics, the concentration of OH^- ions is of considerable importance in the synthesis of aluminum-rich zeolites. As the concentration of OH^- ions rises, the stability of silicate species is reduced, inhibiting the self-condensation of silicate units. Nonetheless, the propensity to condense with aluminate species remains unaffected, promoting the condensation reaction between silicate and aluminate to construct aluminosilicate frameworks [22].

Analogous to the hydroxide ion (OH^-), the fluoride ion (F^-) also can enhance the solubility of framework atoms, such as aluminum (Al) and silicon (Si), by substituting the hydroxyl group and forming a fluoride complex. This fluoride complex creates a relatively neutral crystallization environment, which facilitates the use of organic additives that are unstable under highly alkaline conditions [16]. Similarly, the concentration of the F^- ion influences the composition of the zeolite due to its role in stability control. Among the various framework atoms (T atoms), there is a hierarchy of stability within the fluoride complex, with the order being $Al^{III} > Fe^{III} > Ga^{III} > Si^{IV}$ [22]. Owing to the lower stability of the silicon fluoride complex, the synthesis of silicon-rich zeolites is more feasible when a higher concentration of fluoride ions is used, as the least stable fluoride complex demonstrates increased reactivity in condensation reactions.

The template, also referred to as a structure-directing agent (SDA), plays a pivotal role, surpassing that of the mineralizer, in controlling the framework structure (framework type) of zeolites, as previously discussed. The evolution of zeolite framework types is fundamentally dependent on the advancement of structure-directing agents [24,25]. Structure-directing agents are broadly categorized into two groups: inorganic templates and organic templates. The former generally comprises alkali or alkaline earth metal cations, whereas the latter includes bulky organic molecules such as quaternary ammonium or certain amine compounds. The mechanism through which SDAs facilitate zeolite crystallization involves neutralizing the lattice charge of the framework. The zeolite precursor (T atom) encapsulates the SDA cation, forming the primary building block, which then aggregates into the secondary building unit (SBU), culminating in the formation of the complete zeolite structure [17,23]. The choice of SDA, influenced by the disparity in size and bulkiness between inorganic and organic SDAs, enables control over the zeolite's chemical composition (e.g., Si/Al ratio, content of heteroatoms). As previously mentioned, the mechanism of the SDA neutralizes the lattice charge and fosters the crystallization of the zeolite framework. Owing to the smaller dimensions of inorganic SDAs compared to organic ones, a greater number of inorganic SDAs can be accommodated within the cages of the zeolite precursor's building blocks. Given that the negative charge is predominantly associated with the Al tetrahedra, zeolites synthesized with inorganic SDAs exhibit a low Si/Al ratio due to the lattice charge neutralization by the inorganic SDA. Conversely, the substantial size of organic SDAs limits the insertion of positive charges into the building blocks, leading to a decreased presence of Al atoms in the structure and the synthesis of zeolites with high Si/Al ratios.

The positioning of T atoms near mineralizers and SDAs is influenced by bonding interactions with additives, impacting the reactivity of bifunctional catalysts. The

quantity and ratio of additives play a crucial role in determining the distribution of active species within the framework [26]. Mineralizers, being smaller, typically occupy internal positions within channels or small pores, while SDAs localize at the intersection of channels and larger pores due to their bulkier nature. Additives further influence the positioning of active species by interacting with active components. Adjusting the mineralizer to SDA ratio can modify this distribution, affecting the synergistic activity between active species. Maintaining an optimal distance between these species is vital for fostering effective catalysis, underscoring the importance of carefully adjusting these ratios.

The substitution of a framework silicon atom (Si^{4+}) with a trivalent aluminum atom (Al^{3+}) introduces an anionic charge, which can be neutralized by a compensating cation (e.g., H^+, Na^+, NH^{4+}), positioned on the bridging oxygen atoms (Si–O(H)–Al). This incorporation of an H^+ ion creates a Brønsted acid site within the zeolite framework, thereby endowing it with acid properties and enabling it to function as a solid acid [27]. The acidity of the zeolite can be modulated by the presence and concentration of various trivalent atoms (B, Al, Ga). Shirazi et al. conducted a study on the impact of the Si/Al ratio on the acidity of ZSM-5 zeolite, finding that a lower Si/Al ratio led to increased acidity, as determined through NH_3-TPD analysis [28]. Furthermore, Jones et al. explored how the acid strength of MFI zeolite could be altered by replacing Al with other trivalent atoms (e.g., B, Ga, and Fe) [29]. In their research, methods such as methanol dehydration, chemical titration with pyridine, and DFT calculations of deprotonation energy were utilized to assess the acidity of the zeolite samples. The findings suggest that the acid strength of zeolites doped with trivalent atoms follows the sequence Al > Ga > Fe >> B. By introducing different trivalent atoms, the Brønsted acid strength can be modified without changing the number of trivalent atoms, ensuring the number of acid sites can be controlled precisely for preparing the bifunctional catalyst.

In addition to Brønsted acidity, the porous structure of zeolites provides a large surface area for the dispersion of active species, offering high shape selectivity during catalysis. Wang et al. conducted research aimed at optimizing shape selectivity in the synthesis of p-xylene from toluene by modifying ZSM-5 zeolite [30]. The modified ZSM-5 zeolite, featuring an effective channel system, demonstrated a selective production of p-xylene with a selectivity of 99.3 %, in contrast to the standard ZSM-5, which exhibited only a 50.1 % selectivity towards p-xylene. Furthermore, Rastegar et al. explored the impact of zeolite topology on selectivity in the alkylation of benzene with ethylene. They employed BEA, MOR, and FAU zeolites, which possess similar framework compositions, for the catalytic alkylation of benzene to produce ethylbenzene. The BEA zeolite showed a markedly higher benzene conversion compared to the other two zeolites, attributable to its greater acid strength and relatively large internal cavities

derived from the BEA topology, which promoted activity in benzene alkylation. Moreover, the BEA zeolite exhibited enhanced selectivity towards ethylbenzene, while the other zeolite samples generated heavier side products (C>9) due to a lack of shape selectivity within their supercages, resulting in the formation of diethylbenzene and heavier byproducts. These studies underscore the significance of zeolite topology in influencing the shape selectivity of catalytic products.

This section lays the groundwork for understanding zeolites and introduces strategies for designing zeolites to customize morphology, acidity, and active site distribution within the framework. Subsequent sections will delve into background information on metal-organic frameworks (MOFs) to further broaden the scope of materials for catalytic applications.

Metal-organic frameworks (MOFs)

Metal-organic frameworks (MOFs), also referred to as porous coordination polymers (PCPs) or porous coordination networks (PCNs), constitute a distinctive category of porous materials incorporating metal atoms or clusters as nodes and organic ligands as linkers [31,32]. The morphology, porosity, and functionality of MOFs can be tailored by adjusting the metal nodes and organic linkers. Leveraging the diverse chemical and physical properties of MOFs, these materials exhibit immense potential across various domains, including gas storage, gas separation, sensing, and catalysis [3,4,33]. The pivotal roles of functionality and porosity in MOF chemistry significantly shape their properties, thereby enhancing their performance in diverse applications.

The inherent advantages of MOFs position them as promising materials for catalyst support. To elucidate the process of preparing a suitable MOF for bifunctional catalyst synthesis, the subsequent discussion will introduce the foundational elements and considerations governing MOF synthesis and design.

The International Union of Pure and Applied Chemistry (IUPAC) categorizes porous materials like zeolites, metal-organic frameworks (MOFs), and activated carbon into three pore-size classifications: microporous (<2 nm), mesoporous (2 nm-50 nm), and macroporous (>50 nm). As previously mentioned, the morphology and porosity of MOFs can be altered through variations in metal nodes and organic linkers. An illustrative instance is the creation of isoreticular MOFs through linker modifications. For example, MOF-5 (IRMOF-1) exemplifies a classic MOF comprising Zn_4O clusters and dicarboxylate linkers, showcasing isoreticular MOFs with different pore sizes achieved via linker adjustments. Eddaoudi et al. conducted a porosity analysis of isoreticular MOFs for methane storage [34], demonstrating that replacing 1,4-benzenedicarboxylic acid (the linker in IRMOF-1) with [1,1':4',1''-terphenyl]-4,4''-dicarboxylic acid (the linker in IRMOF-16) increased the free volume from 79.2 % to 91.1 %, while reducing the density from 0.61 g/cm^3 to 0.21 cm^3, yielding significant implications for gas storage applications.

In addition to porosity modulation, functionalizing MOFs presents an effective approach to broaden their potential applications. Functionalization can occur through alterations at two key positions: the metal node and the organic linker. During MOF formation, the metal node can interact with non-framework ligands such as solvent molecules (e.g., water, carboxylic acid), which can be easily removed during subsequent post-treatment procedures. This removal exposes coordination unsaturated sites (CUS) at the metal node, capable of acting as Lewis acid catalysts. However, the formation of CUS introduces defects into the MOF structure. Intentionally inducing defects in MOFs can be achieved through bottom-up synthesis or post-synthetic

treatment methods. In bottom-up synthesis, the addition of a modulator can expedite crystallization, inducing defects in the MOFs. The modulation can enhance crystallinity but excessive amounts can lead to defect formation by blocking metal node coordination sites. Microwave-assisted synthesis and sonication are techniques that can accelerate crystallization, but rapid crystallization may result in incomplete binding between the metal node and organic linker, causing missing linker defects.

Post-synthetic treatments can also be employed to introduce defects in MOFs by removing framework linkers. Techniques such as heat treatment and acid/base treatment facilitate linker removal. Heat treatment involves decomposing framework linkers at high temperatures to selectively expose the metal node after treatment. By controlling the decomposition temperature, partial removal of the linker can be achieved, allowing controlled exposure of the metal node [35,36]. Hybrid linkers can be utilized in synthesis prior to heat treatment to enhance control over defect generation by using linkers with varying decomposition temperatures [37]. Acid/base treatment, similar to heat treatment, breaks the bond between the metal node and the framework linker for linker removal. Functionalizing organic linkers in MOFs can also be accomplished through bottom-up synthesis or post-synthetic treatment. However, direct synthesis of MOFs with specific functional groups may be challenging due to thermal sensitivity or solubility issues, making post-synthetic treatment a viable alternative for organic linker functionalization.

Post-synthetic modification (PSM) is a fundamental method for enhancing the physical properties of MOFs through linker functionalization, enabling the introduction of diverse functional groups or active species into the framework. PSM facilitates the incorporation of various functional groups like organic functional groups, Brønsted acids, and metal sites, thereby expanding the scope of applications without altering the framework structure significantly [38–40]. Introducing acid sites in MOFs through post-synthetic treatment represents a desirable option for creating heterogeneous acid catalysts. Functionalized Brønsted acid MOFs, with their porous structure and tunable pore size, are well-suited for diverse acid catalytic reactions. Fracaroli et al. reported the insertion of a peptide chain via PSM into MOF-74-III to introduce enzyme-like complexity [41]. The stepwise synthesis approach of the tripeptide chain within the framework involved the use of Boc-protected primary amine to prevent the auto-polymerization of the amine source into a peptide (**Figure 1.2**). The synergistic effect between MOF-74 and the peptide chain resulted in an increase in the selectivity of α-chlorination products of butyraldehyde from 2 % *ee* to 20 % *ee* compared to the reference proline catalyst. Zhang et al. reported the functionalization of UiO-66-N_3 with phenylacetylene via PSM for selective mercury detection [42]. Through the click reaction between UiO and phenylacetylene, a triazole unit formed within the UiO framework

for metal binding. Among various transition metals, only mercury exhibited a remarkable fluorescence signal reduction upon binding with the triazole group. The incorporation of Hg^{2+} caused a significant quenching effect on the fluorescence intensity of UiO-66 compared to other transition metal ions. In addition to introducing extra functional groups, the introduction of acid sites is also a desirable option, as heterogeneous acid catalysts serve as alternatives to traditional homogeneous acid catalysts. Leveraging the advantages of porous structure, large surface area, and tunable pore size, functionalized Brønsted acid MOFs are suitable for various acid catalytic reactions. Britt et al. reported the synthesis of Brønsted acid-derived IR-MOF-3 through the ring-opening reaction of 1,3-propane-sultone and subsequent coupling reaction with the amine group on IR-MOF-3, achieving 57 % successful functionalization [43]. Apart from introducing acid sites via coupling reactions, the oxidation of functional groups on the framework linker is also a feasible approach for acid site introduction. Phang et al. reported the synthesis of UiO-66 with sulfonic acid groups by oxidizing thiol groups with hydrogen peroxide into sulfonic acid groups [44]. Leveraging the strong acid properties of sulfonic acid groups, the proton conductivity of UiO-66-$(SO_3H)_2$ increased to 1.4×10^{-2} S cm^{-1} at 25 °C and 90 % RH (3.5×10^{-7} S cm^{-1} for UiO-66 and 6.3×10^{-6} S cm^{-1} for UiO-66-$(SH)_2$.

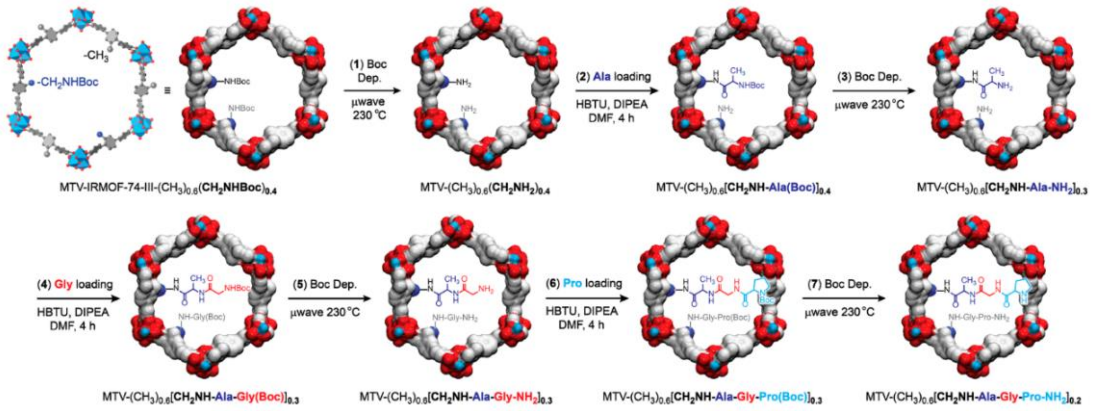

Figure 1.2. Seven Post-synthetic Reactions to Achieve Enzyme-like Complexity in the Pores of MTV-IRMOF-74-III- $(CH_3)0.6(CH_2NHBoc)0.4$. Reprinted with permission from ref. [41]. Copyright © 2016 American Chemical Society.

Post-synthetic exchange (PSE) stands out as an advanced method for functionalizing MOFs, involving the modification of not only the organic linker but also the alteration of the MOFs lattice through the replacement of the organic linker [45,46]. This approach allows for the introduction of ligands with specific functional groups or even linkers doped with metals, especially when certain functional groups are unsuitable for the MOF synthesis environment (e.g., acids, aldehydes, or amino acids), or when achieving the desired MOF preparation through post-ligand modification (PSM) is not feasible

(e.g., metal doping on the ligand). To delve into the potential applications of PSE, Kim et al. investigated MOF functionalization through PSE, considering different aspects, including PSE between two MOFs, PSE from the liquid phase, and (3) diversity of PSE with linkers possessing different functional groups [39]. Regarding PSE between two MOFs, UiO-66-Br and UiO-66-NH_2 were selected for PSE using various parameters such as temperature and solvent. Among the polar solvents tested ($CHCl_3$, MeOH, DMF, and water), water exhibited the highest exchange rate of 97 % at 85 °C. Subsequently, stability tests were conducted on the MOFs after PSE. XRD and TGA results indicated that the crystallinity of the MOFs remained intact after PSE, and their thermal stability was comparable to other UiO-66 derivatives. For PSE from the liquid phase, UiO-66-Br and NH_2-BDC were utilized for PSE in water at different temperatures. The incorporation of NH_2-BDC into MOF increased from approximately 9 % to 76 % as the reaction temperature rose from room temperature to 85 °C, demonstrating the feasibility of MOF functionalization through PSE. Furthermore, PSE trials were performed on MOFs using BDC with different functional groups. Azido-, hydroxyl-, and dihydroxyl-BDC linkers were selected for this experiment. Azido- and hydroxyl-BDC resulted in a degree of incorporation of around 50% after a 2-day reaction in water at room temperature. However, dihydroxyl-BDC exhibited lower incorporation of only approximately 15 %, which increased to 42 % when 10 equivalents of the ligand were used. To achieve highly efficient PSE, Razavi and Morsali reported a novel approach called ultrasonic-assisted linker exchange (USALE) for PSE [47]. In the sonochemical method, acoustic cavitation provides substantial energy to accelerate the activation of PSE. In their experiment, TMU-4 was selected for PSE with H_2DPT ligand, resulting in the conversion to TMU-34 through PSE. When comparing solvent-assisted linker exchange (SALE) and ultrasonic-assisted linker exchange (USALE) for PSE between TMU-4 and H_2DPT, the time required for complete PSE was 52 hours (3120 minutes) and 120 minutes, respectively, with similar exchange ratios for both methods. Moreover, MOF samples prepared via USALE exhibited better performance in gas adsorption experiments compared to samples prepared through SALE, as USALE facilitated higher exchange kinetics of the linker, resulting in a more robust structure and improved porosity and surface area.

This chapter provides a comprehensive background on MOFs, emphasizing key components such as the SBU and framework linkers which can be modified to tailor various aspects of MOFs, including their morphology, pore size, and functionality. After introducing porous materials like zeolites and MOFs, the subsequent chapter will explore strategies for incorporating metals into these materials.

1.2. Metal introduction approach in zeolites

Metals play a pivotal role as active species in the creation of bifunctional catalysts when integrated with zeolites and MOFs as supporting materials. This chapter delves into the strategies for incorporating doped metal species into zeolite.

Within zeolites, metal species can be categorized into two groups based on the method of introduction: extra-framework species and framework species. Extra-framework species are typically located on the surface or within the pores and channels of the zeolite framework. Introducing these species usually involves two common methods: ion exchange and impregnation process [48]. On the other hand, framework species refer to metals that become an intrinsic part of the zeolite framework. The incorporation of framework species can be achieved through two primary approaches: bottom-up synthesis and isomorphous substitution. In the bottom-up synthesis method, the doped metal becomes part of the growing zeolite framework during its formation. Conversely, isomorphous substitution entails replacing framework atoms with metal atoms of similar size, resulting in a modified zeolite structure. The illustration of the position of the metal introduced to the zeolite framework is shown in **Figure 1.3**.

Ion exchange approach

In the ion exchange approach, the introduced metal typically resides at the Brønsted acid site (BAS) and is immobilized through metal-BAS interactions. The bonding types vary depending on the cation present on the BAS. The uniform structure of the zeolite framework ensures the consistent location of the BAS, facilitating the uniform distribution of the doped metal within the channels and pores of the zeolite. However, the amount of doped metal is limited by the availability of BAS, and the solid acid's capacity diminishes as BAS is consumed during metal doping [49].

Impregnation approach

The impregnation approach can be classified into two methods: wet impregnation and wetness impregnation. Wet impregnation involves using a minimal amount of solvent to dissolve the metal salt, which is then absorbed by the zeolite through capillary action. In wetness impregnation, the metal salt is mixed with the zeolite material without solvent dissolution. After adding the metal source, the precursor undergoes calcination to remove the solvent and facilitate the doping process [50]. Unlike the ion exchange method, the doped metal in the impregnation approach is typically located on the material’s surface rather than within the pores and channels, potentially leading to metal aggregation. Since the immobilization of the metal species is based on the bond formation during the calcination step, the presence of binding sites such as Brønsted acid sites (BAS) is no longer crucial for the introduction process.

Ion exchange vs. Impregnation

By comparing the introduction methods, the ion exchange approach offers a significantly uniform distribution of active species, leveraging the presence of BAS. Achieving precise introduction of active species is easier with this method than with the impregnation approach. In contrast, the impregnation method can introduce a higher quantity of metal since only a minimal amount of the doped metal would be extracted during post-treatment. Additionally, there are fewer restrictions on the type of metal that can be incorporated into the support compared to the ion exchange technique. To compensate for the limitation of metal introduction by ion exchange method, the modification of the cation may be able to solve. Changing the cation from H^+ ion into NH_4^+ ion may promote the encapsulation of metal ions by complex formation rather than ion exchange reaction to broaden the type of metal able to be introduced via the ion exchange approach.

Bottom-up synthesis approach

In the bottom-up synthesis approach, the metal salt is added to the silica precursor solution and becomes incorporated into the framework during crystallization. To prevent aggregation of the metal salt, various solutions are employed, such as pH adjustment, multidentate ligands, and organic templates [51]. During the crystallization process, the metal will occupy the most stable positions with minimal impact on the framework's structural integrity. Additionally, the location of the doped metal can be influenced by additives like structure-directing agents and mineralizers [26,52,53]. Due to the significant differences in size and oxidation state between the metal species and framework atoms (Al and Si), the amount of framework metal is limited by the stability of the framework, as the presence of framework metals introduces defects into the zeolite framework.

Isomorphous substitution approach

In the isomorphous substitution approach, the process involves two steps: dealumination/desilication of the framework atoms (tetrahedral sites) and subsequent substitution by the metal atom in the gas phase. The removal of framework atoms (dealumination: Al, desilication: Si) typically occurs prior to the insertion of heteroatoms, resulting in the formation of "silanol nests" [54]. Dealumination, often achieved through steaming or treatment with mineral acids, leads to a decrease in the number of Brønsted acid sites due to the removal of Al from the zeolite framework. Desilication is commonly performed in an alkali medium and does not significantly impact the number of acid sites or cause significant changes in the Si/Al ratio. Depending on the extent of framework atom removal, mesopores may be generated,

and the Al concentration influences the size of the mesoporous texture. Silica-rich domains are prone to leaching, resulting in the formation of larger mesopores.

Bottom-up synthesis vs. Isomorphous substitution

The bottom-up synthesis method offers the advantage of easily controlling the amount of metal by adjusting the precursor solution, enabling the simultaneous introduction of various active species into the framework. However, achieving precise control over the positioning of these active species can be challenging, as they tend to settle in specific locations to maintain the framework's stability. This necessitates intricate adjustments to synthesis parameters, such as the addition of additives and manipulation of the pH environment. On the other hand, isomorphous substitution ensures precise control over the positioning of active species, leveraging the regular variation of aluminum locations in the zeolite framework with specific Si/Al ratios. Despite this advantage, limitations exist regarding the control of metal quantity and the potential structural damage to the framework. Metal substitution relies on dealumination/desilication processes, where the amount of integrated metal depends on the extent of these processes. This dependence makes precise control challenging, and excessive desilication can result in the formation of hierarchical and mesoporous structures due to the breakdown of building units. Additionally, dealumination can lead to a decrease in the number of Brønsted acid sites (BAS).

This chapter serves to present the strategies employed in the preparation of metal-doped zeolite catalysts. By implementing distinct approaches to introduce metals, the doped species can be categorized as framework species and extra-framework species. Extra-framework species are situated on the zeolite framework's surface or within its pores and can be introduced through ion exchange or impregnation processes. Conversely, framework species become an integral component of the zeolite framework and can be incorporated via bottom-up synthesis or isomorphous substitution. The chapter comprehensively explores diverse methodologies and techniques for metal introduction into zeolites, thereby providing valuable insights into the distribution, stability, and characteristics of the doped materials.

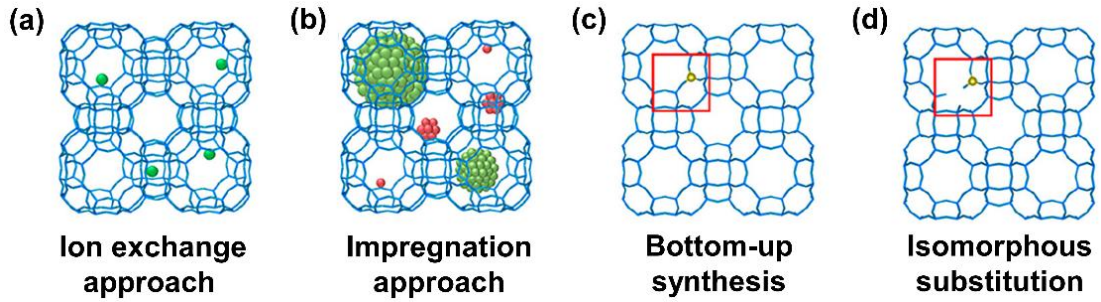

Figure 1.3. the illustration of the location of the metal species doped by (a) ion exchange approach, (b) impregnation approach, (c) bottom-up synthesis, and (d) isomorphous substitution. Reprinted with permission from ref. [48]. Copyright © 2022 American Chemical Society.

1.3. Metal introduction approach in MOFs

In the realm of metal introduction approaches within metal-organic frameworks (MOFs), akin to zeolites, incorporating additional metals stands as a viable method for crafting bifunctional catalysts. Within MOFs, three primary types of active centers facilitate metal introduction: those located on the framework linker, the secondary building unit (SBU), and within the pores, the corresponding scheme of the active center is shown in **Figure 1.4**. These active centers secure the metal atom through interactions such as acid-base and metal-ligand bonding. The key distinctions among these active centers lie in the positioning of the doped active species within the MOFs framework, the parameters governing MOFs preparation, and the impact on the framework structure. The subsequent discussion will delve into the preparation procedures and characteristics of these active centers.

Active center on framework linker

When it comes to metal doping on the framework linker, common methods include post-synthetic modification (PSM) and post-synthetic exchange (PSE). In PSM, diverse functional groups on the framework linker like amine, sulfonic acid, and carboxylic acid facilitate metal atom integration through complex formation. However, certain metals necessitate specific conditions for complex formation, prompting the utilization of the PSE method. In PSE, preassembled MOFs undergo a framework linker replacement. During the creation of metal-doped MOFs, the target metal initially forms a complex with the functionalized framework linker under specific conditions. Subsequently, the metal-doped linker exchanges with the framework linker aided by a solvent or specific conditions [56,57]. The PSE method proves useful when the linker is unsuitable for direct synthesis due to solubility challenges.

Active center on SBU

Regarding metal doping on the SBU, successful integration hinges largely on defects within the MOFs. The SBU's structure is dictated by the number of metal centers, while the MOFs' symmetry and morphology are influenced by the SBUs due to the SBU's geometry and its maximum number of linkers for binding [58]. When introducing the metal species on the SBU, it occupies positions meant for linker binding, potentially generating defects in the MOFs framework. However, not all metal introductions impact framework stability, especially if the SBU of certain MOFs morphologies isn't fully saturated. Since the SBU chiefly comprises the metal atom and bridging ligands like oxo groups and hydroxyl groups, integrating the metal atom on the SBU typically involves forming bonds with the bridging ligand, akin to the framework linker. Therefore, ligands with functional groups resembling those of the framework linker are selected for preparing the metal complex precursor.

Active center within pores

Metal doping within the pores of MOFs entails two primary steps: precursor introduction and nano-particle/cluster formation through heat treatment. Various methods, including chemical vapor deposition (CVD), solid grinding, liquid impregnation, and encapsulation, can be employed for metal precursor introduction [59–61]. The CVD method, a solvent-free approach, allows for the simultaneous synthesis of multiple raw materials in the reaction chamber, ideal for volatile metal precursors with high thermostability. The solid grinding method, also solvent-free, facilitates nanoparticle introduction, with the gold complex serving as a common example. Liquid impregnation techniques, akin to ion exchange processes in zeolites, involve dissolving the metal precursor in a solvent before adding the support for doping. The double solution method, similar to liquid impregnation but utilizing multiple solvents, offers a unique approach. Finally, the encapsulation method involves mixing metal nanoparticles/clusters with the support precursor, surrounded by the as-synthesized MOFs support.

Comparison between three active centers

Comparing the characteristics of the three active centers reveals that introducing the metal on the framework linker exerts the least impact on framework stability. Nevertheless, this approach necessitates additional preparation for MOF support synthesis due to the requirement of specific linkers for different metals. Placing the metal on the SBU may lead to framework defects as the metal occupies the linker's position. However, this approach allows for more modifications and the introduction of additional active species at the linker level. Conversely, positioning the active center in the pores of MOFs results in a higher metal content loaded in the support compared to the other two methods. Additionally, a broader range of metals can be incorporated into the framework relative to zeolites. Nonetheless, as the metal occupies the MOF's pores, the advantages of MOFs such as shape selectivity and control over pore size diffusion are compromised.

This chapter has elucidated the strategies for preparing metal-doped MOF catalysts, showcasing how the position of the doped metal species can influence the SBU, the framework linker, and the framework's pores. By amalgamating various strategies, modifications in distribution, stability, and functionality within the MOF material can be achieved. Subsequent to detailing the strategies for introducing metals into MOF materials, the forthcoming chapter will furnish examples of bifunctional catalysts.

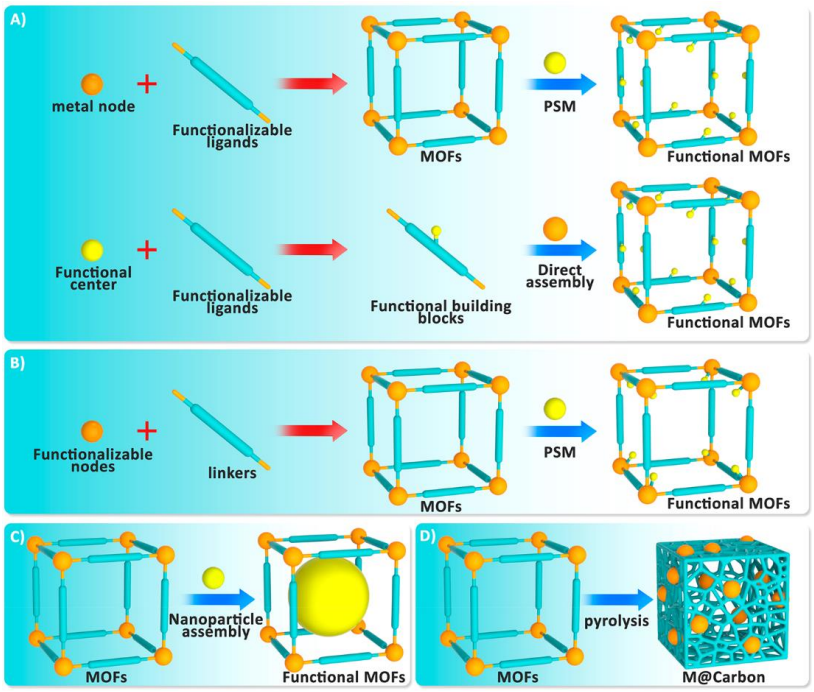

Figure 1.4. the illustration of the location of the active centers at (a) framework linker, (b) SBU, (c) pores of framwork, and (d) MOFs treated as carbon support (this part will not discuss in this thesis). Reprinted with permission from ref. [55]. Copyright © 2020 American Chemical Society.

1.4. Bifunctional catalyst utilizing two metal active species

Bifunctional catalysts with bimetallic systems, consisting of two different metal elements in forms such as nanoparticles, clusters, and alloys, exhibit distinct catalytic properties compared to monometallic catalysts, as the two metal elements synergistically interact. The exploration of bimetallic catalysts dates back to the 1960s, initiated by J.H. Sinfelt [62], and the study of combinations between two 3d transition metal elements has since sparked intense research interest worldwide. Unlike traditional bimetallic heterogeneous catalysts, the development of bimetallic catalysts combined with porous materials primarily focuses on synthesizing isolated atoms, nanoclusters, and nanoparticles [63]. To provide a comprehensive analysis of the development of bimetallic catalysts, the following paragraph will give some examples on 3d-3d bimetallic catalysts.

Regarding the 3d-3d bimetallic catalyst, the frequently encountered combinations involve the late 3d transition metals (Fe, Co, Ni, Cu, and Zn). The design of bimetallic catalysts typically relies on the chemical properties of metal A, such as copper facilitating C-C coupling, nickel enabling hydrogenation, and iron promoting oxidation reactions. Metal B is then introduced to enhance reactivity, leading to increased yields and altered product selectivity.

In the context of 3d bimetallic catalysts, one example is the combination of Fe/Cu (or Cu/Fe), as both Fe and Cu exhibit effective catalytic activity in oxidation reactions, particularly in Fenton-type reactions. A natural Fe/Cu catalyst instance is cytochrome c oxidase (*CcO*), where the Fe and Cu components are spatially separated by the protein scaffold at a few angstroms distance. Xiao et al. and Luo et al. reported successful oxidation reactions of aromatic compounds (benzene and phenol) using Fe/Cu bimetallic zeolite catalysts [64,65]. The Fe and Cu sources were introduced into the zeolite support through ion exchange and wetness impregnation approaches, respectively. During the probe reactions, H_2O_2 was employed and activated by the Fe/Cu bimetallic catalyst via the Fenton pathway. Similarly, the Fe/Cu bimetallic catalyst demonstrated remarkable catalytic performance compared to monometallic Fe or Cu catalysts, owing to the synergistic effect between Fe and Cu, which enhances the activation of H_2O_2 for substrate oxidation reactions. In addition to Fenton oxidation reactions, Fe/Cu bimetallic catalysts are also applicable in reduction reactions. Doan et al. and Zhang et al. reported the catalytic reduction of NOx using Fe/Cu catalysts [66,67]. Similar to the oxidation reaction, the presence of Fe/Cu bimetallic catalysts synergistically promotes the reduction of NO_x at lower reaction temperatures compared to monometallic catalysts.

In the context of the second example of 3d bimetallic catalysts, the combination of Ni/Co (or Co/Ni) focuses on small molecule coupling reactions, exploiting the popularity of Co for hydrogenation and Ni's typical usage in coupling reactions. The inclusion of Co enhances the coupling properties of Ni towards various small molecules, such as methane and carbon dioxide. Alonso et al. and Khan et al. have reported on the catalytic methane dry reforming employing Ni/Co catalysts supported by alumina and MOF-74 [68,69]. The coexistence of Co and Ni extends the catalyst's lifespan by suppressing coke formation during catalysis and enhancing the stability of the active species. In the methane dry reforming system with Co, deactivation of Co species is observed during the reaction. The coke formed during dry reforming oxidizes the cobalt, leading to catalyst deactivation. However, the combination of Co and Ni mitigates the negative effects of coke. Based on the XPS spectra from Khan et al., only Co in Co@CMOF exhibits a change in oxidation state from 0 to +2/+3 with the formation of cobalt oxide, compared to Co and Ni in Ni@CMOF and Ni-Co@CMOF. This indicates that the presence of Ni improves the stability of Co against coke formation.

In addition to Fe/Cu and Ni/Co, the combination of Ni/Cu (or Cu/Ni) is another noteworthy pairing that primarily focuses on hydrogenation reactions. Similar to Ni/Co, the coexistence of Ni and Cu enhances catalyst stability and significantly alters catalytic activity. The presence of Cu in the Ni/Cu catalyst system suppresses coke formation during reactions, thus extending the catalyst's lifespan [70,71]. Kang et al. reported the preparation of a Ni/Cu bimetallic catalyst supported by γ-alumina for the hydrogenation of 1,3-butadiene, where the introduction of Cu enhances selectivity towards 1-butene by modifying the electron density of Ni [72]. Viar et al. reported an improved biomass conversion of 5-hydroxymethylfurfural (HMF) into 2,5-dimethylfuran (DMF) and 2,5-dimethyltetrahydrofuran (DMTHF) using a ZrO_2-supported Ni/Cu bimetallic catalyst. The presence of both Ni and Cu enhances the selectivity towards DMTHF, and the ratio between Ni and Cu can be adjusted to control the selectivity (**Figure 1.5**) [73].

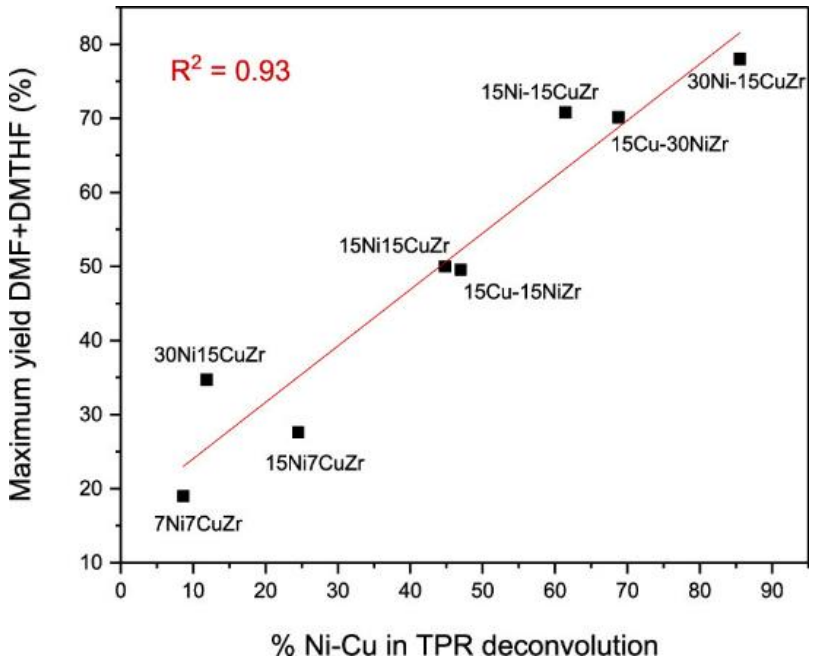

Figure 1.5. Relation between % Ni−Cu and maximum yield. Reprinted with the permission from ref. [73]. Copyright (2020) American Chemical Society.

1.5. Bifunctional catalyst integrating metal active species and support active site

Unlike bimetallic catalysts, bifunctional catalysts consist of active species that include both metal species and functional groups such as Lewis/Brønsted acid sites, base groups, or even acid-base pairs. In addition to these active sites, supporting materials play a crucial role by providing additional active species through modifications in the framework structure. For instance, introducing trivalent atoms as acid sites in zeolites or functionalizing framework linkers to incorporate extra functional groups. Bifunctional catalysts can be synthesized by incorporating the metal species into these modified supporting materials. To provide a detailed understanding of bifunctional catalysts, the following paragraphs will be divided into two parts: zeolite and MOF materials.

Zeolite catalyst

As mentioned previously, the introduction of trivalent atoms (T atoms) such as B, Al, and Ga can impart Brønsted acid sites to zeolites. By combining zeolites with T atoms and metal species, bifunctional zeolite catalysts can be synthesized, incorporating both metal sites and Brønsted acidity. Furthermore, owing to the physical properties of zeolites, they can offer protection to the active species and influence product selectivity based on the pore size and channel shape of the porous material, which in turn affects diffusion limitations.

Shi et al. conducted a study on the preparation of Co and Ni-doped MFI-type zeolite for the upgrading of palmitic acid [74]. The Co and Ni sources were introduced into zeolites ZSM-5 and HZP-5 using the wetness impregnation method. The acid sites present in the zeolite facilitated the hydrodeoxygenation reaction between palmitic acid and n-decane, while the introduction of metal sites (Co and Ni) influenced the product distribution, favoring the formation of C16 products due to altered reaction pathways involving both the metal and acid sites. Furthermore, the incorporation of Co and Ni also reduced the temperature required for the isomerization reaction, leading to the production of iso-alkane products at lower reaction temperatures (240 °C). Wu et al. conducted systematic studies on the acid-metal balance of bifunctional Pt/Beta zeolite catalyst for the hydrogenation of m-cresol [75]. To regulate the acid density of Brønsted acid sites (BASs) in the zeolite, different concentrations of Na salt were employed to block or poison the BASs, followed by the introduction of Pt into the zeolite framework using the wetness impregnation method. As the BAS/Pt ratio decreased (due to the addition of Na), the time required for complete conversion of m-cresol decreased from 1.25 hours to 0.5 hours when the Na concentration increased from 0 to 1.0 M. Furthermore, the reduction of the BAS/Pt ratio enhanced the selectivity towards methylcyclohexane and reduced the formation of ring contraction products. This can be

attributed to the poisoning of BAS, which promotes the diffusion of reactants towards the Pt sites for hydrogenation/dehydrogenation reactions and suppresses the occurrence of ring contraction reactions on the BASs. Wang et al. reported the modification of a Co carbide nanoprism-doped zeolite bifunctional catalyst for the effective conversion of syngas to aromatic products (STA reaction) [76]. Based on previous research conducted by the authors, Co carbide (Co2C) nanoprisms with exposed (020) and (101) facets demonstrated significant results in the Fischer-Tropsch to olefins (FTO) reaction, which showed promise for the STA reaction when combined with ZSM-5 zeolite as a bifunctional catalyst. By combining the CoMnAl oxide + Co nanoprism (CMA) with the zeolite support, aromatics including naphthenes were produced, whereas no aromatics were produced when only the CMA catalyst was used. When using nanosized ZSM-5 (with a similar Si/Al ratio), the selectivity of aromatics increased from 18.0 % to 40.3 %, and the CO conversion rate remained steady over a 102 hour reaction period. This indicated that the CMA component exhibited excellent stability in the STA reaction. Additionally, the selectivity of aromatics produced with the catalyst containing nanosized ZSM-5 remained constant, while the selectivity with the commercial catalyst dropped significantly from 18 % at 24 hours to 10.2 % at 102 hours. This suggests that the nanosized ZSM-5 can enhance the stability of the bifunctional catalyst. Yue et al. reported the utilization of a Cu-ZnO-Al_2O_3-ZrO_2 (Cu/Zn) doped LTA zeolite bifunctional catalyst for enhanced CO2 hydrogenation towards methanol [77]. Initially, the Cu/Zn catalyst was employed alone for CO_2 hydrogenation using a catalytic fixed-bed reactor, yielding moderate catalytic performance with a conversion of 24.7 % and a methanol selectivity of 48.0 % at 250 °C, consistent with previous reports. However, water production as a side product during the reaction impeded the CO_2 hydrogenation to methanol and led to the deactivation of active species within the catalyst. To address the issue of water-side product formation during the reaction, LTA zeolite was incorporated to enable continuous water removal due to its hydrophilic channels (**Figure 1.6**). The introduction of the LTA membrane overcame the limitations imposed by the thermodynamic equilibrium of the CO_2 hydrogenation reaction, thereby promoting methanol synthesis. By employing the catalytic membrane reactor at 260 °C, the CO_2 conversion rate increased to 36.1 % with a methanol selectivity of 100 %. These results indicate a synergistic effect between the Cu/Zn catalyst and LTA zeolite, overcoming the limitations of CO_2 hydrogenation towards methanol.

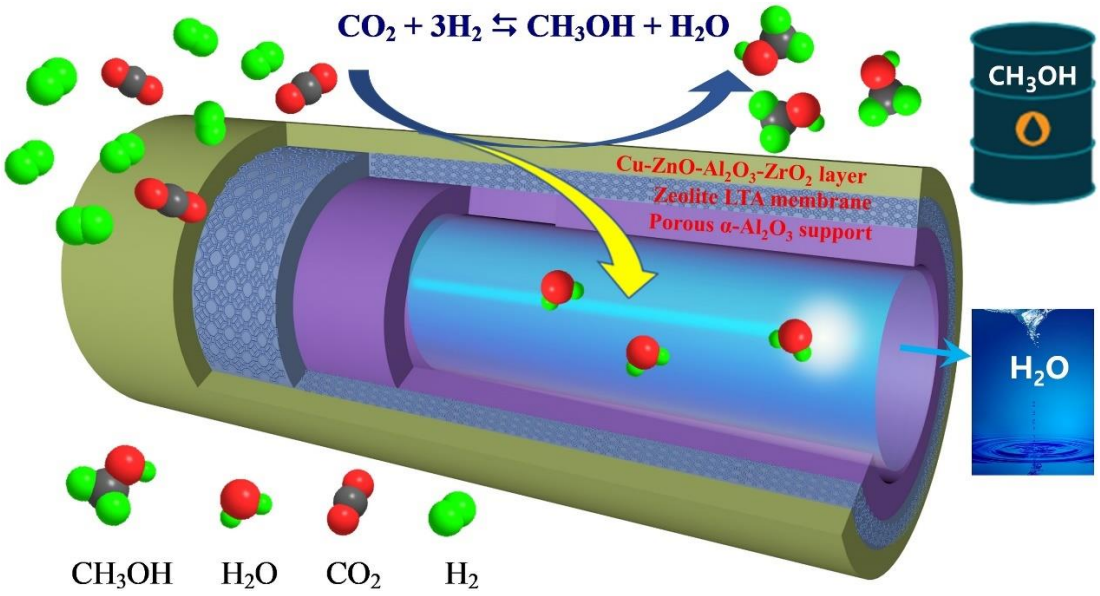

Figure 1.6. Scheme of CO_2 hydrogenation to methanol through in situ and continuous removal of water in a reaction–separation bifunctional LTA@Cu-ZnO-Al_2O_3-ZrO_2 catalytic membrane reactor (CMR). Reprinted with the permission from ref. [73]. Copyright (2021) Wiley-VCH GmbH.

MOFs catalyst

In contrast to zeolites, metal-organic frameworks (MOFs) offer more viable applications as bifunctional catalysts due to the following advantages: The highly flexible structure of MOFs allows for modification and changes in size (expansion and contraction) in response to external stimuli, known as the "breathing effect" [78]; Most of the active species within MOFs can be replaced to adjust their chemical and physical properties. Specific functionality can be tailored by introducing organic linkers that are customized for specific catalytic purposes.

Yao et al. and Xu et al. independently reported the catalytic CO_2 addition reactions utilizing Zn/Mn-doped bifunctional MOFs containing Lewis acid sites and basic functional groups (Zn, N-tricarboxytriphenylamine, and Mn, N-pyridine) [79,80]. Both of these bifunctional MOFs exhibited significant results in CO_2 addition, achieving yields higher than 99 % under solvent-free conditions. To further investigate the capabilities of the Lewis base functional group, Knoevenagel condensation reactions were also conducted. In both cases, the bifunctional MOFs demonstrated remarkable performance in the Knoevenagel condensation reaction, yielding above 99 % with the aldehyde substrate possessing an electron-withdrawing group. Notably, the Mn-doped bifunctional MOFs outperformed the Zn-doped MOFs when the substrate contained an electron-rich group. As previously mentioned, the utilization of Lewis acid-base

bifunctional MOFs proves to be advantageous for Knoevenagel condensation reactions due to the solvent-free conditions and heterogeneous catalysis. Additionally, there are several other notable examples of Zn-based bifunctional MOFs employed in Knoevenagel condensation reactions.

Liu et al. presented a study on the synthesis of a highly efficient Zn-based bifunctional MOF catalyst for Knoevenagel condensation reactions under mild conditions [81]. In this research, a designed ligand was synthesized by combining a triazole and a carboxylic acid group. The triazole nitrogen functioned as the Brønsted base, while the carboxylic acid group served as the binding site for substrate interaction through hydrogen bonding. Differing from the aforementioned catalysts, the Zn-based bifunctional MOFs with a mixed ligand exhibited a significant yield exceeding 99 % at room temperature. The combination of a Lewis acid, base, and carboxylic acid group facilitated substrate interactions and reduced the reaction temperature for Knoevenagel condensation reactions. However, a considerable decrease in yield was observed when using aldehyde substrates with electron-rich groups.

Apart from the design of mixed ligands, Huang et al. reported the preparation of bifunctional MOFs using different Zn-based SBUs to generate cavities with multiple sizes [82]. These bifunctional MOFs also demonstrated impressive results, achieving yields greater than 99 % under solvent-free conditions. Furthermore, due to the enlarged cavity within the MOFs, no performance drop was observed when using aldehyde substrates with electron-rich groups. However, a performance drop occurred only when the substrate contained large rigid functional groups, indicating that diffusion issues may be responsible for the observed decrease in performance.

In addition to the synergistic effect, the utilization of a tandem reaction with a bifunctional catalyst is highly appealing as it reduces the necessity for pre/post-treatments between the multiple steps involved in a chemical process. One prominent example is the deacetalization-Knoevenagel tandem reaction, which necessitates both acid and base sites to facilitate deacetalization and Knoevenagel condensation, respectively. Hu et al. presented a study on the synthesis of Al-based bifunctional MOFs for this tandem reaction [83]. The coexistence of Lewis acid and base sites within the catalyst resulted in a final product yield of approximately 60 % after a 5 hour reaction time. To enhance the overall reaction rate of the tandem reaction, an IRA900 resin was employed in combination with the MOF catalyst. The performance was only slightly improved, reaching a yield of approximately 100 % when the resin was activated by NaOH. This enhancement in performance is likely attributed to the increased number of base sites available for the subsequent Knoevenagel condensation reaction.

1.6. Aim and Objective

This thesis aims to introduce methodologies for the systematic development of bifunctional catalysts integrated with porous materials. The primary objective is to highlight the structural advantages of bifunctional catalysts, focusing on (1) the feasibility of tandem reactions, (2) the synergistic interactions between two active species, and (3) the adjustable activity achieved through combinations of active species. By conducting systematic studies on the preparation of bifunctional catalysts and exploring the corresponding structural-activity relationships, a customized catalyst preparation approach can be developed for diverse applications aimed at optimizing reactions.

To enhance the understanding of the structure-activity relationship of bifunctional catalysts, a blend of advanced characterization techniques, including synchrotron spectroscopy and diffraction methods, is utilized to unveil the precise atomic structure of the active species. Additionally, an investigation into the correlation between the structure and activity of bifunctional catalysts and the reactants is carried out through a series of varied probe reactions.

1.7. Thesis Overviews

The thesis includes 6 chapters inclusive. The discussion of my research work, conducted during this PhD study, is detailed in Chapters 3 to 5.

Chapter 1 introduces the importance of studying bifunctional catalysts, the strategies for synthesizing and modifying catalysts as bifunctional catalysts and reviews the recent advances in the bifunctional catalysts with bimetallic system and dual active site system.

Chapter 2 details the material and characterization techniques used.

Chapter 3 presents the preparation of an atomic-dispersed 3d bimetallic dual-atom zeolite catalyst as the mimic of the SOD enzyme.

Chapter 4 investigates the preparation of Cu-Fe dual-atom catalysts (DACs) on the SBU of UiO-66-NH_2 MOF for highly selective styrene oxidation towards benzaldehyde.

Chapter 5 investigates the synthesis of a bifunctional metal/Brønsted acid zeolite catalyst for the systematic studies of the synergistic cooperativity between two active species.

Chapter 6 concludes and outlooks the impact of the research work.

1.8. Reference

(1) Chaoui, N.; Trunk, M.; Dawson, R.; Schmidt, J.; Thomas, A.Trends and Challenges for Microporous Polymers. *Chem. Soc. Rev.* **2017**, *46* (11), 3302–3321. https://doi.org/10.1039/c7cs00071e.

(2) Corma, A.From Microporous to Mesoporous Molecular Sieve Materials and Their Use in Catalysis. *Chem. Rev.* **1997**, *97* (6), 2373–2419. https://doi.org/10.1021/cr960406n.

(3) Freund, R.; Zaremba, O.; Arnauts, G.; Ameloot, R.; Skorupskii, G.; Dincă, M.; Bavykina, A.; Gascon, J.; Ejsmont, A.; Goscianska, J.; Kalmutzki, M.; Lächelt, U.; Ploetz, E.; Diercks, C. S.; Wuttke, S.The Current Status of MOF and COF Applications. *Angew. Chem. Int. Ed.* **2021**, *60* (45), 23975–24001. https://doi.org/10.1002/anie.202106259.

(4) Serhan, M.; Sprowls, M.; Jackemeyer, D.; Long, M.; Perez, I. D.; Maret, W.; Tao, N.; Forzani, E.From Fundamentals to Applications: A Toolbox for Robust and Multifunctional MOF Materials. *AIChE Annu. Meet. Conf. Proc.* **2019**, *2019-Novem*. https://doi.org/10.1039/x0xx00000x.

(5) Wang, C.; Fang, W.; Liu, Z.; Wang, L.; Liao, Z.; Yang, Y.; Li, H.; Liu, L.; Zhou, H.; Qin, X.; Xu, S.; Chu, X.; Wang, Y.; Zheng, A.; Xiao, F. S.Fischer–Tropsch Synthesis to Olefins Boosted by MFI Zeolite Nanosheets. *Nat. Nanotechnol.* **2022**, *17* (7), 714–720. https://doi.org/10.1038/s41565-022-01154-9.

(6) Peng, X.; Cheng, K.; Kang, J.; Gu, B.; Yu, X.; Zhang, Q.; Wang, Y.Impact of Hydrogenolysis on the Selectivity of the Fischer-Tropsch Synthesis: Diesel Fuel Production over Mesoporous Zeolite-Y-Supported Cobalt Nanoparticles. *Angew. Chem. Int. Ed.* **2015**, *54* (15), 4553–4556. https://doi.org/10.1002/anie.201411708.

(7) Otun, K. O.; Liu, X.; Hildebrandt, D.Metal-Organic Framework (MOF)-Derived Catalysts for Fischer-Tropsch Synthesis: Recent Progress and Future Perspectives. *J. Energy Chem.* **2020**, *51*, 230–245. https://doi.org/10.1016/j.jechem.2020.03.062.

(8) Yin, L.; Liebscher, J.Carbon-Carbon Coupling Reactions Catalyzed by Heterogeneous Palladium Catalysts. *Chem. Rev.* **2007**, *107* (1), 133–173. https://doi.org/10.1021/cr0505674.

(9) Dhakshinamoorthy, A.; Asiri, A. M.; Garcia, H.Formation of C-C and C-Heteroatom Bonds by C-H Activation by Metal Organic Frameworks as Catalysts or Supports. *ACS Catal.* **2019**, *9* (2), 1081–1102. https://doi.org/10.1021/acscatal.8b04506.

(10) Fang, R.; Dhakshinamoorthy, A.; Li, Y.; Garcia, H.Metal Organic Frameworks for Biomass Conversion. *Chem. Soc. Rev.* **2020**, *49* (11), 3638–3687. https://doi.org/10.1039/d0cs00070a.

(11) Robinson, A. M.; Hensley, J. E.; Will Medlin, J.Bifunctional Catalysts for Upgrading of Biomass-Derived Oxygenates: A Review. *ACS Catal.* **2016**, *6* (8), 5026–5043. https://doi.org/10.1021/acscatal.6b00923.

(12) Munyentwali, A.; Li, H.; Yang, Q.Review of Advances in Bifunctional Solid Acid/Base Catalysts for Sustainable Biodiesel Production. *Appl. Catal. A Gen.* **2022**, *633* (November 2021). https://doi.org/10.1016/j.apcata.2022.118525.

(13) Palčić, A.; Valtchev, V.Analysis and Control of Acid Sites in Zeolites. *Appl. Catal. A Gen.* **2020**, *606* (May 2020), 117795. https://doi.org/10.1016/j.apcata.2020.117795.

(14) Henry E. Mgbemere; Kenna C. Ekpe; Ganiyu I. Lawal.Zeolite Synthesis, Characterization and Application Areas: A Review. *Int. Res. J. Environ. Sci.* **2017**, *6* (10), 1–6.

(15) *International Zeolite Association*. http://www.iza-online.org/.

(16) Li, S.; Li, J.; Dong, M.; Fan, S.; Zhao, T.; Wang, J.; Fan, W.Strategies to Control Zeolite Particle Morphology. *Chem. Soc. Rev.* **2019**, *48* (3), 885–907. https://doi.org/10.1039/c8cs00774h.

(17) Asgar Pour, Z.; Sebakhy, K. O.A Review on the Effects of Organic Structure-Directing Agents on the Hydrothermal Synthesis and Physicochemical Properties of Zeolites. *Chem.* **2022**, *4* (2), 431–446. https://doi.org/10.3390/chemistry4020032.

(18) Barrer, R. M.Zeolites: Their Nucleation and Growth. In *Zeolite synthesis*; ACS Publications, 1989; pp 11–27.

(19) Brar, T.; France, P.; Smirniotis, P. G.Control of Crystal Size and Distribution of Zeolite A. *Ind. Eng. Chem. Res.* **2001**, *40* (4), 1133–1139. https://doi.org/10.1021/ie000748q.

(20) Aguado, J.; Serrano, D. P.; Escola, J. M.; Rodríguez, J. M.Low Temperature Synthesis and Properties of ZSM-5 Aggregates Formed by Ultra-Small Nanocrystals. *Microporous Mesoporous Mater.* **2004**, *75* (1–2), 41–49. https://doi.org/10.1016/j.micromeso.2004.06.027.

(21) Lechert, H.The PH-Value and Its Importance for the Crystallization of Zeolites. In *Verified Syntheses of Zeolitic Materials*; Elsevier, 2001; pp 33–38.

(22) Weitkamp, J.; Puppe, L.*Catalysis and Zeolites: Fundamentals and Applications*; Springer Science & Business Media, 2013.

(23) Moliner, M.; Rey, F.; Corma, A.Towards the Rational Design of Efficient Organic Structure-Directing Agents for Zeolite Synthesis. *Angew. Chem. Int. Ed.* **2013**, *52* (52), 13880–13889. https://doi.org/10.1002/anie.201304713.

(24) Lobo, R. F.; Zones, S. I.; Davis, M. E.Structure-Direction in Zeolite Synthesis. *J. Incl. Phenom. Mol. Recognit. Chem.* **1995**, *21* (1–4), 47–78. https://doi.org/10.1007/BF00709411.

(25) Li, J.; Corma, A.; Yu, J.Synthesis of New Zeolite Structures. *Chem. Soc. Rev.* **2015**, *44* (20), 7112–7127.

(26) Yabushita, M.; Osuga, R.; Muramatsu, A.Control of Location and Distribution of Heteroatoms Substituted Isomorphously in Framework of Zeolites and Zeotype Materials. *CrystEngComm* **2021**, *23* (36), 6226–6233. https://doi.org/10.1039/d1ce00912e.

(27) Shamzhy, M.; Opanasenko, M.; Concepción, P.; Martínez, A.New Trends in Tailoring Active Sites in Zeolite-Based Catalysts. *Chem. Soc. Rev.* **2019**, *48* (4), 1095–1149. https://doi.org/10.1039/c8cs00887f.

(28) Shirazi, L.; Jamshidi, E.; Ghasemi, M. R.The Effect of Si/Al Ratio of ZSM-5 Zeolite on Its Morphology, Acidity and Crystal Size. *Cryst. Res. Technol.* **2008**, *43* (12), 1300–1306. https://doi.org/10.1002/crat.200800149.

(29) Jones, A. J.; Carr, R. T.; Zones, S. I.; Iglesia, E.Acid Strength and Solvation in Catalysis by MFI

Zeolites and Effects of the Identity, Concentration and Location of Framework Heteroatoms. *J. Catal.* **2014**, *312*, 58–68. https://doi.org/10.1016/j.jcat.2014.01.007.

(30) Wang, C.; Zhang, L.; Huang, X.; Zhu, Y.; Li, G.; Gu, Q.; Chen, J.; Ma, L.; Li, X.; He, Q.; Xu, J.; Sun, Q.; Song, C.; Peng, M.; Sun, J.; Ma, D.Maximizing Sinusoidal Channels of HZSM-5 for High Shape-Selectivity to p-Xylene. *Nat. Commun.* **2019**, *10* (1), 1–8. https://doi.org/10.1038/s41467-019-12285-4.

(31) Khan, M. S.; Shahid, M.Synthesis of Metal-Organic Frameworks (MOFs): Routes to Various MOF Topologies, Morphologies, and Composites. *Electrochem. Appl. Met. Fram. Adv. Futur. Potential* **2022**, 17–35. https://doi.org/10.1016/B978-0-323-90784-2.00007-1.

(32) Lee, Y. R.; Kim, J.; Ahn, W. S.Synthesis of Metal-Organic Frameworks: A Mini Review. *Korean J. Chem. Eng.* **2013**, *30* (9), 1667–1680. https://doi.org/10.1007/s11814-013-0140-6.

(33) Chen, L.; Zhang, X.; Cheng, X.; Xie, Z.; Kuang, Q.; Zheng, L.The Function of Metal-Organic Frameworks in the Application of MOF-Based Composites. *Nanoscale Adv.* **2020**, *2* (7), 2628–2647. https://doi.org/10.1039/d0na00184h.

(34) Eddaoudi, M.; Kim, J.; Rosi, N.; Vodak, D.; Wachter, J.; O'Keeffe, M.; Yaghi, O. M.Systematic Design of Pore Size and Functionality in Isoreticular MOFs and Their Application in Methane Storage. *Science (80-.).* **2002**, *295* (5554), 469–472. https://doi.org/10.1126/science.1067208.

(35) Feng, Y.; Chen, Q.; Jiang, M.; Yao, J.Tailoring the Properties of UiO-66 through Defect Engineering: A Review. *Ind. Eng. Chem. Res.* **2019**, *58* (38), 17646–17659. https://doi.org/10.1021/acs.iecr.9b03188.

(36) Shearer, G. C.; Chavan, S.; Bordiga, S.; Svelle, S.; Olsbye, U.; Lillerud, K. P.Defect Engineering: Tuning the Porosity and Composition of the Metal-Organic Framework UiO-66 via Modulated Synthesis. *Chem. Mater.* **2016**, *28* (11), 3749–3761. https://doi.org/10.1021/acs.chemmater.6b00602.

(37) Bueken, B.; VanVelthoven, N.; Krajnc, A.; Smolders, S.; Taulelle, F.; Mellot-Draznieks, C.; Mali, G.; Bennett, T. D.; DeVos, D.Tackling the Defect Conundrum in UiO-66: A Mixed-Linker Approach to Engineering Missing Linker Defects. *Chem. Mater.* **2017**, *29* (24), 10478–10486. https://doi.org/10.1021/acs.chemmater.7b04128.

(38) Gadzikwa, T.; Matseketsa, P.The Post-Synthesis Modification (PSM) of MOFs for Catalysis. *Dalt. Trans.* **2024**, *53* (18), 7659–7668. https://doi.org/10.1039/d4dt00514g.

(39) Kim, M.; Cahill, J. F.; Su, Y.; Prather, K. A.; Cohen, S. M.Postsynthetic Ligand Exchange as a Route to Functionalization of "inert" Metal-Organic Frameworks. *Chem. Sci.* **2012**, *3* (1), 126–130. https://doi.org/10.1039/c1sc00394a.

(40) Yin, Z.; Wan, S.; Yang, J.; Kurmoo, M.; Zeng, M. H.Recent Advances in Post-Synthetic Modification of Metal–Organic Frameworks: New Types and Tandem Reactions. *Coord. Chem. Rev.* **2019**, *378*, 500–512. https://doi.org/10.1016/j.ccr.2017.11.015.

(41) Fracaroli, A. M.; Siman, P.; Nagib, D. A.; Suzuki, M.; Furukawa, H.; Toste, F. D.; Yaghi, O. M.Seven Post-Synthetic Covalent Reactions in Tandem Leading to Enzyme-like Complexity

within Metal-Organic Framework Crystals. *J. Am. Chem. Soc.* **2016**, *138* (27), 8352–8355. https://doi.org/10.1021/jacs.6b04204.

(42) Zhang, X.; Xia, T.; Jiang, K.; Cui, Y.; Yang, Y.; Qian, G.Highly Sensitive and Selective Detection of Mercury (II) Based on a Zirconium Metal-Organic Framework in Aqueous Media. *J. Solid State Chem.* **2017**, *253* (June), 277–281. https://doi.org/10.1016/j.jssc.2017.06.008.

(43) Britt, D.; Lee, C.; Uribe-Romo, F. J.; Furukawa, H.; Yaghi, O. M.Ring-Opening Reactions within Porous Metal-Organic Frameworks. *Inorg. Chem.* **2010**, *49* (14), 6387–6389. https://doi.org/10.1021/ic100652x.

(44) Phang, W. J.; Jo, H.; Lee, W. R.; Song, J. H.; Yoo, K.; Kim, B.; Hong, C. S.Superprotonic Conductivity of a Uio-66 Framework Functionalized with Sulfonic Acid Groups by Facile Postsynthetic Oxidation. *Angew. Chem. Int. Ed.* **2015**, *54* (17), 5142–5146. https://doi.org/10.1002/anie.201411703.

(45) Marreiros, J.; Caratelli, C.; Hajek, J.; Krajnc, A.; Fleury, G.; Bueken, B.; DeVos, D. E.; Mali, G.; Roeffaers, M. B. J.; VanSpeybroeck, V.; Ameloot, R.Active Role of Methanol in Post-Synthetic Linker Exchange in the Metal-Organic Framework UiO-66. *Chem. Mater.* **2019**, *31* (4), 1359–1369. https://doi.org/10.1021/acs.chemmater.8b04734.

(46) Fluch, U.; McCarthy, B. D.; Ott, S.Post Synthetic Exchange Enables Orthogonal Click Chemistry in a Metal Organic Framework. *Dalt. Trans.* **2019**, *48* (1), 45–49. https://doi.org/10.1039/C8DT04563A.

(47) Razavi, S. A. A.; Morsali, A.Ultrasonic-Assisted Linker Exchange (USALE): A Novel Post-Synthesis Method for Controlling the Functionality, Porosity, and Morphology of MOFs. *Chem. - A Eur. J.* **2019**, *25* (46), 10876–10885. https://doi.org/10.1002/chem.201901554.

(48) Zhang, Q.; Gao, S.; Yu, J.Metal Sites in Zeolites: Synthesis, Characterization, and Catalysis. *Chem. Rev.* **2023**, *123* (9), 6039–6106. https://doi.org/10.1021/acs.chemrev.2c00315.

(49) Tynjälä, P.; Pakkanen, T. T.Acidic Properties of ZSM-5 Zeolite Modified with Ba2+, Al3+ and La3+ Ion-Exchange. *J. Mol. Catal. A Chem.* **1996**, *110* (2), 153–161. https://doi.org/10.1016/1381-1169(96)00159-8.

(50) Farrusseng, D.; Tuel, A.Perspectives on Zeolite-Encapsulated Metal Nanoparticles and Their Applications in Catalysis. *New J. Chem.* **2016**, *40* (5), 3933–3949. https://doi.org/10.1039/c5nj02608c.

(51) Wu, Q.; Xu, C.; Zhu, L.; Meng, X.; Xiao, F. S.Recent Strategies for Synthesis of Metallosilicate Zeolites. *Catal. Today* **2022**, *390–391* (December 2021), 2–11. https://doi.org/10.1016/j.cattod.2022.01.020.

(52) Pinar, A. B.; Gómez-Hortigüela, L.; McCusker, L. B.; Pérez-Pariente, J.Controlling the Aluminum Distribution in the Zeolite Ferrierite via the Organic Structure Directing Agent. *Chem. Mater.* **2013**, *25* (18), 3654–3661. https://doi.org/10.1021/cm4018024.

(53) Wang, S.; He, Y.; Jiao, W.; Wang, J.; Fan, W.Recent Experimental and Theoretical Studies on Al Siting/Acid Site Distribution in Zeolite Framework. *Curr. Opin. Chem. Eng.* **2019**, *23*, 146–

154. https://doi.org/10.1016/j.coche.2019.04.002.

(54) Ouyang, X.; Hwang, S. J.; Xie, D.; Rea, T.; Zones, S. I.; Katz, A.Heteroatom-Substituted Delaminated Zeolites as Solid Lewis Acid Catalysts. *ACS Catal.* **2015**, *5* (5), 3108–3119. https://doi.org/10.1021/cs5020546.

(55) Bavykina, A.; Kolobov, N.; Khan, I. S.; Bau, J. A.; Ramirez, A.; Gascon, J.Metal-Organic Frameworks in Heterogeneous Catalysis: Recent Progress, New Trends, and Future Perspectives. *Chem. Rev.* **2020**, *120* (16), 8468–8535. https://doi.org/10.1021/acs.chemrev.9b00685.

(56) Liao, W. M.; Zhang, J. H.; Wang, Z.; Yin, S. Y.; Pan, M.; Wang, H. P.; Su, C. Y.Post-Synthetic Exchange (PSE) of UiO-67 Frameworks with Ru/Rh Half-Sandwich Units for Visible-Light-Driven H2 Evolution and CO2 Reduction. *J. Mater. Chem. A* **2018**, *6* (24), 11337–11345. https://doi.org/10.1039/c8ta02962h.

(57) Carson, F.; Martínez-Castro, E.; Marcos, R.; Miera, G. G.; Jansson, K.; Zou, X.; Martín-Matute, B.Effect of the Functionalisation Route on a Zr-MOF with an Ir-NHC Complex for Catalysis. *Chem. Commun.* **2015**, *51* (54), 10864–10867. https://doi.org/10.1039/c5cc03934g.

(58) Kalmutzki, M. J.; Hanikel, N.; Yaghi, O. M.Secondary Building Units as the Turning Point in the Development of the Reticular Chemistry of MOFs. *Sci. Adv.* **2018**, *4* (10). https://doi.org/10.1126/sciadv.aat9180.

(59) Lu, G.; Li, S.; Guo, Z.; Farha, O. K.; Hauser, B. G.; Qi, X.; Wang, Y.; Wang, X.; Han, S.; Liu, X.; Duchene, J. S.; Zhang, H.; Zhang, Q.; Chen, X.; Ma, J.; Loo, S. C. J.; Wei, W. D.; Yang, Y.; Hupp, J. T.; Huo, F.Imparting Functionality to a Metal-Organic Framework Material by Controlled Nanoparticle Encapsulation. *Nat. Chem.* **2012**, *4* (4), 310–316. https://doi.org/10.1038/nchem.1272.

(60) Chen, L.; Chen, X.; Liu, H.; Bai, C.; Li, Y.One-Step Encapsulation of Pd Nanoparticles in MOFs via a Temperature Control Program. *J. Mater. Chem. A* **2015**, *3* (29), 15259–15264. https://doi.org/10.1039/c5ta02860d.

(61) Li, Z.; Rayder, T. M.; Luo, L.; Byers, J. A.; Tsung, C. K.Aperture-Opening Encapsulation of a Transition Metal Catalyst in a Metal-Organic Framework for CO 2 Hydrogenation. *J. Am. Chem. Soc.* **2018**, *140* (26), 8082–8085. https://doi.org/10.1021/jacs.8b04047.

(62) Sinfelt, J. H.Bimetallic Catalysts. *Am. Chem. Soc. Div. Pet. Chem. Prepr.* **1987**, *32* (1–2), 189. https://doi.org/10.1380/jsssj.9.676.

(63) Liu, L.; Corma, A.Bimetallic Sites for Catalysis: From Binuclear Metal Sites to Bimetallic Nanoclusters and Nanoparticles. *Chem. Rev.* **2023**, *123* (8), 4855–4933. https://doi.org/10.1021/acs.chemrev.2c00733.

(64) Xiao, P.; Osuga, R.; Wang, Y.; Kondo, J. N.; Yokoi, T.Bimetallic Fe-Cu/Beta Zeolite Catalysts for Direct Hydroxylation of Benzene to Phenol: Effect of the Sequence of Ion Exchange for Fe and Cu Cations. *Catal. Sci. Technol.* **2020**, *10* (20), 6977–6986. https://doi.org/10.1039/d0cy01216e.

(65) Luo, L.; Dai, C.; Zhang, A.; Wang, J.; Liu, M.; Song, C.; Guo, X.A Facile Strategy for Enhancing

FeCu Bimetallic Promotion for Catalytic Phenol Oxidation. *Catal. Sci. Technol.* **2015**, *5* (6), 3159–3165.

(66) Doan, T.; Dam, P.; Nguyen, K.; Vuong, T. H.; Le, M. T.; Pham, T. H.Copper-Iron Bimetal Ion-Exchanged SAPO-34 for NH3-SCR of NOx. *Catalysts* **2020**, *10* (3), 321.

(67) Zhang, T.; Liu, J.; Wang, D.; Zhao, Z.; Wei, Y.; Cheng, K.; Jiang, G.; Duan, A.Selective Catalytic Reduction of NO with NH3 over HZSM-5-Supported Fe-Cu Nanocomposite Catalysts: The Fe-Cu Bimetallic Effect. *Appl. Catal. B Environ.* **2014**, *148–149*, 520–531. https://doi.org/10.1016/j.apcatb.2013.11.006.

(68) San-José-Alonso, D.; Juan-Juan, J.; Illán-Gómez, M. J.; Román-Martínez, M. C.Ni, Co and Bimetallic Ni-Co Catalysts for the Dry Reforming of Methane. *Appl. Catal. A Gen.* **2009**, *371* (1–2), 54–59. https://doi.org/10.1016/j.apcata.2009.09.026.

(69) Khan, I. S.; Ramirez, A.; Shterk, G.; Garzón-Tovar, L.; Gascon, J.Bimetallic Metal-Organic Framework Mediated Synthesis of Ni-Co Catalysts for the Dry Reforming of Methane. *Catalysts* **2020**, *10* (5). https://doi.org/10.3390/catal10050592.

(70) Reshetenko, T.V; Avdeeva, L. B.; Ismagilov, Z. R.; Chuvilin, A. L.; Ushakov, V. A.Carbon Capacious Ni-Cu-Al2O3 Catalysts for High-Temperature Methane Decomposition. *Appl. Catal. A Gen.* **2003**, *247* (1), 51–63.

(71) Lee, J. H.; Lee, E. G.; Joo, O. S.; Jung, K. D.Stabilization of Ni/Al2O3 Catalyst by Cu Addition for CO2 Reforming of Methane. *Appl. Catal. A Gen.* **2004**, *269* (1–2), 1–6. https://doi.org/10.1016/j.apcata.2004.01.035.

(72) Kang, M.; Song, M. W.; Kim, T. W.; Kim, K. L.γ-Alumina Supported Cu-Ni Bimetallic Catalysts Characterization and Selective Hydrogenation of 1,3-Butadiene. *Can. J. Chem. Eng.* **2002**, *80* (1), 63–70.

(73) Viar, N.; Requies, J. M.; Agirre, I.; Iriondo, A.; Gil-Calvo, M.; Arias, P. L.Ni-Cu Bimetallic Catalytic System for Producing 5-Hydroxymethylfurfural-Derived Value-Added Biofuels. *ACS Sustain. Chem. Eng.* **2020**, *8* (30), 11183–11193. https://doi.org/10.1021/acssuschemeng.0c02433.

(74) Shi, Y.; Xing, E.; Cao, Y.; Liu, M.; Wu, K.; Yang, M.; Wu, Y.Tailoring Product Distribution during Upgrading of Palmitic Acid over Bi-Functional Metal/Zeolite Catalysts. *Chem. Eng. Sci.* **2017**, *166* (x), 262–273. https://doi.org/10.1016/j.ces.2017.03.052.

(75) Wu, X.; Sun, Q.; Wang, H.; Han, J.; Ge, Q.; Zhu, X.Effect of Acid-Metal Balance of Bifunctional Pt/Beta Catalysts on Vapor Phase Hydrodeoxygenation of m-Cresol. *Catal. Today* **2020**, *355* (April 2019), 43–50. https://doi.org/10.1016/j.cattod.2019.04.039.

(76) Wang, H.; Gao, P.; Li, S.; Wang, T.; Yang, C.; Li, J.; Lin, T.; Zhong, L.; Sun, Y.Bifunctional Catalysts with Versatile Zeolites Enable Unprecedented Para-Xylene Productivity for Syngas Conversion under Mild Conditions. *Chem Catal.* **2022**, *2* (4), 779–796. https://doi.org/10.1016/j.checat.2022.01.014.

(77) Yue, W.; Li, Y.; Wei, W.; Jiang, J.; Caro, J.; Huang, A.Highly Selective CO2 Conversion to

Methanol in a Bifunctional Zeolite Catalytic Membrane Reactor. *Angew. Chem. Int. Ed.* **2021**, *60* (33), 18289–18294. https://doi.org/10.1002/anie.202106277.

(78) Natarajan, S.; Manna, K.Bifunctional MOFs in Heterogeneous Catalysis. *ACS Org. Inorg. Au* **2024**, *4* (1), 59–90. https://doi.org/10.1021/acsorginorgau.3c00033.

(79) Yao, C.; Zhou, S.; Kang, X.; Zhao, Y.; Yan, R.; Zhang, Y.; Wen, L.A Cationic Zinc-Organic Framework with Lewis Acidic and Basic Bifunctional Sites as an Efficient Solvent-Free Catalyst: CO2 Fixation and Knoevenagel Condensation Reaction. *Inorg. Chem.* **2018**, *57* (17), 11157–11164. https://doi.org/10.1021/acs.inorgchem.8b01713.

(80) Xu, Z.; Zhao, Y. Y.; Chen, L.; Zhu, C. Y.; Li, P.; Gao, W.; Li, J. Y.; Zhang, X. M.Thermally Activated Bipyridyl-Based Mn-MOFs with Lewis Acid-Base Bifunctional Sites for Highly Efficient Catalytic Cycloaddition of CO2 with Epoxides and Knoevenagel Condensation Reactions. *Dalt. Trans.* **2023**, *52* (12), 3671–3681. https://doi.org/10.1039/d3dt00043e.

(81) Liu, F.; Kumar, S.; Li, S.; You, H.; Ren, P.; Zhao, L.Bifunctional Design of Stable Metal-Organic Framework Bearing Triazole–Carboxylate Mixed Ligand: Highly Efficient Heterogeneous Catalyst for Knoevenagel Condensation Reaction under Mild Conditions. *Catal. Commun.* **2020**, *142* (May), 106032. https://doi.org/10.1016/j.catcom.2020.106032.

(82) Huang, G. Q.; Chen, J.; Huang, Y. L.; Wu, K.; Luo, D.; Jin, J. K.; Zheng, J.; Xu, S. H.; Lu, W.Mixed-Linker Isoreticular Zn(II) Metal-Organic Frameworks as Brønsted Acid-Base Bifunctional Catalysts for Knoevenagel Condensation Reactions. *Inorg. Chem.* **2022**, *61* (21), 8339–8348. https://doi.org/10.1021/acs.inorgchem.2c00941.

(83) Hu, Y.; Zhang, J.; Wang, Z.; Huo, H.; Jiang, Y.; Xu, X.; Lin, K.Ion-Exchange Fabrication of Hierarchical Al-MOF-Based Resin Catalysts for the Tandem Reaction. *ACS Appl. Mater. Interfaces* **2020**, *12* (32), 36159–36167. https://doi.org/10.1021/acsami.0c09544.

Chapter 2 Materials and Methodology

2.1. Materials

All the zeolites used in this thesis for modification and control experiments are commercial samples obtained from the Nankai University Catalyst Co., Ltd (Tianjin, China) and used as received without further purification.

H-ZSM-5 zeolite

Commercial H-ZSM-5 zeolites (SiO_2:Al_2O_3 = 46, chemical formula $H_nAl_nSi_{96-n}O_{192}$ 18 H2O) were purchased from Nankai University Catalyst Co., Ltd. Typical characterization results are displayed on their product website: [http://www.nkcatalyst.com/index.php/en/arc/show/id/49.html]. Briefly, the H-ZSM-5 samples possess high crystallinity (≧95%), a surface area of ca. 340 m^2 g^{-1}, and an average particle size of ca. 2 μm × 1 μm × 1 μm.

Chemicals

All the metal sources, aluminium sulfate, iron(III) nitrate, copper(II) nitrate, bis(ethylenediamine)copper(II) hydroxide, and zinc(II) nitrate were purchased from Sigma Aldrich and used as received without further purification.

Imidazole and 2-methyl imidazole were purchased from Sigma Aldrich and used as received without further purification.

Tetraethyl orthosilicate was purchased from Sigma Aldrich and used as received without further purification.

2.2. Synthesis of catalysts

Zn_A-Cu_B-Z

the preparation of Zn_A-Cu_B-Z is here used as an illustration; by ion exchange with $Zn(NO_3)_2 \cdot 6H_2O$ (Sigma-Aldrich; 98%), mononuclear Zn_A-Z has been prepared as our standard precursor material 'seed'. It is noted that excessive ion-exchange steps have been taken to ensure the maximum ion-exchange capability of the H-ZSM-5 zeolite has been reached. Subsequent Cu metalation to form Zn_A-Cu_B-Z is achieved by applying our seed with Lewis di-basic imidazole (as the linker, 'Im'), followed by the addition of $Cu(NO_3)_2 \cdot 2.5H_2O$ in a controlled manner.

Cu-oxo-Fe-UiO-66-NH_2

0.57 g UiO-66-NH_2 were dispersed in 20 mL H_2O by ultrasonication. 138.35 µL bis(ethylenediamine)copper (II) hydroxide was dropwise added. The mixture was stirred at room temperature for 3 hours. The product was collected by centrifugation and washed with 10 mL double distilled water. It was dried at 70 °C overnight to obtain the product Cu^{2+}-UiO-66-NH_2.

0.57 g Cu^{2+}-UiO-66-NH_2 were dispersed in 20 mL H_2O. 0.057 g 2-methylimidazole was added and reacted for 3 h. The solid sample was collected by centrifugation 3 times and washed by double distilled H_2O to obtain mIem-Cu^{2+}-UiO-66-NH_2 in 20 mL H_2O. 0.28 g $Fe(NO_3)_3$ was then added and reacted at room temperature for 3 h to obtain Fe^{3+}-mIem-Cu^{2+}-UiO-66-NH_2. The sample was washed by double distilled H_2O by 3 times and dried at 70 °C.

Cu^{2+}-mIem-Fe^{3+}-UiO-66-NH_2 are heated at 180 °C for 1 h with a heating rate of 10 °C/min. By calcination of the samples at 180 °C, the organic 2-methyl imidazole linker can be removed as shown in previous TGA studies. The vacant coordination sites are reactive which are hence stabilised by the neighboring O atoms, akin to the calcination of metal-exchanged zeolites.

M/X-Z zeolites (M = Fe, Cu, X = Al, Ga, B)

Synthesis of M/X-Z samples was attempted by the "acidic co-hydrolysis route". Metal nitrate (0.00048 mol) was added to the solution of TEOS (10 g) and DI water (32.5 g). the pH of the mixture was adjusted to 1.0 by drop-wise adding sulfuric acid. After the pH adjustment, the mixture was stirred at room temperature for 20 h to get a complete co-hydrolysis and condensation of TEOS with the metal salt. After that, the source of Brønsted acid site (1.2 mmol), 0.75 g of aluminum (aluminum sulfate octadecahydrate as an example), and TPAOH (4.8 mmol) was added into the mixture with the dripping of NaOH solution to get a basic gel (pH = 9.8). The final gel composition was $1SiO_2$: 0.01 Metal: 40 H_2O: 0.1 TPAOH. Finally, the slurry was transferred into the 100 mL

Teflon-lined stainless-steel autoclave and statically crystallized at 180 °C for 72 h. After that, the zeolite was separated by centrifugation, followed by washing with DI water, and air drying at 70 °C overnight. The obtained as-synthesized samples were calcinated at 550 °C for 5 h to remove the organic template. H-form of the zeolite was prepared by ammonia treatment. The zeolite was firstly converted into NH_4-form by ion exchange with 1.0 M ammonia solution at room temperature for 24 h (1g solid to 100 mL solution). The zeolite samples were separated by centrifugation, followed by washing with DI water, and air drying at 70 °C overnight. The NH_4-form samples were converted to H-form by calcination at 500 °C under dry air for 4h.

2.3. Characterisation techniques

The elucidation and investigation of active species within bifunctional catalysts play a crucial role in studying the structure-activity relationship between these species and the reaction substrates. Several advanced techniques have been developed to elucidate the properties of these active species, which are summarized in **Table 2.1**.

Table 2.1. A summary of various selected characterization techniques for the elucidation of the properties of the active species in porous material.

Characterization techniques	Catalyst properties	Examples	Ref.
SXRD	Atomic and crystallographic information	Cu_2-ZSM-5	[1,2]
XAFS	coordination environment	Cu-Co-ZSM-5	[3,4]
XPS	Chemical states of metal	Cu-SSZ-13	[5,6]
UV-Vis	Electronic properties	Cu-SSZ-13	[7,8]
FT-IR	Vibration properties	Ni-ZSM-5	[9,10]
NH_3-TPD	Acidity measurement	Ge-SSZ-13	[11,12]
SEM/STEM	Morphology and active site analysis	Cu-MFI	[13,14]

Powder diffraction is a powerful technique for obtaining atomic and crystallographic information. With the assistance of synchrotron X-rays, high-quality XRD patterns can be obtained for further analysis. According to the diffraction peak intensity equation, the composition of peaks in an XRD pattern depends on various factors, including electron density, plane angle, and vibration factors, which exhibit fingerprint-like properties. The combination of synchrotron XRD (SXRD) and Rietveld analysis directly illustrates the crystalline material. The precise positioning of active species and guest molecules can be achieved through the simulated annealing technique. Chen et al. reported the structural elucidation of the stepwise assembly of bimetallic ligand-mediated metal ensembles (LMMEs) supported on a zeolite framework [15]. Based on the refinement results, the Cu-Cu and Cu-Zn LMMEs were found to be located at the intersection of the sinusoidal and straight channels, as well as at the opening of the straight channel. The LMMEs model was confirmed through several characterization techniques, including EXAFS fitting, MALDI-TOF-TOF-MS, XPS, and UV-Vis analysis.

X-ray absorption fine structure (XAFS) is a specific structure obtained from X-ray absorption spectroscopy, which enables the analysis of the local structure of the target element. The shape of the spectrum varies depending on changes in the electron density of the coordination environment. The XAFS spectrum can be divided into two regions: X-ray absorption near edge structure (XANES) and extended X-ray absorption fine

structure (EXAFS). The former provides concise information about the coordination environment, including geometry and oxidation state, while the latter offers detailed coordination information such as path length, coordination number, and the type of coordinated atom. Chen et al. elucidated the detailed coordination information of the Cu-Co bimetallic active site supported on hierarchical USY zeolite through quantitative fitting of EXAFS data [3]. The scattering paths of Co-N/O and Cu-N/O were determined to be in the range of 2.0 to 2.1 Å, and the average coordination numbers for Co and Cu were both approximately 4. These findings align with the assigned model of the Cu-Co bimetallic active site.

X-ray photoelectron spectroscopy (XPS) is a powerful technique used to determine the chemical state of metal elements based on the photoelectric effect. The variations in chemical state and electronic structure directly impact the electron population spectra of the element, leading to chemical shifts. These spectral changes serve as unique fingerprints and provide precise information regarding the chemical state of the target element. Chen et al. reported on the changes in the chemical state of Cu in SSZ-13 zeolite in the presence of Sm for enhanced Cu stability [5]. The peak corresponding to Cu^{2+} at approximately 935 eV exhibited a shift towards lower binding energy with increasing Sm loading (from 935.7 eV to 934.8 eV). This shift indicates a higher electronegativity of Cu^{2+} ions and SSZ-13 zeolite, which may be attributed to electron transfer between Sm^{3+} and Cu^{2+} ions (**Figure 2.1**).

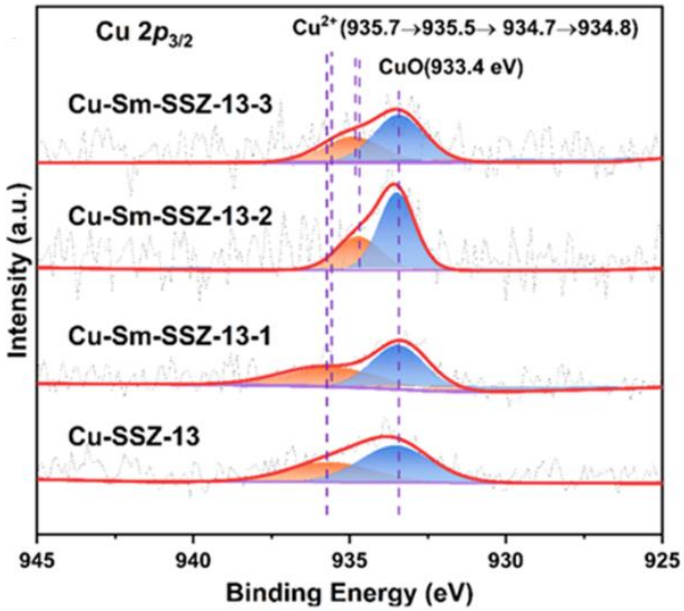

Figure 2.1. Cu 2p3/2 XPS spectra of SSZ-13 samples. Reprinted with permission from ref. [5]. Copyright © 2022 American Chemical Society.

Ultraviolet-visible spectroscopy (UV-Vis) is a technique used to observe electron transitions in a sample, including π-π*, σ-σ*, and d-d transitions. The shifting of the absorption peak provides insights into the changes in the electronic structure of transition metals, including alterations in the coordination environment and oxidation state. Lei et al. demonstrated the application of UV-Vis spectroscopy to uncover electronic structure changes in Cu within SSZ-13 zeolite [7]. The presence of an intense peak around 250 nm after O_2 activation indicates the interaction between O_2 and Cu through an $O \rightarrow Cu^{II}$ LMCT transition. Furthermore, the shift of the peak from around 700 nm to 800 nm corresponds to the Cu^{II} d-d transition, which aligns with the bonding between O_2 and Cu^{II} (**Figure 2.2**).

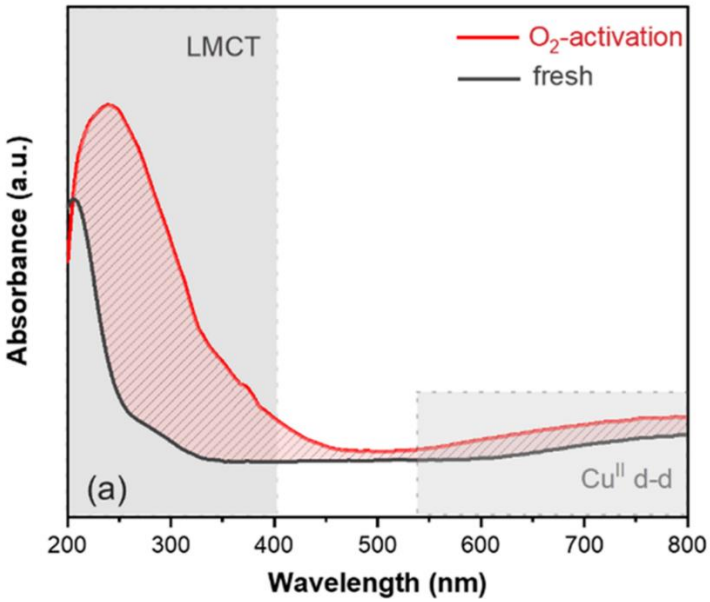

Figure 2.2. In situ DRUVS spectra of the fresh and O_2-activated Cu-SSZ-13 at room temperature. Reprinted with permission from ref. [7]. Copyright © 2023 American Chemical Society.

Unlike UV-Vis spectroscopy, Fourier-transform infrared spectroscopy (FT-IR) generates absorption spectra with lower energy to gather information about molecular motion rather than electronic state changes. Specific molecular motions generate signals within specific wavenumber ranges, and the absorption peaks provide information about interactions between different molecules. Consequently, FT-IR has found several applications for the analysis of specific active sites or species, such as pyridine-adsorbed FT-IR (Py-IR) for acid site analysis and carbon monoxide adsorbed FT-IR (CO-IR) for metal species analysis. Deng et al. demonstrated the use of Py-IR to determine the acid type in zeolite Y with the modification of different metal ions [9]. The intensity of the peak corresponding to Brønsted acid sites significantly decreased with the introduction of La and Ca, indicating the occupation of Brønsted acid sites by the metal ions. Hadjiivanov et al. employed CO-IR to uncover the presence of two types of

Ni^{2+} ions in ZSM-5 zeolite [10]. Based on literature data, two bands at 2220 and 2212 cm^{-1} were detected, displaying higher stability than other physisorption peaks, and were assigned to the two kinds of Ni^{2+}-CO species.

Ammonia temperature programmed desorption (NH_3-TPD) is a characterization technique that quantifies the number of base molecules (ammonia) chemisorbed on acid sites to calculate the number of acid sites in zeolite materials. Additionally, the desorption temperature of the base molecule can determine the acid strength [10]. Kokuryo et al. reported the enhancement of acid strength in SSZ-13 zeolite through Ge incorporation using NH_3-TPD [11]. The high-temperature peak (HT peak), typically associated with Brønsted acid sites, exhibited a higher desorption temperature in Ge/SSZ-13, ranging from 516 °C (SSZ-13) to 550 °C. This indicates an enhancement of the Brønsted acid sites.

Scanning electron microscopy (SEM) and scanning transmission electron microscopy (STEM) are the characterization techniques to confirm the morphology, particle size, and thickness by acquiring the sample image with the electron beam. With the combination of energy-dispersive X-ray spectroscopy (EDX), the distribution of the doped metal can also be confirmed [16,17]. Tang et.al. employed the STEM for the characterization of Cu/ZSM-5 zeolite samples with different Si/Al ratios [13]. The Al shows uniform distribution in the zeolite framework and the Cu also follows the same trend with Al, indicating the choring role of Al over the Cu species in the zeolite framework.

2.4. Characterisation experiment details

High-resolution synchrotron PXRD

Synchrotron PXRD measurements for structural determination were collected at beamline BL02B2 at SPring-8, Japan. The energy of the incident X-ray flux was set at 17.7 keV[18]. The wavelength (λ = 0.700261 Å) and the 2θ-zero point (ZP = 0.00020°) were calibrated using a diffraction pattern obtained from a high-quality CeO_2 powder (NIST SRM674b). High-resolution synchrotron PXRD data were obtained from the zeolite samples (loaded in 0.5-mm borosilicate capillaries) using the Microstrip sYstem for Time rEsolved experimeNts (MYTHEN) detectors, with a modular system constructed by six MYTHEN detectors. The patterns were collected in the 2θ range 2-70° with 0.006° data binning. Each synchrotron PXRD pattern was collected for 5 min for each 2θ-step, i.e., 10 min in total for MYTHEN data summation. This procedure produced good quality patterns of a high signal-to-noise ratio. It should be particularly noted that the R-factors using the MYTHEN detectors are artificially high. Therefore, the quality of the Rietveld refinement should be best judged by the difference between the fitted and observed data.

(Zeolite part)

Using the TOPAS software, the lattice parameters were obtained using Le Bail and Rietveld refinement analyses of the diffraction patterns were performed. The starting coordinates used were based on the H-ZSM-5 zeolite model by Heo *et al.* for refinement [19]. The background curve was fitted by a Chebyshev polynomial with an average of 20 coefficients. The Thompson-Cox-Hastings (pseudo-Voigt) function was applied to describe the diffraction peaks [20]. The scale factor and lattice parameters were allowed to vary for all the histograms.

(UiO part)

Using the TOPAS 6.0 software, the lattice parameters were obtained using Pawley and Rietveld refinement analyses of the diffraction patterns were performed. The background curve was fitted by a Chebyshev polynomial with an average of 16 coefficients. The Thompson-Cox-Hastings (pseudo-Voigt) function was applied to describe the diffraction peaks[21]. The scale factor and lattice parameters were allowed to vary for all the histograms.

The final refined structural parameters for each data histogram were carried out using the Rietveld method with the fractional coordinates (*x, y, z*) and isotropic displacement factors (B_{eq}) for all atoms. In addition, the R_{wp} and *gof* values ($gof = R_{wp}/R_{exp}$) helped assess the quality of fit, where R_{exp} represents the quality of the data. So, the R_{wp} value should be close to R_{exp} for a good fit.

Resonant Synchrotron PXRD

Resonant X-ray diffraction is unique to synchrotron light sources due to the energy or wavelength tunability of the incident beam. It can be used to determine crystallographic sites occupied by atoms with low electronic contrast. The resonant technique enables elements with close atomic numbers like Fe (Z = 26) and Co (Z = 27), or Cu (Z = 29) and Zn (Z = 30) to be distinguished by utilizing the contrast between their anomalous scattering factors *f'* (real, the change in scattering factor magnitude) and *f''* (imaginary, phase shift). In our recent RXRD work, the relative proportion of the Cu and Zn sites in copper-zinc-tin sulfide was determined [22]. As it is vital to differentiate the site occupancies of Cu and Zn in the clusters, the technique was therefore used again in this study.

Synchrotron X-ray powder diffraction measurements were collected in Beamline I11 at Diamond Light Source (UK) using the ultra-high resolution multi-analyzer crystal (MAC) detector at 295 K. The angular resolution of the data collected was 1 mdeg per step. Cu^{2+} ion-exchange ZSM-5 sample was used as an external for X-ray energy calibration and for the determination of the K adsorption edge from the fluorescence signals of the samples by scanning the monochromator. Resonant diffraction patterns were taken at 10 eV, 15 eV and 21 eV below the Cu K-edge and a comparative non-resonant diffraction pattern was taken at 15 keV. Rietveld refinement was carried out using TOPAS v.6.0. Resonant and non-resonant data were modelled simultaneously by refining the fractional coordinates (*x, y, z*) and site occupancy factors. The corresponding *f'* and *f''* values were obtained from using the subroutine library by Brennan and Cowan.[23]

Extended X-ray Absorption Fine Structure (EXAFS) Spectroscopy

The XAFS data were collected at Beamline BL07A of the Taiwan Light Source (Taiwan) and Beamline BL01B2 of SPring-8 (Japan). A Si(111) double crystal monochromator (DCM) was used to scan the photon energy.

X-ray Photoelectron Spectroscopy (XPS)

The XPS measurements were collected using Thermo Scientific Nexsa (12kV cathode-biased Al Kα, $h\nu$ = 1486.6 eV) spectrometer with a spot size of 400 µm at the base pressure < 5 x 10^{-10} mbar. An Ar ion gun was used to etch the samples with the etching rate of 0.5 nm s^{-1}, and the XPS spectra were obtained at approximately 20 nm depth intervals. The raw data were corrected for substrate charging with the binding energy (BE) of the C 1*s* peak at 284.5 eV.

Thermogravimetric Analysis (TGA)

The TGA measurements of as-synthesised samples were performed in air (40 mL min^{-1}) up to 700 °C using Thermogravimetric Analyzer/Differential Scanning Calorimeter (Mettler Toledo TGA/DSC^{3+}).

Ultraviolet-visible-Near-Infrared Diffuse Reflection Spectroscopy (UV-Vis-NIR DRS)

The UV-vis-NIR DRS measurements were carried out with the obtained samples in a Perkin-Elmer Lambda 1050-UV-Vis-NIR spectrophotometer with an Integrating Sphere-150 mm UV/vis/NIR (InGaAs) Module. The equipment was calibrated with a Spectral on standard, and the reflectance was measured in the 200 – 2500 nm range at an interval of 2 nm.

Fourier-Transform Infrared Spectroscopy (FT-IR)

The FT-IR in attenuated total reflection (ATR) mode was measured using Thermo Scientific Nicolet iS50 equipped with a single bounce diamond crystal and a deuterated triglycine sulfate (DTGS) detector.

2.5. Reference

(1) Chen, T.; Wang, Y.; Xue, Q.; Wun, C. K. T.; So, P. K.; Yung, K. F.; Wu, T. S.; Soo, Y. L.; Taniya, K.; Day, S.; Tang, C. C.; Li, Z.; Huang, B.; Tsang, S. C. E.; Wong, K. yin; Lo, T. W. B.Atomically Precise Bimetallic Metal Ensembles with Tailorable Synergistic Effects. *Cell Reports Phys. Sci.* **2022**, *3* (4), 100850. https://doi.org/10.1016/j.xcrp.2022.100850.

(2) Xue, Q.; Ng, B. K. Y.; Man, H. W.; Wu, T. S.; Soo, Y. L.; Li, M. M.; Kawaguchi, S.; Wong, K. Y.; Tsang, S. C. E.; Huang, B.; Lo, T. W. B.Controlled Synthesis of Bi- And Tri-Nuclear Cu-Oxo Nanoclusters on Metal-Organic Frameworks and the Structure-Reactivity Correlations. *Chem. Sci.* **2022**, *13* (1), 50–58. https://doi.org/10.1039/d1sc05495c.

(3) Chen, T.; Yu, W.; Wun, C. K. T.; Wu, T. S.; Sun, M.; Day, S. J.; Li, Z.; Yuan, B.; Wang, Y.; Li, M.; Wang, Z.; Peng, Y. K.; Yu, W. Y.; Wong, K. Y.; Huang, B.; Liang, T.; Lo, T. W. B.Cu-Co Dual-Atom Catalysts Supported on Hierarchical USY Zeolites for an Efficient Cross-Dehydrogenative C(Sp2)-N Coupling Reaction. *J. Am. Chem. Soc.* **2023**. https://doi.org/10.1021/jacs.3c00114.

(4) Xue, Q.; Xie, Y.; Wu, S.; Wu, T. S.; Soo, Y. L.; Day, S.; Tang, C. C.; Man, H. W.; Yuen, S. T.; Wong, K. Y.; Wang, Y.; Lo, B. T. W.; Tsang, S. C. E.A Rational Study on the Geometric and Electronic Properties of Single-Atom Catalysts for Enhanced Catalytic Performance. *Nanoscale* **2020**, *12* (45), 23206–23212. https://doi.org/10.1039/d0nr06006b.

(5) Chen, M.; Li, J.; Xue, W.; Wang, S.; Han, J.; Wei, Y.; Mei, D.; Li, Y.; Yu, J.Unveiling Secondary-Ion-Promoted Catalytic Properties of Cu-SSZ-13 Zeolites for Selective Catalytic Reduction of NO X. *J. Am. Chem. Soc.* **2022**, *144* (28), 12816–12824. https://doi.org/10.1021/jacs.2c03877.

(6) Zsoldos, Z.; Vass, G.; Lu, G.; Guczi, L.XPS Study on the Effects of Treatments on Pt2+ and Co2+ Exchanged into NaY Zeolite. *Appl. Surf. Sci.* **1994**, *78* (4), 467–475. https://doi.org/10.1016/0169-4332(94)90070-1.

(7) Lei, H.; Chen, D.; Yang, J. Y.; Khetan, A.; Jiang, J.; Peng, B.; Simon, U.; Ye, D.; Chen, P.Revealing the Formation and Reactivity of Cage-Confined Cu Pairs in Catalytic NOx Reduction over Cu-SSZ-13 Zeolites by In Situ UV−Vis Spectroscopy and Time-Dependent DFT Calculation. *Environ. Sci. Technol.* **2023**, *57* (33), 12465–12475. https://doi.org/10.1021/acs.est.3c00458.

(8) Sarohan, N.; Ozbek, M. O.; Kaya, Y.; Abdellatief, M.; Ipek, B.Hydrogen Adsorption on Co2+ - and Ni2+- Exchanged -US-Y and -ZSM-5. A Combined Sorption, DR UV–Vis, Synchrotron XRD and DFT Study. *Int. J. Hydrogen Energy* **2022**, *47* (75), 32181–32201. https://doi.org/10.1016/j.ijhydene.2022.07.130.

(9) Deng, C.; Zhang, J.; Dong, L.; Huang, M.; Li, B.; Jin, G.; Gao, J.; Zhang, F.; Fan, M.; Zhang, L.; Gong, Y.The Effect of Positioning Cations on Acidity and Stability of the Framework Structure of y Zeolite. *Sci. Rep.* **2016**, *6*, 1–13. https://doi.org/10.1038/srep23382.

(10) Hadjiivanov, K.; Knözinger, H.; Mihaylov, M.FTIR Study of CO Adsorption on Ni-ZSM-5. *J.*

Phys. Chem. B **2002**, *106* (10), 2618–2624. https://doi.org/10.1021/jp0132782.

(11) Kokuryo, S.; Jabri, H.Al; Miyake, K.; Uchida, Y.; Tanaka, S.; Miyamoto, M.; Oumi, Y.; Nishiyama, N.A Novel Strategy to Enhance Acid Strength of Zeolites by Incorporating Ge into Zeolite Framework. *ChemistrySelect* **2022**, *7* (17), 1–4. https://doi.org/10.1002/slct.202200756.

(12) Hunger, B.; Heuchel, M.; Clark, L. A.; Snurr, R. Q.Characterization of Acidic OH Groups in Zeolites of Different Types: An Interpretation of NH3-TPD Results in the Light of Confinement Effects. *J. Phys. Chem. B* **2002**, *106* (15), 3882–3889. https://doi.org/10.1021/jp012688n.

(13) Tang, X.; Ye, J.; Guo, L.; Pu, T.; Cheng, L.; Cao, X. M.; Guo, Y.; Wang, L.; Guo, Y.; Zhan, W.; Dai, S.Atomic Insights into the Cu Species Supported on Zeolite for Direct Oxidation of Methane to Methanol via Low-Damage HAADF-STEM. *Adv. Mater.* **2023**, *35* (25), 1–9. https://doi.org/10.1002/adma.202208504.

(14) Alswat, A. A.; Ahmad, M.Bin; Saleh, T. A.Preparation and Characterization of Zeolite\Zinc Oxide-Copper Oxide Nanocomposite: Antibacterial Activities. *Colloids Interface Sci. Commun.* **2017**, *16*, 19–24. https://doi.org/10.1016/j.colcom.2016.12.003.

(15) Chen, T.; Wang, Y.; Xue, Q.; Kit Tommy Wun, C.; Kin So, P.; Fu Yung, K.; Wu, T.-S.; Soo, Y.-L.; Taniya, K.; Day, S.; Tang, C. C.; Li, Z.; Huang, B.; Chi Edman Tsang, S.; Wong, K.; Woon Benedict Lo, T.Atomically Precise Bimetallic Metal Ensembles with Tailorable Synergistic Effects. *Cell Reports Phys. Sci.* **2022**, *4*, 100850.

(16) Yokoi, T.Characterization of Zeolites by Advanced SEM / STEM Techniques. *Sci. Instrum. News* **2016**, *7*, 17–23.

(17) Zhang, J.; Tang, X.; Yi, H.; Yu, Q.; Zhang, Y.; Wei, J.; Yuan, Y.Synthesis, Characterization and Application of Fe-Zeolite: A Review. *Appl. Catal. A Gen.* **2022**, *630* (August 2021), 118467. https://doi.org/10.1016/j.apcata.2021.118467.

(18) Kawaguchi, S.; Takemoto, M.; Osaka, K.; Nishibori, E.; Moriyoshi, C.; Kubota, Y.; Kuroiwa, Y.; Sugimoto, K.High-Throughput Powder Diffraction Measurement System Consisting of Multiple MYTHEN Detectors at Beamline BL02B2 of SPring-8. *Rev. Sci. Instrum.* **2017**, *88* (8). https://doi.org/10.1063/1.4999454.

(19) Heo, N. H.; Kim, C. W.; Kwon, H. J.; Kim, G. H.; Kim, S. H.; Hong, S. B.; Seff, K.Detailed Determination of the Tl+ Positions in Zeolite Tl-ZSM-5. Single-Crystal Structures of Fully Dehydrated Tl-ZSM-5 and H-ZSM-5 (MFI, Si/Al = 29). Additional Evidence for a Nonrandom Distribution of Framework Aluminum. *J. Phys. Chem. C* **2009**, *113* (46), 19937–19956. https://doi.org/10.1021/jp9061913.

(20) Thompson, P.; Cox, D. E.; Hastings, J. B.Rietveld Refinement of Debye–Scherrer Synchrotron X-Ray Data from Al2O3. *J. Appl. Crystallogr.* **1987**, *20* (2), 79–83. https://doi.org/10.1107/S0021889887087090.

(21) Thompson, P.; Cox, D. E.; Hastings, J. B.Rietveld Refinement of Debye-Scherrer Synchrotron X-Ray Data from Al2O3. *J. Appl. Crystallogr.* **1987**, *20* (2), 79–83. https://doi.org/10.1107/S0021889887087090.

(22) Bosson, C. J.; Birch, M. T.; Halliday, D. P.; Tang, C. C.; Kleppe, A. K.; Hatton, P. D.Polymorphism in Cu2ZnSnS4 and New Off-Stoichiometric Crystal Structure Types. *Chem. Mater.* **2017**, *29* (22), 9829–9839. https://doi.org/10.1021/acs.chemmater.7b04010.

(23) Brennan, S.; Cowan, P. L.A Suite of Programs for Calculating X-ray Absorption, Reflection, and Diffraction Performance for a Variety of Materials at Arbitrary Wavelengths. *Rev. Sci. Instrum.* **1992**, *63* (1), 850–853.

Chapter 3 Atomically dispersed 3d metal bimetallic dual atom catalysts and classification of the structural descriptors

Highlight of this chapter

Solid atomic catalysts possessing well-defined and intricate structures are considered to effectively bridge the gap between homogeneous and heterogeneous catalysis. However, the current limitations in achieving 'precise engineering' for solid atomic catalysts result in structural heterogeneity and consequently unsatisfactory catalytic selectivity. In this study, we present the assembly of late 3d metal cations, such as Co^{2+}, Ni^{2+}, Cu^{2+}, and Zn^{2+}, to form combinations of 'dual atoms' within zeolitic micropores, thereby circumventing issues related to uncontrolled metal aggregation during synthesis. Through a quantitative evaluation of structural descriptors via a probe superoxide dismutation reaction, we demonstrate the distinct synergistic advantage arising from the presence of two metal species, the tertiary structure surrounding the zeolitic support, and the local coordination environment. The identification and adjustability of these structural descriptors, as revealed in this work, provide a reliable approach to the precise engineering of next-generation solid dual-atom catalysts. Most of the content in this chapter has been published recently in Chem Catalysis [1]. The novelty and significance of this work have been particularly highlighted by Han et al. in Chem [2].

3.1 Introduction

Unlike the enzymatic or homogeneous counterparts, the distribution of active species and the local chemical environments in solid catalysts are often uneven due to intrinsic limitations in materials preparation, leading to generally less satisfactory catalytic selectivity. 'Precision engineering' has hence long been recognized to be an ideal solution but also a grand challenge by the heterogeneous catalysis community [3]. The reactivity and product selectivity over related atomic catalysts have been shown clearly different in various recent studies [4–6], such as the catalytic heterogeneity on related mono-, bi-, and tri-nuclear Cu-oxo catalysts done by our group[7].

A notable class of 'precisely engineered' examples is supported dual-atom catalysts. Modern approaches for developing supported dual-atom catalysts can be put into several major categories (**see Figure 3.1**) [8,9], including through (a) pyrolysis of multi-metallic precursors (such as oxides and reticular compounds), (b) modular decoration on the surfaces of metals or metal oxides/sulfides [10,11], (c) engineering of unique and pre-organized microporous scaffolds (such as zeolites and metal-organic frameworks) [12–20], and (d) the use of low-dimensional networks [21–23]. These modern approaches, however, may often suffer from various limitations, such as the difficulty in the control of the interatomic distances and limited transferability to other metal species.

We, herein, report a creative synthetic approach to assemble two late 3*d* metal cations (M^{2+}) within microporous domains in a modular manner. This approach allows for the systematic investigation of various structural descriptors, including metal nuclearity, elemental composition, local environment, and tertiary structure around the metal active sites. This is achieved by the utilization of the underlying principles of coordination chemistry (*via* modular formation of specific acid-base adducts) and solid-state chemistry (*via* spatial confinement). Interestingly, our Zn_A-Cu_B-Z sample shows a high resemblance of the structural features to those of the native Cu,Zn-containing superoxide dismutase (Cu,Zn-SOD), which further allows a comparable catalytic reactivity. The microporous framework not only offers rigid support for the immobilization of foreign metal species but also provides a quasi-isolated cavity for the effective catalysis reaction.

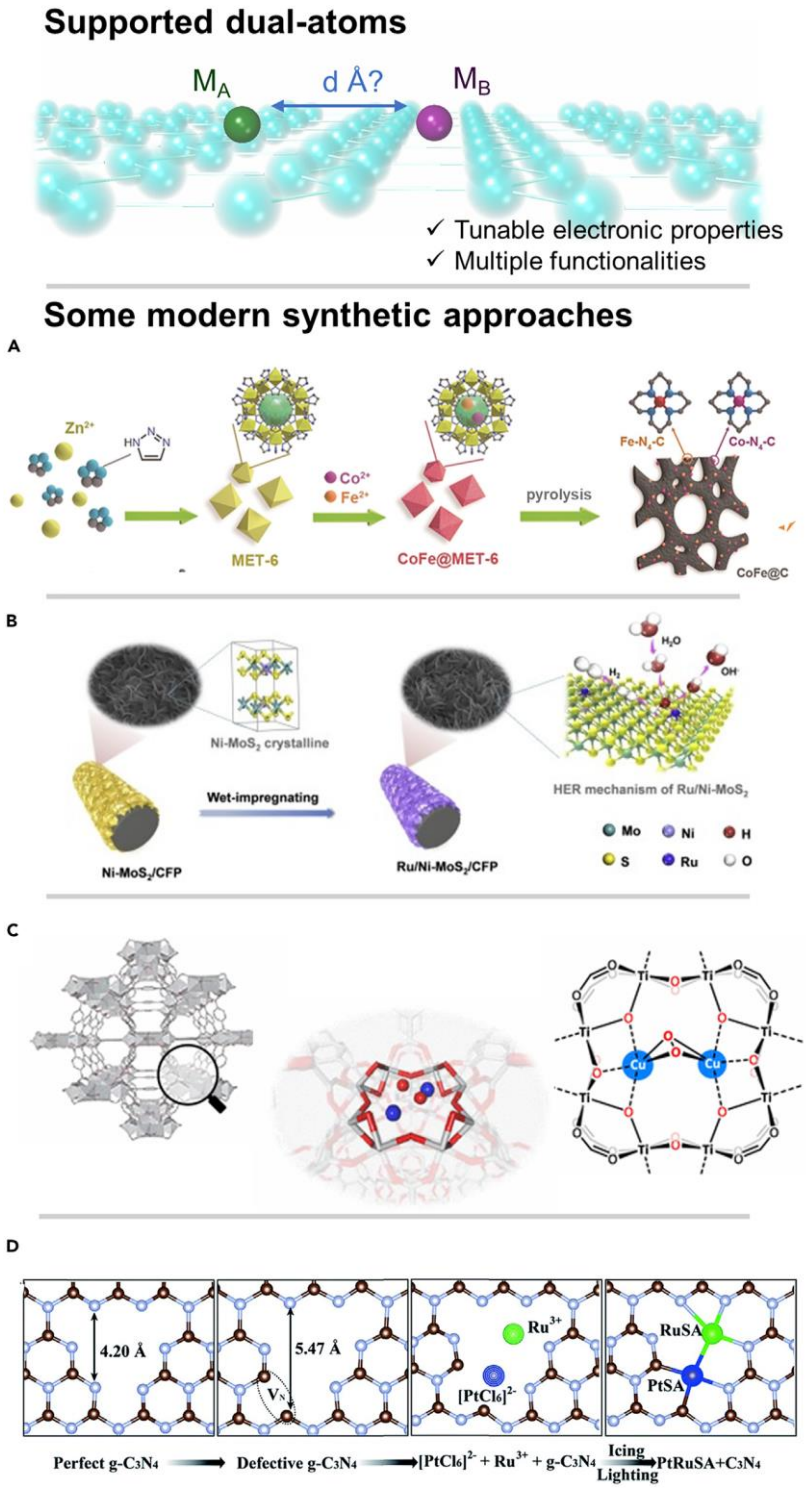

Figure 3.1. Overview of modern approaches for developing supported dual-atom catalysts, through (a) pyrolysis of multi-metallic precursors. Reproduced with permission [24]. Copyright 2018, Wiley-VCH; (b) modular decoration on the surfaces of metals or metal oxides/sulfides. Reproduced with permission [10]. Copyright 2021, Elsevier; (c) engineering of microporous scaffolds. Reproduced with permission [25]. Copyright 2021, American Chemical Society; (d) the use of low-dimensional network. Reproduced with permission [21]. Copyright 2019, Royal Society of Chemistry.

3.2 Experimental procedure

Catalyst preparation

We employ a modular assembly approach published in our earlier work over metal-organic frameworks [26]. As shown in **Scheme 3.1**, the preparation of Zn_A-Cu_B-Z is here used as an illustration; by ion exchange with $Zn(NO_3)_2 \cdot 6H_2O$ (Sigma-Aldrich; 98%), mononuclear Zn_A-Z has been prepared as our standard precursor material 'seed'. It is noted that excessive ion-exchange steps have been taken to ensure the maximum ion-exchange capability of the H-ZSM-5 zeolite has been reached. Subsequent Cu metalation to form Zn_A-Cu_B-Z is achieved by applying our seed with Lewis di-basic imidazole (as the linker, 'Im'), followed by the addition of $Cu(NO_3)_2 \cdot 2.5H_2O$ in a controlled manner.

Catalyst characterization

Resonant X-ray diffraction is unique to synchrotron light sources due to the energy or wavelength tunability of the incident beam. It can be used to determine crystallographic sites occupied by atoms with low electronic contrast. The resonant technique enables elements with close atomic numbers like Fe (Z = 26) and Co (Z = 27), or Cu (Z = 29) and Zn (Z = 30) to be distinguished by utilizing the contrast between their anomalous scattering factors *f'* (real, the change in scattering factor magnitude) and *f''* (imaginary, phase shift). In our recent RXRD work, the relative proportion of the Cu and Zn sites in copper-zinc-tin sulfide was determined [27]. As it is vital to differentiate the site occupancies of Cu and Zn in the clusters, the technique was therefore used again in this study.

Synchrotron X-ray powder diffraction measurements were collected in Beamline I11 at Diamond Light Source (UK) using the ultra-high resolution multi-analyzer crystal (MAC) detector at 295 K. The angular resolution of the data collected was 1 mdeg per step. Cu^{2+} ion-exchange ZSM-5 sample was used as an external for X-ray energy calibration and for the determination of the K adsorption edge from the fluorescence signals of the samples by scanning the monochromator, as shown in **Figure 3.4b**, Resonant diffraction patterns were taken 10 eV, 15 eV, and 21 eV below the Cu K-edge and a comparative non-resonant diffraction pattern was taken at 15 keV. Rietveld refinement was carried out using TOPAS v.6.0. Resonant and non-resonant data were modeled simultaneously by refining the fractional coordinates (*x, y, z*) and site occupancy factors. The corresponding *f'* and *f''* values were obtained by using the subroutine library by Brennan and Cowan [28]. The verification of the accuracy of the combined Rietveld refinement process is presented in **Table 3.7**. A total of 2783 *hkl* independent observables from a combination of 4 SXRD patterns have been used to refine 43 parameters.

Catalytic reactivity

The SOD activity was evaluated by measuring the inhibition of the photoreduction of nitro blue tetrazolium chloride (NBT). The reaction of methionine and riboflavin acts as the source of superoxide. The suspension was prepared in a 50 mm phosphate buffer in pH 7.8, riboflavin (3.4 μm), methionine (10 mm), NBT (46 μm), and different amounts of Zn_A-Cu_B-Z (0–100 μm). Riboflavin was last added. The reaction was initiated by illumination of the mixtures with an 18 W fluorescent lamp placed at 15 cm, at 25 °C. The reduction of NBT was measured at 560 nm after an illumination period of 30 min.

Human hepatocellular carcinoma (HCC) cell lines MHCC-97L (Liver Cancer Institute, Fudan University) and PLC/PRF/5 (Japan Cancer Research Bank) were cultured in Dulbecco's Modified Eagle Medium (DMEM) with high glucose supplemented with 10% heat-inactivated fetal bovine serum (FBS), 100 mg mL^{-1} penicillin G, and 50 μg mL^{-1} streptomycin at 37 °C in a humidified chamber containing 5% CO_2. Cells were used within five passages after thawing. Culturing medium was refreshed every two to three days and cells were passaged every three to four days.

HCC cell lines were seeded on 96-well plate 24 hours prior to the addition of Zn_A-Cu_B-Z. Concentrations of Zn_A-Cu_B-Z ranging from 1.56 μm to 200 μm in 5% FBS were then added. After 48 hours, MTT dye, at a concentration of 5 mg/mL, was added and the plates were incubated for 3 hours in a moist chamber at 37 °C. Optical density was determined by eluting the dye with isopropanol supplemented with hydrochloric acid. The absorbance was measured at 570 nm. The experiments of each cell line were performed in triplicates.

3.3 Results and Discussion

A highly crystalline H-ZSM-5 sample (***MFI***-type, SiO_2:Al_2O_3 = 46) was employed as the inorganic support that was extensively characterized in our previous reports [29,30]. **Scheme 3.1** shows the bio-inspired synthesis procedures of the supported dual-atom catalysts. Imidazolate-based species ('Im', akin to the bridging histidine (His_{61}) in Cu,Zn-SOD enzyme) was used to connect two cationic metal M^{2+} (M = Co, Ni, Cu, and Zn) nuclei. Imidazolate was chosen because of its rigid aromatic structure and well-balanced di-basicity. A series of dual-atoms comprised of late 3*d* metals supported on ZSM-5 zeolites have been accordingly synthesized, denoted as 'M_A-M_B-Z' according to the order in the metalation step. **Figure 3.2** shows their powder X-ray diffraction (PXRD) patterns, where only marginal shifts of the Bragg peaks (space group: *Pnma*) have been observed with respect to the parent H-ZSM-5 support, suggesting that the metalation process did not greatly alter the host crystallinity. No major structural change nor metal/metal oxide aggregation was observed, which signifies the uniform dispersion of the extra-framework species. The elemental analysis by X-ray fluorescence spectroscopy (XRF) is shown in **Table 3.1** in the Supporting Information (SI). For instance, the Cu:Zn content in Zn_A-Cu_B-Z is about 1:1, and the Zn contents in Zn_A-Z and Zn_A-Zn_B-Z are 1.36 wt% and 2.66 wt%, respectively. Our control experiments show that the metal content does not change without applying Im. This comparative analysis clearly shows the efficacy of our dual-atom synthesis [31].

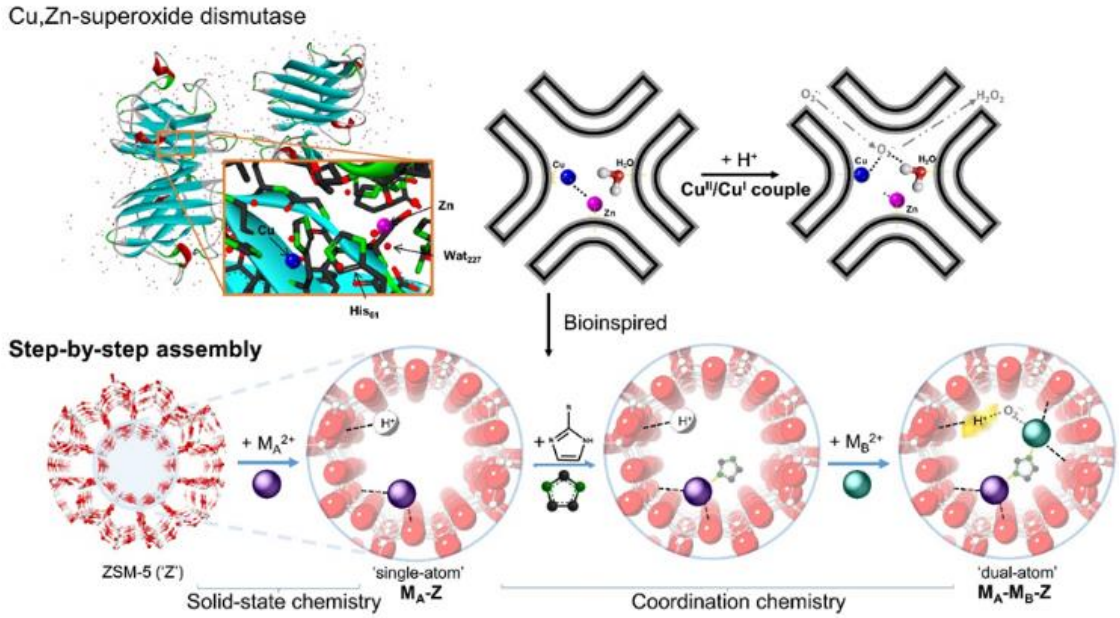

Scheme 3.1. Schematic illustration of the bio-inspired 'step-by-step' assembly approach. View of the enzyme structure and active site of the native Cu,Zn-SOD enzyme. (PDB: 1Z9P; Crystal Database of the National Center for Biotechnology Information) [32].

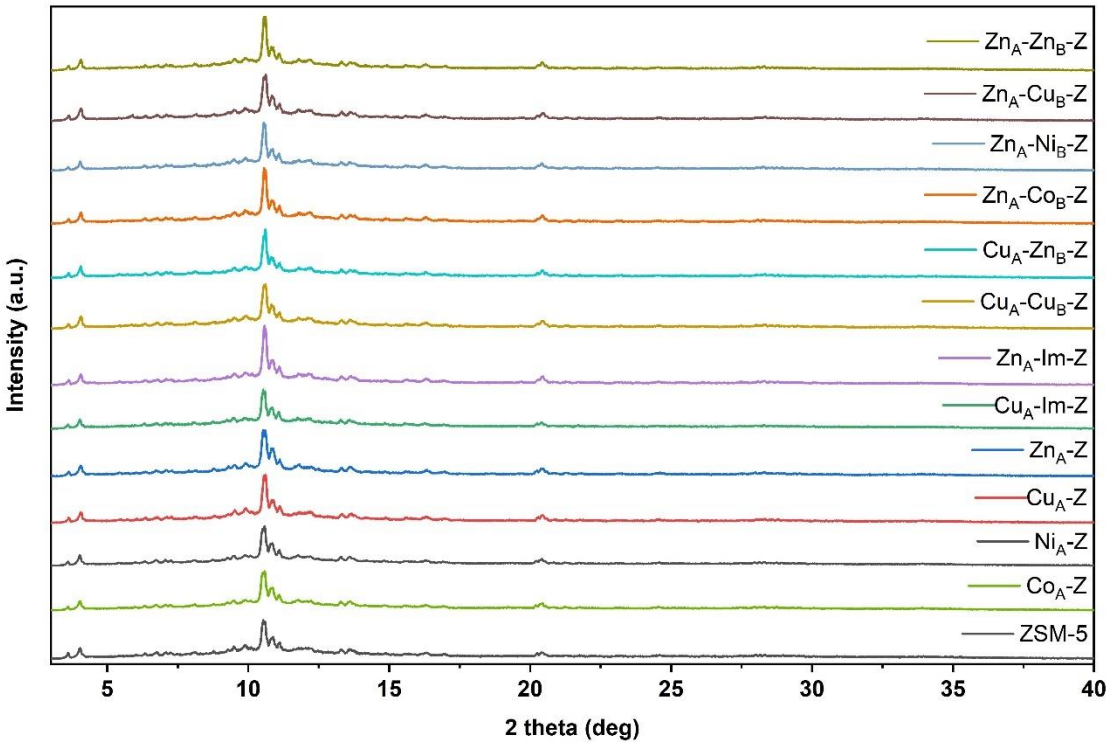

Figure 3.2. PXRD patterns of the zeolite samples as labeled (λ = 0.7093 Å).

We first employed matrix-assisted laser desorption/ionization time-of-flight/time-of-flight mass spectroscopy (MALDI-TOF-TOF MS) to investigate the structural features of the samples. Cu_A-Cu_B-Z and Zn_A-Cu_B-Z were chosen for major illustration in our subsequent materials characterization due to their superior property in our model catalytic reaction (discussed in the section below). As shown in **Figure 3.3**, the MS peak patterns can be assigned to dimeric Cu_2 and Cu_1Zn_1, which match well with the theoretical mass intensity ratio. Monomeric Cu_1 and Zn_1 in the low mass region are also observed potentially due to experimental residual of Cu_1 and Zn_1 and fragmentation from laser irradiation. Any trace of peak patterns that can correspond to metal clusters with higher nuclearity was not detected. In contrast, the absence of the structural features of Cu_A-Z, Zn_A-Z, and derivatives is shown in **Figures 3.4–3.7**, suggesting that imidazole is necessary (aromatic stabilization) to facilitate the desorption of the embedded species from the zeolite host.

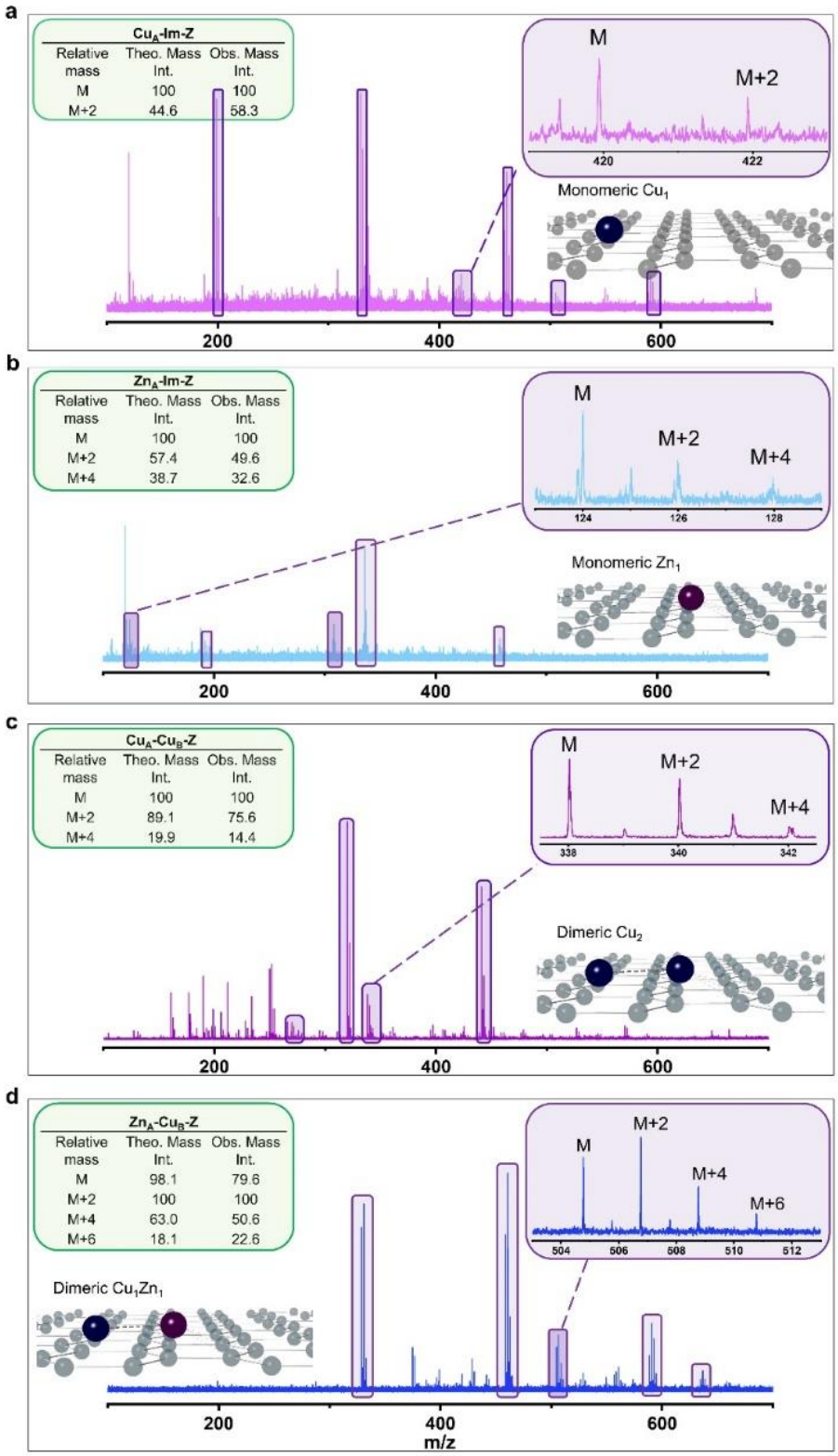

Figure 3.3. MALDI-TOF-TOF mass spectra of (a) Cu_1-meIm-Z, (b) Zn_1-meIm-Z, (c) Cu_A-Cu_B-Z, and (d) Zn_A-Cu_B-Z. The theoretical mass intensity (theo. mass int.) analysis of the major features based on the relative isotope distribution of the proposed nuclear combinations is presented in the inset tables. The regions highlighted in brown are shown in the inset, whereas the regions highlighted in yellow show comparable mass intensity distribution.

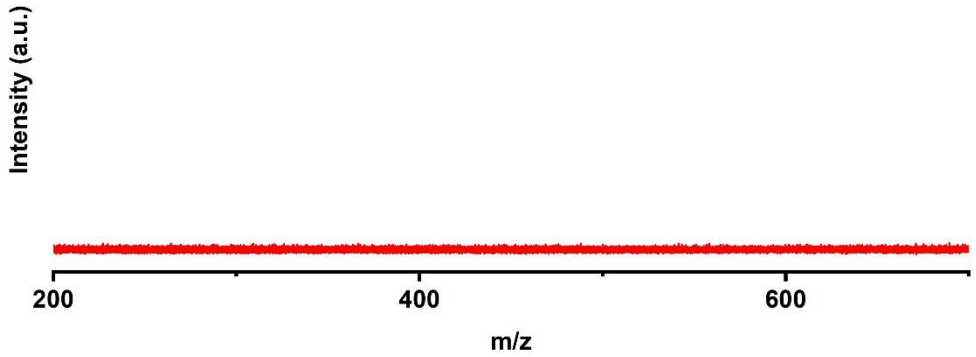

Figure 3.4. MALDI-TOF-TOF mass spectrum of Cu_A-Z. No structural feature can be detected at any given laser power.

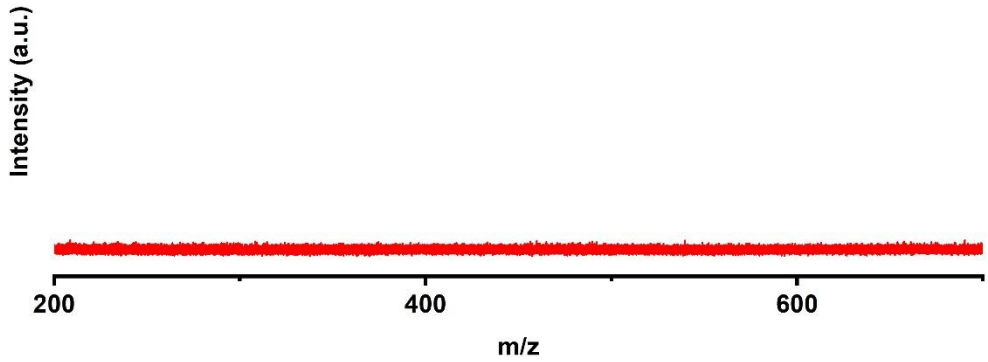

Figure 3.5. MALDI-TOF-TOF mass spectrum of Zn_A-Z. No structural feature can be detected at any given laser power.

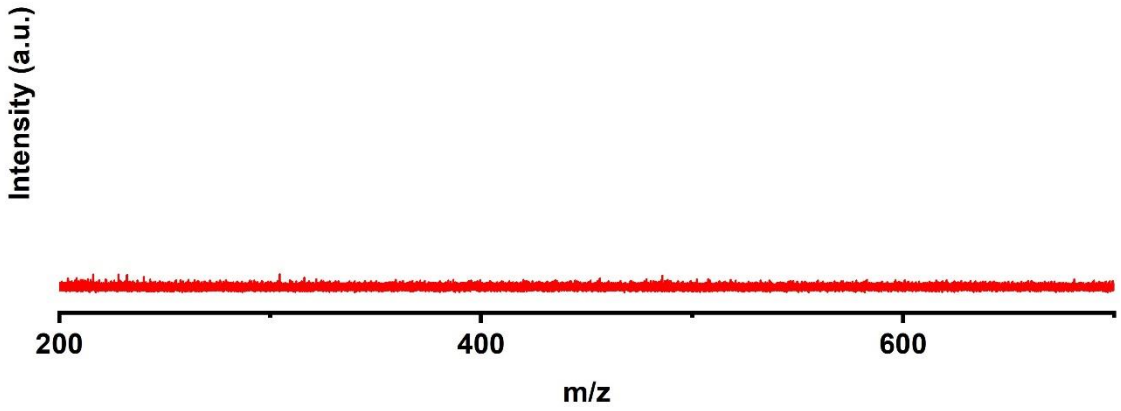

Figure 3.6. MALDI-TOF-TOF mass spectrum of Cu_A-Cu_B-Z (no linker).

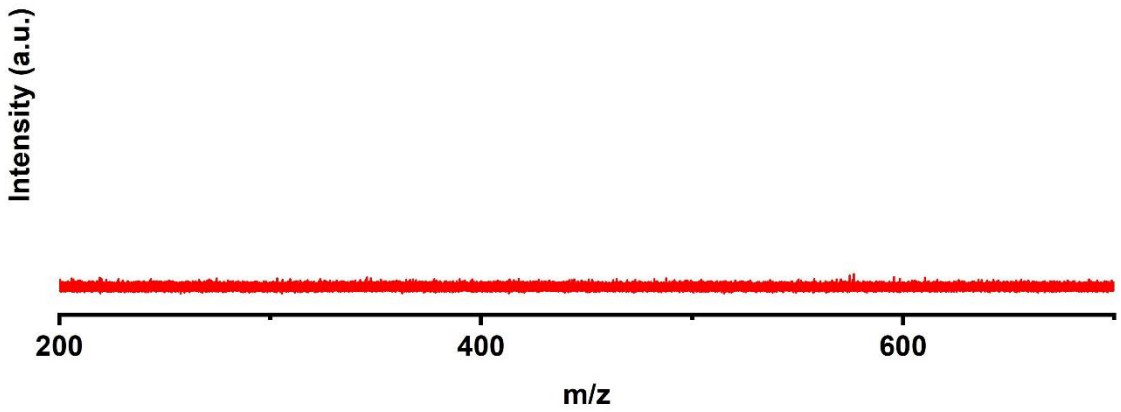

Figure 3.7. MALDI-TOF-TOF mass spectrum of Zn_A-Cu_B-Z (no linker).

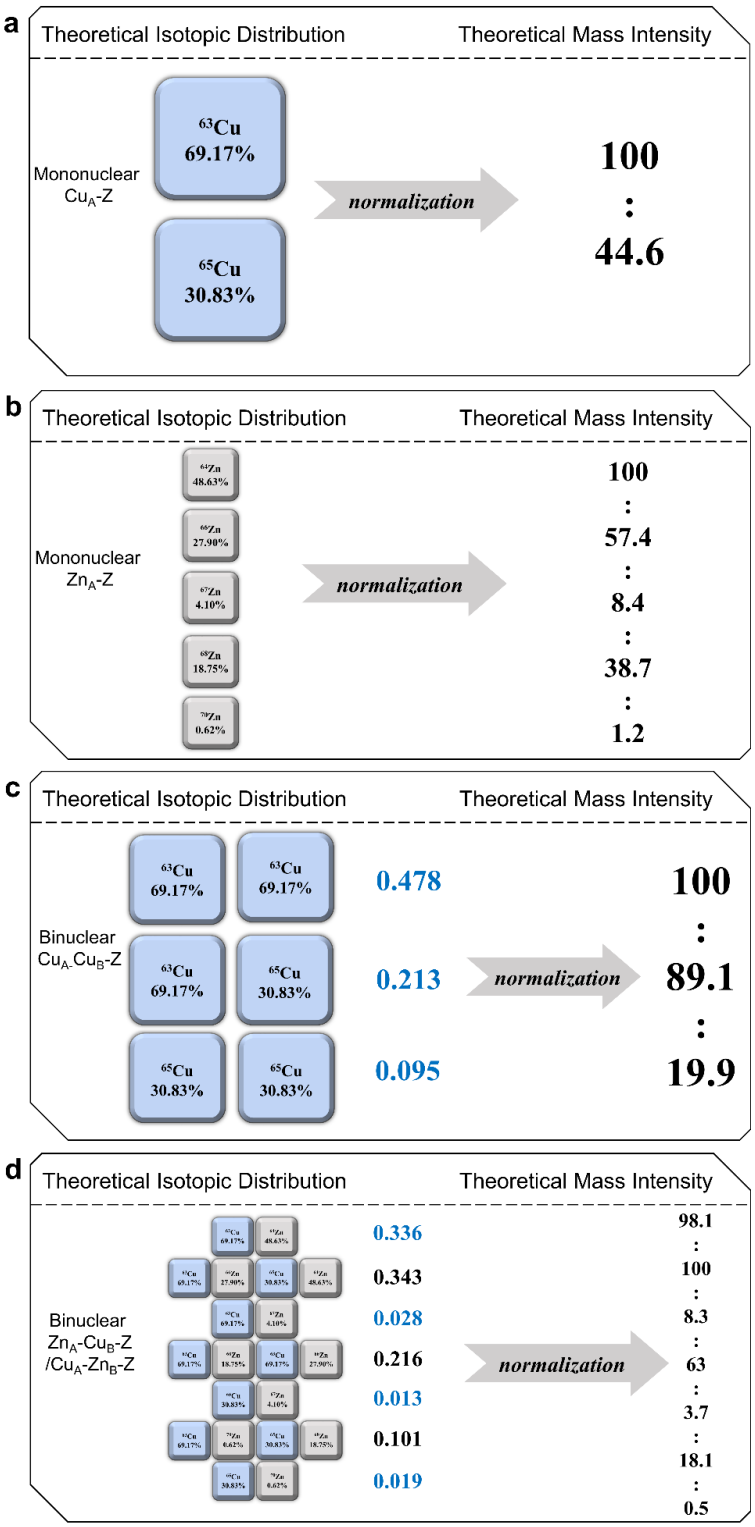

Figure 3.8. Detailed derivation of the theoretical mass intensity of (a) Cu_A-Z, (b) Zn_A-Z, (c) Cu_A-Cu_B-Z, and (d) Cu_A-Zn_B-Z or Zn_A-Cu_B-Z. The calculation of the theoretical mass intensity of the zeolite samples labeled was done according to the theoretical isotopic distribution of copper and zinc.

The oxidation states of Cu and Zn in Zn_A-Cu_B-Z were both determined as +2 as revealed by X-ray absorption near-edge spectroscopy (XANES, **Figure 3.9**) and X-ray photoelectron spectroscopy (XPS, **Figure 3.10**). Conventional spectroscopic measurements have been employed to study the metal-linker interactions. The UV-vis-NIR diffuse reflectance (**Figure 3.11(a)**) and FTIR (**Figure 3.11(b)**) spectra reveal the formation of Cu–Im and Zn–Im interactions, respectively. The detailed discussion is described in the SI (also see **Figure 3.12**).

The coordination environments of Cu and Zn in Zn_A-Cu_B-Z have been discerned by extended X-ray absorption fine structure (EXAFS) spectroscopy. The wavelet transform (WT) analysis of the EXAFS data is presented in **Figure 3.11(c)–(d)**, which can better correlate the absorption data in k- and R-space. The highest WT intensities belong to the lobes centered at k ~ 7.0 $Å^{-1}$, R ~ 1.5 Å, and k ~ 6.0 $Å^{-1}$, R ~ 1.5 Å, respectively, which correspond to the N/O atoms around the Cu and Zn centers. No significant backscattering at higher k-space (at k > 10 $Å^{-1}$, R > 2.5 Å) was observed, indicating the absence of Cu or Zn aggregation. The quantitative fittings of the EXAFS data are summarized in **Table 3.2** and **Figure 3.13**, with the average bond lengths of Cu–N/O and Zn–N/O calculated as 1.96(1) Å and 1.99(1) Å in Zn_A-Cu_B-Z, respectively. Both the average coordination numbers of Cu–N/O and Zn–N/O were determined as *ca.* 4. By combining thermogravimetric analysis with elemental analysis (**Figure 3.14** and **Table 3.3**)[7], the Zn:Im ratio was calculated as *ca.* 1:2 in Zn_A-Cu_B-Z. We further applied this information to construct an appropriate initial rigid body Z-matrix for the subsequent structural refinement.

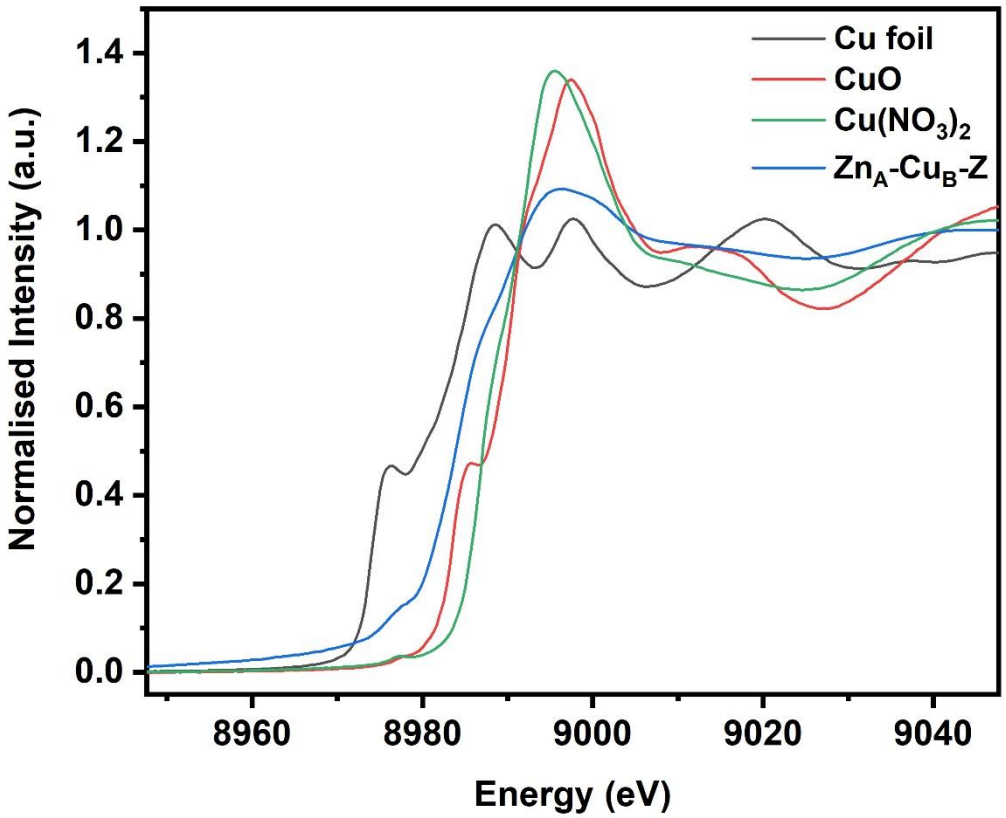

Figure 3.9. The Cu K-edge XANES spectrum of Zn_A-Cu_B-Z.

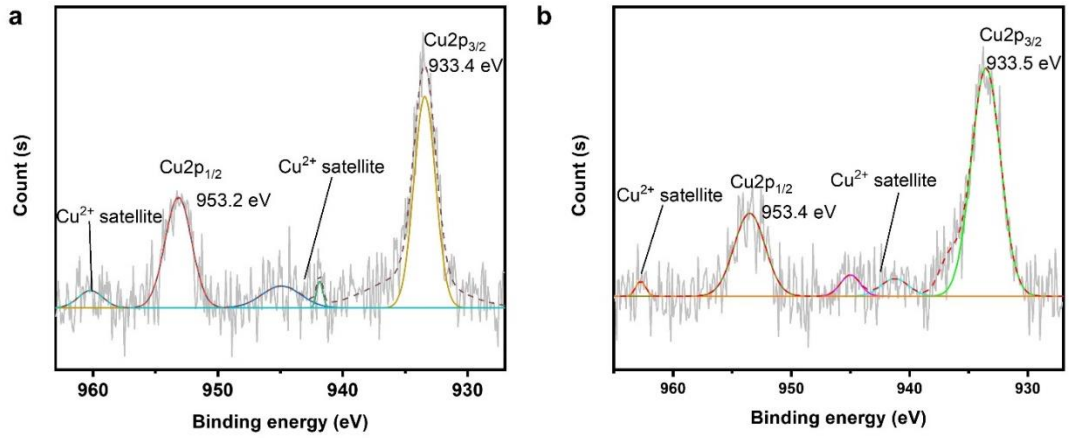

Figure 3.10. X-ray photoelectron spectra of the Cu 2*p* species in (a) Cu_A-Z and (b) Zn_A-Cu_B-Z. The presence of satellite peaks further verifies the Cu oxidation state of +2.

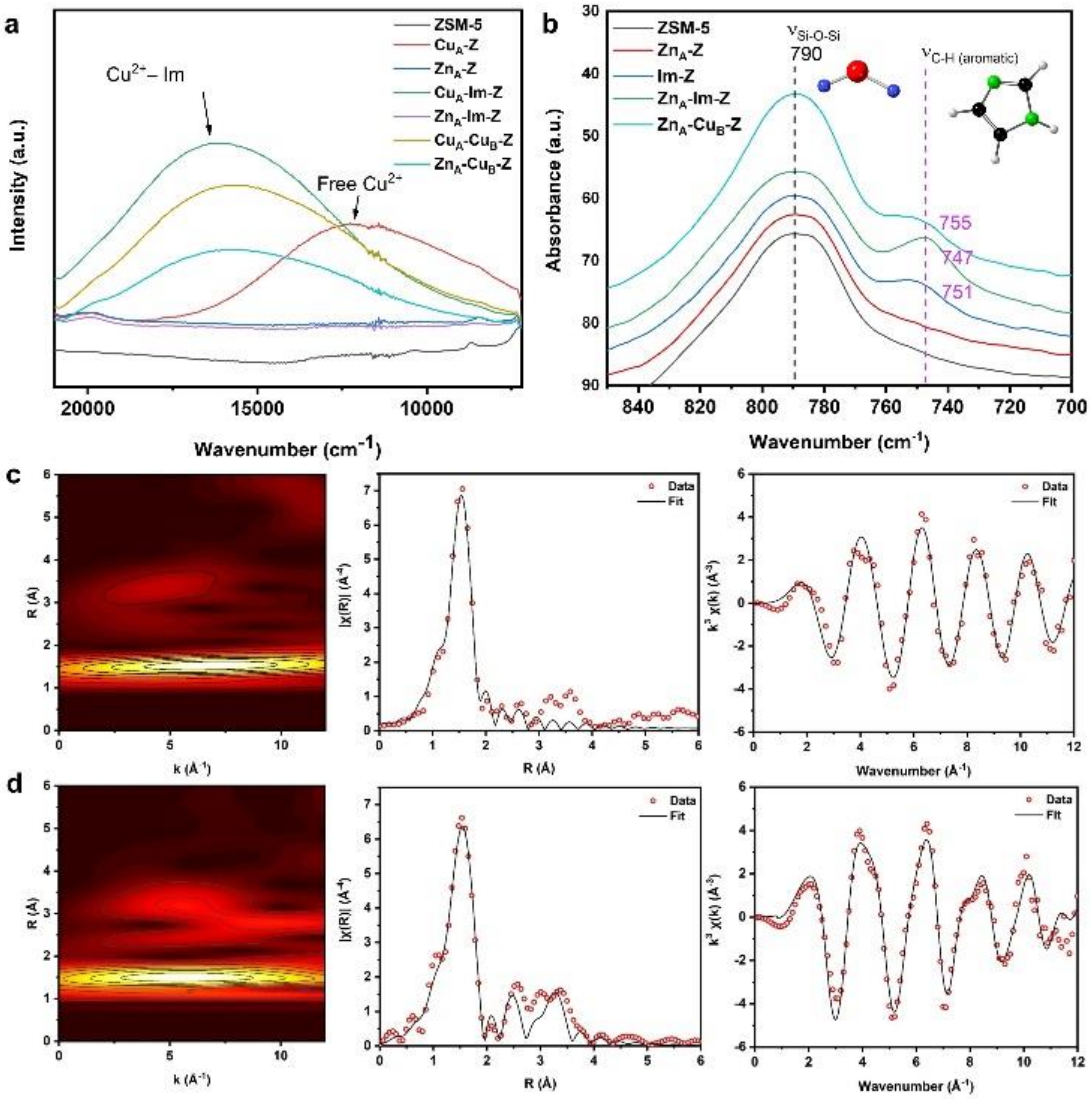

Figure 3.11. (a) UV-Vis-NIR DR spectra of the zeolite samples as labelled. (b) FT-IR spectra of the zeolite samples labeled. Wavelet transforms for k^3 weighted EXAFS signal of Zn_A-Cu_B-Z, and the corresponding (c) Cu and (d) Zn K-edge EXAFS (red) and fitting profile (black) in k^3 weighted k-space and R-space.

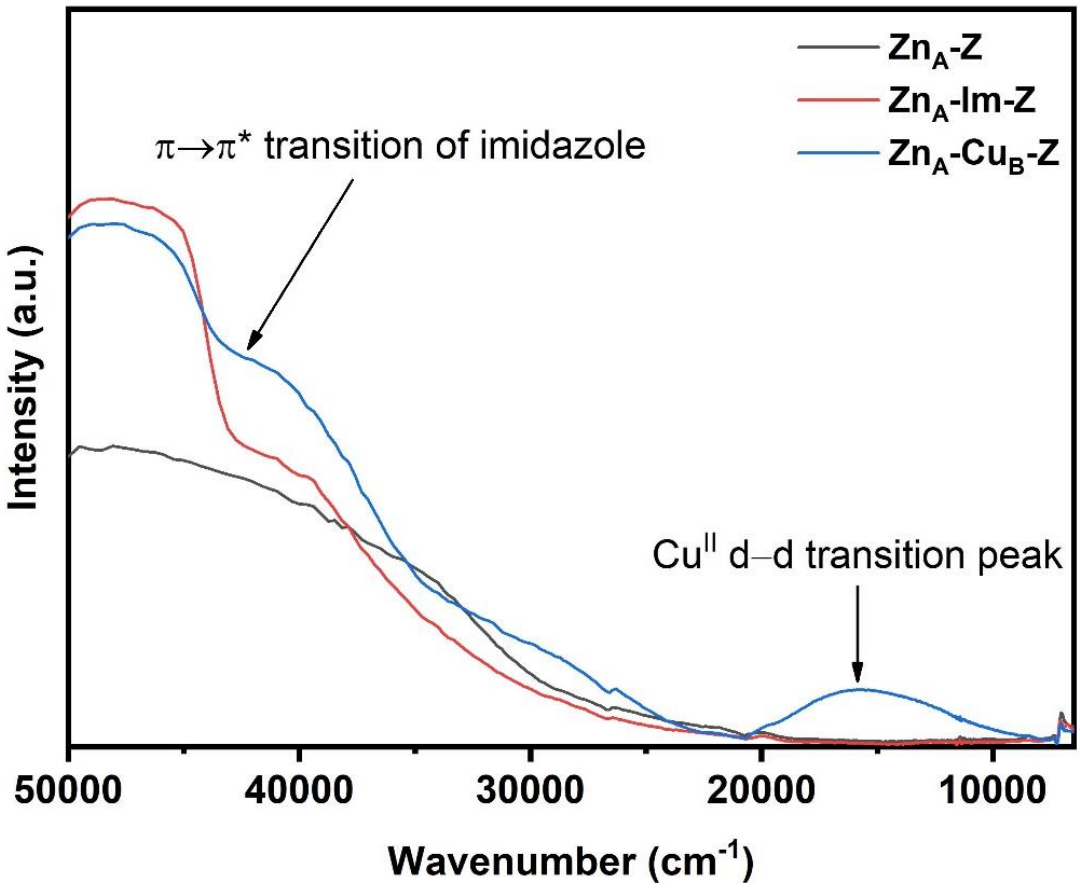

Figure 3.12. UV-Vis-NIR DR spectra of Zn_A-Z, Zn_A-Im-Z, and Zn_A-Cu_B-Z.

From the UV-vis-NIR diffuse reflectance spectra (**Figure 3.11(a)**), we noted broad absorption peaks in the regime of *d–d* transition of Cu^{2+} species [33]. Upon applying Im (*i.e.*, in Cu_A-Im-Z, Zn_A-Cu_B-Z, and Cu_A-Cu_B-Z), a large hypsochromic shift of the *d–d* transition peak was noted which can be ascribed to the interactions from coordination with Im (strong σ donor and weak π acceptor ligand). The hypsochromic peak shift suggests the formation of Cu–N interaction. The π–π* transition of Im is also observed in regions > 39,000 cm^{-1} (**Figure 3.12**). The Fourier-transform infrared spectroscopy (FTIR, **Figure 3.11(b)**) shows the presence of Zn–Im interactions. The characteristic vibration mode of the C–H bond of Im (ν_{C-H}) shifts from 752 cm^{-1} in an H^+-adsorbed state (H-ZSM-5 pre-adsorbed with Im) to 747 cm^{-1} in the presence of Zn^{2+}, which indicates the coordination interaction between Zn^{2+} and N_{Im} in the Zn_A-Im-Z and Zn_A-Cu_B-Z samples [34,35].

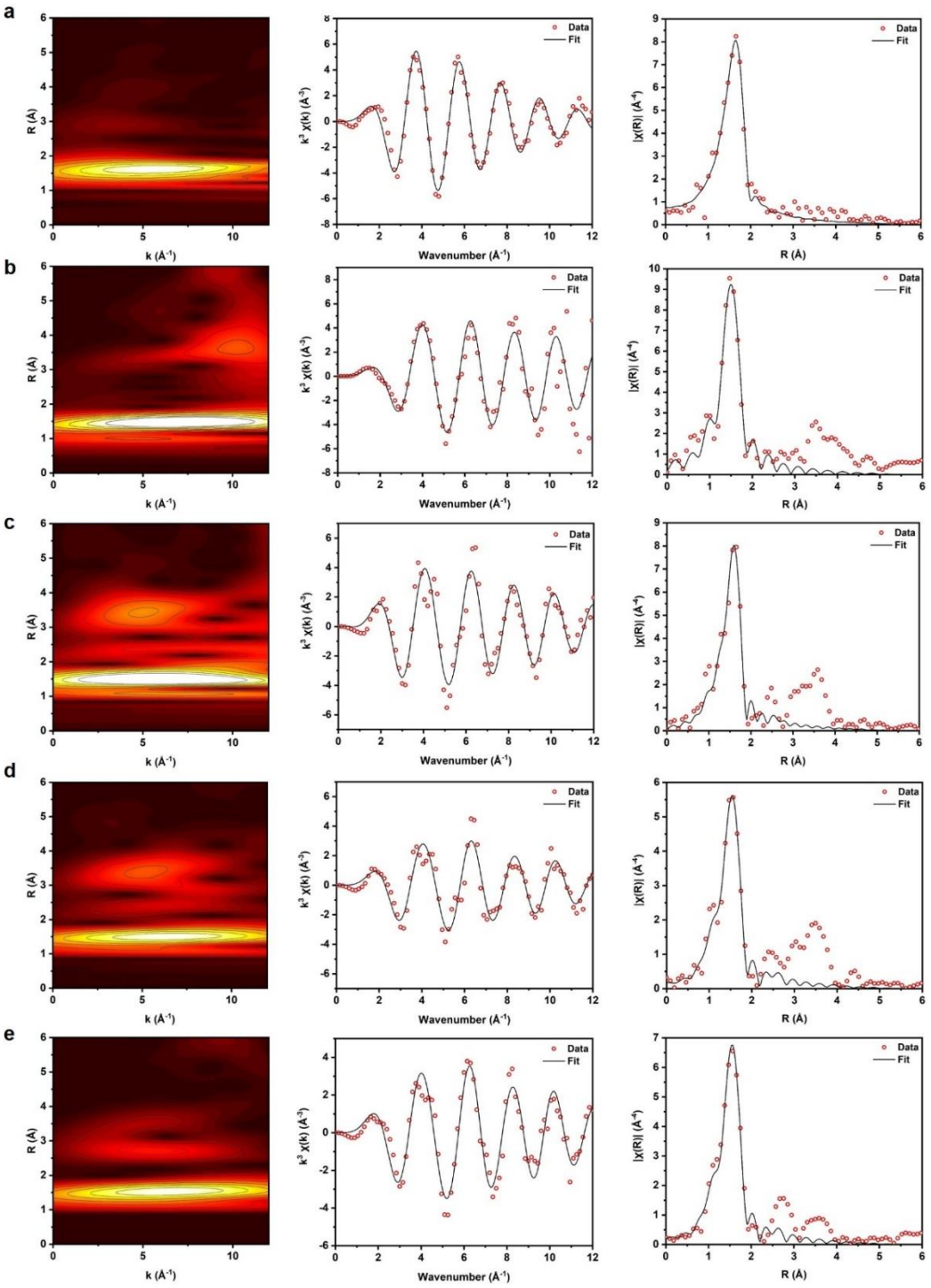

Figure 3.13. Spectroscopic studies of zeolitic sample with EXAFS data.

(**left**) Wavelet transform for k^3 weighted EXAFS data of (a) Cu_A-Z, (b) Zn_A-Z, (c) Cu_A-Im-Z, (d) Zn_A-Im-Z, and (e) Cu_A-Cu_B-Z, and the corresponding Cu and Zn K-edge EXAFS (red) and fitting profiles (black) in k^3 weighted k-space (**middle**) and R-space (**right**).

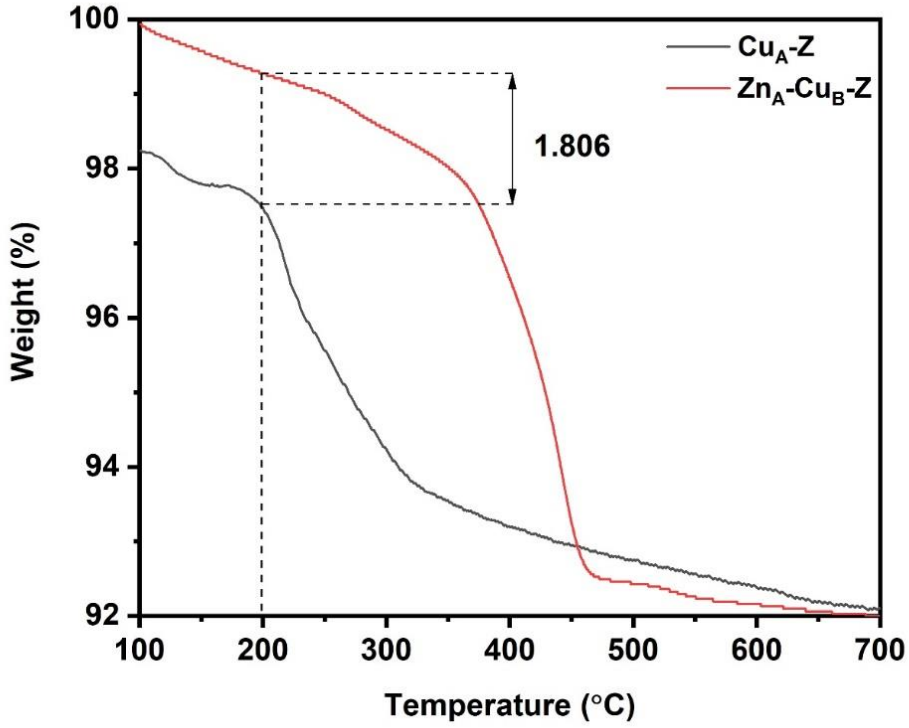

Figure 3.14. TGA profiles of Cu_A-Z and Zn_A-Cu_B-Z. The derivation of the Cu to imidazolate ratio can be subsequently extrapolated, as shown in **Table 3.3**.

The Rietveld refinement of high-resolution synchrotron X-ray powder diffraction (SXRD) can be used to determine the atomic and structural parameters (including the fractional coordinates (*x, y, z*) and site occupancy factors (SOFs)) of extra-framework species in crystalline and microporous materials [36]. Even small organic molecules, such as methanol, ammonia, and pyridine, can be determined in zeolites in terms of bond angles and distances [30,37,38]. Here, we collected SXRD data on Beamline I11 at Diamond Light Source (UK) and Beamline BL02B2 at SPring-8 (Japan). The SXRD patterns are presented in **Figures 3.15-3.19**. Homogeneous metalation is noted from the highly symmetrical Bragg's peaks. The X-ray energy of the incident beam was optimized at 15 keV and 18 keV, respectively **(Table 3.4),** which allows an optimum X-ray brightness for high contrast (signal-to-noise ratio) and high resolution. By performing the charge flipping algorithm in TOPAS refinement software, the extra-framework metal sites have been found separated by about 5.7 Å apart (**Figure 3.20**). This atomic separation implies the presence of a bridging Im linker between the two metal crystallographic sites, as it is consistent with the Zn···Cu interatomic distance in our postulated structural model.

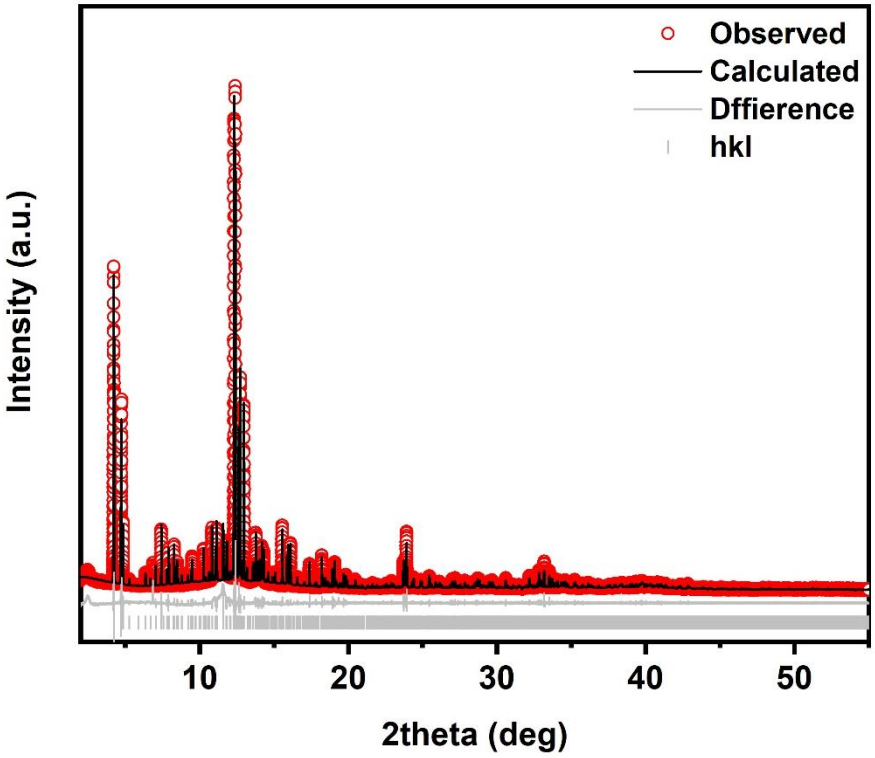

Figure 3.15. SXRD data and refinement profile of Cu_A-Cu_B-Z measured at 15 keV.

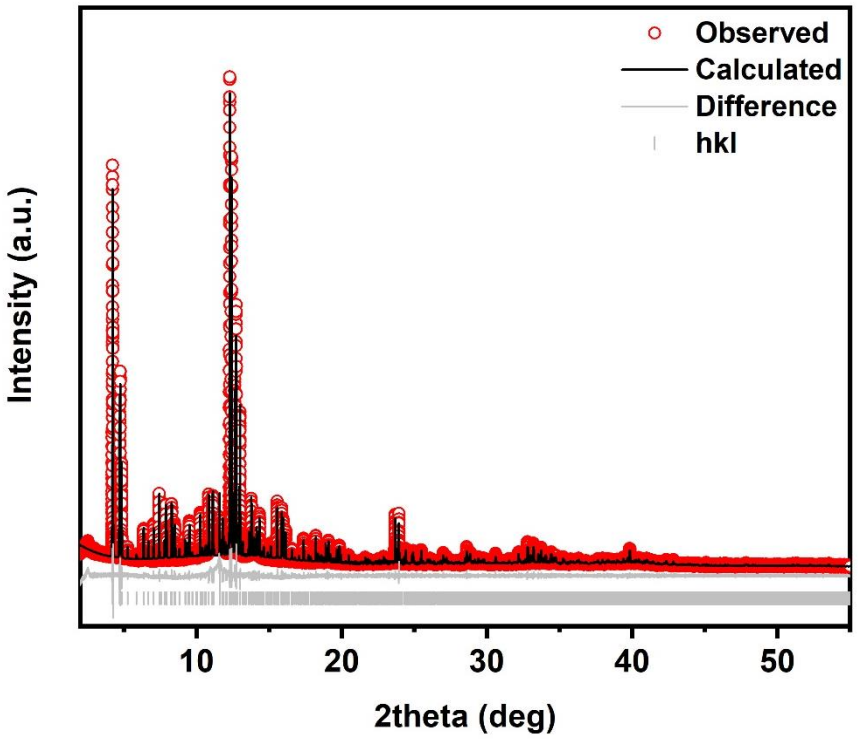

Figure 3.16. SXRD data and refinement profile of Cu_A-Zn_B-Z measured at 15 keV.

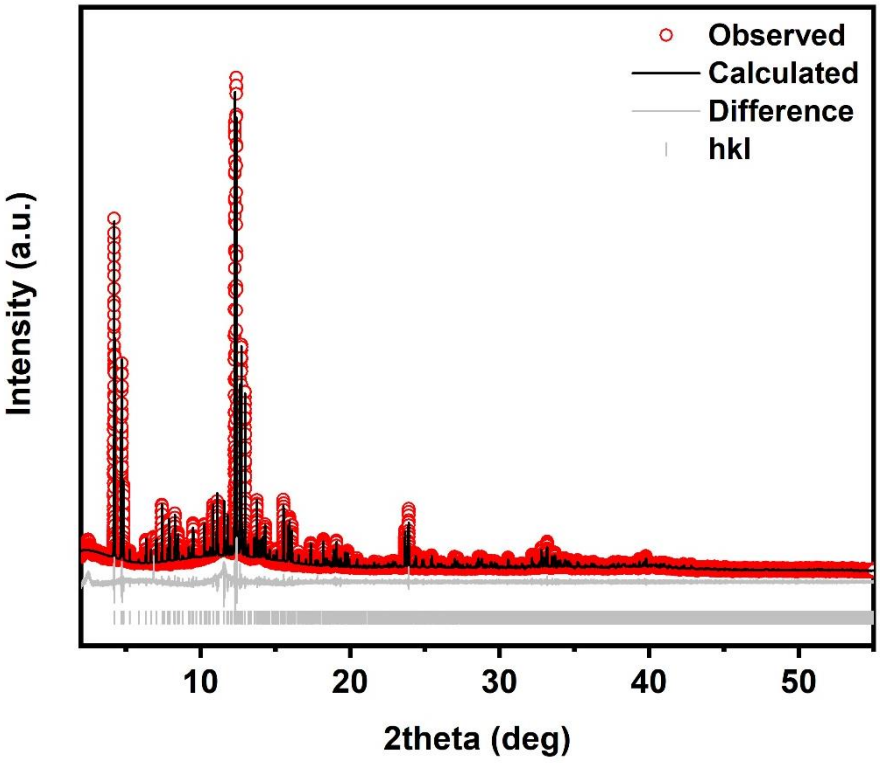

Figure 3.17. SXRD data and refinement profile of Zn_A-Cu_B-Z measured at 15 keV.

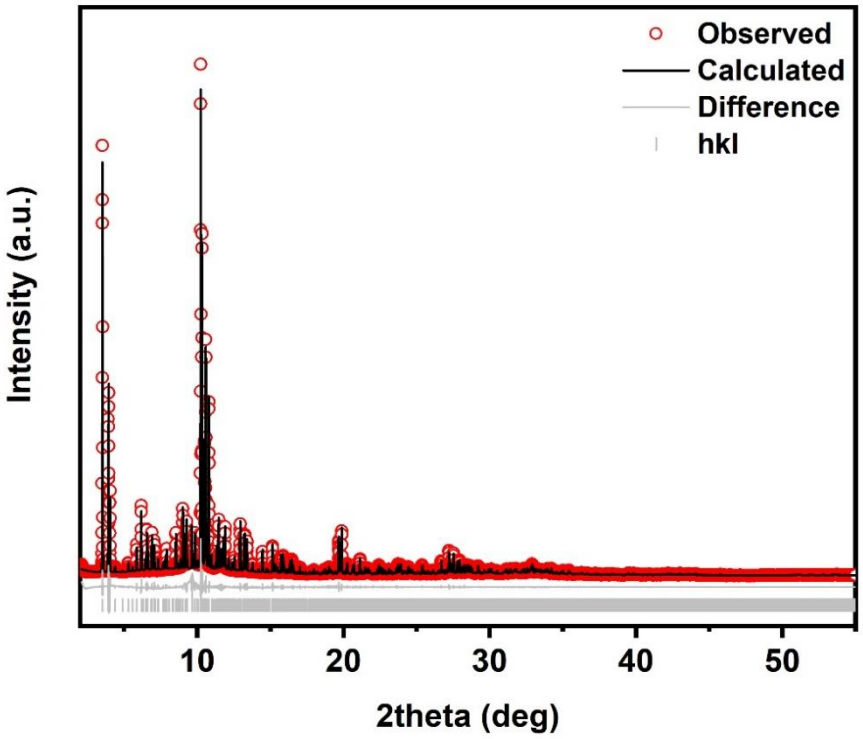

Figure 3.18. SXRD data and refinement profile of Cu_A-Im-Z measured at 18 keV.

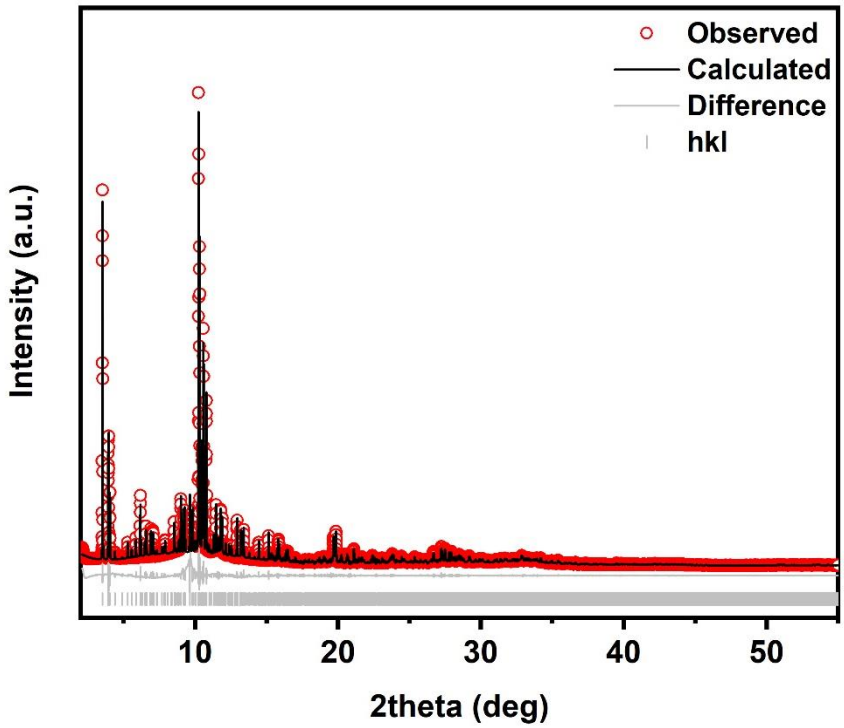

Figure 3.19. SXRD data and refinement profile of Zn_A-Im-Z measured at 18 keV.

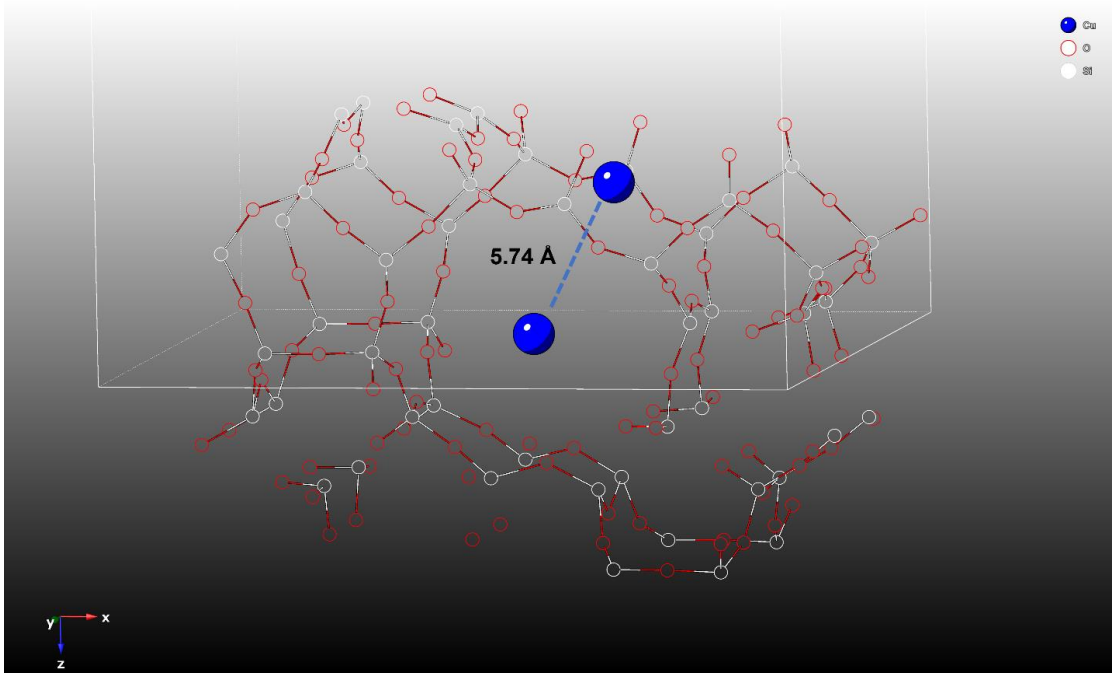

Figure 3.20. Charge flipping (by TOPAS v.6.0) for the determination of the crystallographic locations of the metal sites; the charge flipping of Zn_A-Cu_B-Z is presented here. The interatomic distance between the M_A and M_B sites is found at *ca*. 5.74 Å Note that Cu and Zn are indistinguishable by non-resonant X-ray diffraction techniques.

However, atoms with proximate atomic numbers are hardly distinguishable due to low electronic contrast by using conventional X-ray crystallographic techniques. We have specifically employed *state-of-the-art* synchrotron resonant X-ray diffraction (RXRD, on Beamline I11 at Diamond), unique to synchrotron-based instruments to determine the crystal structure of Zn_A-Cu_B-Z where the extra-framework crystallographic sites of interest are occupied by Cu and Zn atoms with marginal electronic contrast. The RXRD technique can enable Cu (Z = 29) and Zn (Z = 30) to be distinguished by utilizing the contrast between their anomalous scattering factors *f'* (real) near the elemental absorption edge. Synchrotron diffraction measurements of Zn_A-Cu_B-Z were collected at 10 eV, 15 eV, and 21 eV below the K-edge of Cu^{II} to maximize the contrast in *f'* (**Figure 3.21(a)**). The energy selections were aided by **Figure 3.21(a)**, with the details of the fluorescence measurement described in the RXRD method (SI). The combined Rietveld refinement profiles (together with a high-resolution diffraction measurement at 15 keV) are presented in **Figure 3.21(b)** which utilized the initial rigid body Z-matrix described above. As seen in the refined crystal structure in **Figure 3.21(c)**, the Zn_A site is found located at the intersection between the straight and sinusoidal channels of ZSM-5, whereas Cu_B is located closer to the wall of the straight channel. As discussed later (in Figure 6), we have further optimized its crystal structure by density functional theory (DFT) calculation, with Zn_A located at the inner position along the sinusoidal channel of ZSM-5 and saturated with three free water ligands. By analyzing the interatomic distances carefully, these water ligands are seen stabilized by multiple framework O atoms *via* a hydrogen-bonding network through the formation of Brønsted acid-base adducts ($O_{framework}\cdots HO_{ligand}$). The computed bond distances are around 1.8–2.3 Å, which fall in the regime of hydrogen bonds with moderate bond strength [39].

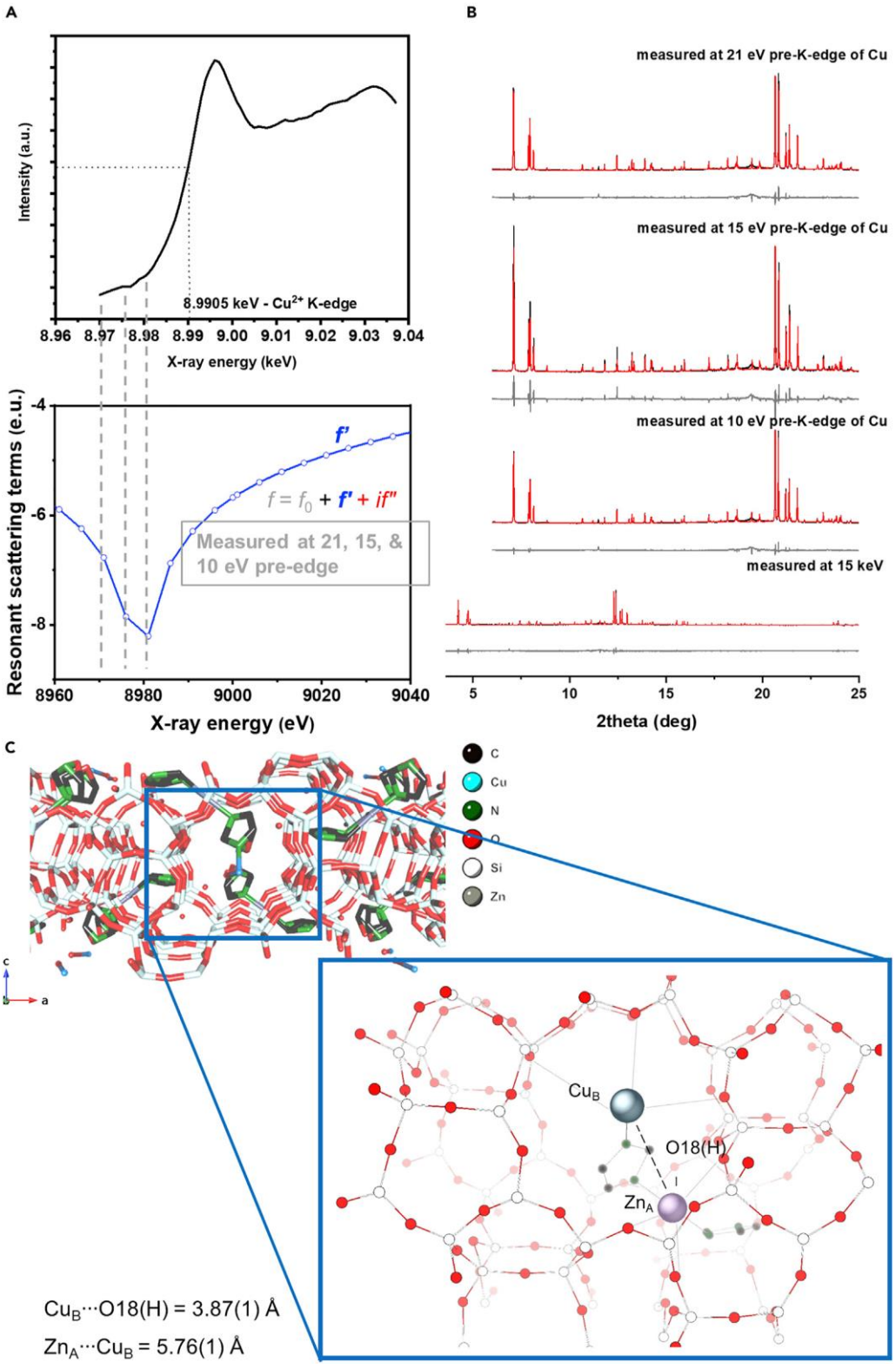

Figure 3.21. (**a**) X-ray energy calibration for the determination of the corresponding adsorption K-edge of Zn_A-Cu_B-Z. (**b**) RXRD data and Rietveld refinement profiles of Zn_A-Cu_B-Z at different X-ray energies. A series of verification procedures have been taken to test the refinement sensitivity of the resonant X-ray measurement (**Table 3.5 and 3.6**). (**c**) View of the Rietveld refined crystal structure of Zn_A-Cu_B-Z. The atomic parameters are summarized in **Table 3.7**.

High structural similarity between Zn_A-Cu_B-Z and Cu,Zn-SOD can be observed clearly. We hence probed the reactivity of our dual-atom catalysts using a chemical superoxide dismutation assay. In this assay, $O_2^{\cdot-}$ is generated by the UV-induced reaction between riboflavin and methionine. $O_2^{\cdot-}$ will then reduce nitro blue tetrazolium chloride into formazan purple. The detailed assay procedure is described in the Method section (SI). As summarized in **Figure 3.22**, Zn_A-Cu_B-Z shows the highest activity among the samples with k_{cat} of 4.88 × 10^7 $m^{-1}s^{-1}$, and the lowest normalized half-maximal inhibitory concentration (IC_{50}) of 0.056 μm. It is comparable to that of native Cu,Zn-SOD enzyme (*cf.* IC_{50} = 0.015 μm [40]; k_{cat} = 18.6 × 10^7 $m^{-1}s^{-1}$; **Table 3.8**). The linear fits for the IC_{50} derivation are shown in **Figure 3.23**. In stark contrast, analogous Cu_A-Cu_B-Z and Cu_A-Zn_B-Z dual-atom catalysts show much lower rates of k_{cat} = 2.78 × 10^6 $m^{-1}s^{-1}$ and k_{cat} = 0.710 × 10^6 $m^{-1}s^{-1}$, respectively. Nil or negligible activity (unmeasurable IC_{50}) has been noted over the samples without Cu or the 'single-atom' samples. The variation of using different bridging imidazolate-based linkers in Zn_A-Cu_B-Z on the SOD activity has been found less significant than the other variations in structural descriptors (**Table 3.8**). The samples can be repeated for at least three catalytic cycles with no noticeable drop in activity (**Table 3.9**). Minimal metal leaching (<0.5%) has been observed in our incubation experiment (**Table 3.10**).

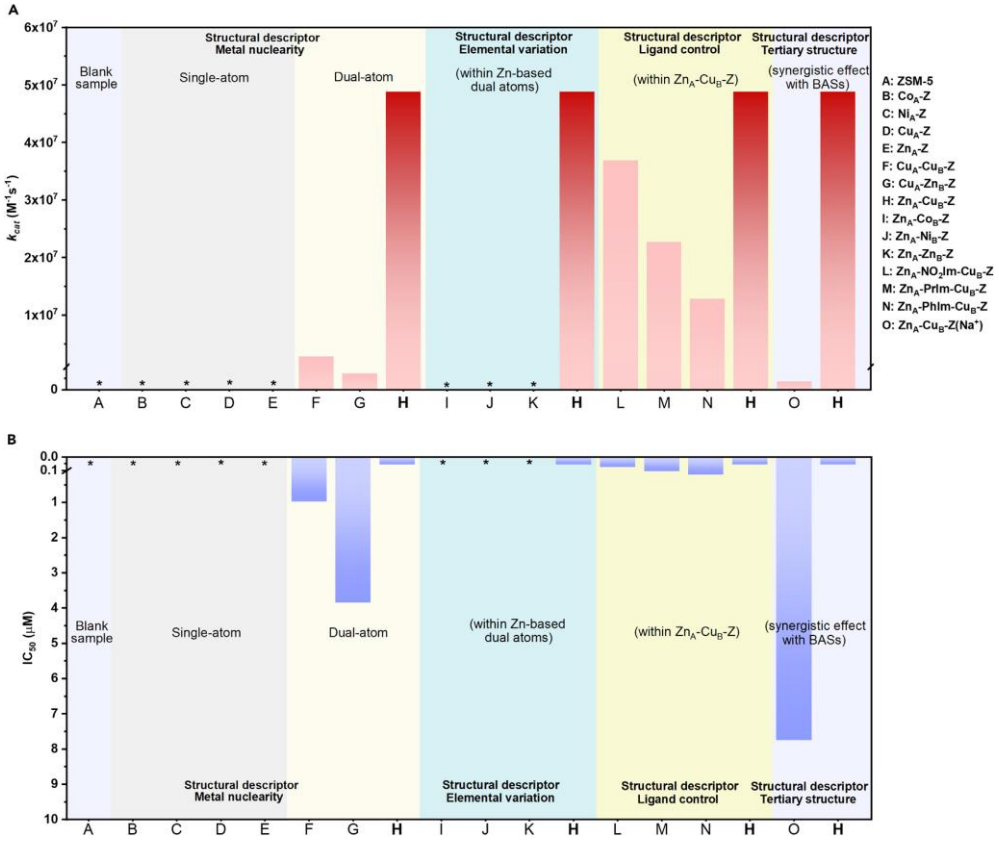

Figure 3.22. Bar chart showing the rate in terms of (A) k_{cat} and (B) IC_{50}. The numerical values are summarized in Table S8. Bars marked with asterisks refer to undetectable SOD activity.

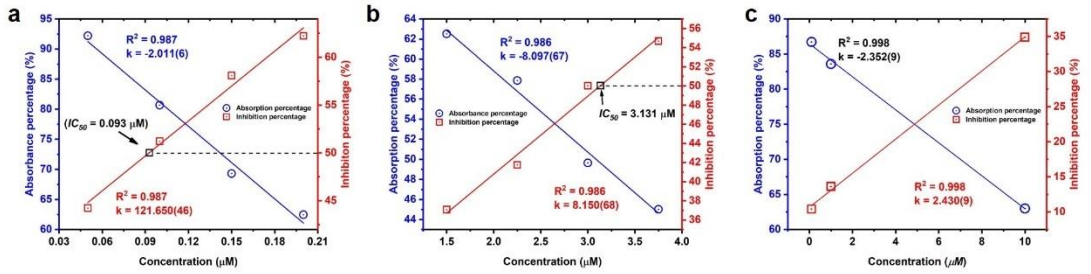

Figure 3.23. Linear fit of the formazan absorbance percentage versus the concentration of a series of zeolite samples (a) Cu_A-Cu_B-Z, (b) Cu_A-Zn_B-Z, and (c) Cu_A-Zn_B-Z.

The inhibition efficiencies of the zeolite samples were determined by the absorbance (concentration) of formazan (the product of the photoreduction of nitro blue tetrazolium), which is inversely proportional to the inhibition efficiency. The inhibition percentage was calculated according to the following equation:

$$\frac{\left(\frac{\Delta Abs}{t}\right)_{\text{without catalyst}} - \left(\frac{\Delta Abs}{t}\right)_{\text{with catalyst}}}{\left(\frac{\Delta Abs}{t}\right)_{\text{without catalyst}}} \times 100\%$$

After calculating the inhibition percentage, the IC_{50} value was determined from the concentration-dependent plot of the inhibition percentage against the concentration of the catalyst used.

For the element analysis of Zn_A-Cu_B-Z, the weight percentage of Al, Si, Cu, and Zn are 2.82 wt%, 93.51 wt%, 1.27 wt%, and 1.34 wt%, respectively. Based on the elemental ratio between Al and Cu/Zn, there are 0.603 Zn_A-Cu_B dual-atom per unit cell of ZSM-5. The IC_{50} values were accordingly normalized with respect to the number of active sites in ZSM-5.

The IC_{50} value obtained from the linear fit was used to calculate the McCord-Fridovich catalytic constant for superoxide scavenging (k_{cat}) according to the equation of $k_{cat} = \frac{k_{NBT} \times [NBT]}{IC_{50}}$ [41]. The k_{cat} value is suitable to compare with the reported values from other catalytic studies since it is independent to the concentration of the nitroblue tetrazolium (NBT) chloride solution.

Such reactivity patterns and the presence of reactivity discontinuities prompted us to investigate the mechanistic basis of different structural descriptors. From the above findings, we identified four key structural descriptors about our dual-atom catalysts, namely, choice of metal, metal nuclearity, tertiary structures about the zeolitic support, and linker control, that are critical in mapping the structure-reactivity correlations.

Choice of metal

Through a series of experiments using different late 3*d* metal species, we found that Cu^{II} is essential for superoxide dismutation as no activity is observed in the samples without Cu^{II}. In contrast, Zn^{II} acts as a catalytic promoter, whereas Co^{II} and Ni^{II} do not show any catalytic effect in the dismutation system. It is believed that, based on the conventional understanding of Cu,Zn-SOD enzyme, Zn^{II} plays two major roles, (i) to hold the dual-atoms intact (as the Cu–N_{His61} bond is partially broken when Cu^{II} is reduced to Cu^{I}), and (ii) to position the proton of the 'just-broken' His_{61} in place for hydrogen bonding and subsequent transfer to the incoming $O_2^{\cdot-}$ for the second step of the catalytic cycle, *i.e.*, H_2O_2 production [42].

Metal nuclearity

The activity of the mononuclear sample, Cu_A-Z, exhibits extremely low activity when compared with the Cu-M dual-atoms, *i.e.*, Cu_A-Zn_B-Z, Cu_A-Cu_B-Z, and Zn_A-Cu_B-Z, suggesting the more superior effect of the Cu-M dual-atoms. This can be attributed to the structural similarities between these Cu-M and the native Cu,Zn-SOD enzyme. The Cu^{II} and Zn^{II} nuclei are held together by Im-containing histidine (His_{61}) in the native enzyme; similarly, M_A^{II} and M_B^{II} are held together by an Im linker in M_A-M_B-Z. The proximity between these two metal sites makes synergistic cooperation highly favored. The DFT-optimized structures of the Cu-M dual-atoms are shown in **Figure 3.24**. Clearly, their atomic arrangements and ground-state energies (E_0) are highly comparable to each other. Typically, the M_A site locates at the inner part of the sinusoidal channel and is hence more constrained (aperture of around 6 Å). The M_B site locates at the more open intersection of the straight and sinusoidal channel (aperture of around 8 Å) and is hence less sterically hindered. Zn_A-Cu_B-Z shows the highest activity at $k_{cat} = 4.88 \times 10^7\ m^{-1}s^{-1}$ and $IC_{50} = 0.056$ μm. If Zn^{II} is replaced by Cu^{II} (*i.e.*, Cu_A-Cu_B-Z), the superoxide dismutation activity decreases notably to $k_{cat} = 2.78 \times 10^6\ m^{-1}s^{-1}$ and $IC_{50} = 0.982$ μm. The activity of Cu_A-Zn_B-Z is even lower at $k_{cat} = 0.710 \times 10^6\ m^{-1}s^{-1}$ and $IC_{50} = 3.847$ μm. This can be caused by the stabilization effect of Zn^{II} [43]. By comparing the activities of Zn_A-Cu_B-Z, Cu_A-Cu_B-Z and, Cu_A-Zn_B-Z, the respective locations of the metal nuclei also constitute an important role, as the M_B site (second metalation site) is more exposed to interact with incoming $O_2^{\cdot-}$ substrates.

Indeed, the catalytic disparity between these highly analogous Cu-M dual-atom catalysts reveals the importance of the engineering of microenvironments of the dual-

atom catalysts. By our creative synthetic approach, the metal sites can be assembled in a modular manner, enabling a more precise control in the microenvironments.

Tertiary structures about the zeolitic support

As shown in many enzymatic catalysis examples, the tertiary structure plays a critical role, where favorable reactive intermediates and transition states can be stabilized by steric confinement effect, additional functionality or both combined. As seen in **Figure 3.21(c)**, the interatomic distance between Cu_B and adjacent O18 was measured as 4.27(1) Å. The O18 position has been determined to be the crystallographic location of the protonic Brønsted acid site (BAS) in the same zeolite based on our probe-assisted diffraction study [37]. We note that this is structurally and chemically comparable to the tertiary structure around the Cu,Zn-containing co-factor of the natural Cu,Zn-SOD, where two protons are taken from the nearby Wat_{227} and the N atom of His_{61} in the second step of the biological SOD cycle [44].

Hence, it is anticipated that the Cu,Zn dual-atoms inside the ZSM-5 pores may interact with BASs nearby. This is illustrated by comparing the catalytic activities of Zn_A-Cu_B-Z and Zn_A-Cu_B-Z(Na^+) (**Figure 3.22**). In the absence of BASs (H^+ replaced with Na^+), Zn_A-Cu_B-Z(Na^+) clearly delivers much lower catalytic activity by more than 2-fold of magnitude to Zn_A-Cu_B-Z (*cf.* k_{cat} decreases from $48.8 \times 10^6\ m^{-1}s^{-1}$ to $0.352 \times 10^6\ m^{-1}s^{-1}$; IC_{50} increases from 0.056 μM to 7.747 μM). Note that our group has conducted a similar poisoning experiment to selectively replace BASs with Na^+, which can probe the synergy between the neighboring active motifs in zeolites [45]. This selective poisoning experiment clearly supports our hypothesis that BASs in zeolite work in synergy with the Cu,Zn dual-atoms that are crucial in the overall catalytic activity. As illustrated in the proposed reaction mechanism in **Scheme 3.2**, the proximity of multiple catalytic active motifs (*i.e.*, the redox-active Cu_B site and the zeolitic Brønsted acid site) within molecular distances would facilitate the tandem reactions in the dismutation of $O_2^{\cdot-}$ in a cooperative manner, where the second step in the catalytic redox cycle (H_2O_2 formation) that requires an additional H^+ source can be warranted.

In addition, in the first step of the catalytic cycle in the SOD enzyme where Cu^{II} is reduced to Cu^I, it is coupled with the cleavage of Cu–N_{His61} bond [42]. The Cu^I is stabilized by the hydrogen bonding network by the protein scaffold. An analogous structural stabilization is also observed, based on combined Rietveld refinement and DFT calculations, where the $O_{framework}$ atoms stabilize the Cu^{II}/Cu^I center *via* hydrogen bonds along the ligated water. It acts as a physical confinement barrier to prevent the Cu and Zn centers from separating upon the Cu^{II}/Cu^I redox cycle.

Imidazolate-based linker control

We have also compared the effect of using different substituted imidazolate ligands in Zn_A-Cu_B-Z (**Figure 3.22**). Despite the electronic structures of the supported species could be altered upon different imidazolate substituents, the variation in the SOD activity is found much less significant than those of other structural descriptors. Although definitive correlations have not yet been made, we believe that extensive possibilities could be opened by the design of the bridging linker which would not only affect the electronic and steric properties but could offer additional functionality for specific substrate activation.

Various reactive oxygen species (ROS)-based therapeutics have been proposed as anticancer theranostics in recent years [46–49]. High concentrations of ROS, such as superoxide radicals ($O_2^{\cdot-}$), hydroxyl radicals (OH•), and singlet oxygen ($^1O_2$), are known to be harmful to biomolecules in human bodies. SOD enzymes play a biological role to catalyze the decomposition of $O_2^{\cdot-}$ to H_2O_2 and O_2. Typically, the ROS level in tumor cells is generally higher as a consequence of accelerated metabolic rate, gene mutation, and relative hypoxia [50]. The cellular H_2O_2 generated from native SOD enzymes is typically removed by catalase which readily degrades cellular H_2O_2 to H_2O and O_2. It is hence insufficient to create a notable impact to significantly augment cell apoptosis. On the contrary, upon the applications of many anticancer drugs, oxidative stress will be induced, leading to the lease of a substantial concentration of $O_2^{\cdot-}$ followed by a series of biological pathways [51]. We, therefore, examine if the *in-situ* generated $O_2^{\cdot-}$ could be dismutated rapidly to enhance the cellular concentration of H_2O_2 by incorporating an effective SOD mimic while drug is applied, which would subsequently promote the apoptosis rate of tumor cells.

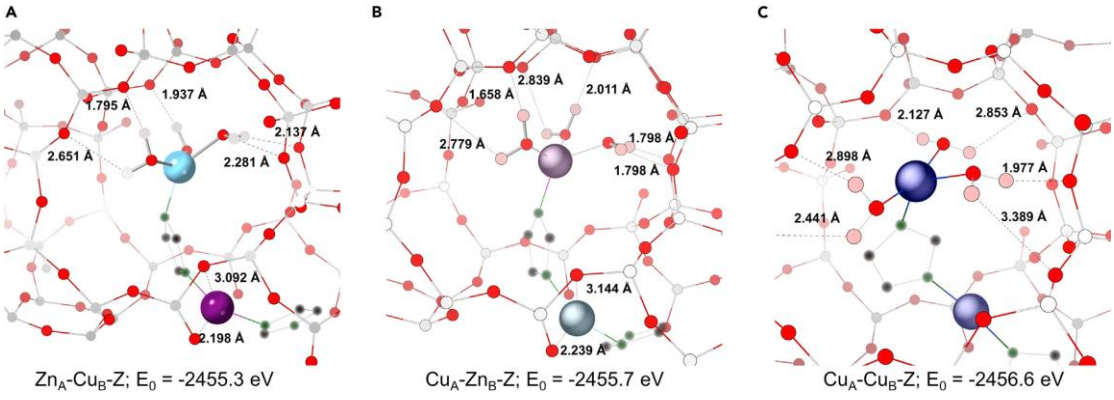

Zn_A-Cu_B-Z; E_0 = -2455.3 eV Cu_A-Zn_B-Z; E_0 = -2455.7 eV Cu_A-Cu_B-Z; E_0 = -2456.6 eV

Figure 3.24. Local structures optimized by DFT calculations of (a) Zn_A-Cu_B-Z, (b) Cu_A-Zn_B-Z, and (c) Cu_A-Cu_B-Z, and the corresponding ground state energy (E_0). The corresponding close-up views are shown. The stabilization of Cu_B through the hydrogen bonding network is highlighted for clarity. **Figures 3.25-3.27** show the more detailed DFT-optimized structure.

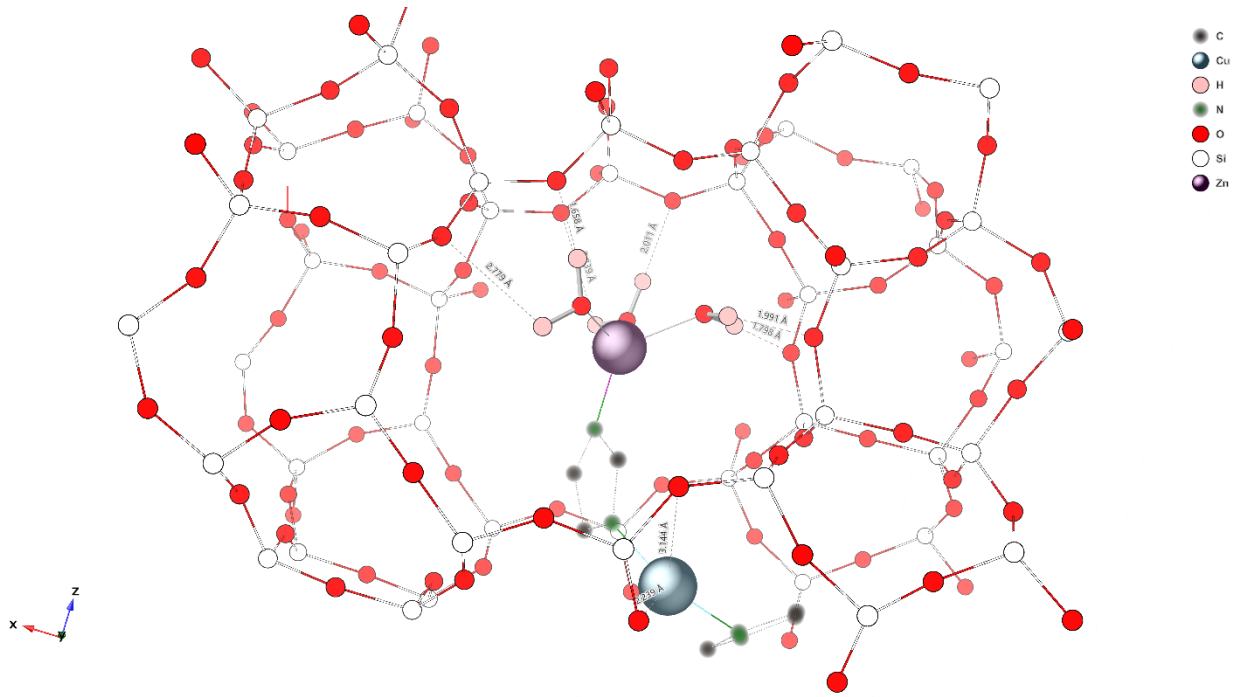

Figure 3.25. Optimized crystal structure of Cu_A-Zn_B-Z by DFT calculations.

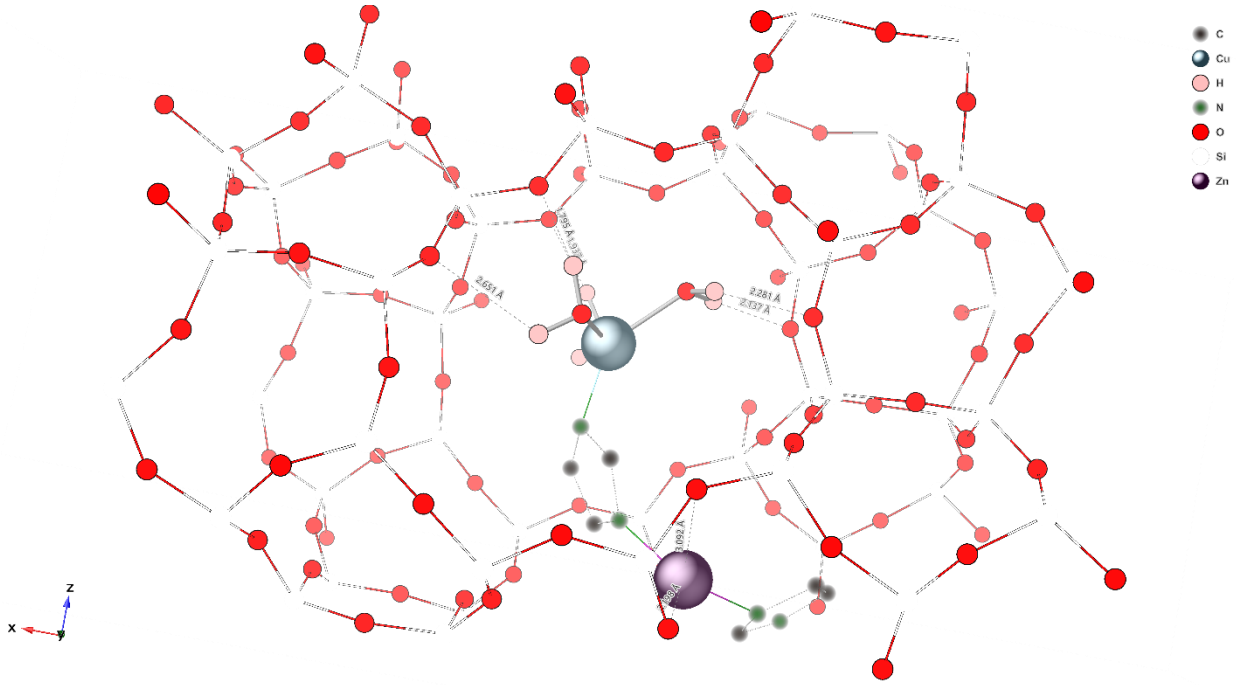

Figure 3.26. Optimized crystal structure of Zn_A-Cu_B-Z by DFT calculations.

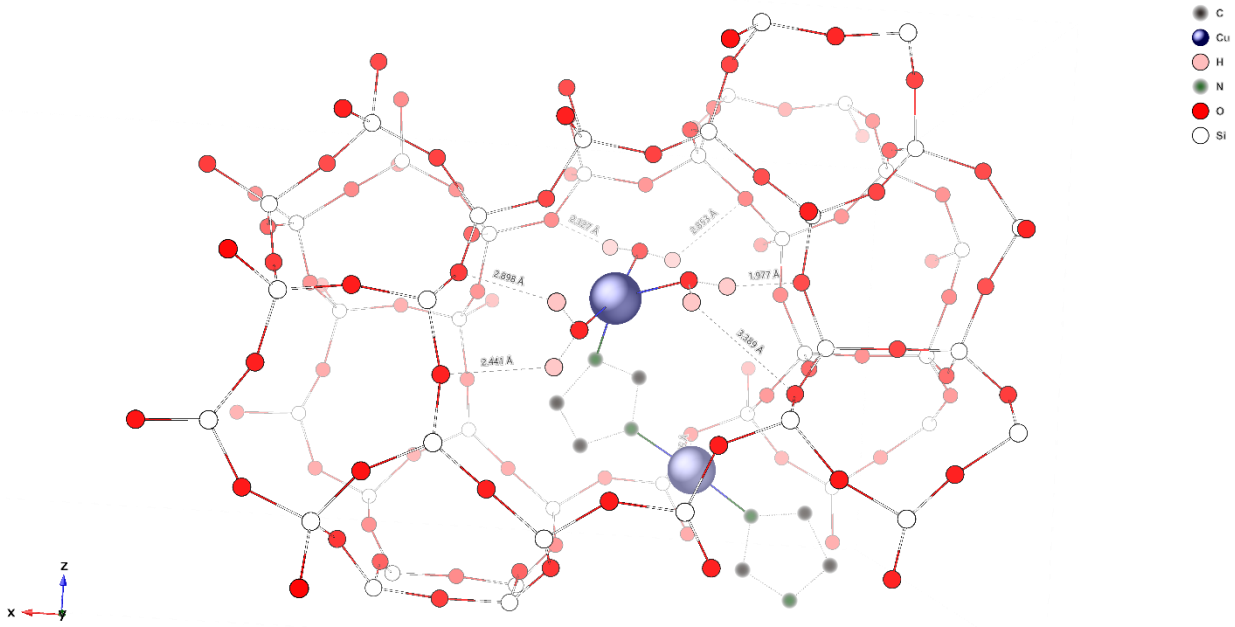

Figure 3.27. Optimized crystal structure of Cu_A-Cu_B-Z by DFT calculations.

Here, we have investigated the apoptotic effect of Zn_A-Cu_B-Z, in combination with sorafenib, a molecular-targeted drug for patients with advanced-stage hepatocellular carcinoma (HCC). The cytotoxicity of Zn_A-Cu_B-Z in two HCC cell lines, namely PLC/PRF/5 and MHCC-97L has been first examined. The IC_{50} values were determined as 15.77 and 73.20 μm by the MTT assay, respectively (**Figure 3.28**). We subsequently employed the Annexin-V apoptotic assay to examine the potential combination effect between sorafenib and Zn_A-Cu_B-Z. As shown in **Figure 3.29(a)**, **(c)**, the percentage of apoptotic cells in PLC/PRF/5 increases significantly from 32.21% (sorafenib (10 μm) alone) to 75.77% when both sorafenib (10 μm) and Zn_A-Cu_B-Z (6.25 μm) were simultaneously applied (a). By Bliss independence analysis, Zn_A-Cu_B-Z in combination with sorafenib showed statistical synergistic induction of apoptosis in PLC/PRF/5 cells (**Table 3.11**). (The microscopic views of the cell line PLC/PRF/5 with Zn_A-Cu_B-Z and sorafenib in different concentrations are displayed in **Figure 3.30**.) Similarly, we have also observed a drastic increase in cell apoptosis in the MHCC-97L cells, with a concentration of Zn_A-Cu_B-Z at 50 μm (**Figure 3.29(b)**, **(d)**, **Table 3.12**). Only a marginal increase (0.29-fold increase) in cell apoptosis was observed in H-ZSM-5-treated PLC/PRF/5 cells, indicating the specificity of the Cu-Zn dual atoms in Zn_A-Cu_B-Z in the sensitization of sorafenib.

We further examined the sensitization effect of Zn_A-Cu_B-Z by investigating the cellular level of ROS upon the administration of sorafenib in combination with Zn_A-Cu_B-Z. As shown in **Figure 3.31**, the ROS level was increased substantially when PLC/PRF/5

cells were treated with Zn_A-Cu_B-Z (a 3.10-fold increase), which can be attributed to the generation of H_2O_2 from its strong dismutation property. Meanwhile, the ROS level also notably increased upon application of sorafenib (a 4.06-fold increase), which can be caused by the drug-induced oxidative stress. From the combined treatment of sorafenib and Zn_A-Cu_B-Z, a synergistic effect has been observed statistically that has led to much-enhanced ROS level concentration. By the subsequent application of N-acetyl-L-cysteine (a common radical scavenger), the ROS level only decreased by around 20%, which suggests that the H_2O_2 constitutes a majority of ROS present. This analysis of the ROS level is consistent with our above findings on the role of H_2O_2-induced cell death in HCC cells [51–54].

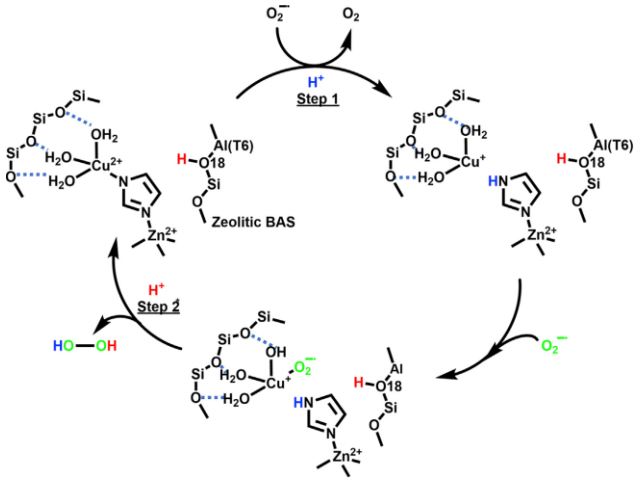

Scheme 3.2. Proposed reaction mechanism of superoxide dismutation over Zn_A-Cu_B-Z within the confined three-dimensional space of the zeolitic micropore Step 2 cannot proceed without the presence of the framework BAS, as probed in our selective poisoning (Na^+) experiment.

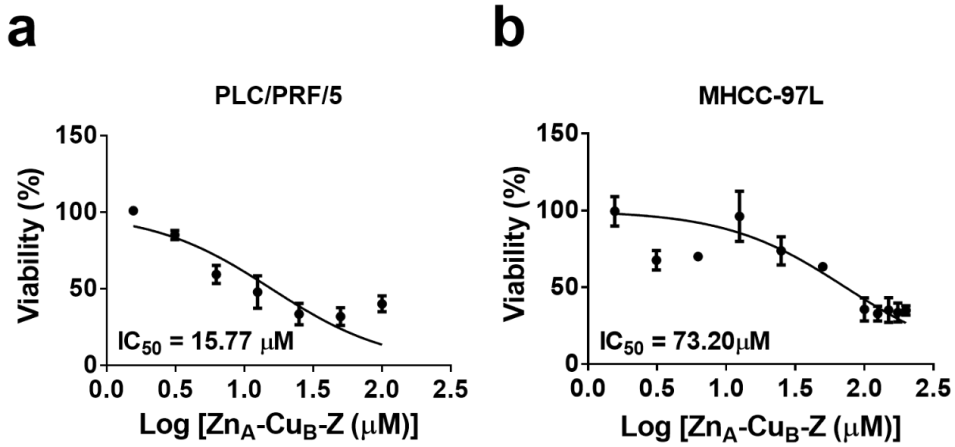

Figure 3.28. IC_{50} of Zn_A-Cu_B-Z on (a) PLC/PRF/5 and (b) MHCC-97L by MTT assay.

Accordingly, we propose the following reaction mechanism, as summarized in **Scheme 3.3**. (1) During the exposure of sorafenib to the tumor cells, the concentration of ROS increases from cell apoptosis. (2) The neighboring Zn_A-Cu_B-Z acts as an $O_2^{\cdot-}$ dismutation catalyst that converts the greatly enhanced cellular concentration of $O_2^{\cdot-}$ species to H_2O_2 and O_2. (3) The cellular concentration of H_2O_2 accumulates and greatly augments the apoptosis of the HCC tumor cells [55,56].

In brief, we have developed supported dual-atoms comprised of two late 3*d* metals within the microporous cavity of ZSM-5 zeolites. The success of such precise engineering relies on the utilization of the fundamental concepts of solid-state chemistry (*via* spatial confinement) and coordination chemistry (*via* formation of acid-base adducts). By investigating the catalytic properties of our model superoxide dismutation reaction, we have identified a few key structural descriptors in the dual-atom catalytic systems. In addition to metal nuclearity and elemental composition, the optimization of the tertiary structure(s) around the metal center has also been shown crucial. As demonstrated in catalytic superoxide dismutation over Zn_A-Cu_B-Z, the protonic Brønsted acid site in proximity to the redox-active Cu center offers a regenerative source of protons with the confined microenvironment (pore aperture of *ca*. 8 Å), which leads to a highly efficient catalytic process. The well-engineered quasi-isolated space, akin to the 'induced-fit' concept in natural enzymes, not only offers a three-dimension catalytic landscape that contains multiple active motifs but also offers stabilization of the reactive intermediates.

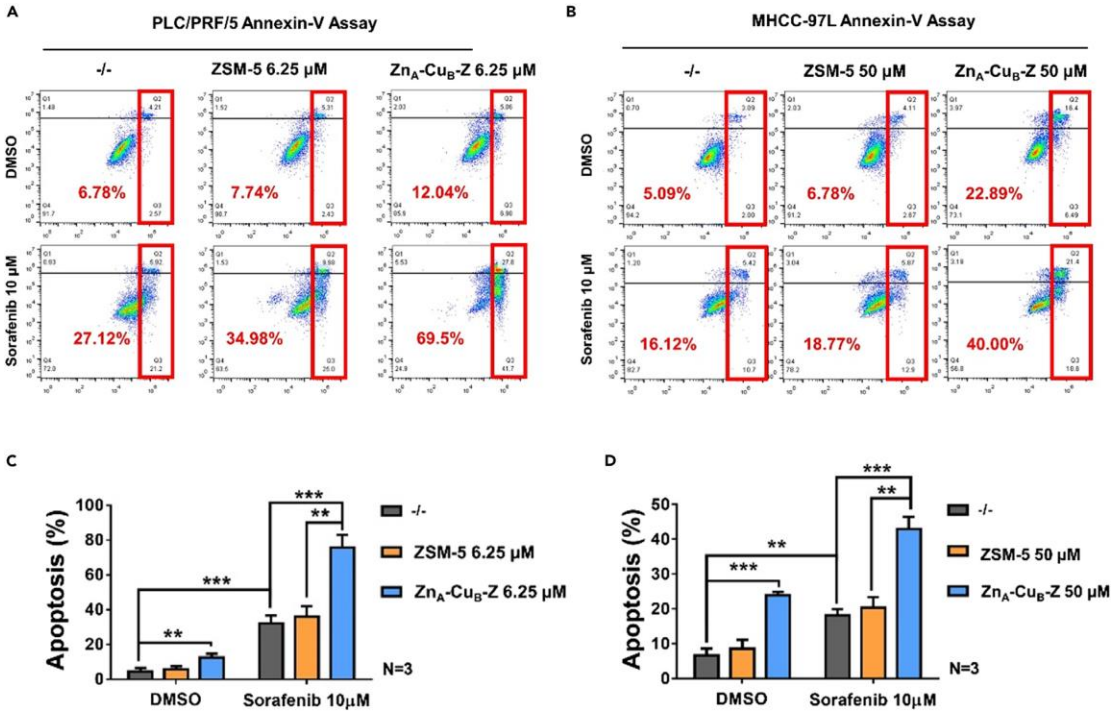

Figure 3.29. Apoptosis evaluated by Annexin-V staining of (**a**) PLC/PRF/5 cells induced by sorafenib (10 µm), ZSM-5 (6.25 µm), Zn_A-Cu_B-Z (6.25 µm), or in combination, (**b**) MHCC-97L cells induced by sorafenib (10 µm), ZSM-5 (50 µm), Zn_A-Cu_B-Z (50 µm) or in combination. Zn_A-Cu_B-Z synergized the effect of (**c**) PLC/PRF/5, and (**d**) MHCC-97L cells to sorafenib treatment. Error bars indicate mean±SD (n=3). **p<0.01, and ***p<0.001 from Student's t-test.

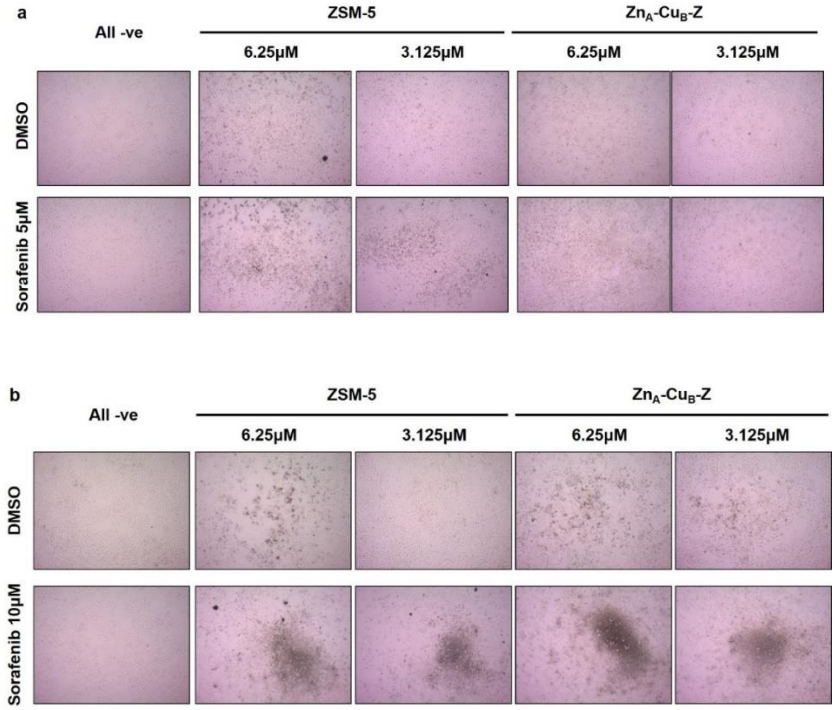

Figure 3.30. Microscopic images of HCC cell line PLC/PRF/5 with Zn_A-Cu_B-Z and sorafenib with the concentration of (a) 5 µM and (b) 10 µM in reduced serum for 48 hours.

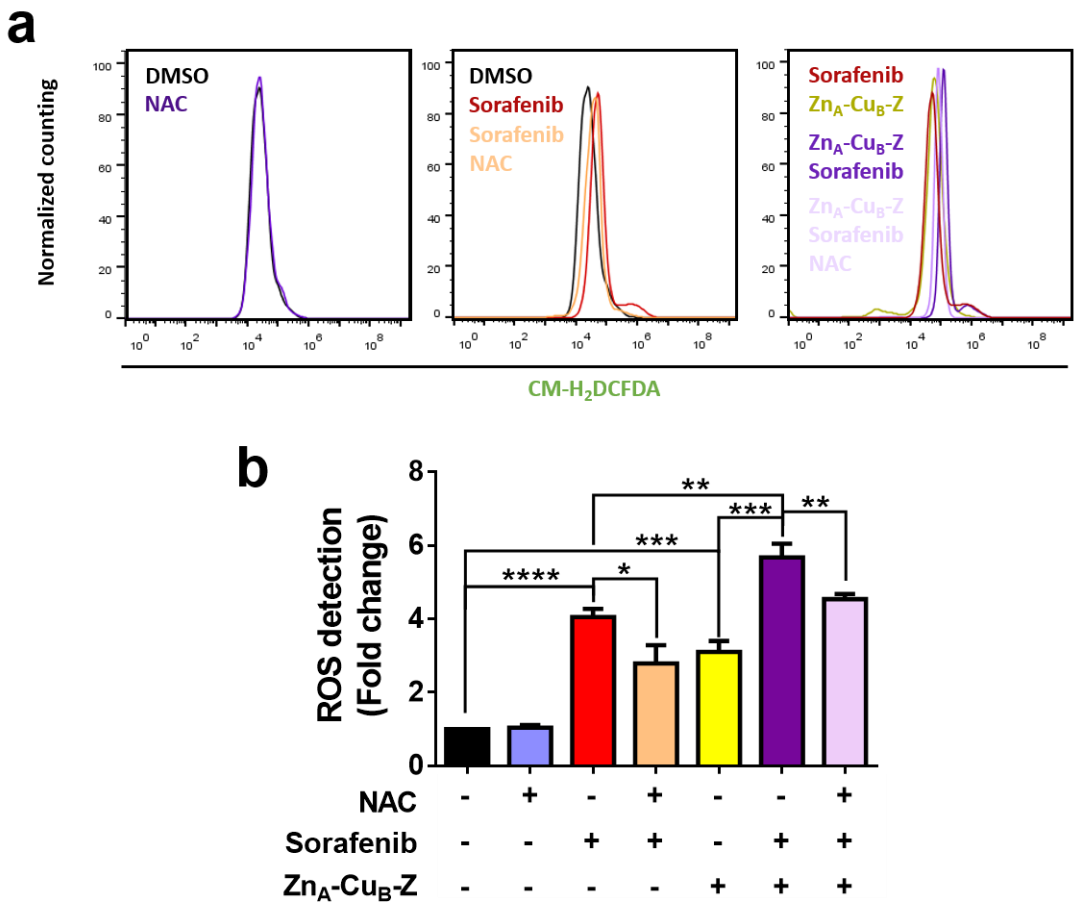

Figure 3.31. Sensitization effect studies of Zn_A-Cu_B-Z in cellular level of ROS.

(a) Flow cytometry analysis revealed that sorafenib (10 μM), Zn_A-Cu_B-Z (6.25 μM), and combined treatment increased the levels of reactive oxygen species (ROS) in PLC/PRF/5 cells. NAC (5 mM), or decreased the ROS level accordingly. (b) NAC reduced the combined ROS level produced by sorafenib and Zn_A-Cu_B-Z. Error bars indicate mean±SD (n=3). *p<0.05, **p<0.01, ***p<0.001, and ****p<0.0001 from Student's t-test.

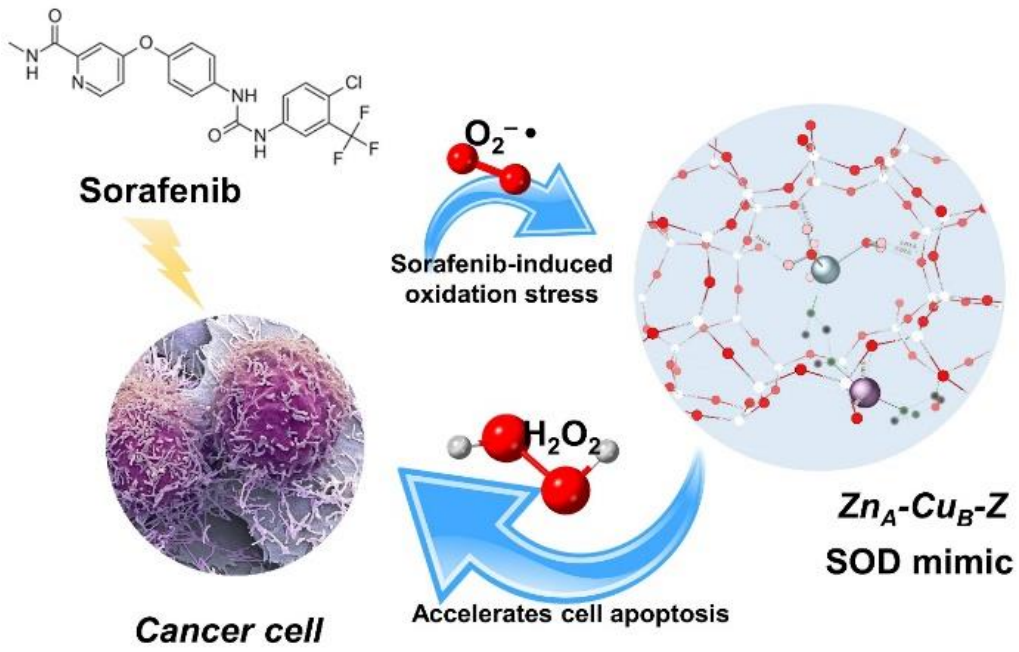

Scheme 3.3. Proposed schematic showing the mechanism of the synergistic effect between sorafenib and Zn_A-Cu_B-Z that augments apoptosis of tumor cells.

3.4 Conclusion

We, herein, offer a reliable assembly approach that can synthesize supported dual-atoms with controllable elemental constituent composition. We envisaged that this approach can be widely transferable to the synthesis of different atom-precise catalysts over other inorganic and organic support materials for not only biochemical but also more extensive applications.

3.5 Reference

(1) Wun, C. K. T.; Mok, H. K.; Chen, T.; Wu, T. S.; Taniya, K.; Nakagawa, K.; Day, S.; Tang, C. C.; Huang, Z.; Su, H.; Yu, W. Y.; Lee, T. K. W.; Lo, T. W. B.Atomically Dispersed 3d Metal Bimetallic Dual-Atom Catalysts and Classification of the Structural Descriptors. *Chem Catal.* **2022**, *2* (9), 2346–2363. https://doi.org/10.1016/j.checat.2022.07.027.

(2) Han, X.; Yang, S.Bimetallic Dual-Atom Catalysts: A Step toward Bioinspired Catalysis. *Chem* **2022**, *8* (10), 2584–2586. https://doi.org/10.1016/j.chempr.2022.09.010.

(3) Mitchell, S.; Pérez-Ramírez, J.Atomically Precise Control in the Design of Low-Nuclearity Supported Metal Catalysts. *Nat. Rev. Mater.* **2021**, *6* (11), 969–985.

(4) Zhang, J.; Wang, M.; Gao, Z.; Qin, X.; Xu, Y.; Wang, Z.; Zhou, W.; Ma, D.Importance of Species Heterogeneity in Supported Metal Catalysts. *J. Am. Chem. Soc.* **2022**, *144* (11), 5108–5115. https://doi.org/10.1021/jacs.2c00202.

(5) Liu, L.; Corma, A.Metal Catalysts for Heterogeneous Catalysis: From Single Atoms to Nanoclusters and Nanoparticles. *Chem. Rev.* **2018**, *118* (10), 4981–5079. https://doi.org/10.1021/acs.chemrev.7b00776.

(6) Kumari, A.; Kaushal, S.; Singh, P. P.Bimetallic Metal Organic Frameworks Heterogeneous Catalysts: Design, Construction, and Applications. *Mater. Today Energy* **2021**, *20*, 100667. https://doi.org/https://doi.org/10.1016/j.mtener.2021.100667.

(7) Xue, Q.; Ng, B. K. Y.; Man, H. W.; Wu, T. S.; Soo, Y. L.; Li, M. M.; Kawaguchi, S.; Wong, K. Y.; Tsang, S. C. E.; Huang, B.; Lo, T. W. B.Controlled Synthesis of Bi- And Tri-Nuclear Cu-Oxo Nanoclusters on Metal-Organic Frameworks and the Structure-Reactivity Correlations. *Chem. Sci.* **2022**, *13* (1), 50–58. https://doi.org/10.1039/d1sc05495c.

(8) Zhang, W.; Chao, Y.; Zhang, W.; Zhou, J.; Lv, F.; Wang, K.; Lin, F.; Luo, H.; Li, J.; Tong, M.; Wang, E.; Guo, S.Emerging Dual-Atomic-Site Catalysts for Efficient Energy Catalysis. *Adv. Mater.* **2021**, *33* (36), 2102576. https://doi.org/10.1002/adma.202102576.

(9) Zhang, J.; Huang, Q. an; Wang, J.; Wang, J.; Zhang, J.; Zhao, Y.Supported Dual-Atom Catalysts: Preparation, Characterization, and Potential Applications. *Chinese J. Catal.* **2020**, *41* (5), 783–798. https://doi.org/10.1016/S1872-2067(20)63536-7.

(10) Ge, J.; Zhang, D.; Qin, Y.; Dou, T.; Jiang, M.; Zhang, F.; Lei, X.Dual-Metallic Single Ru and Ni Atoms Decoration of MoS2 for High-Efficiency Hydrogen Production. *Appl. Catal. B Environ.* **2021**, *298*, 120557. https://doi.org/10.1016/j.apcatb.2021.120557.

(11) Jiao, J.; Lin, R.; Liu, S.; Cheong, W. C.; Zhang, C.; Chen, Z.; Pan, Y.; Tang, J.; Wu, K.; Hung, S. F.; Chen, H. M.; Zheng, L.; Lu, Q.; Yang, X.; Xu, B.; Xiao, H.; Li, J.; Wang, D.; Peng, Q.; Chen, C.; Li, Y.Copper Atom-Pair Catalyst Anchored on Alloy Nanowires for Selective and Efficient Electrochemical Reduction of CO 2. *Nat. Chem.* **2019**, *11* (3), 222–228. https://doi.org/10.1038/s41557-018-0201-x.

(12) Liu, L.; Díaz, U.; Arenal, R.; Agostini, G.; Concepción, P.; Corma, A.Generation of Subnanometric Platinum with High Stability during Transformation of a 2D Zeolite into 3D. *Nat.*

Mater. **2017**, *16* (1), 132–138.

(13) Fang, X.; Shang, Q.; Wang, Y.; Jiao, L.; Yao, T.; Li, Y.; Zhang, Q.; Luo, Y.; Jiang, H.-L.Single Pt Atoms Confined into a Metal-Organic Framework for Efficient Photocatalysis. *Adv. Mater.* **2018**, *30* (7), 1705112. https://doi.org/10.1002/adma.201705112.

(14) Jiao, L.; Wan, G.; Zhang, R.; Zhou, H.; Yu, S. H.; Jiang, H. L.From Metal–Organic Frameworks to Single-Atom Fe Implanted N-Doped Porous Carbons: Efficient Oxygen Reduction in Both Alkaline and Acidic Media. *Angew. Chem. Int. Ed.* **2018**, *57* (28), 8525–8529. https://doi.org/10.1002/anie.201803262.

(15) Wang, X.; Chen, Z.; Zhao, X.; Yao, T.; Chen, W.; You, R.; Zhao, C.; Wu, G.; Wang, J.; Huang, W.; Yang, J.; Hong, X.; Wei, S.; Wu, Y.; Li, Y.Regulation of Coordination Number over Single Co Sites: Triggering the Efficient Electroreduction of CO2. *Angew. Chem. Int. Ed.* **2018**, *57* (7), 1944–1948. https://doi.org/10.1002/anie.201712451.

(16) Katana, B.; Varga, G.; May, N.V.; Szilagyi, I.Superoxide Dismutase Mimicking Nanocomposites Based on Immobilization of Metal Complexes on Nanotubular Carriers. *J. Mol. Struct.* **2022**, *1256*, 132492. https://doi.org/10.1016/j.molstruc.2022.132492.

(17) Patriarca, M.; Daier, V.; Camí, G.; Rivière, E.; Hureau, C.; Signorella, S.Preparation, Characterization and Activity of CuZn and Cu2 Superoxide Dismutase Mimics Encapsulated in Mesoporous Silica. *J. Inorg. Biochem.* **2020**, *207*, 111050. https://doi.org/10.1016/j.jinorgbio.2020.111050.

(18) Patriarca, M.; Daier, V.; Camí, G.; Pellegri, N.; Rivière, E.; Hureau, C.; Signorella, S.Biomimetic Cu, Zn and Cu2 Complexes Inserted in Mesoporous Silica as Catalysts for Superoxide Dismutation. *Microporous Mesoporous Mater.* **2019**, *279*, 133–141. https://doi.org/10.1016/j.micromeso.2018.12.027.

(19) Li, J.; Huang, H.; Xue, W.; Sun, K.; Song, X.; Wu, C.; Nie, L.; Li, Y.; Liu, C.; Pan, Y.; Jiang, H. L.; Mei, D.; Zhong, C.Self-Adaptive Dual-Metal-Site Pairs in Metal-Organic Frameworks for Selective CO2 Photoreduction to CH4. *Nat. Catal.* **2021**, *4* (8), 719–729. https://doi.org/10.1038/s41929-021-00665-3.

(20) Lin, L.; Sheveleva, A. M.; daSilva, I.; Parlett, C. M. A.; Tang, Z.; Liu, Y.; Fan, M.; Han, X.; Carter, J. H.; Tuna, F.; McInnes, E. J. L.; Cheng, Y.; Daemen, L. L.; Rudić, S.; Ramirez-Cuesta, A. J.; Tang, C. C.; Yang, S.Quantitative Production of Butenes from Biomass-Derived γ-Valerolactone Catalysed by Hetero-Atomic MFI Zeolite. *Nat. Mater.* **2020**, *19* (1), 86–93. https://doi.org/10.1038/s41563-019-0562-6.

(21) Zhou, P.; Hou, X.; Chao, Y.; Yang, W.; Zhang, W.; Mu, Z.; Lai, J.; Lv, F.; Yang, K.; Liu, Y.; Li, J.; Ma, J.; Luo, J.; Guo, S.Synergetic Interaction between Neighboring Platinum and Ruthenium Monomers Boosts CO Oxidation. *Chem. Sci.* **2019**, *10* (23), 5898–5905. https://doi.org/10.1039/c9sc00658c.

(22) Yan, H.; Lin, Y.; Wu, H.; Zhang, W.; Sun, Z.; Cheng, H.; Liu, W.; Wang, C.; Li, J.; Huang, X.; Yao, T.; Yang, J.; Wei, S.; Lu, J.Bottom-up Precise Synthesis of Stable Platinum Dimers on

Graphene. *Nat. Commun.* **2017**, *8* (1), 1070. https://doi.org/10.1038/s41467-017-01259-z.

(23) He, Z.; He, K.; Robertson, A. W.; Kirkland, A. I.; Kim, D.; Ihm, J.; Yoon, E.; Lee, G.Do; Warner, J. H.Atomic Structure and Dynamics of Metal Dopant Pairs in Graphene. *Nano Lett.* **2014**, *14* (7), 3766–3772. https://doi.org/10.1021/nl500682j.

(24) Zhao, R.; Liang, Z.; Gao, S.; Yang, C.; Zhu, B.; Zhao, J.; Qu, C.; Zou, R.; Xu, Q.Puffing Up Energetic Metal–Organic Frameworks to Large Carbon Networks with Hierarchical Porosity and Atomically Dispersed Metal Sites. *Angew. Chem. Int. Ed.* **2019**, *58* (7), 1975–1979. https://doi.org/10.1002/anie.201811126.

(25) Feng, X.; Song, Y.; Chen, J. S.; Xu, Z.; Dunn, S. J.; Lin, W.Rational Construction of an Artificial Binuclear Copper Monooxygenase in a Metal-Organic Framework. *J. Am. Chem. Soc.* **2021**, *143* (2), 1107–1118. https://doi.org/10.1021/jacs.0c11920.

(26) Xue, Q.; Ng, B. K. Y.; Man, H. W.; Wu, T. S.; Soo, Y. L.; Li, M. M.; Kawaguchi, S.; Wong, K. Y.; Tsang, S. C. E.; Huang, B.; Lo, T. W. B.Controlled Synthesis of Bi- And Tri-Nuclear Cu-Oxo Nanoclusters on Metal-Organic Frameworks and the Structure-Reactivity Correlations. *Chem. Sci.* **2022**, *13* (1), 50–58. https://doi.org/10.1039/d1sc05495c.

(27) Bosson, C. J.; Birch, M. T.; Halliday, D. P.; Tang, C. C.; Kleppe, A. K.; Hatton, P. D.Polymorphism in Cu2ZnSnS4 and New Off-Stoichiometric Crystal Structure Types. *Chem. Mater.* **2017**, *29* (22), 9829–9839. https://doi.org/10.1021/acs.chemmater.7b04010.

(28) Brennan, S.; Cowan, P. L.A Suite of Programs for Calculating X-ray Absorption, Reflection, and Diffraction Performance for a Variety of Materials at Arbitrary Wavelengths. *Rev. Sci. Instrum.* **1992**, *63* (1), 850–853.

(29) Coudert, F. X.Molecular Mechanism of Swing Effect in Zeolitic Imidazolate Framework ZIF-8: Continuous Deformation upon Adsorption. *ChemPhysChem* **2017**, *18* (19), 2732–2738. https://doi.org/10.1002/cphc.201700463.

(30) Ye, L.; Song, Q.; Lo, B. T. W.; Zheng, J.; Kong, D.; Murray, C. A.; Tang, C. C.; Tsang, S. C. E.Decarboxylation of Lactones over Zn/ZSM-5: Elucidation of the Structure of the Active Site and Molecular Interactions. *Angew. Chem. Int. Ed.* **2017**, *56* (36), 10711–10716. https://doi.org/10.1002/anie.201704347.

(31) Chen, T.; Wang, Y.; Wong, K.; Woon, T.; Lo, B.; Chen, T.; Wang, Y.; Xue, Q.; Kit, C.; Wun, T.; So, P. K.; Yung, K. F.; Wu, T.; Soo, Y.; Taniya, K.; Day, S.; Tang, C. C.; Li, Z.; Huang, B.Article Atomically Precise Bimetallic Metal Ensembles with Tailorable Synergistic Effects Atomically Precise Bimetallic Metal Ensembles with Tailorable Synergistic Effects. *Cell Reports Phys. Sci.* **2022**, 100850. https://doi.org/10.1016/j.xcrp.2022.100850.

(32) Töro, I.; Petrutz, C.; Pacello, F.; D'Orazio, M.; Battistoni, A.; Djinović-Carugo, K.Structural Basis of Heme Binding in the Cu,Zn Superoxide Dismutase from Haemophilus Ducreyi. *J. Mol. Biol.* **2009**, *386* (2), 406–418. https://doi.org/10.1016/j.jmb.2008.12.004.

(33) Giordanino, F.; Vennestrøm, P. N. R.; Lundegaard, L. F.; Stappen, F. N.; Mossin, S.; Beato, P.; Bordiga, S.; Lamberti, C.Characterization of Cu-Exchanged SSZ-13: A Comparative FTIR, UV-

Vis, and EPR Study with Cu-ZSM-5 and Cu-β with Similar Si/Al and Cu/Al Ratios. *Dalt. Trans.* **2013**, *42* (35), 12741–12761. https://doi.org/10.1039/c3dt50732g.

(34) Naumov, P.; Ristova, M.; Šoptrajanov, B.; Zugik, M.Vibrational Spectra of Bis (Acetato) Tetrakis (Imidazole) Copper (II). *J. Mol. Struct.* **2001**, *598* (2–3), 235–243.

(35) Risoluti, R.; Piazzese, D.; Napoli, A.; Materazzi, S.Study of [2-(2′-Pyridyl)Imidazole] Complexes to Confirm Two Main Characteristic Thermoanalytical Behaviors of Transition Metal Complexes Based on Imidazole Derivatives. *J. Anal. Appl. Pyrolysis* **2016**, *117*, 82–87. https://doi.org/10.1016/j.jaap.2015.11.018.

(36) Lo, B. T. W.; Ye, L.; Tsang, S. C. E.The Contribution of Synchrotron X-Ray Powder Diffraction to Modern Zeolite Applications: A Mini-Review and Prospects. *Chem* **2018**, *4* (8), 1778–1808. https://doi.org/10.1016/j.chempr.2018.04.018.

(37) Chen, T.; Huang, B.; Day, S.; Tang, C. C.; Tsang, S. C. E.; Wong, K.; Lo, T. W. B.Differential Adsorption of l - and d -Lysine on Achiral MFI Zeolites as Determined by Synchrotron X-Ray Powder Diffraction and Thermogravimetric Analysis. *Angew. Chem. Int. Ed.* **2020**, *132* (3), 1109–1113. https://doi.org/10.1002/ange.201909352.

(38) Lo, B. T. W.; Ye, L.; Murray, C. A.; Tang, C. C.; Mei, D.; Tsang, S. C. E.Monitoring the Methanol Conversion Process in H-ZSM-5 Using Synchrotron X-Ray Powder Diffraction-Mass Spectrometry. *J. Catal.* **2018**, *365*, 145–152. https://doi.org/10.1016/j.jcat.2018.06.027.

(39) Ye, L.; Lo, B. T. W.; Qu, J.; Wilkinson, I.; Hughes, T.; Murray, C. A.; Tang, C. C.; Tsang, S. C. E.Probing Atomic Positions of Adsorbed Ammonia Molecules in Zeolite. *Chem. Commun.* **2016**, *52* (16), 3422–3425. https://doi.org/10.1039/c5cc10476a.

(40) Le, X.; Liao, S.; Liu, X.; Feng, X.Synthesis, Structure and SOD-like Activity of a Ternary Cu(II) Complex with 1,10-Phenanthroline and L-Valinate. *J. Coord. Chem.* **2006**, *59* (9), 985–995. https://doi.org/10.1080/00958970500443144.

(41) Bielski, B. H. J.; Richter, H. W.A Study of the Superoxide Radical Chemistry by Stopped-Flow Radiolysis and Radiation Induced Oxygen Consumption. *J. Am. Chem. Soc.* **1977**, *99* (9), 3019–3023. https://doi.org/10.1021/ja00451a028.

(42) Tainer, J. A.; Getzoff, E. D.; Richardson, J. S.; Richardson, D. C.Structure and Mechanism of Copper, Zinc Superoxide Dismutase. *Nature* **1983**, *306* (5940), 284–287. https://doi.org/10.1038/306284a0.

(43) Shen, J.; Wong, C. F.; Subramaniam, S.; Albright, T. A.; McCammon, J. A.Partial Electrostatic Charges for the Active Center of Cu, Zn Superoxide Dismutase. *J. Comput. Chem.* **1990**, *11* (3), 346–350. https://doi.org/10.1002/jcc.540110309.

(44) Hart, P. J.; Balbirnie, M. M.; Ogihara, N. L.; Nersissian, A. M.; Weiss, M. S.; Valentine, J. S.; Eisenberg, D.A Structure-Based Mechanism for Copper - Zinc Superoxide Dismutase †,‡. *Biochemistry* **1999**, *38* (7), 2167–2178.

(45) Zhao, P.; Ye, L.; Sun, Z.; Lo, B. T. W.; Woodcock, H.; Huang, C.; Tang, C.; Kirkland, A. I.; Mei, D.; Edman Tsang, S. C.Entrapped Single Tungstate Site in Zeolite for Cooperative Catalysis

of Olefin Metathesis with Brønsted Acid Site. *J. Am. Chem. Soc.* **2018**, *140* (21), 6661–6667. https://doi.org/10.1021/jacs.8b03012.

(46) Lau, A. T. Y.; Wang, Y.; Chiu, J. F.Reactive Oxygen Species: Current Knowledge and Applications in Cancer Research and Therapeutic. *J. Cell. Biochem.* **2008**, *104* (2), 657–667. https://doi.org/10.1002/jcb.21655.

(47) Zou, Z.; Chang, H.; Li, H.; Wang, S.Induction of Reactive Oxygen Species: An Emerging Approach for Cancer Therapy. *Apoptosis* **2017**, *22* (11), 1321–1335. https://doi.org/10.1007/s10495-017-1424-9.

(48) Perillo, B.; DiDonato, M.; Pezone, A.; DiZazzo, E.; Giovannelli, P.; Galasso, G.; Castoria, G.; Migliaccio, A.ROS in Cancer Therapy: The Bright Side of the Moon. *Exp. Mol. Med.* **2020**, *52* (2), 192–203. https://doi.org/10.1038/s12276-020-0384-2.

(49) Sosa, V.; Moliné, T.; Somoza, R.; Paciucci, R.; Kondoh, H.; LLeonart, M. E.Oxidative Stress and Cancer: An Overview. *Ageing Res. Rev.* **2013**, *12* (1), 376–390. https://doi.org/10.1016/j.arr.2012.10.004.

(50) Matés, J. M.; Sánchez-Jiménez, F. M.Role of Reactive Oxygen Species in Apoptosis: Implications for Cancer Therapy. *Int. J. Biochem. Cell Biol.* **2000**, *32* (2), 157–170. https://doi.org/10.1016/S1357-2725(99)00088-6.

(51) Coriat, R.; Nicco, C.; Cheŕeau, C.; Mir, O.; Alexandre, J.; Ropert, S.; Weill, B.; Chaussade, S.; Goldwasser, F.; Batteux, F.Sorafenib-Induced Hepatocellular Carcinoma Cell Death Depends on Reactive Oxygen Species Production in Vitro and in Vivo. *Mol. Cancer Ther.* **2012**, *11* (10), 2284–2293. https://doi.org/10.1158/1535-7163.MCT-12-0093.

(52) López-Lázaro, M.Dual Role of Hydrogen Peroxide in Cancer: Possible Relevance to Cancer Chemoprevention and Therapy. *Cancer Lett.* **2007**, *252* (1), 1–8. https://doi.org/10.1016/j.canlet.2006.10.029.

(53) Lange, M.; Abhari, B. A.; Hinrichs, T. M.; Fulda, S.; Liese, J.Identification of a Novel Oxidative Stress Induced Cell Death by Sorafenib and Oleanolic Acid in Human Hepatocellular Carcinoma Cells. *Biochem. Pharmacol.* **2016**, *118*, 9–17. https://doi.org/10.1016/j.bcp.2016.08.011.

(54) Tesori, V.; Piscaglia, A. C.; Samengo, D.; Barba, M.; Bernardini, C.; Scatena, R.; Pontoglio, A.; Castellini, L.; Spelbrink, J. N.; Maulucci, G.; Puglisi, M. A.; Pani, G.; Gasbarrini, A.The Multikinase Inhibitor Sorafenib Enhances Glycolysis and Synergizes with Glycolysis Blockade for Cancer Cell Killing. *Sci. Rep.* **2015**, *5* (1), 9149. https://doi.org/10.1038/srep09149.

(55) Hwang, T. S.; Choi, H. K.; Han, H. S.Differential Expression of Manganese Superoxide Dismutase, Copper/Zinc Superoxide Dismutase, and Catalase in Gastric Adenocarcinoma and Normal Gastric Mucosa. *Eur. J. Surg. Oncol.* **2007**, *33* (4), 474–479. https://doi.org/10.1016/j.ejso.2006.10.024.

(56) Alexandre, J.; Batteux, F.; Nicco, C.; Chéreau, C.; Laurent, A.; Guillevin, L.; Weill, B.; Goldwasser, F.Accumulation of Hydrogen Peroxide Is an Early and Crucial Step for Paclitaxel-Induced Cancer Cell Death Both in Vitro and in Vivo. *Int. J. Cancer* **2006**, *119* (1), 41–48.

https://doi.org/10.1002/ijc.21685.

3.6 Supplementary information for Chapter 3

Table 3.1. The elemental contents of metal-modified ZSM-5 zeolites.

Sample	**Cu (wt%)**	**Zn (wt%)**	**IC_{50} (μM) (normalized)**
ZSM-5	–	–	No activity
Cu_A-Z	1.90	–	> 100
Zn_A-Z	–	1.36	No activity
Zn_A-Cu_B-Z	1.27	1.34	0.056
Cu_A-Cu_B-Z	2.56	–	0.982
Cu_A-Zn_B-Z	1.94	0.50	3.847
Zn_A-Zn_B-Z	–	2.66	No activity
Native Cu,Zn-SOD	–	–	0.015[1]

Table 3.2. Fitting parameters for Cu and Zn K-edge EXAFS for the zeolite samples labelled. CN is the average coordination number around the central atoms. R and σ^2 are the average bond distance (Å) and the Debye-Waller factor (Å^2), respectively. The ΔE_0 values of two Cu–O/Zn–O shells are constrained to share the same value in the fitting models.

Sample	**Path**	**CN**	**R/Å**	**σ^2/Å^2**	**ΔE_0**
Cu_A-Z					
	Cu–N/O	3.7(3)	1.932(6)	0.0028(8)	-7.2(9)
Zn_A-Z					
	Zn–N/O	6.0(4)	2.067(7)	0.0084(10)	0.3(8)
Cu_A-Im-Z					
	Cu–N/O	3.4(3)	1.965(9)	0.00050(12)	-4.6(13)
Zn_A-Im-Z					
	Zn–N/O	4.1(4)	1.982(9)	0.0043(11)	1.4(12)
Cu_A-Cu_B-Z					
	Cu–N/O	3.8(3)	1.976(9)	0.0041(11)	-4.5(12)
Zn_A-Cu_B-Z					
	Cu–N/O	3.6(3)	1.961(8)	0.0037(10)	-5.3(11)
	Zn–N/O	4.6(2)	1.988(7)	0.0072(10)	2.5(5)
	Zn–C	1.2(5)	3.008(20)	0.00040(44)	2.5(5)
	Zn–O	3.3(9)	3.839(29)	0.0049(74)	2.5(5)

Table 3.3. Quantitative analysis of imidazole pre-absorbed on Zn_A-Cu_B-Z.

	At 200 °C (%)	**ΔW (%)**	***n* Im (mol)**	**Cu:Im**	**Cu:Zn**
Cu_A-Z	97.471	–	–	–	–
Zn_A-Cu_B-Z	99.277	1.806	0.027	0.047	0.96

Table 3.4. Crystallographic data of the SXRD measurements of the zeolite samples labelled.

	Cu_A-Cu_B-Z	**Cu_A-Zn_B-Z**	**Zn_A-Cu_B-Z**	**Cu_A-Im-Z**	**Zn_A-Im-Z**
X-ray energy (keV)	15	15	15	18	18
Beamline	Diamond I11	Diamond I11	Diamond I11	Spring-8 BL02B2	Spring-8 BL02B2
Wavelength (Å) (synchrotron)	0.826552(5)	0.826552(5)	0.826552(5)	0.688606(1)	0.688606(1)
2θ – zero point (°)	0.000189	0.000189	0.000189	0.00166	0.00166
Space group	*Pnma*	*Pnma*	*Pnma*	*Pnma*	*Pnma*
Crystal system	Orthorhombic	Orthorhombic	Orthorhombic	Orthorhombic	Orthorhombic
a (Å)	20.10236(6)	20.13277(6)	20.13407(6)	20.11946(11)	20.10819(18)
b (Å)	19.94225(5)	19.92647(5)	19.94311(5)	19.93809(11)	19.95780(19)
c (Å)	13.44913(5)	13.42452(5)	13.44385(5)	13.45839(9)	13.46677(15)
V (Å^3)	5391.57(3)	5385.58(3)	5398.19(3)	5398.75(6)	5404.42(9)
2θ range for refinement (°)	2-55	2-55	2-55	2-55	2-55
Detector	MAC	MAC	MAC	MYTHEN	MYTHEN
Number of parameters	24	21	24	21	21
Number of *hkl*s	4172	4168	4178	7191	7197
Refinement methods	Le Bail	Le Bail	Le Bail	Le Bail	Le Bail
$R_{wp}/R_{exp}/R_p$ (%)	11.773/3.385/8.068	11.209/5.251/7.914	10.674/5.611/7.770	7.900/0.776/4.478	8.214/0.888/4.613
Gof	3.478	2.135	1.902	10.174	9.250

R_{wp}: weighted profile; R_{exp}: expected; R_p: profile; *gof:* goodness-of-fit.

Table 3.5. Sensitivity investigation of the metal sites from the combined Rietveld refinement of RXRD measurement of Zn_A-Cu_B-Z. Impact on the site occupancy factors over a manual change of Cu and Zn sites.

	SOF of site A	Element (site A)	SOF of site B	Element (site B)	R_{wp} (%)	Gof	Note
1	0.23443(8)	Zn	0.22377(8)	Cu	12.57	3.35	Cu:Zn ratio constrained at 0.96 based on the elemental analysis by XRF
2	0.23443(8)	Zn	0.22377(8)	Zn	12.63	3.37	Site B replaced with Zn
3	0.23443(8)	Cu	0.22377(8)	Cu	12.62	3.37	Site A replaced with Cu
4	0.23443(8)	Cu	0.22377(8)	Zn	12.65	3.38	Element swapped between sites A and B.
5	0.23443(8)	Zn	0.22377(8)	Cu	12.62	3.37	Manually increased the SOF of Zn by 0.03.
6	0.23443(8)	Zn	0.22377(8)	Cu	12.60	3.36	Manually increased the SOF of Cu by 0.03.

Table 3.6. Atomic parameters of Zn_A-Cu_B-Z derived from RXRD.

Species	Atom	x	y	z	SOF	Beq	Wyckoff
Zeolite framework	O1	0.38046	0.05892	-0.24534	1	2.3106	8d
	O2	0.31592	0.06118	-0.07979	1	2.3106	8d
	O3	0.19593	0.05162	0.03528	1	2.3106	8d
	O4	0.08717	0.06005	-0.07704	1	2.3106	8d
	O5	0.11838	0.05262	-0.27461	1	2.3106	8d
	O6	0.24800	0.05362	-0.23783	1	2.3106	8d
	O7	0.37693	0.84547	0.79270	1	2.3106	8d
	O8	0.31754	-0.15891	-0.05215	1	2.3106	8d
	O9	0.19531	-0.15792	0.03547	1	2.3106	8d
	O10	0.08479	-0.15874	-0.07809	1	2.3106	8d
	O11	0.11493	-0.15482	-0.24588	1	2.3106	8d
	O12	0.23615	-0.15524	-0.24058	1	2.3106	8d
	O13	0.30624	-0.05484	-0.17627	1	2.3106	8d
	O14	0.07403	-0.04313	-0.18763	1	2.3106	8d
	O15	0.42779	0.13212	-0.39122	1	2.3106	8d
	O16	0.41518	-0.00044	-0.41379	1	2.3106	8d
	O17	0.40568	-0.13984	-0.43111	1	2.3106	8d
	O18	0.18042	0.13203	-0.38340	1	2.3106	8d
	O19	0.20316	0.01525	-0.40294	1	2.3106	8d
	O20	0.21027	-0.12386	-0.43893	1	2.3106	8d
	O21	0.00128	0.04992	-0.21613	1	2.3106	8d
	O22	-0.01374	-0.15449	-0.21957	1	2.3106	8d
	O23	0.41329	-0.25	-0.39153	1	2.3106	4c

	O24	0.18988	-0.25	-0.34109	1	2.3106	4c
	O25	0.31159	-0.25	0.09233	1	2.3106	4c
	O26	0.09229	-0.25	0.06091	1	2.3106	4c
	Si1	0.42558	0.05727	-0.33984	1	0.79737	8d
	Si2	0.30886	0.03287	-0.19521	1	0.79737	8d
	Si3	0.27763	0.05984	0.02423	1	0.79737	8d
	Si4	0.11837	0.06243	0.04024	1	0.79737	8d
	Si5	0.07314	0.03163	-0.18156	1	0.79737	8d
	Si6	0.18389	0.05665	-0.31837	1	0.79737	8d
	Si7	0.42227	-0.16922	-0.33133	1	0.79737	8d
	Si8	0.31274	-0.13224	-0.17682	1	0.79737	8d
	Si9	0.27979	-0.17096	0.03549	1	0.79737	8d
	Si10	0.12085	-0.17430	0.03229	1	0.79737	8d
	Si11	0.06890	-0.12836	-0.18494	1	0.79737	8d
	Si12	0.18962	-0.17543	-0.32062	1	0.79737	8d
Dual-atom	Cu	-0.09488	-0.28460	-0.74393	0.29902	8	4c
	N	-0.04797	-0.27080	-0.61678	0.29902	8	4c
	C	0.014726	-0.26718	-0.60192	0.29902	8	4c
	C	0.036702	-0.21013	-0.56244	0.29902	8	4c
	N	-0.0090	-0.16702	-0.54516	0.29902	8	4c
	C	-0.07031	-0.20212	-0.57909	0.29902	8	4c
	Zn	0.005497	-0.07739	-0.48718	0.17357	8	4c
	N	-0.14179	-0.2984	-0.87108	0.29902	8	4c
	C	-0.18264	-0.25877	-0.91441	0.29902	8	4c
	C	-0.24342	-0.28284	-0.92958	0.29902	8	4c

Coordinated water	N	-0.25176	-0.34285	-0.89798	0.29902	8	4c
	C	-0.18552	-0.36012	-0.85562	0.29902	8	4c
	Ow1	0.14105	-0.23885	0.38217	0.23125	8	4c
	Ow2	0.06493	-0.23739	0.26282	0.14205	8	4c
	Ow3	0.00227	-0.35978	0.51504	0.83063	8	4c

Table 3.7. SOD activity of different SOD mimic samples.

Catalyst		IC_{50} (μM) (normalized)	k_{cat} [$M^{-1}s^{-1}$][a]	Ref.
1.	Native Cu,Zn-SOD enzyme	0.0147	185.9×10^6	[1]
2.	1@SBA-15	0.109	25.1×10^6	[2]
3.	2@SBA-15	0.116	23.5×10^6	[2]
4.	2a@SBA-15	2.02	2.02×10^6	[2]
5.	3@SBA-15	5.99	5.99×10^6	[2]
6.	1@MCM-41	0.044	62.1×10^6	[3]
7.	2@MCM-41	0.053	51.5×10^6	[3]
8.	3@MCM-41	4.61	0.59×10^6	[3]
9.	Cu_2(bdpi) (1)	0.32	–	[4]
10.	Cu_2(Mebdpi) (2)	1.1	–	[4]
11.	CuZn(bdpi) (3)	0.24	–	[4]
12.	Cu(MeIm(Py)$_2$) (4)	0.56	–	[4]
13.	Zn_A-Cu_B-Z	0.056	48.8×10^6	This work
14.	Zn_A-NO_2Im-Cu_B-Z	0.074	36.9×10^6	This work
15.	Zn_A-PrIm-Cu_B-Z	0.120	22.7×10^6	This work
16.	Zn_A-PhIm-Cu_B-Z	0.213	12.8×10^6	This work
17.	Cu_A-Cu_B-Z	0.982	2.78×10^6	This work
18.	Cu_A-Zn_B-Z	3.847	0.710×10^6	This work
19.	Zn_A-Cu_B-Z(Na^+)	7.747	0.352×10^6	This work
20.	ZSM-5	Not measurable	Cannot be calculated	This work
21.	Co_A-Z	Not measurable	Cannot be calculated	This work
22.	Ni_A-Z	Not measurable	Cannot be calculated	This work
23.	Cu_A-Z	Not measurable	Cannot be calculated	This work
24.	Zn_A-Z	Not measurable	Cannot be calculated	This work

[a] Derived form the reported IC_{50} value using k_{NBT} (pH = 7.8) = 5.94×10^4 $M^{-1}s^{-1}$. [5]

Table 3.8. Incubation test of Zn_A-Cu_B-Z in phosphate buffer (pH 7.8). Zn concentration analyzed by ICP-OES. Metal leaching is marginally observed.

Incubation time (min)	Zn concentration (ppm)	Percentage (%)
15	1.423	0.34
30	1.069	0.26
45	1.103	0.27
60	1.685	0.41

Table 3.9. Bliss index for effect of sorafenib/ Zn_A-Cu_B-Z combination on apoptosis in PLC/PRF/5 cells.

Trial	Sorafenib 10 μM	Zn_A-Cu_B-Z 6.25 μM				
		DMSO	Sorafenib 10 μM	Fold change	Bliss index[6]	Synergistic effect
1	27.12%	12.04%	69.50%	+1.56	35.89%	Yes
2	34.40%	14.94%	74.00%	+1.15	44.20%	Yes
3	35.10%	10.76%	83.80%	+1.39	42.08%	Yes
Avg.	32.21%	12.58%	75.77%	+1.35	40.74%	Yes

Table 3.10. Bliss index for effect of sorafenib/ Zn_A-Cu_B-Z combination on apoptosis in MHCC-97L cells.

Trial	Sorafenib 10 μM	Zn_A-Cu_B-Z 50 μM				
		DMSO	Sorafenib 10 μM	Fold change	Bliss index[6]	Synergistic effect
1	19.34%	24.70%	46.80%	+1.42	39.26%	Yes
2	16.12%	22.89%	40.00%	+1.48	35.32%	Yes
3	18.97%	24.14%	42.00%	+1.21	38.53%	Yes
Avg.	18.14%	23.91%	42.93%	+1.37	37.71%	Yes

The Bliss index (combined inhibition percentage) is calculated by the following equation:

$$Combined\ inhibtion\ \%_{drugA,B} = Inhibiton\ \%_{DrugA} + Inhibition\ \%_{DrugB} - Inhibiton\ \%_{DrugA} \times Inhibition\ \%_{DrugB}$$

Typically, when the experimental value is greater than the Bliss index, it represents two drugs work synergistically. When the observed value is identical or less than the Bliss index, two drugs work independently or antagonistically respectively.

Reference

(1) Le, X.; Liao, S.; Liu, X.; Feng, X.Synthesis, Structure and SOD-like Activity of a Ternary Cu(II) Complex with 1,10-Phenanthroline and L-Valinate. *J. Coord. Chem.* **2006**, *59* (9), 985–995. https://doi.org/10.1080/00958970500443144.

(2) Patriarca, M.; Daier, V.; Camí, G.; Pellegri, N.; Rivière, E.; Hureau, C.; Signorella, S.Biomimetic Cu, Zn and Cu2 Complexes Inserted in Mesoporous Silica as Catalysts for Superoxide Dismutation. *Microporous Mesoporous Mater.* **2019**, *279*, 133–141. https://doi.org/10.1016/j.micromeso.2018.12.027.

(3) Patriarca, M.; Daier, V.; Camí, G.; Rivière, E.; Hureau, C.; Signorella, S.Preparation, Characterization and Activity of CuZn and Cu2 Superoxide Dismutase Mimics Encapsulated in Mesoporous Silica. *J. Inorg. Biochem.* **2020**, *207*, 111050. https://doi.org/10.1016/j.jinorgbio.2020.111050.

(4) Ohtsu, H.; Shimazaki, Y.; Odani, A.; Yamauchi, O.; Mori, W.; Itoh, S.; Fukuzumi, S.Synthesis and Characterization of Imidazolate-Bridged Dinuclear Complexes as Active Site Models of Cu,Zn-SOD. *J. Am. Chem. Soc.* **2000**, *122* (24), 5733–5741. https://doi.org/10.1021/ja994050j.

(5) Bielski, B. H. J.; Richter, H. W.A Study of the Superoxide Radical Chemistry by Stopped-Flow Radiolysis and Radiation Induced Oxygen Consumption. *J. Am. Chem. Soc.* **1977**, *99* (9), 3019–3023. https://doi.org/10.1021/ja00451a028.

(6) Zhao, W.; Sachsenmeier, K.; Zhang, L.; Sult, E.; Hollingsworth, R. E.; Yang, H.A New Bliss Independence Model to Analyze Drug Combination Data. *J. Biomol. Screen.* **2014**, *19* (5), 817–821. https://doi.org/10.1177/1087057114521867.

Chapter 4 Controlled synthesis of Cu, Fe dual atom catalysts restrained on metal-organic frameworks for efficient O_2 activation

Highlight of this chapter

Supported bimetallic dual-atom catalysts (DACs) have been regarded as a promising class of materials for small molecule activation, despite their challenging syntheses. We have successfully synthesised supported Cu,Fe dual-atom catalysts (DACs) on the Zr_6O_4 secondary building units of UiO-66-NH_2, enabling efficient activation of O_2. Our model photocatalytic styrene oxidation reaction achieved remarkably high product selectivity (>92%) towards benzaldehyde. This superior reactivity is attributed to the well-balanced synergy between the electronic and steric characteristics, enabling efficient O_2 activation by the sterically restrained Cu and Fe sites in proximity for the formation of the bridging peroxy group. This group facilitates the selective oxidation of styrene similar to many peroxide-based oxidants. The confined microporous environment allows for control of the electronic and geometric properties of the DACs, shedding light towards more precise atomistic engineering that approaches the conventional inorganic metal(s)-complex counterparts. Overall, supported bimetallic dual-atom catalysts (DACs) are a promising class of materials for small molecule activation, despite their challenging syntheses. Most of the content in this chapter has been published recently in Journal of Materials Chemistry A [1].

4.1 Introduction

Supported atom-precise metal clusters (with low nuclearity) are increasingly recognized to be the next-generation catalytic materials in the coming era [2–4]. Atom-precise clusters not only are highly atom-economical, but they also offer unique catalytic properties compared with their atomic and bulk counterparts. It is largely related to the widely tunable electronic and geometric characteristics. Furthermore, the pairing of metals, *e.g.*, in bimetallic dual-atom catalysts (DACs), could alter the electronic states and break the linear scale relationship, which could ultimately be an additional handle to tune the catalytic properties [5–7]. The catalytic properties in this class of supported DACs are often governed by the adsorption configurations of substrates and the corresponding energetics [8–12]. However, it has been a grand challenge to decipher the correlations between the structural descriptors and catalytic reactivity, which hinders the 'target-engineering' of a specific structure with regard to a catalytic reaction.

The activation of small molecules, such as O_2, water, and methanol, is crucial in many catalytic processes. Interactions between two neighboring motifs often play a significant role in their activation. Microporous materials, such as zeolites and metal-organic frameworks (MOFs), with spatial restraints, can facilitate the design and engineering of neighboring active motifs. Our team has recently demonstrated the presence of 'frustrated' active pairs between protonic Brønsted acid sites and metal sites within the confined cavity of zeolites for the initial cleavage of water and methanol, followed by subsequent reactions that produce high selectivity products [13].

In recent studies, a series of 3d metal-based dual-atom catalysts (DACs) were immobilized on microporous supports, where the bridging O species were identified as pivotal factors in their catalytic reactivities [14–17]. One notable example is the Cu_2-oxo and Cu_3-oxo clusters supported on zeolites. These clusters have been shown to be effective in the selective oxidation of methane to methanol, with the Cu-O-Cu site being highly active and specific for the activation of the inert and non-polar C-H bonds in methane [18–20]. In addition to M–O–M, M–O_2–M (in various O_2 binding modes) is also a highly attractive functional group that could facilitate more extensive catalytic possibilities. A popular example is Cytochrome c oxidase (C*c*O), where the Fe and Cu moieties are held apart by a rigid protein scaffold to a few angstroms distance. This unique arrangement enables the activation of O_2 (by Fe) and subsequent multi-electron reduction (by Cu) to form the well-known 'Cu-O_2-Fe' co-factor [21,22]. Despite the design of many organometallic complexes with well-defined electronic and steric properties, it remains fundamentally challenging to design well-controlled, atomically dispersed bimetallic dual-atom catalysts (DACs) supported on solid materials.

Here, we present a method for the controlled synthesis of atomically precise Cu,Fe dual-atom catalysts (DACs) stabilized by the same Zr_6O_4 secondary building unit of UiO-66-NH_2 using a modular assembly approach that exploits fundamental coordination and solid-state chemistry concepts. This approach enables the selective photocatalytic oxidation of styrene to the benzaldehyde product with high selectivity (>92%). The superior catalytic behavior is attributed to the formation of a bridging 'μ-η^1:η^1-O_2' species resulting from O_2 activation by neighboring Fe and Cu motifs. Additionally, we employ theoretical calculations to discuss the structure-activity correlations regarding the interactions between the DACs and the MOF framework at the atomic resolution.

4.2 Experimental procedure

Synthesis of UiO-66-NH_2

The synthesis procedure is according to the previously reported UiO-66-NH_2 with the structural formula of $Zr_6O_4(OH)_4(ATA)_{5.8}$ (ATA = 2-aminoterephthalic acid) [23]. 0.240 g zirconium tetrachloride and 0.186 g ATA were dissolved in 20 mL N,N-dimethylformamide (DMF). The solution was transferred into a 100 mL hydrothermal vessel and heated at 120 °C for 12 hours. The UiO-66-NH_2 powder was collected by centrifugation and washed with water 5 times. Dried at 60 °C overnight.

Synthesis of Cu^{2+}-UiO-66-NH_2

A related modular approach has been used in our previous study to synthesize Cu_2 and Cu_3 clusters supported on the Zr_6O_4 secondary building units of UiO-66-NH_2 [24,25]. 0.57 g UiO-66-NH_2 were dispersed in 20 mL H_2O by ultrasonication. 138.35 μL bis(ethylenediamine)copper(II) hydroxide was dropwise added. The mixture was stirred at room temperature for 3 hours. The product was collected by centrifugation and washed with 10 mL of double distilled water. It was dried at 70 °C overnight to obtain the product Cu^{2+}-UiO-66-NH_2.

Synthesis of Fe^{3+}-UiO-66-NH_2

0.57 g UiO-66-NH_2 were dispersed in 20 mL H_2O by ultrasonication, then 0.28 g $Fe(NO_3)_3$ was added. The mixture was stirred at room temperature for 3 hours to obtain Fe^{3+}-UiO-66-NH_2. The product was collected by centrifugation and washed with 10 mL distilled water.

Synthesis of Cu^{2+}-mIem-Fe^{3+}-UiO-66-NH_2

0.57 g Cu^{2+}-UiO-66-NH_2 were dispersed in 20 mL H_2O. 0.057 g 2-methylimidazole was added and reacted for 3 h. The solid sample was collected by centrifugation by 3 times and washed by double distilled H_2O to obtain mIem-Cu^{2+}-UiO-66-NH_2 in 20 mL H_2O. 0.28 g $Fe(NO_3)_3$ was then added and reacted at room temperature for 3 h to obtain Fe^{3+}-mIem-Cu^{2+}-UiO-66-NH_2. The sample was washed by double distilled H_2O by 3 times and dried at 70 °C.

Synthesis of Cu_1-UiO, Fe_1-UiO, and Cu,Fe-UiO

Cu^{2+}-UiO-66-NH_2, Fe^{3+}-UiO-66-NH_2, and Cu^{2+}-mIem-Fe^{3+}-UiO-66-NH_2 are heated at 180 °C for 1 h with a heating rate of 10 °C/min. By calcination of the samples at 180 °C, the organic meIm linker can be removed. The vacant coordination sites are reactive which are hence stabilized by the neighboring O atoms.

Photocatalytic styrene oxidation

2.5 mg catalysts were dispersed in 1.5 mL 1,2-dichloroethane. 0.5 mL styrene was added and reacted in air for 30 min under UV irradiation (365 nm). Gas chromatography-mass spectrometry (GC-MS; Agilent) analyzed the products.

4.3 Results and Discussion

A crystalline UiO-66-NH_2 powder sample as a host solid support has been prepared (as used before [23,26,27], see **Figures 4.1–4.2** in the Supporting Information (SI) for basic structural and morphological characterization) with a chemical formula of $Zr_6O_4(OH)_4(CO_2C_6H_3NH_2CO_2)_{5.8}$ (space group: Fm-3m) with a metal-to-linker ratio of 1:0.97. As shown in **Scheme 4.1**, a rational modular approach has been applied to provide an exclusive environment for the formation of Cu,Fe DACs (denoted as '**Cu,Fe-UiO**'). This approach takes advantage of the microporous confinement effect and formation of Lewis acid-base adducts. A dibasic 2-methylimidazole linker was applied to connect the step-by-step added Cu^{2+} and Fe^{3+}. It was then calcined at 180 °C in air to yield the final '**Cu,Fe-UiO**' by removing the connecting meIm linker and water ligands. The effectiveness of this modular approach was evaluated by elemental analysis (**Table 4.1**), and Raman and Fourier-transform infrared (FTIR) spectroscopic results (**Figure 4.3**). By the energy dispersive X-ray (EDX) mapping analysis (**Figure 4.4**), a homogeneous distribution of Cu and Fe species can be observed. Analogous 'single-atom' **Fe_1-UiO** (**Figure 4.5**) and **Cu_1-UiO** (**Figure 4.6**) samples (as synthesised before [23,27]) were used for a comparison study.

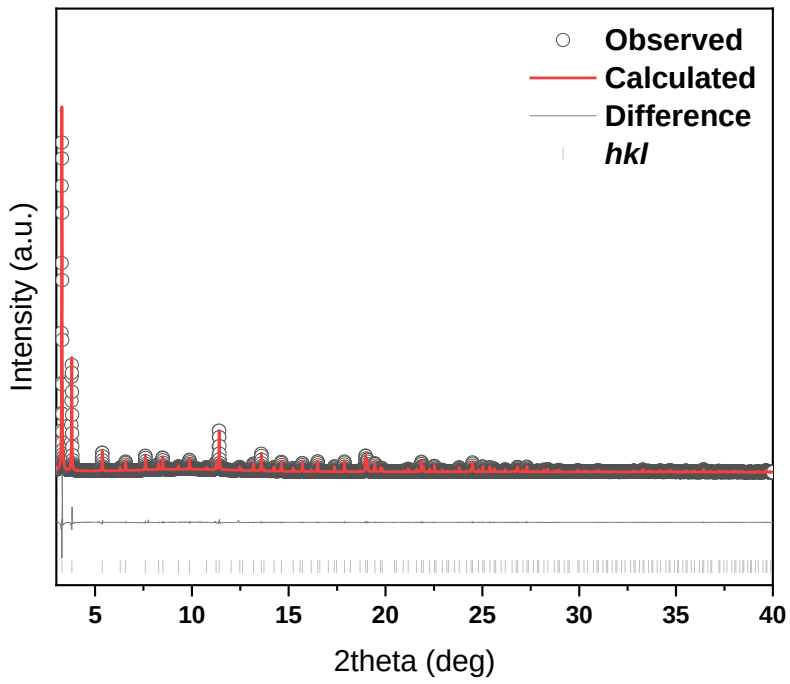

Figure 4.1. High-resolution synchrotron X-ray powder diffraction data of UiO-66-NH_2 collected on Beamline BL02B2 at SPring-8. The X-ray energy was optimized at 17.8 keV.

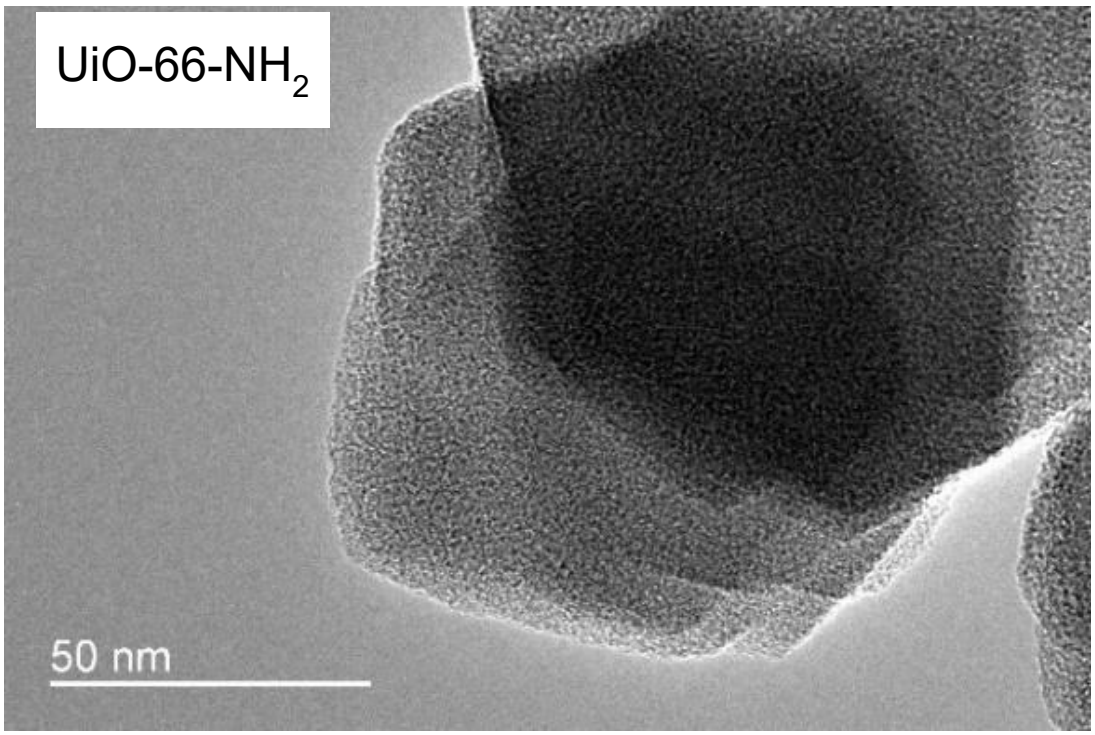

Figure 4.2. Transmission electron microscopy image of pristine UiO-66-NH_2 on Ni grid.

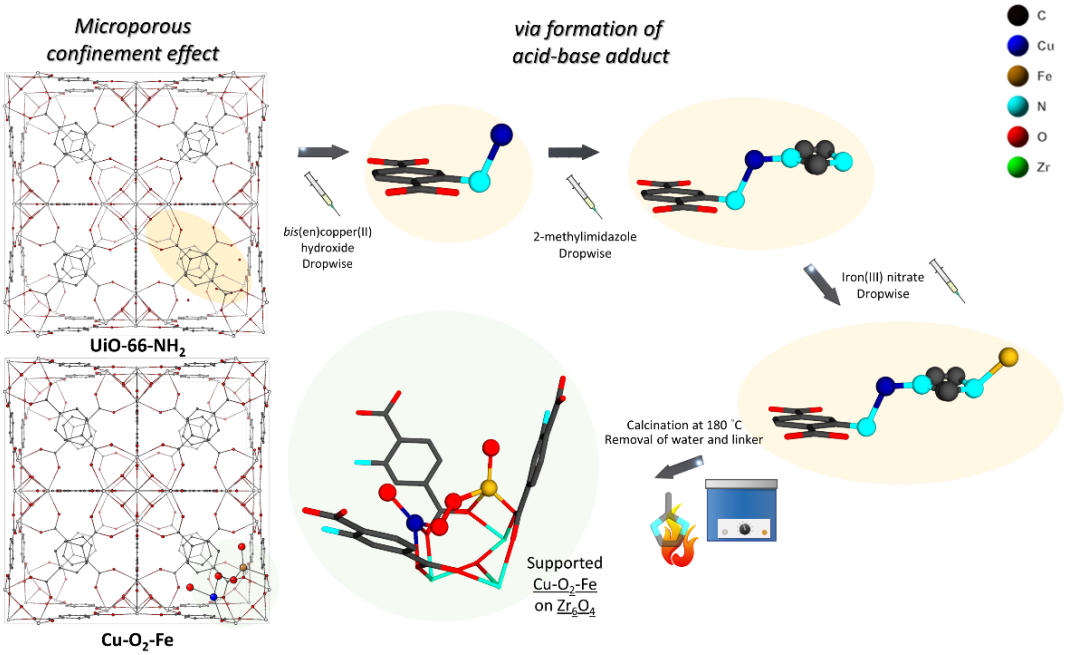

Scheme 4.1. Schematic illustration of the modular assembly approach that combines the underlying principles of solid-state chemistry and coordination chemistry for the synthesis of Cu,Fe DAC on UiO-66-NH_2 (denoted as '**Cu,Fe-UiO**'). In the preparation of **Cu,Fe-UiO**, a dibasic 2-methylimidazole linker was applied to connect the modularly added Cu^{2+} and Fe^{3+}. The linker was removed by calcination in air at 180 °C.

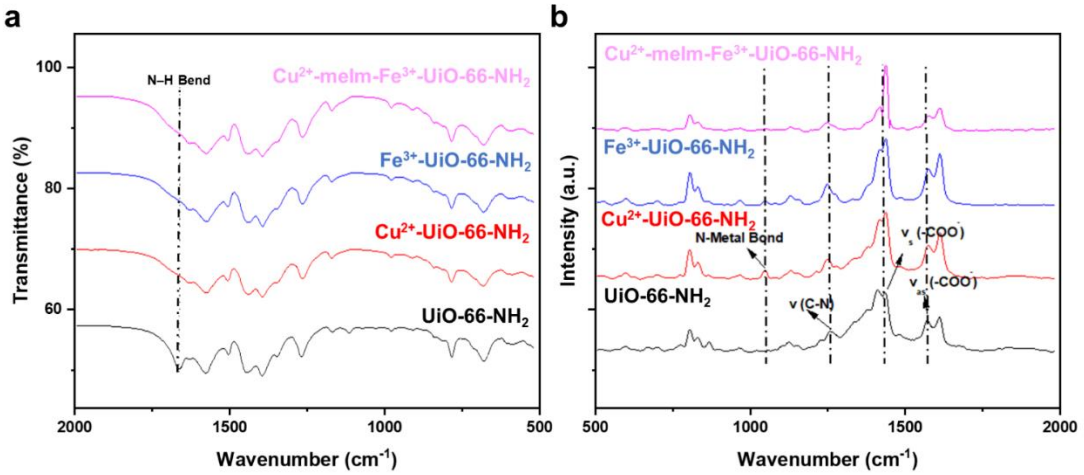

Figure 4.3. (**a**) Fourier-transform infrared and (**b**) Raman spectroscopic study of the non-calcined (precursor) samples, i.e., Cu^{2+}-, Fe^{3+}-, and Cu^{2+}-meIm-Fe^{3+}-UiO-66-NH_2.

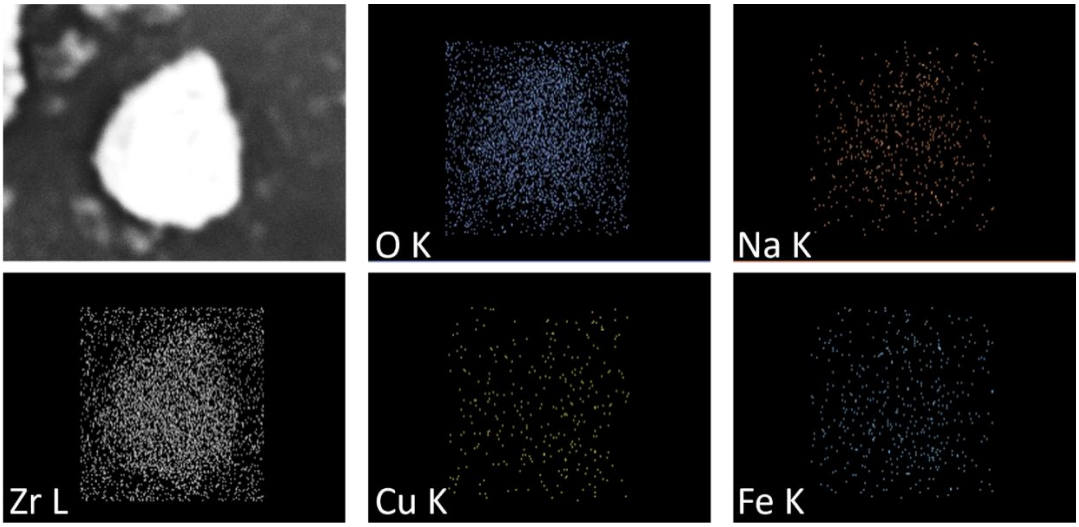

Figure 4.4. Scanning electron microscopy/energy-dispersive X-ray spectroscopy (SEM/EDX) mapping analysis of **Cu,Fe-UiO** showing the homogeneous distribution of Cu and Fe within a UiO-66-NH_2 nanocrystallite.

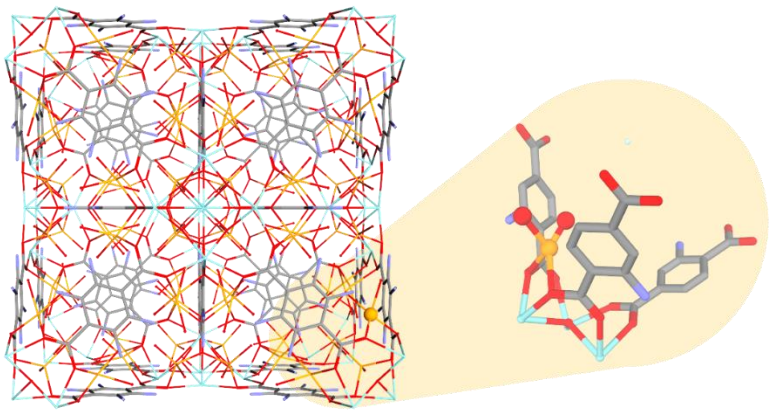

Figure 4.5. Rietveld refined crystal structure of **Fe_1-UiO** as synthesized before [23].

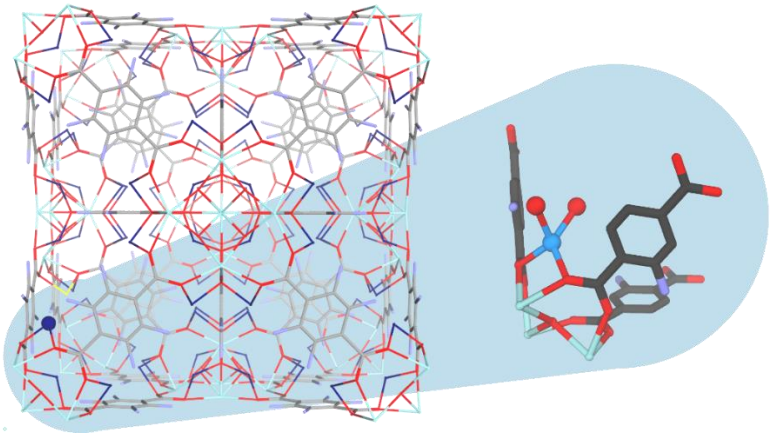

Figure 4.6. Rietveld refined crystal structure of **Cu_I-UiO** as synthesized before [28].

In-situ synchrotron X-ray powder diffraction (PXRD) at elevated temperatures was employed to serve as a guide to selecting a reasonable calcination temperature (**Figure 4.7a–4.7b**, the full patterns are presented in **Figures 4.8–4.9**). This is an important step as a low calcination temperature will not be able to remove water and 2-methylimidazole linker, but a too-high calcination temperature will break the crystallinity of the MOF framework. The crystalline MOF framework was retained upon the post-synthetic metalation approach (see **Figure 4.10** with the crystallographic parameters summarised in **Tables 4.2–4.3**). As seen in **Figure 4.7a–4.7b** the most notable change in the Bragg peak intensities (taking (111), the strongest peak, as an illustration, **Figure 4.7c**) was observed just above 175 °C, which may indicate the removal of meIm and water. It is in contrast to the calcination of the analogous Cu^{2+}-UiO-66-NH_2 sample where the most notable change occurs at around 250 °C. In addition, as shown in **Figure 4.7d**, the unit cell parameters decrease much more rapidly in the calcination study of Cu^{2+}-melm-Fe^{3+}-UiO-66-NH_2. The alternation in the crystallographic parameters up to 200 °C was negligible. At higher temperatures (> 200 °C), the intensity of the Bragg peaks decreased significantly, with the formation of an apparent amorphous phase from structural deformation. The ultraviolet-visible-near Infrared (UV-vis-NIR) spectra before and after calcination also reveal that a notable change in absorption can be observed which can be ascribed to the removal of water and meIm linker species (**Figure 4.11**) [29,30].

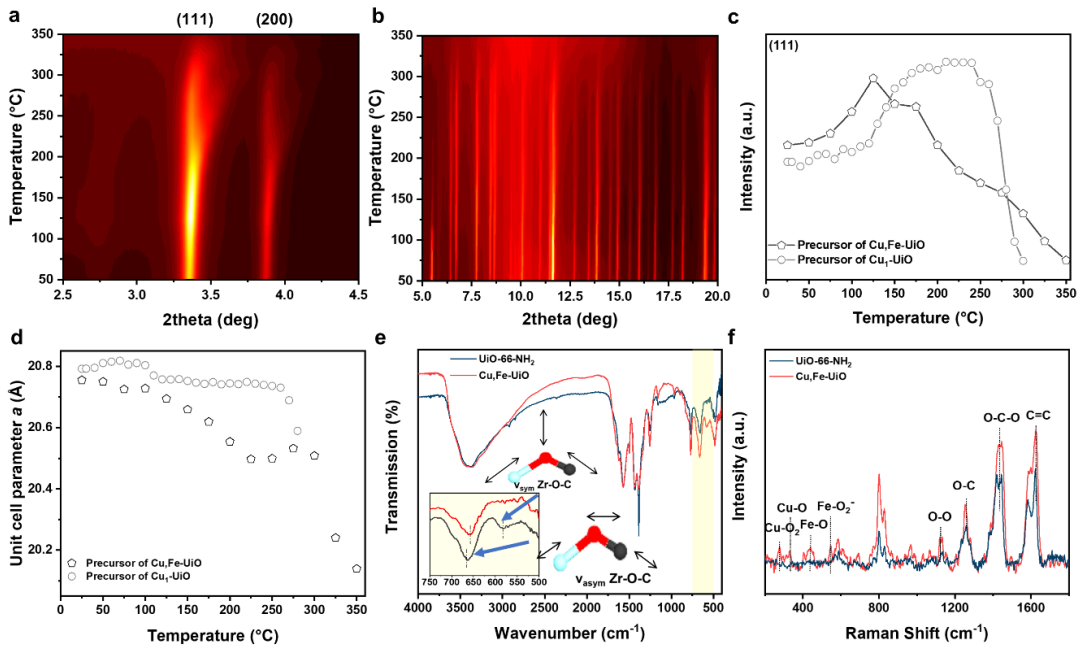

Figure 4.7. (**a, b**) Temperature-resolved synchrotron PXRD two-dimensional contour plot of the calcination treatment of the precursor of **Cu,Fe-UiO**. Data collected on BL02B2 SPring-8. Energy optimized at 17.8 keV. (**c**) A temperature-resolved plot of the Bragg peak intensities of the (111) reflection. (**d**) Quantitative analysis of the unit cell parameters by Pawley refinement with the fitting parameters summarised in **Table 4.3**, and fitting profiles in **Figure 4.9**. (**e**) FTIR and (**f**) Raman spectra of UiO-66-NH_2 and **Cu,Fe-UiO**.

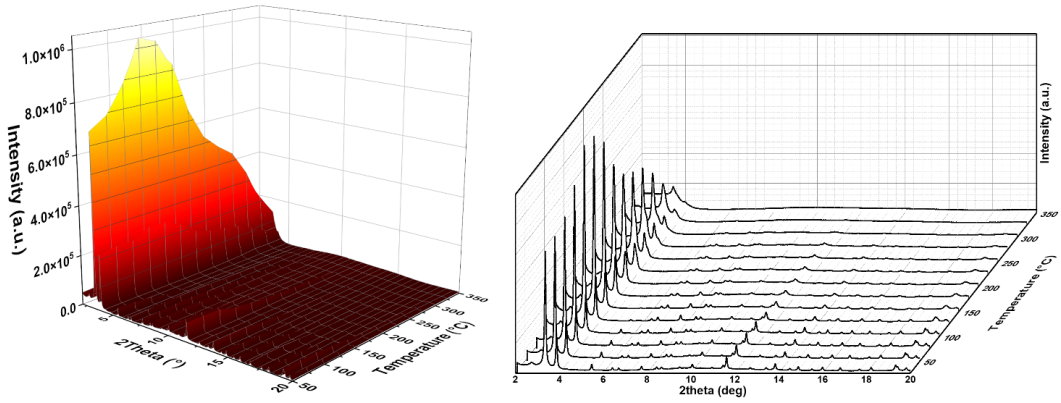

Figure 4.8. *In-situ* synchrotron PXRD shows the dynamic change of Cu^{2+}-meIm-Fe^{3+}-UiO-66-NH_2 in the diffraction profiles at elevated temperatures. Data was collected on Beamline BL02B2 at SPring-8, at the X-ray energy of 17.8 keV.

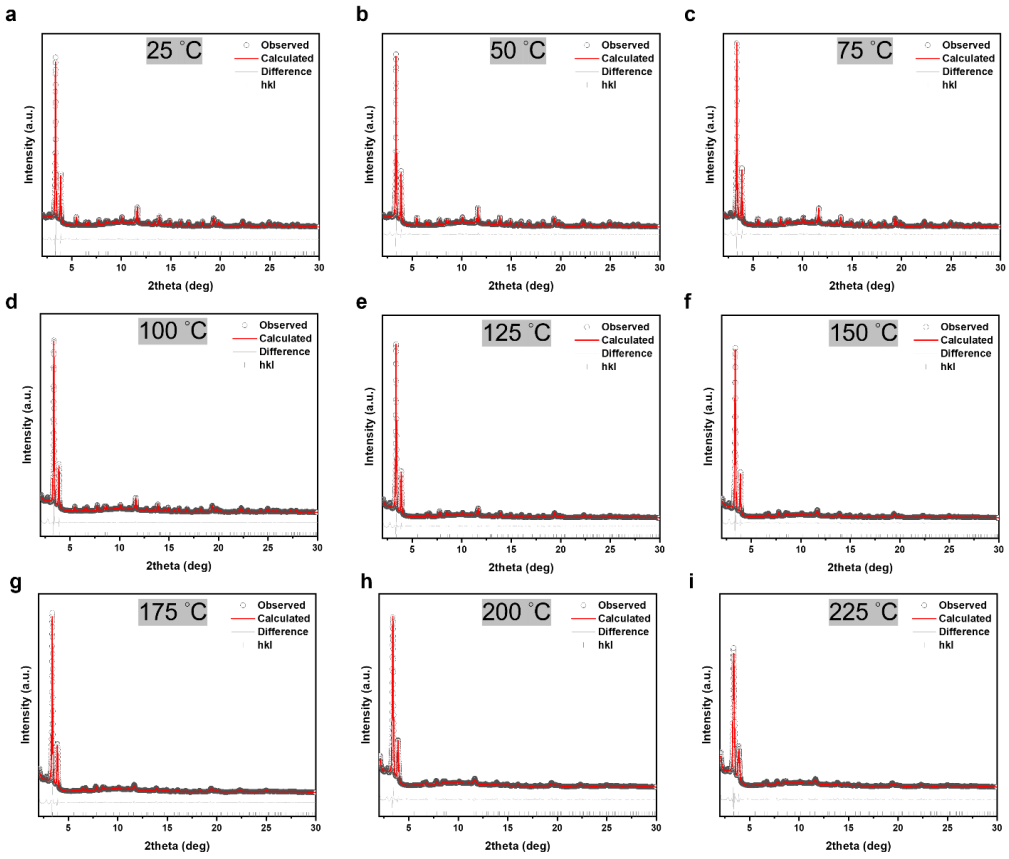

Figure 4.9. Pawley refinement profiles of *in-situ* synchrotron PXRD data.

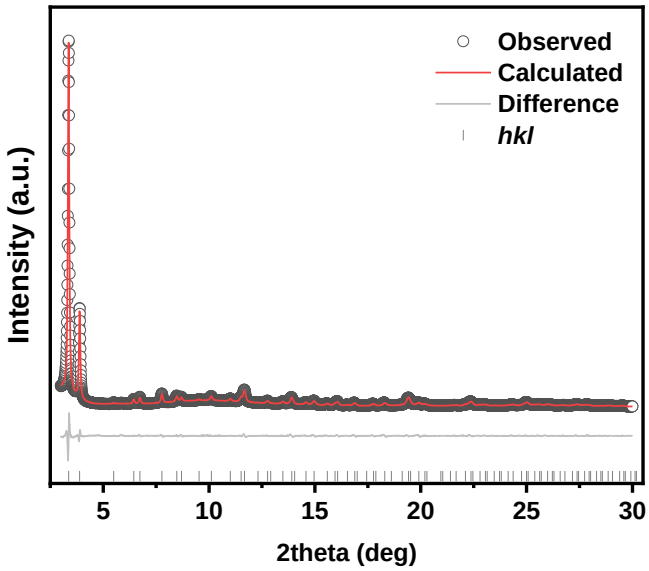

Figure 4.10. High-resolution synchrotron PXRD of **Cu,Fe-UiO**, and the corresponding Pawley refinement profile. Data was collected on Beamline BL02B2 at SPring-8. The X-ray energy was optimised at 17.8 keV.

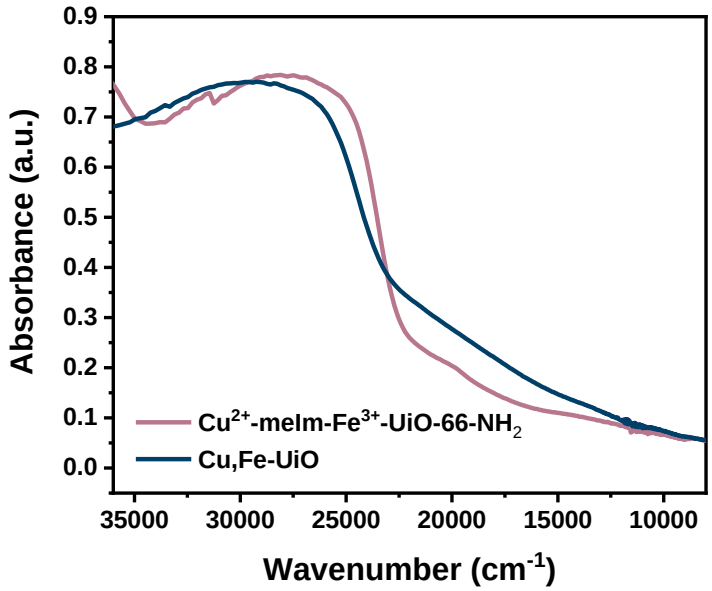

Figure 4.11. UV-vis-NIR spectra of Cu^{2+}-meIm-Fe^{3+}-UiO-66-NH_2 (precursor of **Cu,Fe-UiO**), and **Cu,Fe-UiO**, showing the effect of calcination.

We subsequently employed FTIR spectroscopy to investigate the location of the Cu,Fe DACs with respect to the UiO-66 framework (**Figure 4.7e**). The peaks at 577 cm^{-1} and 664 cm^{-1} are characteristic of the asymmetric and symmetric mode of Zr–(O–C) in UiO-66-NH_2 [31,32]. Noticeable shifts in these peak positions can be observed in **Cu,Fe-UiO**. This suggests a change in the Zr–(O–C) bonding caused by the direct interaction of the Zr_6O_4 secondary building unit with the extra-framework DACs. A similar observation is also observed in related studies of Cu-based DACs on the Zr_6O_4 of UiO-66-NH_2 [27]. As a complementary technique to FTIR, we employed Raman spectroscopy to further study the bonding information in the samples (**Figure 4.7f**). Characteristic Raman peaks, such as Zr–O stretching at 801 cm^{-1}, O–C–O symmetric stretching in-phase peak at 1450 cm^{-1} and C=C stretching of aromatic rings, of UiO-66-NH_2 are noted. The peak at 276 cm^{-1} can be assigned to Cu–O [33]. Extra peaks observed at 420, 543 and 1122 cm^{-1} in **Cu,Fe-UiO** can be attributed to the Fe–O, Fe–O_2 and O–O (in the form of O_2^{2-}) stretching modes, respectively [34]. These features agree with previous Raman studies on C*c*O which contains a highly comparable 'Cu-O_2-Fe' co-factor [33–35]. The Raman spectra of **Cu_1-UiO** and **Fe_1-UiO** are presented in **Figure 4.12** where the respective Fe–O_2 or Cu–O_2 features were not observed.

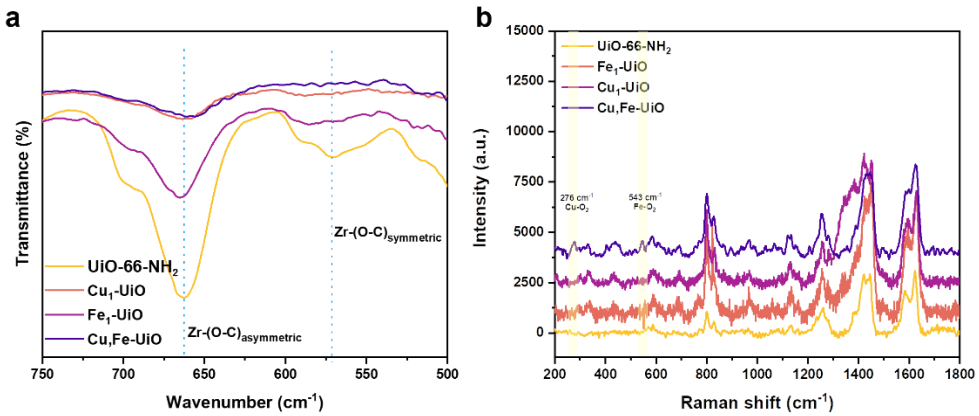

Figure 4.12. (**a**) UV-vis-NIR spectra and (**b**) Raman spectra of UiO-66-NH_2, **Fe_1-UiO**, **Cu_1-UiO**, and **Cu,Fe-UiO**

X-ray absorption spectroscopy has been accordingly employed to discern the electronic and local geometric structures of **Cu,Fe-UiO**. The Cu and Fe K-edge X-ray absorption near-edge structures are shown in **Figures 4.13a** and **4.13b**. The oxidation states of Cu and Fe can be confirmed at +2 and +3, which are highly comparable to the absorption edge of CuO and α-Fe_2O_3, respectively. However, as seen in the zoom-in illustration, the Fe K-edge of **Cu,Fe-UiO** locates at a slightly lower energy (closer to the Fe foil standard) than the Fe K-edge of **Fe_1-UiO**, which indicates that the valence state of Fe in **Cu,Fe-UiO** is less positive than that of **Fe_1-UiO**. By performing a quantitative linear combination fitting analysis (as summarised in **Table 4.4** and **Figure S12/4.14**), the Fe K-edge of **Cu,Fe-UiO** possesses 12% Fe foil and 88% α-Fe_2O_3 characteristics, which is further verified by our Bader charge analysis (see **Figure 4.15**). It is in great contrast to that of **Fe_1-UiO**, which possesses only 1% Fe foil but 99% α-Fe_2O_3 characteristics. Considering the structural similarities between the two samples, the much less positive valence state of Fe in **Cu,Fe-UiO** can be attributed to the combined electronic effect of neighboring Cu^{2+} and bridging peroxy species.

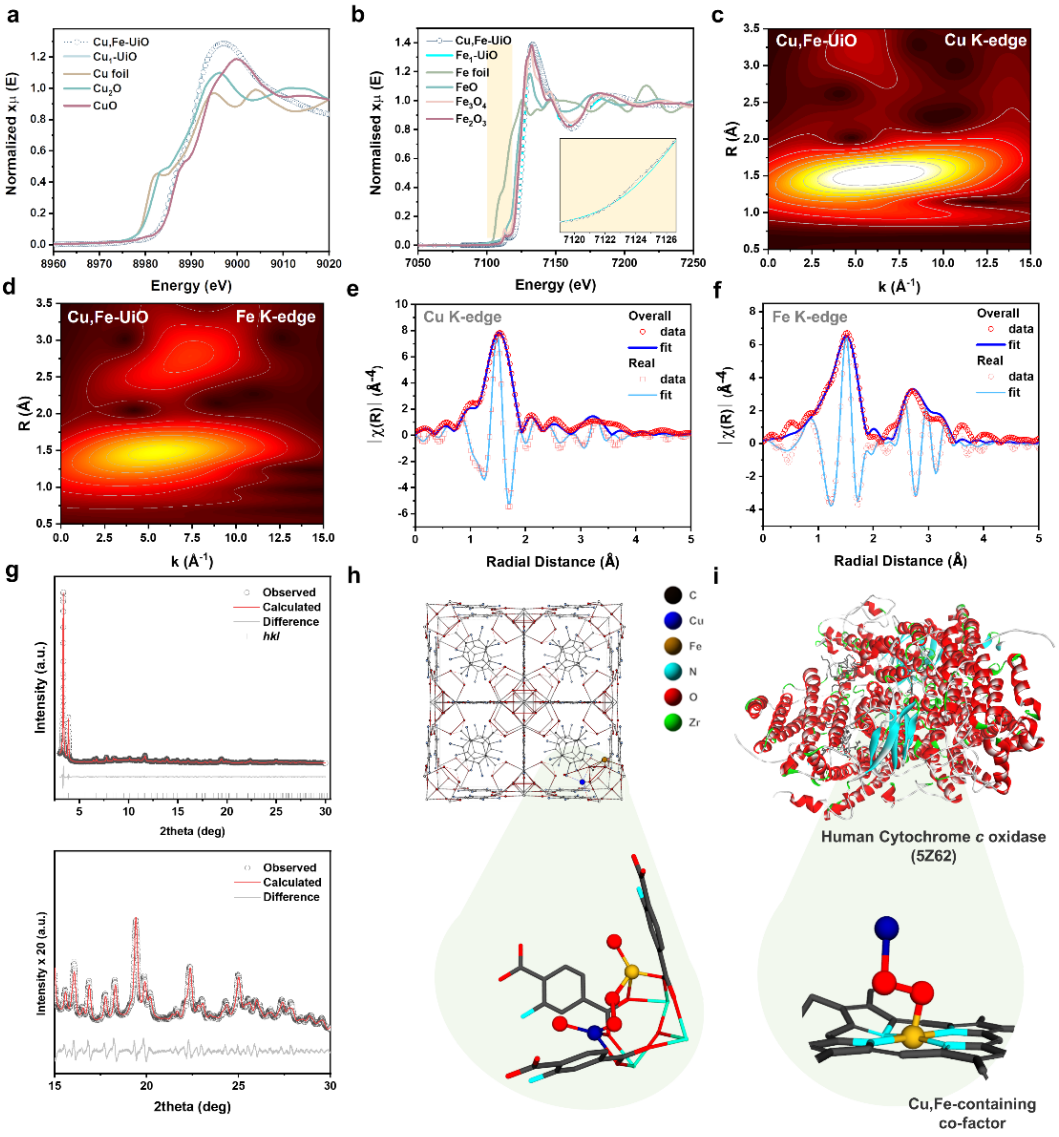

Figure 4.13. XANES measurements of **Cu,Fe-UiO** at the (**a**) Cu K-edge, and (**b**) Fe K-edge. Wavelet transforms for the EXAFS signals of (**c**) Cu K-edge and (**d**) Fe K-edge. The Fourier-transformed magnitude of the experimental (**e**) Cu K-edge, (**f**) Fe K-edge, and the fitting profiles. The quantitative analysis is summarised in **Tables 4.4–4.5**. (**g**) High-resolution SXRD pattern and the corresponding Rietveld refinement profile. Data were collected on beamline BL02B2 at SPring-8 ($\lambda = 0.700261(10)$ Å; E = 17.8 keV) with the Rietveld refinement profiles using TOPAS v6.0 academic. The atomic parameters are summarised in **Table 4.7**. (**h**) The optimized crystal structure by the Rietveld refinement. (**i**) Illustration of human Cytochrome *c* oxidase (5Z62) to show the structural similarity [36].

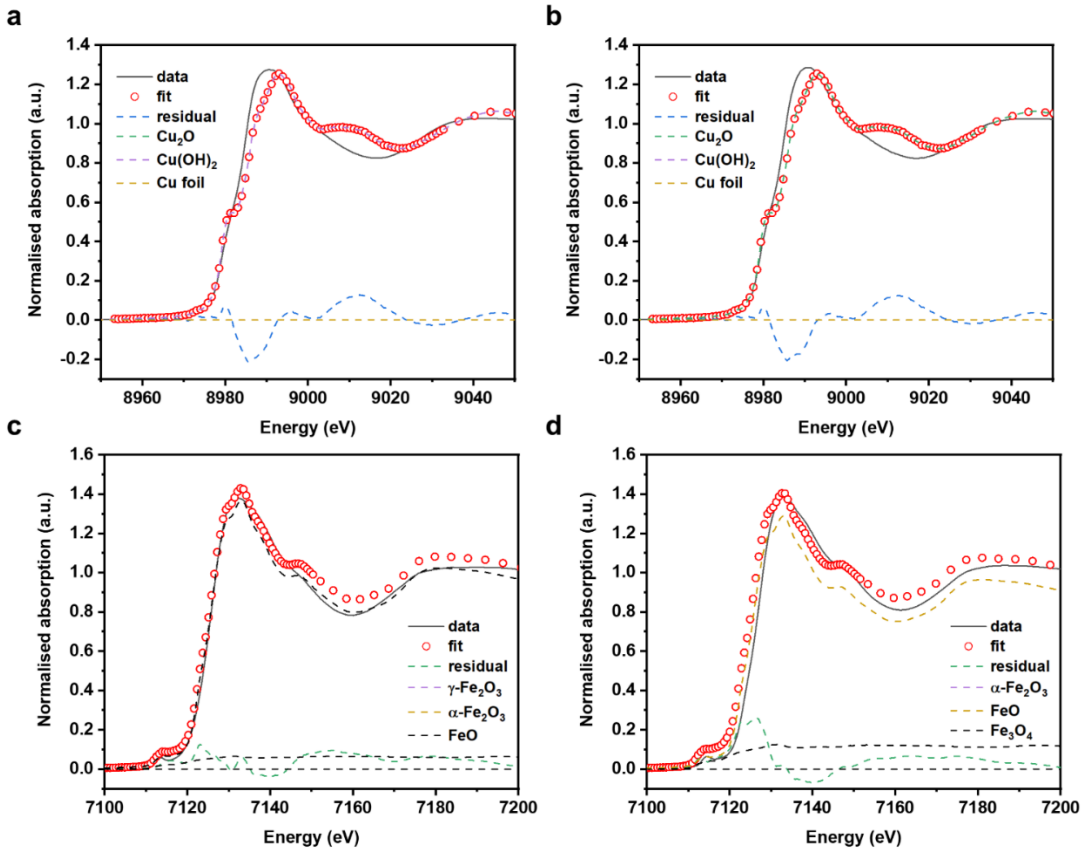

Figure 4.14. Quantitative fitting analysis of XANES measurements (**a**) **Cu_1-UiO**, (**b**) **Cu,Fe-UiO**, at the Cu K-edge, and (**c**) **Fe_1-UiO**, (**d**) **Cu,Fe-UiO**, at the Fe K-edge.

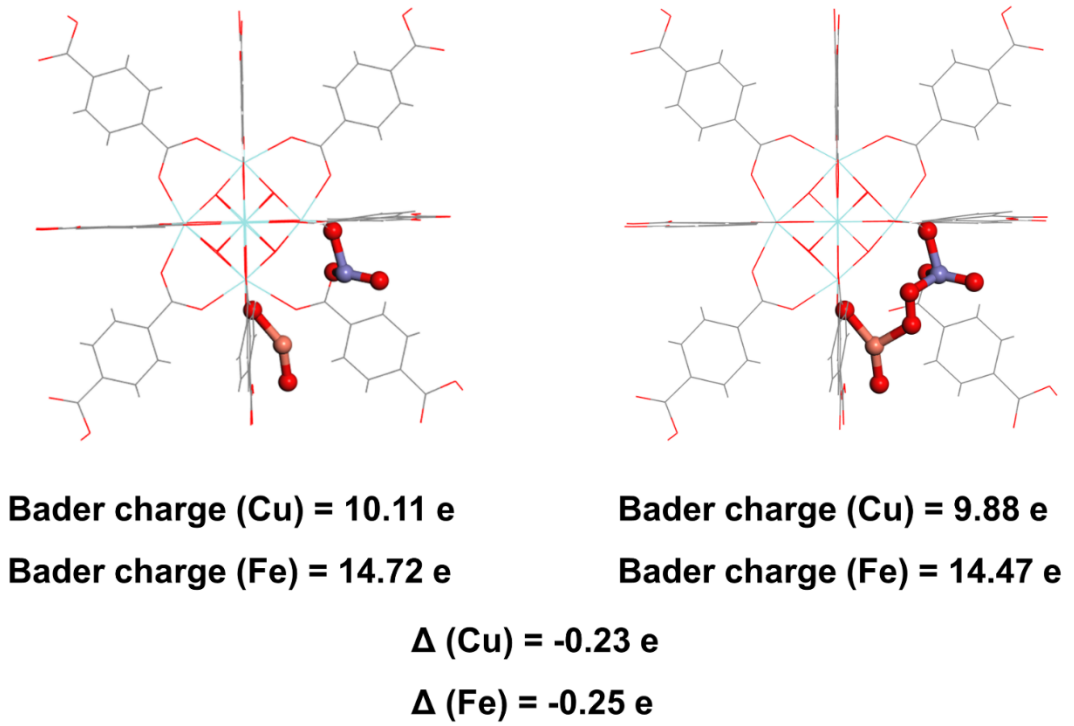

Figure 4.15. Bader charge analysis before and after O_2 attachment.

We further examined the structural properties of **Cu,Fe-UiO** by studying the coordination environments using extended X-ray absorption fine structure (EXAFS) spectroscopy. To better correlate the EXAFS peaks with k-space, wavelet transformation (WT) was employed (**Figure 4.13c–4.13d**). The highest intensity belongs to the lobe centered at k ~ 6.5 $Å^{-1}$, R ~ 1.5 Å, which corresponds to the O atoms around the Cu and Fe centers. Lobes with weaker intensity can also be observed at R > 2.0 Å, which can be attributed to the backscattering contribution of the long-range (second-shell) M_A–M_B interaction. From the quantitative analysis of the EXAFS results (**Figure 4.13e–4.13f** and **Table 4.5 and 4.6**), the Cu–O and Fe–O bond lengths are calculated as 1.95(1) and 1.95(1) Å, with the average coordination number (CN) of 3.6(1) and 4.6(1), respectively. The Cu···Fe backscattering contribution is calculated as 3.37(1) Å, with a CN of 1.0(1). The difference in the local environments and coordination environments between **Cu,Fe-UiO** and its single-atom analogous (Cu_1-UiO and Fe_1-UiO) is summarised in **Figures 4.16–4.17** and **Table S6**.

The high-resolution SXRD patterns of **Cu,Fe-UiO** are shown in **Figure 4.15g**. The positions of the Bragg peaks are only altered marginally compared to the parent UiO-66-NH_2, **Cu_1-UiO**, and **Fe_1-UiO**, with the space group remaining unchanged at *Fm-3m* (see **Figure 4.18**), suggesting that the extra-framework Cu and Fe species do not significantly alter the crystalline MOF framework. Highly symmetrical Bragg peaks are retained after metalation, suggesting a homogeneous metalation process. The crystallographic parameters are summarised in **Table 4.2**. In contrast, the variation in the Bragg peaks' intensities, particularly over the range of higher 2θ regime, is apparent, which can be attributed to the significant changes in the scattering factors that arose from the addition of heavier metal atoms. We subsequently employed Rietveld refinement to investigate the atomic parameters, including the fractional coordinates (*x*, *y*, *z*) of the extra-framework species with respect to the parent structure. High-quality of the Rietveld refinement can be confirmed by a small difference between the data and the fitting profile and a low R_{wp} value. The site occupancy factors of the Fe and Cu sites have been fixed based on elemental analysis to ensure the reliability of the Rietveld refinement.

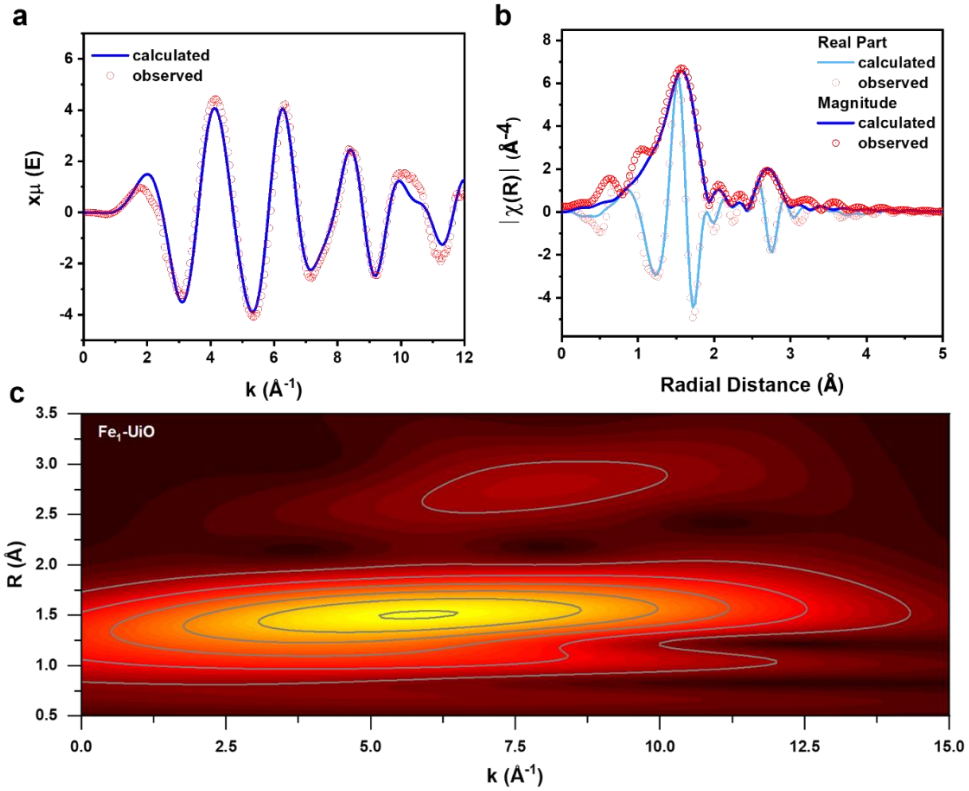

Figure 4.16. EXAFS data and fitting profiles of **Fe_1-UiO**, (**a**) k-space, (**b**) R-space, and (**c**) wavelet transformation.

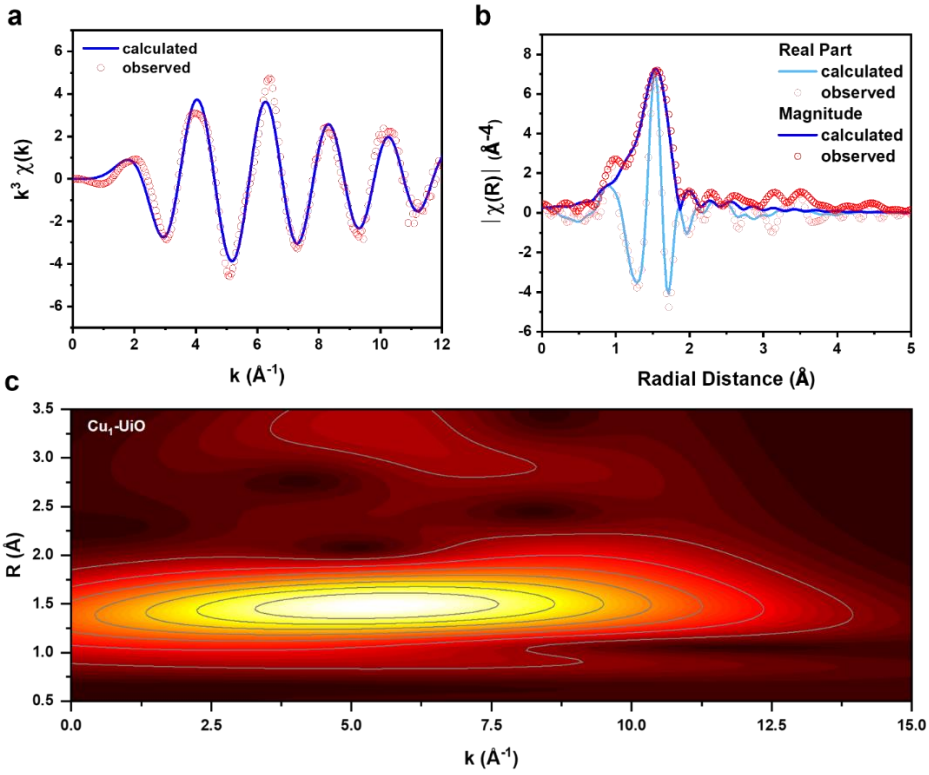

Figure 4.17. EXAFS data and fitting profiles of **Cu_1-UiO**, (**a**) k-space, (**b**) R-space, and (**c**) wavelet transformation.

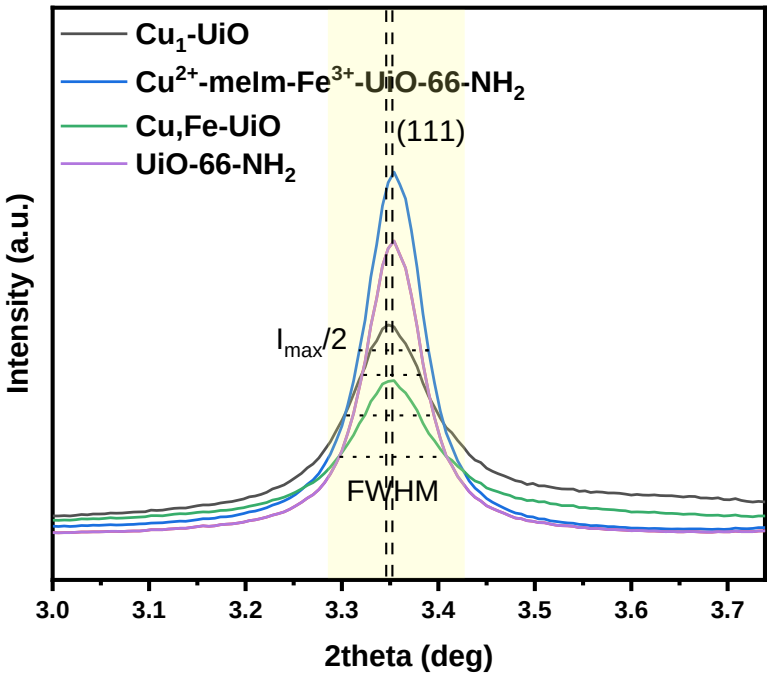

Figure 4.18. Comparison of the Bragg peak (111) of different samples from synchrotron PXRD measurements. Highly symmetrical peaks before and after metalation can be seen.

In the refined structure shown in **Figure 4.13h**, Cu_A and Fe_B are directly anchored on the Zr_6O_4 secondary building units, with derived bond lengths of 1.914(2) Å for Cu_A–O and 1.968(1) Å for Fe_B–O, which were restrained according to the EXAFS findings during the refinement process. The Cu···Fe interatomic distance was found at 3.348(2) Å, which is in close agreement with that derived in the EXAFS analysis (of 3.37(1) Å). A μ-η^1:η^2-O_2 bridge is found located between the Cu and Fe sites forming the Cu-(μ-η^1:η^2-O_2)-Fe, which verifies the spectroscopic findings as discussed above. We have also employed density functional theory (DFT) calculations for the optimization and verification of the atomic parameters and overall crystal structure (as later discussed). Non-framework oxygen atoms in the form of the terminal –OH_2 are present. Based on the optimized bond angles and distances, we found that both Cu_A and Fe_B sites in the refined crystal structures all adopt pseudo tetrahedral geometry, with a slight deviation from perfect tetrahedron. Interestingly, the Cu–(μ_2-O_2)–Fe moiety is highly analogous to the active site of C*c*O, as shown in **Figure 4.13i** [36].

The photocatalytic styrene oxidation was employed as a model reaction to investigate its catalytic characteristics. The photocatalytic styrene oxidation was performed using a LED lamp with a UV wavelength of 365 nm at the power of 10 W (see experimental details in SI†/methods). A typical photocatalytic

experiment uses 2.5 mg of catalysts dispersed in 0.5 mL styrene in 1.5 mL of 1,2-dichloromethane in air with UV illumination (λ = 365 nm). Interestingly, upon the illumination of **Cu,Fe-UiO**, the catalytic selectivity towards benzaldehyde reached >92% based on gas chromatography-mass spectrometry (GC-MS) analysis. Other common aromatic products, including benzoic acid, acetophenone, and phenylacetaldehyde, were detected at very low selectivity. In stark contrast, we noted nearly nil products from the catalysis over UiO-66-NH_2, **Cu_1-UiO**, and **Fe_1-UiO**. The detailed GC-MS spectra are summarised in **Figure 4.19**. The product selectivity towards benzaldehyde over **Cu,Fe-UiO** remains extremely high at >92% for five catalytic cycles (**Figure 4.20a**), with the yield decreased marginally possibly due to a small amount of sample being physically washed away from recycling. >92% selectivity towards benzaldehyde using air as the oxidant (instead of using peroxides) is superior to most reported catalysts (as summarised in **Table 4.8**, typically in the range of 60% to 80% because of highly competitive the epoxidation pathway). As seen in **Figure 4.20b**, the yield of benzaldehyde increased steadily over **Cu,Fe-UiO** at a rate of around 10 μmol mg_{cat}^{-1} h^{-1}, which contrasts with nearly nil product formation over the support UiO-66-NH_2 and its 'single-atom' **Cu_1-UiO** and **Fe_1-UiO** analogs. It should be noted that an extremely low yield of catalytic product over UiO-66-NH_2, **Cu_1-UiO** and **Fe_1-UiO** (< 0.5 μmol mg_{cat}^{-1} h^{-1}), was observed based on our GC-MS analysis. We have also explored the reaction conditions and found that air (O_2) and UV illumination are necessary for this reaction, as nil product was observed when the reaction vessel was degassed with N_2 or using light with longer wavelengths (**Figure 4.20c**). From the PXRD pattern collected three catalytic cycles (**Figure 4.20d**), the crystalline structure remained at *Fm-3m*.

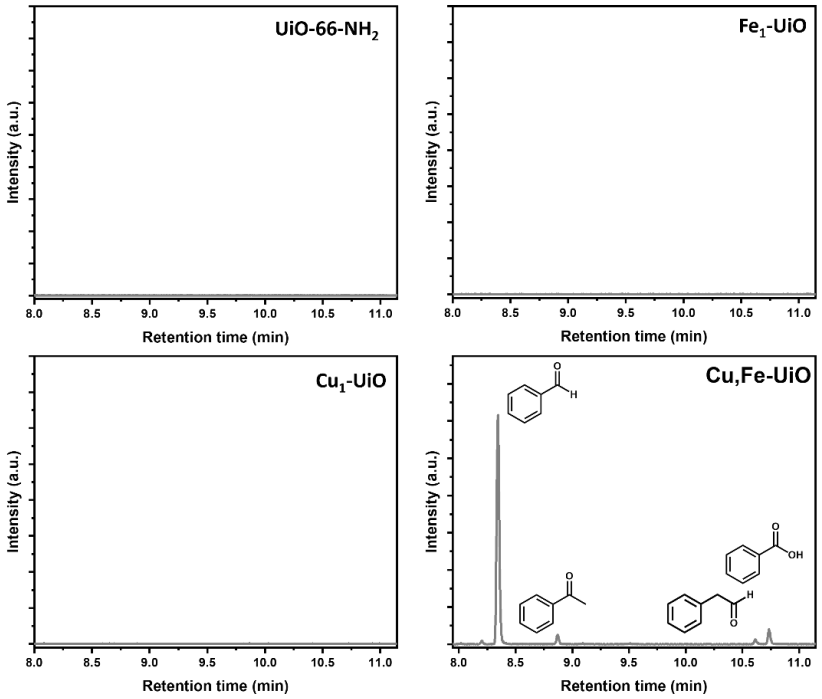

Figure 4.19. Product distribution from GC-MS of different catalysts. Nil converted aromatic products were observed over UiO-66-NH_2, **Cu_1-UiO** or **Fe_1-UiO**.

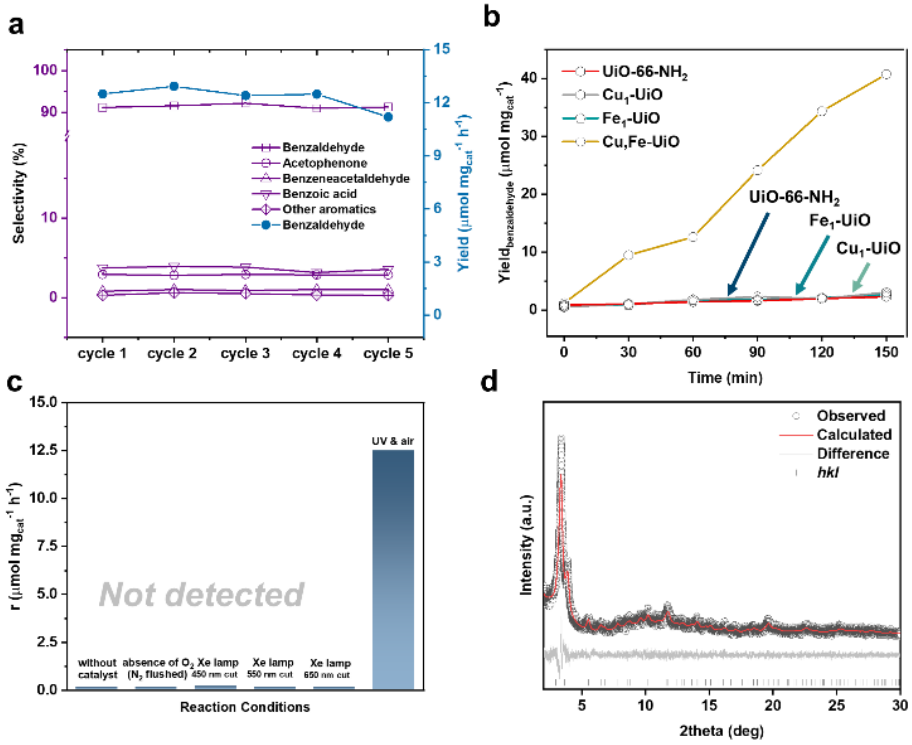

Figure 4.20. (**a**) Product distribution from the photocatalytic oxidation of styrene (λ = 365 nm) over **Cu,Fe-UiO**. (**b**) Time-resolved catalytic reactivity towards benzaldehyde over different catalysts. (**c**) Evaluation of different reaction conditions. (**d**) PXRD pattern of **Cu,Fe-UiO** collected after three photocatalytic cycles (Mo X-ray).

It is intriguing why **Cu,Fe-UiO** exhibits such high product selectivity, which is possibly related to the synergy between the Cu and Fe sites, as well as the unique Cu–(μ-η^1:η^2-O_2)–Fe bridging structure, that renders peroxide-like property. We first investigated the electronic properties by UV-vis spectroscopy (**Figure 4.21a**). The presence of Cu^{2+} (highlighted in blue) and Fe^{3+} species (in yellow) can also be seen in **Cu,Fe-UiO** as seen in their analogous single-atom counterparts. Weak absorption peaks related to the *d–d* transitions were observed primarily because of their coordination with framework O atoms (weak field). As shown in the corresponding Tauc plots (**Figure 4.21b**), the apparent bandgap of UiO-66-NH_2 was extrapolated at 2.83 eV. An insignificant difference in the apparent bandgaps of other samples has been extrapolated (between 2.74 eV and 2.79 eV), which suggests that the superior catalytic reactivity should originate from the local structures. It is consistent with our previous study on structurally related Cu_1-UiO and Cu_2-UiO where the remarkably different surface sensitivity and product selectivity (in photocatalytic formic acid reforming reaction) have been attributed to the difference in the adsorption configurations [27].

Electrochemical measurements were subsequently employed to study if synergy is present, as probed by the UV-vis results above, between the Cu^{2+} and Fe^{3+} sites. As seen in the cyclic voltammogram conducted in O_2-saturated 0.5 M H_2SO_4 (**Figure 4.21c**), much more electropositive curves of **Cu,Fe-UiO** than those of **Cu_1-UiO** and **Fe_1-UiO** (which can be reflected by the current density, 'j@0.85 V_{RHE}', in **Figure 4.21d**) can be seen. This suggests that its much superior ability in the activation of O_2 should be originated from the synergistic interactions between the Cu^{2+} and Fe^{3+} motifs. The onset potentials (E_0) and half-wave potentials ($E_{1/2}$) for **Cu,Fe-UiO** are notably different from **Cu_1-UiO** and **Fe_1-UiO**, which also infers the presence of Cu-Fe electronic interactions. As shown in **Figure 4.21d**, two reduction behaviors were observed in **Cu,Fe-UiO** with the first one possessing comparable properties with that of **Cu_1-UiO**. Another reduction peak was observed with an onset potential of 0.80 V_{RHE} and a peak potential of 0.85 V_{RHE}. This could be attributed to the electronic stabilization by the peroxy bridge between the Cu^{2+} and Fe^{3+}, which enhances the peak oxidation potential of Fe^{3+} from 0.75 V_{RHE} (**Fe_1-UiO**) to 0.85 V_{RHE} (**Cu,Fe-UiO**) [37]. In the absence of O_2, the oxidation peak disappeared, indicating that the peak is a result of O_2 activation but not directly from the catalyst. The presence of the Cu,Fe system promotes the activation of O_2 from the electrolyte, facilitating further styrene oxidation.

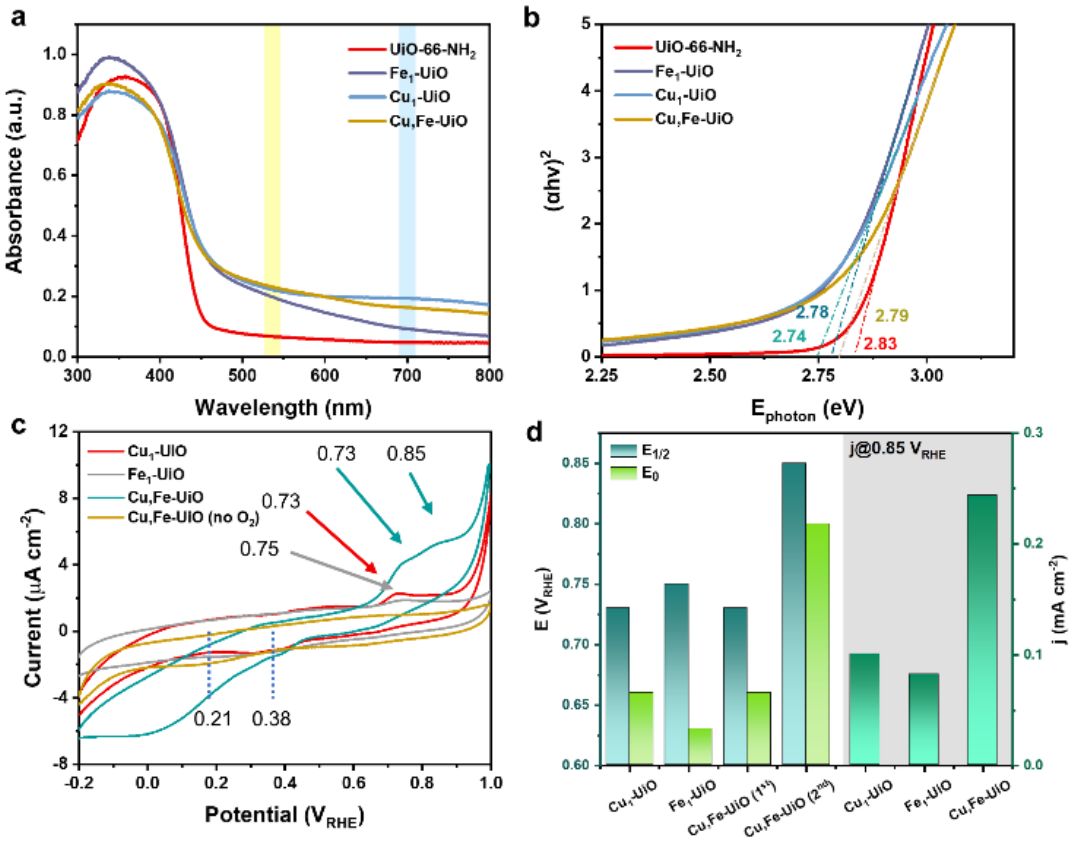

Figure 4.21. (**a**) UV-vis spectra of **Cu,Fe-UiO** and other samples, and (**b**) the corresponding Tauc plots for the extrapolation of the apparent bandgaps. (**c**) Cyclic voltammetric measurements, and (**d**) the corresponding onset potential (E_0), half-wave potential ($E_{1/2}$), and current density at 0.85 V_{RHE} on different samples in O_2-saturated 0.5 M H_2SO_4 solution with a scan rate of 100 mV s^{-1}.

Density functional theory calculations were subsequently employed to investigate the energetics of **Cu,Fe-UiO** which illustrates superior catalytic reactivity in styrene oxidation. We have investigated the strain on the UiO framework by anchoring the Cu–(μ_2-O_2)–Fe on the Zr_6O_4 secondary building units. A cluster model consisting of one Zr_6O_4 secondary building unit and six benzenedicarboxylate linker species constructed with Cu–(μ_2-O_2)–Fe was adopted from the above structure elucidation. As shown in **Figure 4.22a**, the structure was optimized by first fixing the linker species perpendicular to each other. We subsequently studied the effect on the structure (in the cluster model) by fully relaxing the framework (see **Figure 4.22b**). By fully relaxing the linker rotation, not only the μ-η^1:η^1-O_2 bridging group becomes μ-η^1:η^2-O_2 with η^2 on Fe, but we also observed a clear alternation in the inter-linker angles, which deviates from being perpendicular to each other. The transformation from μ-η^1:η^1-O_2 to μ-η^1:η^2-O_2 agrees with many conventional understandings on the

binding of O_2 in related Cu,Fe-containing species [22,38]. However, the rigid UiO framework with linker perpendicular to each other should limit the formation of μ-η^1:η^2-O_2 bridging at the ground state. The apparent strain in the ground state system, as revealed experimentally, may explain why **Cu,Fe-UiO** is particularly catalytically active for O_2 activation.

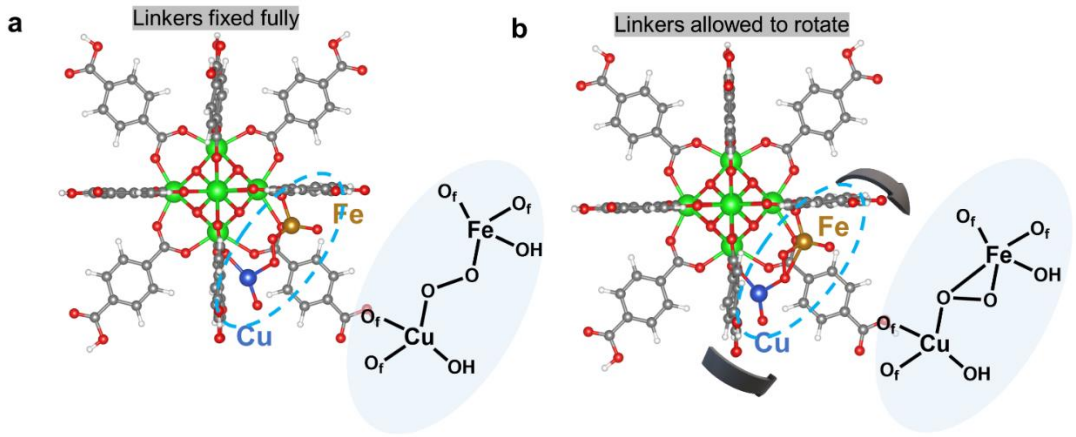

Figure 4.22. Optimisation of the structure of **Cu,Fe-UiO** by studying the effect of linker rotation.

In general, there are two proposed reaction pathways in the catalytic oxidation of styrene using peroxides or O_2 as the oxidant, namely, the epoxidation pathway, and the peroxy pathway. The epoxidation pathway typically yields a range of aromatic products, such as acetophenone, benzeneacetaldehyde, benzoic acid, and 1-phenylethane-1,2-diol, through rearrangement or further oxidation of styrene epoxide. The catalytic oxidation of styrene using peroxides, such as H_2O_2 and tert-butyl hydroperoxide as the oxidant can generally yield higher selectivity towards benzaldehyde (often reported >90%), which generally involves the peroxy pathway [39].

High product selectivity towards benzaldehyde can be achieved by the favourable formation of peroxy intermediates *via* the oxidative cleavage of the C=C bond ('2+2-like' mechanism) while limiting the direct epoxidation pathway [40]. Indeed, compared with peroxides, using O_2 (or even more preferably just air) as an oxidant is more desirable from cost consideration. However, the control of product selectivity is more difficult due to the difference in the transient structures, where epoxidation is also a dominant competing route. Attaining high product selectivity towards benzaldehyde using O_2 as the oxidant remains challenging as the formation of the epoxidation intermediate cannot be effectively circumvented. From the result of our photocatalytic reaction over **Cu,Fe-UiO**, we have only detected <10% non-benzaldehyde aromatic products (including benzoic acid, acetophenone, and benzeneacetaldehyde), which

indicates the preference for the direct formation of benzaldehyde over the epoxidation pathway.

The reaction steps of styrene oxidation over Cu,Fe-UiO are summarised in **Figure 4.23b**, with a styrene molecule first placed close to the peroxy group at the initial stage of the calculation (supported by our probe-assisted FTIR measurements in **Figure 4.24**). Upon UV illumination, the peroxy group undergoes homolytic cleavage to form two O radicals, which then attack the electron deficit C=C bond of styrene to form the intermediate species. This step shows a high resemblance to those of many peroxide oxidants, such as H_2O_2 and tert-butyl hydroperoxide [39]. The intermediate species will accordingly rearrange to yield the final benzaldehyde and formaldehyde products. With regard to the low production of styrene oxide (or other styrene oxide-derived products), the calculations have shown that the total energy of the epoxidation pathway (black line) is 1.8 eV higher than that of the peroxy pathway (red line). As presented in the proposed catalytic cycle (see **Figure 4.25**), the oxidation states of the Cu and Fe sites should reduce from +2 and +3 to +1 and +2 in the rearrangement step (Step (4) in **Figure 4.25**), respectively.

To complete the catalytic cycle, a final O_2 activation step (Step (5) in **Figure 4.25**) was included in the calculation at the end, with the reaction coordinates presented in **Figure 4.23c**. The O_2 molecule is reduced by then-vacant neighboring Cu^{I} and Fe^{II} motifs to re-create the initial Cu–(μ-η^1:η^2-O_2)–Fe structure. The facile activation of O_2 to render peroxy property is particularly noteworthy which can be attributed to the well-balanced electronic and steric properties within the MOF support with the Cu and Fe sites located at *ca*. 3.35 Å apart. A hypothetical analogous **Cu,Cu-UiO** has been modeled for a comparative study. The change in the total energy in the O_2 activation process in **Cu,Fe-UiO** was calculated as –3.17 eV, which is noticeably more negative than that in **Cu,Cu-UiO** (*cf.* change of energy of –2.54 eV). In addition, the binding energy of O_2 between Cu and Fe is also much stronger than that between two Cu sites (*cf.* $E_{binding}$ (O_2) of –3.64 eV versus –2.05 eV). Much more favorable energetics in the activation of O_2 has been noted in **Cu,Fe-UiO** when compared with the hypothetical **Cu,Cu-UiO**. As shown in the Bader charge analysis in **Figure 4.14**, the Bader charges of Cu and Fe decrease by 0.23 e and 0.25 e, respectively, suggesting the simultaneous oxidation of Cu^{I} and Fe^{II} to Cu^{II} and Fe^{III} during the O_2 activation process. Interestingly, this is highly analogous to the catalytic cycle of the structurally related C*c*O that involves an O_2 activation step, where the Cu and Fe sites undergo a similar redox cycle. In brief, the interplay between pathway selection and theoretical product distribution of styrene oxidation over

Cu,Fe-UiO has been presented in **Figure 4.23d** to offer a more comprehensive understanding of the structure-reactivity correlation.

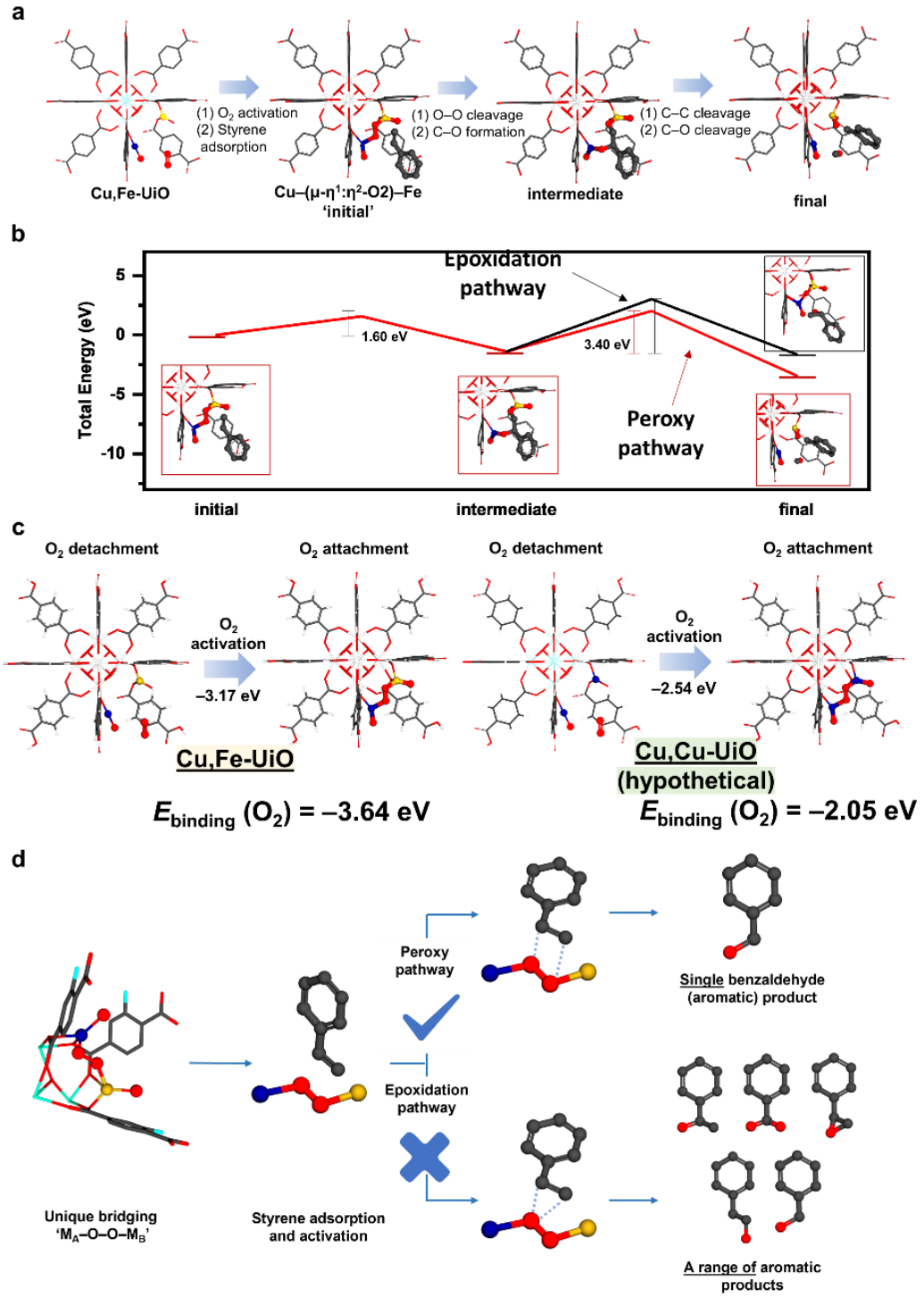

Figure 4.23. (a) The proposed reaction profile, showing the key reaction steps of styrene oxidation to benzaldehyde over Cu,Fe-UiO, and (b) the corresponding reaction coordinates. (c) Calculations on the energetics of O_2 activation in Cu,Fe-UiO and a hypothetical Cu,Cu-UiO. (d) The proposed reaction pathways of styrene oxidation over Cu,Fe-UiO, showing the interplay between pathway selection and theoretical product distribution. The same color scheme as adopted in Figure 2.

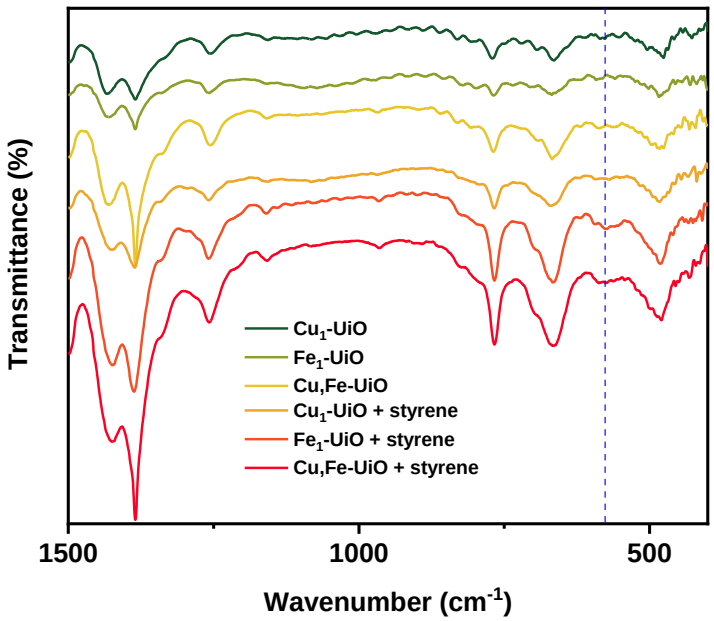

Figure 4.24. FTIR spectra of samples with and without styrene adsorption.

To investigate the preference in the reaction mechanism (epoxidation pathway versus peroxy pathway), we first employed probe-assisted FTIR to investigate the adsorption property of styrene of **Cu,Fe-UiO**. As seen in **Figure 4.24**, a band characteristic of Fe–O bond appeared upon the adsorption of styrene. The original FTIR-hidden Fe–O bond became visible, which suggests the interaction between styrene and **Cu,Fe-UiO**.

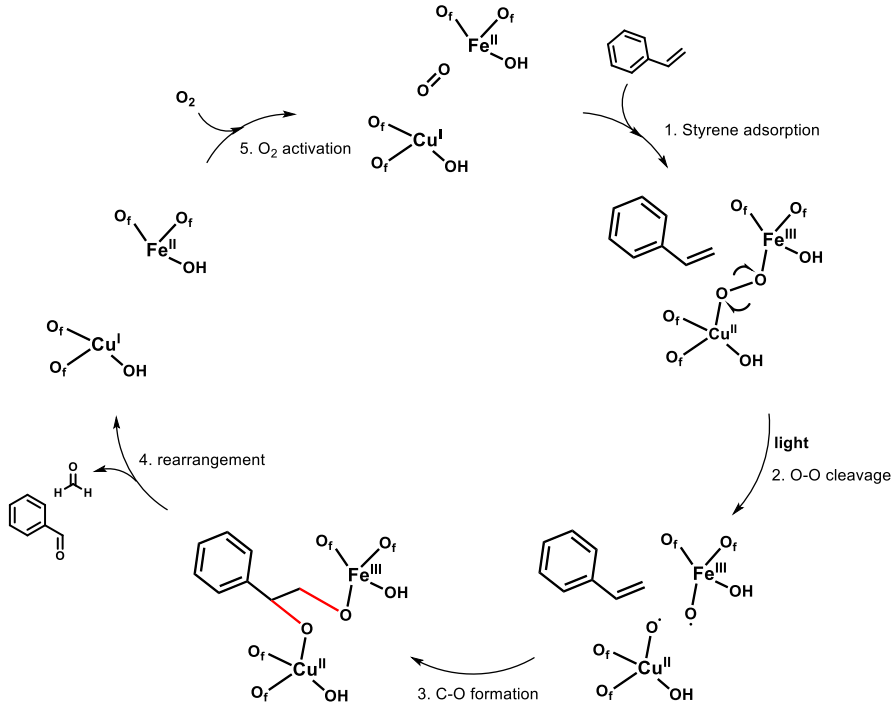

Figure 4.25. The proposed catalytic cycle of photocatalytic styrene oxidation over **Cu,Fe-UiO**.

4.4 Conclusion

To conclude, we have presented the precise engineering of supported bimetallic Cu,Fe dual-atom sites in the Zr_6O_4 secondary building units of UiO-66-NH_2. The atomic and crystallographic parameters have been determined by a multi-modal characterisation approach to ensure data reliability. As illustrated in the model photocatalytic styrene oxidation reaction, **Cu,Fe-UiO** allows an efficient activation of O_2 which facilitates the direct formation of benzaldehyde while circumventing the competing epoxidation reaction pathway. The ultra-high product selectivity towards benzaldehyde has been attributed to (i) the unique bridging O_2 group and (ii) the well-balanced synergy between the Cu^{II} and Fe^{III} sites located in close proximity (*ca*. 3.35 Å). Clearly, the manipulation of the electronic and geometric characteristics, as shown in **Cu,Fe-UiO**, has allowed a sophisticated control of catalytic reactivity and product selectivity. We warrant that the preparation and application of this class of DACs will become broadly studied and therefore deserve urgent attention.

4.5 Reference

(1) Xue, Q.; Wun, C. K. T.; Chen, T.; Kawaguchi, S.; Day, S.; Tang, C.; Wu, T. S.; Soo, Y. L.; Lin, C.; Peng, Y. K.; Yin, J.; Lo, T. W. B.Controlled Synthesis of Cu,Fe Dual-Atom Catalysts Restrained on Metal-Organic Frameworks for Efficient O2 Activation. *J. Mater. Chem. A* **2023**, *11* (26), 14204–14212. https://doi.org/10.1039/d3ta01675g.

(2) Yao, Y.; Hu, S.; Chen, W.; Huang, Z. Q.; Wei, W.; Yao, T.; Liu, R.; Zang, K.; Wang, X.; Wu, G.; Yuan, W.; Yuan, T.; Zhu, B.; Liu, W.; Li, Z.; He, D.; Xue, Z.; Wang, Y.; Zheng, X.; Dong, J.; Chang, C. R.; Chen, Y.; Hong, X.; Luo, J.; Wei, S.; Li, W. X.; Strasser, P.; Wu, Y.; Li, Y.Engineering the Electronic Structure of Single Atom Ru Sites via Compressive Strain Boosts Acidic Water Oxidation Electrocatalysis. *Nat. Catal.* **2019**, *2* (4), 304–313. https://doi.org/10.1038/s41929-019-0246-2.

(3) Zhao, J.; Ji, S.; Guo, C.; Li, H.; Dong, J.; Guo, P.; Wang, D.; Li, Y.; Toste, F. D.A Heterogeneous Iridium Single-Atom-Site Catalyst for Highly Regioselective Carbenoid O–H Bond Insertion. *Nat. Catal.* **2021**, *4* (6), 523–531. https://doi.org/10.1038/s41929-021-00637-7.

(4) Xue, Q.; Zhang, Z.; Ng, B. K. Y.; Zhao, P.; Lo, B. T. W.Recent Advances in the Engineering of Single-Atom Catalysts Through Metal–Organic Frameworks. *Top. Curr. Chem.* **2021**, *379* (2), 11. https://doi.org/10.1007/s41061-021-00324-y.

(5) Liu, L.; Arenal, R.; Meira, D. M.; Corma, A.Generation of Gold Nanoclusters Encapsulated in an MCM-22 Zeolite for the Aerobic Oxidation of Cyclohexane. *Chem. Commun.* **2019**, *55* (11), 1607–1610.

(6) Sun, Q.; Wang, N.; Bing, Q.; Si, R.; Liu, J.; Bai, R.; Zhang, P.; Jia, M.; Yu, J.Subnanometric Hybrid Pd-M(OH)2, M = Ni, Co, Clusters in Zeolites as Highly Efficient Nanocatalysts for Hydrogen Generation. *Chem* **2017**, *3* (3), 477–493. https://doi.org/10.1016/j.chempr.2017.07.001.

(7) Ding, K.; Cullen, D. A.; Zhang, L.; Cao, Z.; Roy, A. D.; Ivanov, I. N.; Cao, D.A General Synthesis Approach for Supported Bimetallic Nanoparticles via Surface Inorganometallic Chemistry. *Science (80-.).* **2018**, *362* (6414), 560–564.

(8) Saadun, A. J.; Kaiser, S. K.; Ruiz-Ferrando, A.; Pablo-García, S.; Büchele, S.; Fako, E.; López, N.; Pérez-Ramírez, J.Nuclearity and Host Effects of Carbon-Supported Platinum Catalysts for Dibromomethane Hydrodebromination. *Small* **2021**, *17* (16), 2005234. https://doi.org/10.1002/smll.202005234.

(9) Sommer, C.; Adamska-Venkatesh, A.; Pawlak, K.; Birrell, J. A.; Rüdiger, O.; Reijerse, E. J.; Lubitz, W.Proton Coupled Electronic Rearrangement within the H-Cluster as an Essential Step in the Catalytic Cycle of [FeFe] Hydrogenases. *J. Am. Chem. Soc.* **2017**, *139* (4), 1440–1443. https://doi.org/10.1021/jacs.6b12636.

(10) Sun, L.; Zhang, Q.; Li, G. G.; Villarreal, E.; Fu, X.; Wang, H.Multifaceted Gold-Palladium Bimetallic Nanorods and Their Geometric, Compositional, and Catalytic Tunabilities. *ACS Nano* **2017**, *11* (3), 3213–3228. https://doi.org/10.1021/acsnano.7b00264.

(11) Mu, Q.; Zhu, W.; Yan, G.; Lian, Y.; Yao, Y.; Li, Q.; Tian, Y.; Zhang, P.; Deng, Z.; Peng, Y.Activity and Selectivity Regulation through Varying the Size of Cobalt Active Sites in Photocatalytic CO2 Reduction. *J. Mater. Chem. A* **2018**, *6* (42), 21110–21119. https://doi.org/10.1039/c8ta06151c.

(12) Gong, L.; Zhang, D.; Shen, Y.; Wang, X.; Zhang, J.; Han, X.; Zhang, L.; Xia, Z.Enhancing Both Selectivity and Activity of CO2 Conversion by Breaking Scaling Relations with Bimetallic Active Sites Anchored in Covalent Organic Frameworks. *J. Catal.* **2020**, *390*, 126–134. https://doi.org/10.1016/j.jcat.2020.07.021.

(13) Lin, W. C.; Wu, S.; Li, G.; Ho, P. L.; Ye, Y.; Zhao, P.; Day, S.; Tang, C.; Chen, W.; Zheng, A.; Lo, B. T. W.; Edman Tsang, S. C.Cooperative Catalytically Active Sites for Methanol Activation by Single Metal Ion-Doped H-ZSM-5. *Chem. Sci.* **2021**, *12* (1), 210–219. https://doi.org/10.1039/d0sc04058d.

(14) Chen, T.; Xue, Q.; Leung, K. C.; Lo, B. T. W.Recent Advances of Precise Cu Nanoclusters in Microporous Materials. *Chem. - An Asian J.* **2020**, *15* (12), 1819–1828. https://doi.org/10.1002/asia.202000331.

(15) Feng, X.; Song, Y.; Chen, J. S.; Xu, Z.; Dunn, S. J.; Lin, W.Rational Construction of an Artificial Binuclear Copper Monooxygenase in a Metal-Organic Framework. *J. Am. Chem. Soc.* **2021**, *143* (2), 1107–1118. https://doi.org/10.1021/jacs.0c11920.

(16) Huang, Y. B.; Liang, J.; Wang, X. S.; Cao, R.Multifunctional Metal-Organic Framework Catalysts: Synergistic Catalysis and Tandem Reactions. *Chem. Soc. Rev.* **2017**, *46* (1), 126–157. https://doi.org/10.1039/c6cs00250a.

(17) Liu, L.; Corma, A.Confining Isolated Atoms and Clusters in Crystalline Porous Materials for Catalysis. *Nat. Rev. Mater.* **2021**, *6*, 244–263. https://doi.org/10.1038/s41578-020-00250-3.

(18) Dinh, K. T.; Sullivan, M. M.; Narsimhan, K.; Serna, P.; Meyer, R. J.; Dincă, M.; Román-Leshkov, Y.Continuous Partial Oxidation of Methane to Methanol Catalyzed by Diffusion-Paired Copper Dimers in Copper-Exchanged Zeolites. *J. Am. Chem. Soc.* **2019**, *141* (29), 11641–11650. https://doi.org/10.1021/jacs.9b04906.

(19) Grundner, S.; Markovits, M. A. C.; Li, G.; Tromp, M.; Pidko, E. A.; Hensen, E. J. M.; Jentys, A.; Sanchez-Sanchez, M.; Lercher, J. A.Single-Site Trinuclear Copper Oxygen Clusters in Mordenite for Selective Conversion of Methane to Methanol. *Nat. Commun.* **2015**, *6*, 7546-. https://doi.org/10.1038/ncomms8546.

(20) Smeets, P. J.; Groothaert, M. H.; Schoonheydt, R. A.Cu Based Zeolites: A UV-Vis Study of the Active Site in the Selective Methane Oxidation at Low Temperatures. *Catal. Today* **2005**, *110* (3–4), 303–309. https://doi.org/10.1016/j.cattod.2005.09.028.

(21) Lieberman, R. L.; Rosenzweig, A. C.Crystal Structure of a Membrane-Bound Metalloenzyme That Catalyses the Biological Oxidation of Methane. *Nature* **2005**, *434* (7030), 177–182. https://doi.org/10.1038/nature03311.

(22) Wikström, M.; Krab, K.; Sharma, V.Oxygen Activation and Energy Conservation by

Cytochrome c Oxidase. *Chem. Rev.* **2018**, *118* (5), 2469–2490.

(23) Xue, Q.; Xie, Y.; Wu, S.; Wu, T. S.; Soo, Y. L.; Day, S.; Tang, C. C.; Man, H. W.; Yuen, S. T.; Wong, K. Y.; Wang, Y.; Lo, B. T. W.; Tsang, S. C. E.A Rational Study on the Geometric and Electronic Properties of Single-Atom Catalysts for Enhanced Catalytic Performance. *Nanoscale* **2020**, *12* (45), 23206–23212. https://doi.org/10.1039/d0nr06006b.

(24) Wun, C. K. T.; Mok, H. K.; Chen, T.; Wu, T.-S.; Taniya, K.; Nakagawa, K.; Day, S.; Tang, C. C.; Huang, Z.; Su, H.; Yu, W.-Y.; Lee, T. K. W.; Lo, T. W. B.Atomically Dispersed 3d Metal Bimetallic Dual-Atom Catalysts and Classification of the Structural Descriptors. *Chem Catal.* **2022**, *2* (9), 2346–2363. https://doi.org/https://doi.org/10.1016/j.checat.2022.07.027.

(25) Chen, T.; Wang, Y.; Xue, Q.; Kit Tommy Wun, C.; Kin So, P.; Fu Yung, K.; Wu, T.-S.; Soo, Y.-L.; Taniya, K.; Day, S.; Tang, C. C.; Li, Z.; Huang, B.; Chi Edman Tsang, S.; Wong, K.; Woon Benedict Lo, T.Atomically Precise Bimetallic Metal Ensembles with Tailorable Synergistic Effects. *Cell Reports Phys. Sci.* **2022**, *4*, 100850.

(26) Xue, Q.; Chan, K. H.; Yim, C. K.; Kit, B.; Ng, Y.; Chen, T.; Day, S. J.; Tang, C.; Kawaguchi, S.; Wong, K.; Woon, T.; Lo, B.Guest-Anion-Induced Rotation-Restricted Emission in UiO-66-NH 2 and Advanced Structure Elucidation. *Chem. Mater.* **2021**, *33*, *13*, *54* (13), 5422–5429. https://doi.org/10.1021/acs.chemmater.1c01674.

(27) Xue, Q.; Ng, B. K. Y.; Man, H. W.; Wu, T. S.; Soo, Y. L.; Li, M. M.; Kawaguchi, S.; Wong, K. Y.; Tsang, S. C. E.; Huang, B.; Lo, T. W. B.Controlled Synthesis of Bi- And Tri-Nuclear Cu-Oxo Nanoclusters on Metal-Organic Frameworks and the Structure-Reactivity Correlations. *Chem. Sci.* **2022**, *13* (1), 50–58. https://doi.org/10.1039/d1sc05495c.

(28) Xue, Q.; Ng, B. K. Y.; Man, H. W.; Wu, T. S.; Soo, Y. L.; Li, M. M.; Kawaguchi, S.; Wong, K. Y.; Tsang, S. C. E.; Huang, B.; Lo, T. W. B.Controlled Synthesis of Bi- And Tri-Nuclear Cu-Oxo Nanoclusters on Metal-Organic Frameworks and the Structure-Reactivity Correlations. *Chem. Sci.* **2022**, *13* (1), 50–58. https://doi.org/10.1039/d1sc05495c.

(29) Yang, J.; Dai, Y.; Zhu, X.; Wang, Z.; Li, Y.; Zhuang, Q.; Shi, J.; Gu, J.Metal–Organic Frameworks with Inherent Recognition Sites for Selective Phosphate Sensing through Their Coordination-Induced Fluorescence Enhancement Effect. *J. Mater. Chem. A* **2015**, *3* (14), 7445–7452.

(30) Fox, S.; Nanthakumar, A.; Wikström, M.; Karlin, K. D.; Blackburn, N. J.XAS Structural Comparisons of Reversibly Interconvertible Oxo-and Hydroxo-Bridged Heme-Copper Oxidase Model Compounds. *J. Am. Chem. Soc.* **1996**, *118* (1), 24–34.

(31) Yang, X.; Jiang, X.; Huang, Y.; Guo, Z.; Shao, L.Building Nanoporous Metal-Organic Frameworks “Armor” on Fibers for High-Performance Composite Materials. *ACS Appl. Mater. Interfaces* **2017**, *9* (6), 5590–5599. https://doi.org/10.1021/acsami.6b15098.

(32) Wang, G.; He, C. T.; Huang, R.; Mao, J.; Wang, D.; Li, Y.Photoinduction of Cu Single Atoms Decorated on UiO-66-NH_2 for Enhanced Photocatalytic Reduction of CO2 to Liquid Fuels. *J. Am. Chem. Soc.* **2020**, *142* (45), 19339–19345. https://doi.org/10.1021/jacs.0c09599.

(33) Fang, J.; Xuan, Y.Investigation of Optical Absorption and Photothermal Conversion Characteristics of Binary CuO/ZnO Nanofluids. *RSC Adv.* **2017**, *7* (88), 56023–56033.

(34) Nakashima, S.; Ogura, T.; Kitagawa, T.Infrared and Raman Spectroscopic Investigation of the Reaction Mechanism of Cytochrome c Oxidase. *Biochim. Biophys. Acta (BBA)-Bioenergetics* **2015**, *1847* (1), 86–97.

(35) Das, T. K.; Couture, M.; Ouellet, Y.; Guertin, M.; Rousseau, D. L.Simultaneous Observation of the O—O and Fe—O2 Stretching Modes in Oxyhemoglobins. *Proc. Natl. Acad. Sci.* **2001**, *98* (2), 479–484.

(36) Zong, S.; Wu, M.; Gu, J.; Liu, T.; Guo, R.; Yang, M.Structure of the Intact 14-Subunit Human Cytochrome c Oxidase. *Cell Res.* **2018**, *28* (10), 1026–1034.

(37) Du, C.; Gao, Y.; Chen, H.; Li, P.; Zhu, S.; Wang, J.; He, Q.; Chen, W.A Cu and Fe Dual-Atom Nanozyme Mimicking Cytochrome c Oxidase to Boost the Oxygen Reduction Reaction. *J. Mater. Chem. A* **2020**, *8* (33), 16994–17001. https://doi.org/10.1039/d0ta06485h.

(38) Meunier, B.; DeVisser, S. P.; Shaik, S.Mechanism of Oxidation Reactions Catalyzed by Cytochrome P450 Enzymes. *Chem. Rev.* **2004**, *104* (9), 3947–3980.

(39) Andrade, M. A.; Martins, L. M. D. R. S.Selective Styrene Oxidation to Benzaldehyde over Recently Developed Heterogeneous Catalysts. *Molecules* **2021**, *26* (6), 1680. https://doi.org/10.3390/molecules26061680.

(40) Bansal, V. K.; Thankachan, P. P.; Prasad, R.Oxidation of Benzyl Alcohol and Styrene Using H2O2 Catalyzed by Tetraazamacrocycle Complexes of Cu (II) and Ni (II) Encapsulated in Zeolite-Y. *Appl. Catal. A Gen.* **2010**, *381* (1–2), 8–17.

4.6 Supplementary information for Chapter 4

T**able 4.1.** The elemental analysis, showing the Zr: metal atomic ratio, of **Cu_1-UiO**, **Fe_1-UiO**, and **Cu,Fe-UiO** by SEM/EDX.

	Zr	**Cu**	**Fe**
Cu_1-UiO	1	0.091	-
Fe_1-UiO	1	-	0.039
Cu,Fe-UiO	1	0.069	0.074

Table 4.2. Crystallographic parameters derived from the synchrotron PXRD measurements of samples as labelled.

	UiO-66-NH_2	Cu^{2+}-meIm-Fe^{3+}-UiO-66-NH_2	**Cu,Fe-UiO**	**Cu,Fe-UiO (post-mortem)**
Diffractometer	MYTHEN	MYTHEN	MYTHEN	Dectris 1D area detector
X-ray source	SPring-8 BL02B2	SPring-8 BL02B2	SPring-8 BL02B2	Rigaku SmartLab SE
Wavelength (Å)	0.688213(2) (Synchrotron)	0.700261(2) (Synchrotron)	0.700261(2) (Synchrotron)	0.71073 (Mo X-ray)
2θ - zero point (°)	-0.000106(2)	0.00037	0.00037	0.0009(1)
Space group	*Fm-3m*	*Fm-3m*	*Fm-3m*	*Fm-3m*
Crystal system	Cubic	Cubic	Cubic	Cubic
a (Å)	20.78902(46)	20.7559(30)	20.75787(29)	20.7341(30)
V (Å^3)	8984.66(59)	8766.4(17)	8944.3(4)	8913.7(1)
2θ range for refinement (°)	2-30	2-30	2-30	2-30
Refinement methods	Rietveld	Rietveld	Rietveld	Rietveld
$R_{wp}/R_{exp}/R_p$ (%)	2.258/0.777/1.553	5.672/0.618/4.28	5.840/0.674/4.192	10.928/8.620/8.578
gof	2.905	9.171	8.668	1.267

R_{wp}: weighted profile; R_{exp}: expected; R_p: profile; *gof:* goodness-of-fit. The wavelengths and zero-point errors were calibrated by NIST CeO_2 standard.

Table 4.3. Crystallographic parameters derived from the *in-situ* synchrotron PXRD measurements at elevated temperatures of Cu^{2+}-meIm-Fe^{3+}-UiO-66-NH_2.

Temperature (°C)	**R_{wp} (%)**	**R_{exp} (%)**	**R_p (%)**	**Lattice parameter (Å)**
25	4.61	0.638	3.13	20.7559(30)
50	4.31	0.639	3.06	20.751(29)
75	5.45	0.629	3.81	20.725(38)
100	4.38	0.636	3.14	20.728(30)
125	5.30	0.617	3.78	20.692(28)
150	5.43	0.617	4.02	20.659(20)
175	5.67	0.618	4.28	20.619(14)
200	5.55	0.618	4.21	20.554(22)
225	5.91	0.617	4.52	20.497(30)
250	7.95	0.617	5.66	20.49(5)
275	8.38	0.616	5.23	20.53(5)
300	7.10	0.617	4.34	20.50(5)
325	2.77	0.619	2.04	20.24(5)
350	1.92	0.620	1.44	20.13(9)

R_{wp}: weighted profile; R_{exp}: expected; R_p: profile.

Table 4.4(a). Quantitative fitting of the XANES measurements of sample **Cu_1-UiO** and **Cu,Fe-UiO** at the Cu K-edge.

Reference	**Cu_1-UiO**	**Cu,Fe-UiO**
$Cu(OH)_2$	1.00	1.00
Cu_2O	0	0
Cu foil	0	0

Table 4.4(b). Quantitative fitting of the XANES measurements of sample **Fe_1-UiO** and **Cu,Fe-UiO** at the Fe K-edge.

Reference	**Fe_1-UiO**	**Cu,Fe-UiO**
a-Fe_2O_3	0.99	0.88
FeO	0	0
Fe_3O_4	0	0
Fe foil	0.01	0.12

Table 4.5(a). Quantitative analysis of the EXAFS results of **Cu,Fe-UiO** at Cu K-edge.

Paths	**CN**	**R (Å)**	**σ^2 (Å^2)**	**E_{not} (eV)**
Cu-O	3.6(1)	1.95(1)	0.005	-4.1(9)
Cu-Fe	1.0(3)	3.37(1)	0.010	-4.1(9)
Cu-O (2^{nd} shell)	3.2(7)	3.68(1)	0.010	-4.1(9)

Table 4.5(b). Quantitative analysis of the EXAFS results of **Cu,Fe-UiO** at Fe K-edge.

Paths	**CN**	**R (Å)**	**σ^2 (Å^2)**	**E_{not} (eV)**
Fe-O	4.6(1)	1.95(1)	0.005	-5.0(4)
Fe-Cu	1.3(3)	3.37(1)	0.010	-5.0(4)
Fe-Fe	0.8(2)	3.04(1)	0.005	-5.0(4)
Fe-O (2^{nd} shell)	5.2(17)	3.68(1)	0.010	-5.0(4)

Table 4.6(a). Quantitative analysis of the EXAFS results of **Cu_1-UiO** at Cu K-edge.

Paths	**CN**	**R(Å)**	**σ^2(Å^2)**	**E_{not} (eV)**
Cu-O	3.6(1)	1.95(1)	0.005	-4.2(9)

Table 4.6(b). Quantitative analysis of the EXAFS results of **Fe_1-UiO** at Fe K-edge.

Paths	**CN**	**R(Å)**	**σ^2(Å^2)**	**E_{not} (eV)**
Fe-O	3.8(1)	1.99(1)	0.007	-2.1(6)
Fe-Fe	0.4(1)	3.05(1)	0.003	-2.1(6)

Table 4.7. Atomic parameters derived from the Rietveld refinement of the synchrotron PXRD measurement of **Cu,Fe-UiO**, measured at 25 °C.

Species	Atom	x	y	z	SOF	B_{eq} (Å^2)	Wyckoff letter
MOF-host	Zr1	0.12145	0	0	1	0.6	d
	O2	0.06566	0.06566	0.06566	1	2	f
	C1	0.15679	0	0.15679	1	4	h
	C2	0.20875	0	0.20875	1	4	h
	C3	0.27255	0	0.27255	1	4	j
	O1	0.17288	0	0.09674	1	4	j
	N1	0.28946	0	0.12818	0.25	4	j
Extra-framework site	Cu1	0.0910	0.0910	0.2048	0.069[#]	5	l
	Fe2	0.0915	0.2048	0.0915	0.074[#]	5	l
	OCu1	0.1051	0.2952	0.1273	0.069[#]	5	l
	OFe2	0.1598	0.0909	0.2820	0.074[#]	5	l
	OB3	0.1341	0.1836	0.1695	0.070	5	l
	OB4	0.1950	0.8910	0.4220	0.070	5	l
Physisorbed water (dummy)	OH1	0.0922	0.0030	0.2714	0.33212	10	l
	OH2	0.0205	-0.0149	0.1217	0.40349	10	l
	OH3	0.0899	-0.0487	0.2752	0.1157	10	l

#: site occupancy factor fixed based on elemental analysis in **Table S1**.

Table 4.8. The catalytic performance of a series of related and recently reported heterogeneous catalysts.

Catalyst	Oxidative reagent	Conditions	Selectivity of benzaldehyde (%)	Reference
MOF-74(Co)	O_2	80 °C	47	[1]
MOF-74(Cu-90/Co-10)	O_2	80 °C	75	[1]
MOF-74(Cu-75/Co-25)	O_2	80 °C	50	[1]
MOF-74(Cu-30/Co-70)	O_2	80 °C	43	[1]
Pd-Y-bpydc$_{0.8}$/bpdc$_{0.2}$	O_2	80 °C	82	[2]
Pd-Y-bpydc$_{0.5}$/bpdc$_{0.5}$	O_2	80 °C	86	[2]
Pd-Y-bpydc$_{0.2}$/bpdc$_{0.8}$	O_2	80 °C	90	[2]
PW10	$^1O_2$	365 nm at 10 °C	80	[3]
Mn-MIL-100	TBHP	70 °C	82	[4]
Fe-MIL-100	TBHP	70 °C	76	[4]
Fe-MIL-101	TBHP	70 °C	68	[4]
Cr-MIL-101	TBHP	70 °C	91	[4]
Co-MCM-41	H_2O_2	60 °C	44	[5]
Ag-MCM-41	H_2O_2	60 °C	38	[5]
Ag-Co-MCM-41	H_2O_2	60 °C	53	[5]
UiO-66-NH_2@MIL-101(Fe)heterostructures	O_2	> 420 nm	~ 90	[6]
V-Y	TBHP	80 °C	46	[7]
Mn-Y	TBHP	80 °C	42	[7]
Fe-Y	TBHP	80 °C	49	[7]
Co-Y	TBHP	80 °C	47	[7]
Ni-Y	TBHP	80 °C	51	[7]
Cu-Y	TBHP	80 °C	57	[7]

Y-bpdc: hexanuclear yttrium clusters MOFs
PW10: pyrene-alt-dibenzothiophene-S,S-dioxide (P16PySO)/tungsten trioxide composite
Y: Y-zeolite

Reference

(1) Fu, Y.; Xu, L.; Shen, H.; Yang, H.; Zhang, F.; Zhu, W.; Fan, M.Tunable Catalytic Properties of Multi-Metal–Organic Frameworks for Aerobic Styrene Oxidation. *Chem. Eng. J.* **2016**, *299*, 135–141.

(2) Zhang, Y.; Wei, N.; Xing, Z.; Han, Z.-B.Functional Hexanuclear Y (III) Cluster-Based MOFs Supported Pd (II) Single Site Catalysts for Aerobic Selective Oxidation of Styrene. *Appl. Catal. A Gen.* **2020**, *602*, 117668.

(3) Cheng, C.; Zhu, B.; Cheng, B.; Macyk, W.; Wang, L.; Yu, J.Catalytic Conversion of Styrene to Benzaldehyde over S-Scheme Photocatalysts by Singlet Oxygen. *ACS Catal.* **2022**, *13*, 459–468.

(4) Ha, Y.; Mu, M.; Liu, Q.; Ji, N.; Song, C.; Ma, D.Mn-MIL-100 Heterogeneous Catalyst for the Selective Oxidative Cleavage of Alkenes to Aldehydes. *Catal. Commun.* **2018**, *103*, 51–55.

(5) Jiang, T.; Gao, G.; Yang, C.; Mao, Y.; Fang, M.; Zhao, Q.Catalytic Activity of Ag-Co-MCM-41 for Liquid-Phase Selective Oxidation of Styrene to Benzaldehyde. *J. Nanosci. Nanotechnol.* **2020**, *20* (3), 1670–1677.

(6) Liu, L.; Zhang, L.; Wang, F.; Qi, K.; Zhang, H.; Cui, X.; Zheng, W.Bi-Metal–Organic Frameworks Type II Heterostructures for Enhanced Photocatalytic Styrene Oxidation. *Nanoscale* **2019**, *11* (16), 7554–7559.

(7) Desai, N. C.; Chudasama, J. A.; Karkar, T. J.; Patel, B. Y.; Jadeja, K. A.; Godhani, D. R.; Mehta, J. P.Studies of Styrene Oxidation by Catalyst Based on Zeolite-Y Nanohybrid Materials. *J. Mol. Catal. A Chem.* **2016**, *424*, 203–219.

Chapter 5 Investigating Synergistic Cooperativity of Metal-Brønsted Acid Site Pair in MFI-type Zeolites by Synchrotron X-ray Powder Diffraction

Highlight of this chapter

Atomistic engineering of active sites with multiple functional motifs has gained significant attention in heterogeneous catalytic science due to their potential synergistic cooperativity. While these catalysts have demonstrated superior performance in various applications, a lack of systematic study hampers the understanding of intricate synergism. In this study, we present a comprehensive investigation into the synergistic cooperativity between a combination of metal sites (M = Fe^{3+} and Cu^{2+}) and dominant Brønsted acid sites (BASs, X = B, Ga, and Al) in ***MFI***-type zeolites with delicate control over their quantities and respective distribution. By employing two model catalytic reactions that simultaneously utilize the two active motifs in proximity, we examined the cooperativity required to modulate catalytic reactivity. Combined synchrotron X-ray powder diffraction and theoretical evidence revealed the synergism and the respective contribution of the active pairs of metal-BAS within molecular distances. Most of the content in this chapter has been published recently in the Journal of Materials Chemistry A [1].

5.1 Introduction

Understanding the interplay between proximate catalytically active motifs in heterogeneous catalysts has been a long-standing challenge for designing more active and selective catalysts [2,3]. Inspired by biological enzymes, the synergistic cooperation between neighboring active motifs in proximity is key for effective catalysis. While the variety of metal atoms within the active sites is not the only parameter to depict the catalytic landscape, the protein scaffolds also clearly illustrate the importance of a confined environment with suitable configurations to promote adsorption and stabilize specific transition states and reaction intermediates [4]. Such control is often observed *via* ligand control in natural enzymes and homogeneous catalytic systems. Specifically, the active motifs within molecular distance have usually been shown to work synergistically to offer unique catalytic reactivities [5]. The synergistic interaction is especially crucial in reactions involving tandem or cascade reaction steps, where distinct active motifs respectively provide different functionalities, and allow the co-activation of the same reaction substrate [5–8]. To systemically investigate and comprehend the correlation between synergistic interactions and catalytic reactivity, precise engineering of analogous synergistic cooperation in solid-state materials is essential, such an approach benefits both homogeneous catalysts, known for its high selectivity and heterogeneous catalysts for the ease of separating and recovering products and catalysts for process intensification [9,10].

Porous materials, such as zeolites, metal-organic frameworks, covalent-organic frameworks, and porous carbon materials, are increasingly recognized as ideal domain matrices for the immobilization of foreign molecular metal species [11–14]. Their unique porous frameworks serve as a scaffold for (i) uniformly dispersing metal sites to maximize the most atom-economical utility, (ii) tuning hydrophilic and hydrophobic pore nature for reactant/product recognition, and more importantly, (iii) creating a collaborative microenvironment to enable synergistic catalysis [15]. Within the specific microenvironment, the interactions between proximate motifs, the inherent functionality (such as zeolitic Brønsted acid sites (BASs)), and metal sites can offer unique synergistic catalytic properties and facilitate tandem reactions [16]. The synergistic effects among proximate active motifs can lead to enhanced reaction yield or yield transformations unachievable with conventional bulk or “single-atom” analogs, as shown in many *state-of-the-art* systems [17–20].

The product selectivity can be notably tuned by the properties of the microenvironments and reaction mechanisms. The rational design of the constituent components in the microenvironments within the confined porous

framework is an effective handle for controlling the catalytic landscape as illustrated in Scheme 1. Recently, high-resolution synchrotron X-ray powder diffraction (PXRD) in combination with Rietveld refinement has been shown to be a powerful technique in elucidating how reaction substrates are activated cooperatively by neighboring active motifs in terms of bond distances and angles [21]. For example, we revealed how small molecules such as water and methanol are cleaved heterolytically by neighboring metal-BAS pairs in metal-doped ZSM-5 zeolite [22]. The metal-BAS pair features frustrated Lewis pair property which leads to high product selectivity for subsequent reactions. Nevertheless, less progress has been made to systematically study the combined effects over such solid-state host domain matrices due to synthetic limitations and material characterization challenges.

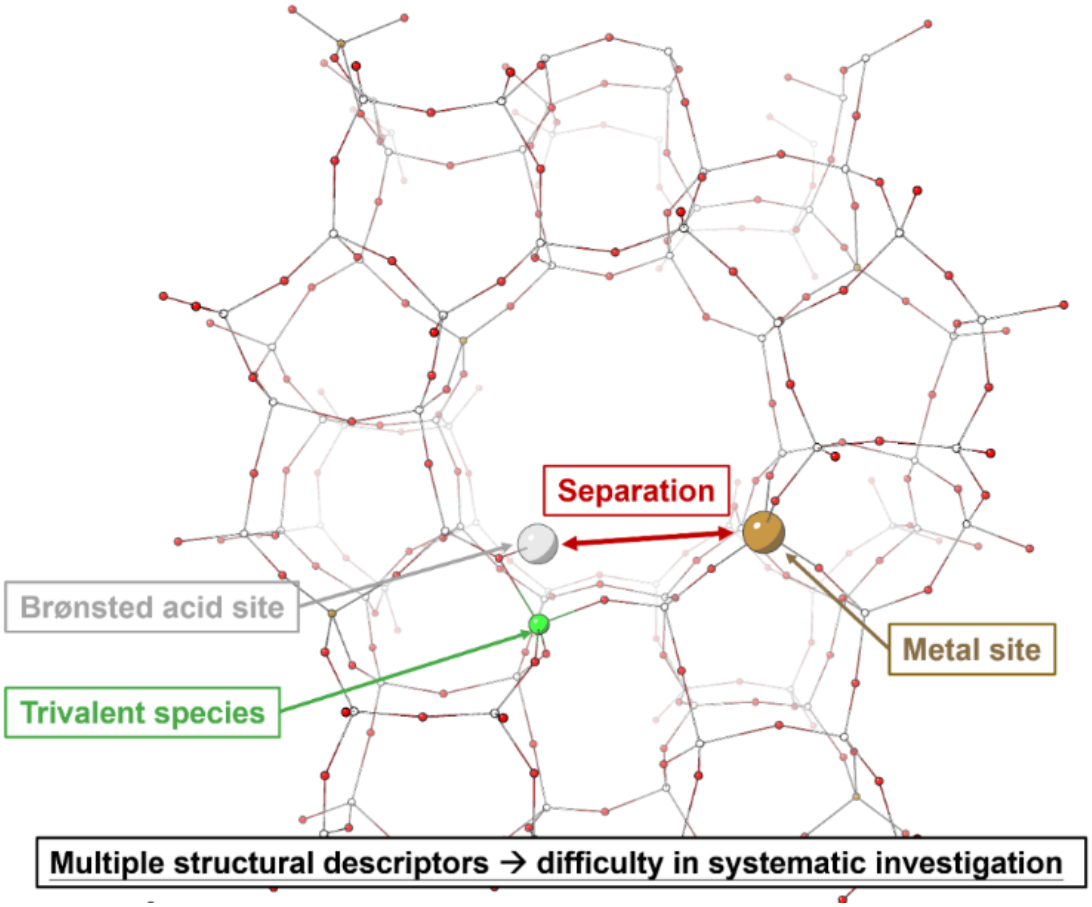

Scheme 5.1. Schematic illustration showing some key structural descriptors in the zeolitic system involving varying framework metal species and Brønsted acidities.

Here, we report a systematic investigation of the interplay between the dominant zeolitic BASs with different acid strengths (BASs, X = B, Ga, and Al) and two framework metal sites (M = Fe and Cu) in ZSM-5 zeolites while maintaining their separation and distribution controlled. By extensively investigating the chemical and structural properties, samples with comparable metal content and metal-BAS separation have been prepared and well-characterized. We have employed the oxidation of 4-chlorostyrene and the decarboxylation of gamma-valerolactone (GVL) as the model reactions to map the corresponding structure-reactivity correlations. Using the Rietveld refinement of high-resolution synchrotron PXRD data, we have revealed the adsorbate structures of the reaction substrates with respect to the metal-BAS pair at an atomistic level. Combined catalytic and diffraction findings suggest that modulating the Brønsted acidity can notably improve substrate conversion with a preferred mechanism as it is critical in substrate activation. Meanwhile, the framework metal sites provide a much more complex role than providing sheer Lewis acidity. It should be emphasized that we here aim to provide insights into the synergistic interaction between the proximate active motifs without providing a comprehensive account of the subsequent reactions.

5.2 Experimental procedure

M/X-Z zeolites (M = Cu, Fe; X = Al, Ga, B)

Synthesis of M/X-Z samples was attempted by the "acidic co-hydrolysis route". Metal nitrate (0.00048 mol) was added to the solution of TEOS (10 g) and DI water (32.5 g). the pH of the mixture was adjusted to 1.0 by drop-wise adding sulfuric acid. After the pH adjustment, the mixture was stirred at room temperature for 20 h to get a complete co-hydrolysis and condensation of TEOS with the metal salt. After that, the source of Brønsted acid site (1.2 mmol), 0.75 g of aluminum (aluminum sulfate octadecahydrate as an example), and TPAOH (4.8 mmol) was added into the mixture with the dripping of NaOH solution to get a basic gel (pH = 9.8). The final gel composition was 1 SiO_2: 0.01 Metal: 40 H_2O: 0.1 TPAOH. Finally, the slurry was transferred into the 100 mL Teflon-lined stainless-steel autoclave and statically crystallized at 180 °C for 72 h. After that, the zeolite was separated by centrifugation, followed by washing with DI water, and air drying at 70 °C overnight. The obtained as-synthesized samples were calcinated at 550 °C for 5 h to remove the organic template. H-form of the zeolite was prepared by ammonia treatment. The zeolite was firstly converted into NH_4-form by ion exchange with 1.0 M ammonia solution at room temperature for 24 h (1g solid to 100 mL solution). The zeolite samples were separated by centrifugation, followed by washing with DI water, and air drying at 70 °C overnight. The NH_4-form samples were converted to H-form by calcination at 500 °C under dry air for 4h.

Styrene oxidation

The catalytic performance of M/X-Z for styrene oxidation was evaluated by the following procedure: 0.5 mmol of 4-chlorostyrene, 0.05 g M/X-Z, 1.5 mmol of 30% H_2O_2 and 5 mL CH_3CN were added into a 10 mL flask and then stirred at different temperature (50/70/90/110 °C) for 24 h. The reaction solution was analyzed by gas chromatography (Agilent 6890 N, flame ion detector, a 0.45 μm × 5mm× 30m capillary column). The conversion of styrene and the selectivity of products were calculated by an internal standard method with dimethoxybenzene as the internal standard sample. Meanwhile, the main products were testified by GC–MS (Agilent 7890/5975C GC/MSD).

GVL decarboxylation

The catalytic performance of M/X-Z for alkene oxidation was evaluated by the following procedure: 0.10 g of catalyst and 1.00 g of γ-valerolactone were added into the stainless-steel batch-stirred reactor (100 mL). Subsequently, the reactor was purged with N_2 three times to replace the air from the reactor. Then the reactor was heated to 250 °C to react for 12 h under stirred with 700 rpm. Finally, the reactor was cooled down to room temperature with cold water after the reaction immediately. For the liquid and gas products, it was collected in a gas storage bag and qualitatively analyzed by the GC–MS, while the liquid products were dissolved in acetone and quantified and analyzed by the GC-MS.

5.3 Results and Discussion

A library of six ZSM-5 samples (M/X-Z) with the ***MFI*** topology was synthesized to conduct an orderly comparison, considering the variations in the dominant BASs (X = B, Ga, Al) and framework metal sites (M = Fe, Cu). High-resolution synchrotron PXRD reveals a homogeneous distribution of heteroatomic species (M's and X's) without additional Bragg peaks or weak background profiles, indicating the absence of metal or metal oxide aggregates. The whole profile Le Bail refinements of the PXRD patterns show that all six samples exhibit the same space group of *Pnma*, indicating that their crystal structures are comparable. The unit cell parameters only show insignificant variations (**Table 5.1**), further supporting the similarity of the crystal structures among the samples. The scanning electron microscopy (SEM) images also complement this finding: the polycrystalline particles in all samples had similar particle sizes of 2 to 5 μm, and comparable morphologies (**Figure 5.1**). These results thus confirm the successful preparation of M/X-Z with consistent basic structural characteristics. For a fair assessment, the samples contain comparable contents of Cu, Fe (at around 1.0 wt%), and X atom (**Table 5.2**).

We first employed temperature-programmed desorption with ammonia (NH_3-TPD) and pyridine-assisted Fourier-transform infrared spectroscopy (Py-FTIR) to study the acidic properties. The NH_3-TPD curves of Fe/X-Z show the presence of two desorption regimes. The low temperature (LT) desorption peaks at around 150 to 250 °C characterize the weak acid site, whereas the high temperature (HT) desorption peak at around 450 °C corresponds to the strong acid site (**Figure 5.2a-5.2f**) [23,24]. The total amount of acid sites (LT and HT) shows comparable values between the samples between 0.4 and 1.8 mmol g^{-1} from our quantitative analyses (**Table 5.3**). Fe/Al-Z and Fe/Ga-Z show relatively larger desorption peaks at the HT desorption regime, whereas Fe/B-Z shows a notably larger peak at the LT regime. This observation signifies that the ratio of strong to weak acid sites varies with the type of trivalent atom (X's), with the Fe/B-Z sample showing the lowest ratio among the samples. The strong-to-weak acid ratio differences are in good agreement with the literature [25,26]. Spectroscopic analysis from Py-FTIR reveals the distribution of BASs and LASs (**Figures 5.4–5.6**). The absorption peaks at ~1550 and 1450 cm^{-1} are attributed to the BASs and LASs, respectively [27,28]. The BAS: LAS ratio of Fe/X-Z (X = Al, Ga, B) is calculated to be 0.507, 0.481, and 0.213, respectively, indicating that Fe/B-Z exhibits the lowest BAS to LAS ratio. The Brønsted acidity of Fe/X-Z, following the trend of Fe/Al-Z > Fe/Ga-Z > Fe/B-Z, is consistent with the blueshift of the Si–O–T band at around 1100 cm^{-1} in FTIR (**Figure 5.3**) [29]. Integrating NH_3-TPD and Py-

FTIR analyses indicates that the BASs predominantly represent strong acid sites within these zeolite materials. The acid site properties of Cu/X-Z are closely comparable to those observed in Fe/X-Z (**Figure 5.2d–5.2f, Figure 5.7–5.9**).

It is noted that the generation of BASs depends on the charge disparity between two neighboring tetrahedral atoms, typically Al^{3+} and Si^{4+}. The incorporation of metal atoms into the framework can sometimes also result in the formation of BASs. From the acid property assessments and elemental analyses, it is indicated that the quantity of BASs primarily varies with the concentration of X atoms (X = Al, Ga, and B). This observation suggests that the introduction of X atoms into the zeolite framework plays a much more dominant role in the formation of BASs among the doped species, encompassing both metal species and X atoms.

We first conducted the Rietveld refinement of high-resolution synchrotron PXRD patterns to confirm the successful incorporation of metal species into the framework. The incorporation of the metal species induces apparent variations in the Bragg peak intensities at higher 2θ values. These variations can be ascribed to changes in the overall scattering factors resulting from the presence of heavier metal atoms. To elucidate the atomic parameters of the M sites, we employed the whole-pattern Rietveld refinement, by first conducting a charge-flipping algorithm to identify the crystallographic sites with higher electron contrast. We did not observe significant electron density at the extra-framework positions, indicating that the metal sites are primarily incorporated as "framework sites". During the refinement process, the crystallographic positions of the M species were determined by individually refining the site occupancy factors (SOFs) of the framework sites and constrained based on our elemental analysis, see **Tables 5.11–5.12**. Since the M species possess a higher electron density than Si atoms, the crystallographic T sites with significantly higher SOFs are the locations where the M species should be located. The Rietveld refinement profiles are summarized in **Figure S9**. The datasets identified the Fe sites at T6, T6, and T2 positions for Fe/Al-Z, Fe/Ga-Z, and Fe/B-Z, respectively. The Cu sites were similarly found at T12, T6, and T12 positions for Cu/Al-Z, Cu/Ga-Z, and Cu/B-Z, respectively.

After the confirmation of the location of the metal site in the zeolite framework, we further employed the Rietveld refinement of the pyridine-adsorbed synchrotron PXRD data to locate the BASs, as done before in related ZSM-5 samples (**Figure 5.2g–5.2l**) [30]. The BAS locations can be revealed (in terms of X–O(H)–Si) by analyzing the crystallographic sitting of the pyridine site and measuring the shortest interatomic distance between the framework oxygen site and the lone pair electron donor of pyridine (*i.e.*, $N_{pyridine}$). Among the three Fe/X-

Z samples, the shortest interatomic distances were found at O18···$N_{pyridine}$ = 2.75(2) Å in Fe/Al-Z, O18···$N_{pyridine}$ = 3.20(2) Å in Fe/Ga-Z, and O26···$N_{pyridine}$ = 3.45(2) Å in Fe/B-Z, as shown **Figure 5.2g–5.2i**. For the Cu/X-Z samples, the shortest interatomic distances with the same trend were found at O1···$N_{pyridine}$ = 2.79(2) Å in Cu/Al-Z, O1···$N_{pyridine}$ = 3.32(2) Å in Cu/Ga-Z, and O1···$N_{pyridine}$ = 3.48(2) Å in Cu/B-Z, as shown in **Figure 5.2j–5.2l**. Furthermore, there is a consistent pattern of increasing shortest interatomic distances, indicative of stronger acidity, following the order of X = Al < Ga < B. This trend aligns with the previously determined Brønsted acidity, providing further support to the findings.

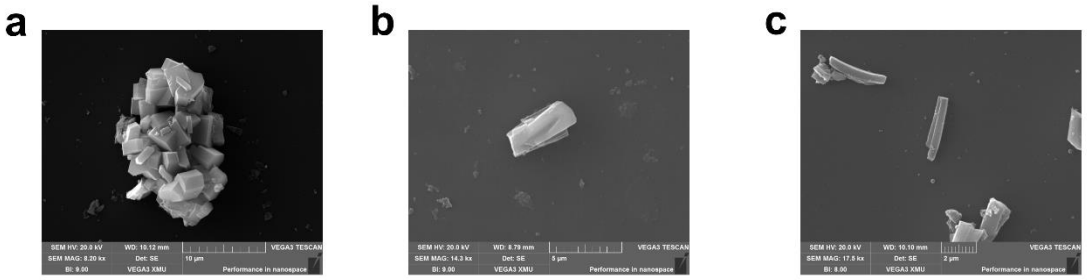

Figure 5.1. Morphology analysis by SEM. SEM images of (a) Fe/Al-Z, (b) Fe/Ga-Z, and (c) Fe/B-Z.

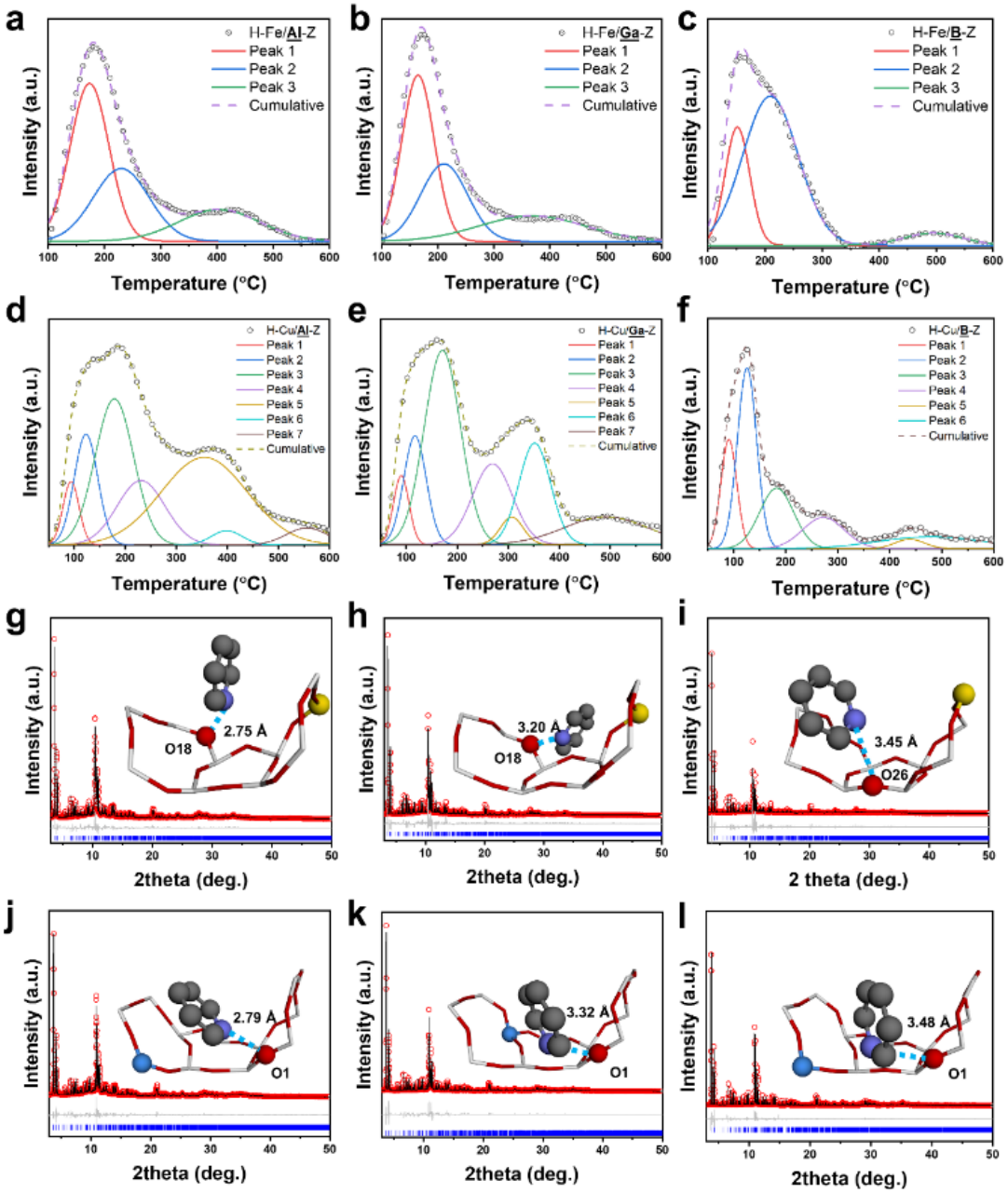

Figure 5.2. The quantitative analysis of NH_3-TPD data of (**a**) Fe/Al-Z, (**b**) Fe/Ga-Z, (**c**) Fe/B-Z, (**d**) Cu/Al-Z, (**e**) Cu/Ga-Z, and (**f**) Cu/B-Z. The Rietveld refinement profiles of high-resolution synchrotron PXRD of pyridine-adsorbed materials and the corresponding Rietveld refined crystal structures of (**g**) Fe/Al-Z, (**h**) Fe/Ga-Z, (**i**) Fe/B-Z, (**j**) Cu/Al-Z, (**k**) Cu/Ga-Z, and (**l**) Cu/B-Z. For clarity, the present views only show zoom-in, mirror-disregarded, and hydrogen-disregarded views along {010}. Atoms are represented in the ball-and-stick model (yellow = Fe, blue = Cu, grey = C, purple = N, white = Si, and red = O). The corresponding refinement parameters, atomic parameters, and crystal structures showing the complete unit cell are summarized in **Tables 3.3–3.9**.

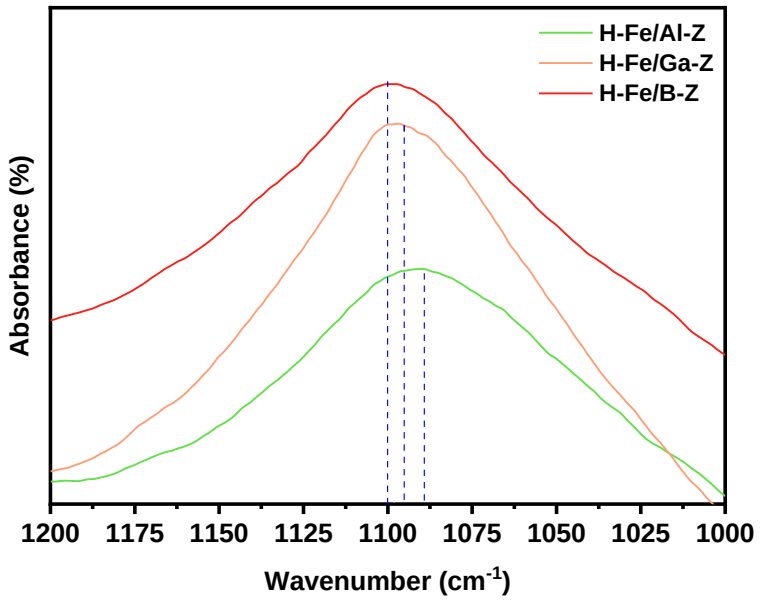

Figure 5.3. FTIR spectra of Fe/Al-Z, Fe/Ga-Z, and Fe/B-Z.

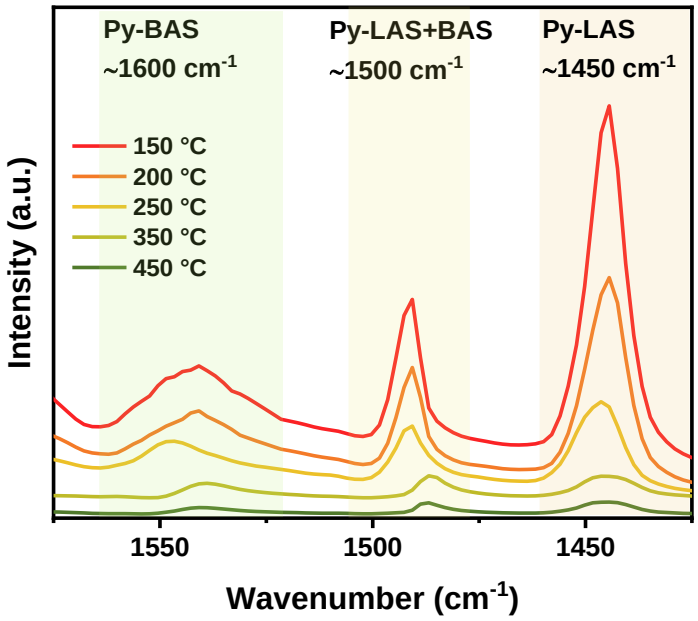

Figure 5.4. Py-FTIR spectra of Fe/Al-Z.

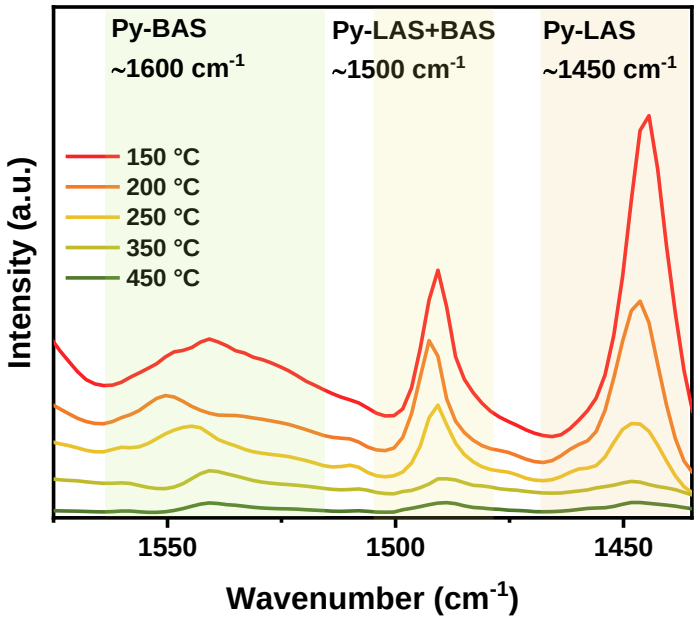

Figure 5.5. Py-FTIR spectra of Fe/Ga-Z.

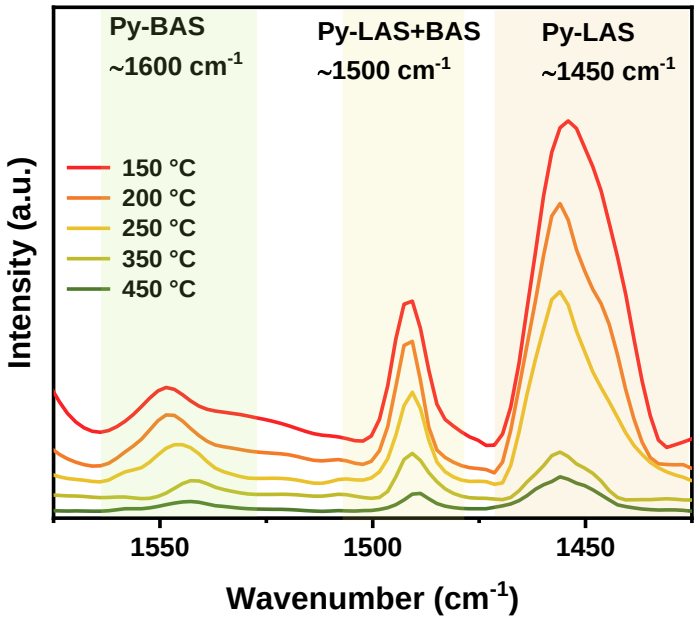

Figure 5.6. Py-FTIR spectra of Fe/B-Z.

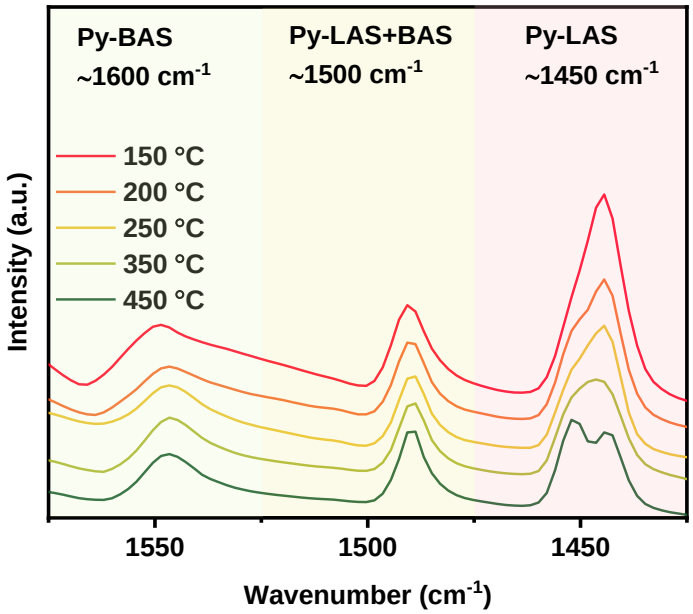

Figure 5.7. Py-FTIR spectra of Cu/Al-Z.

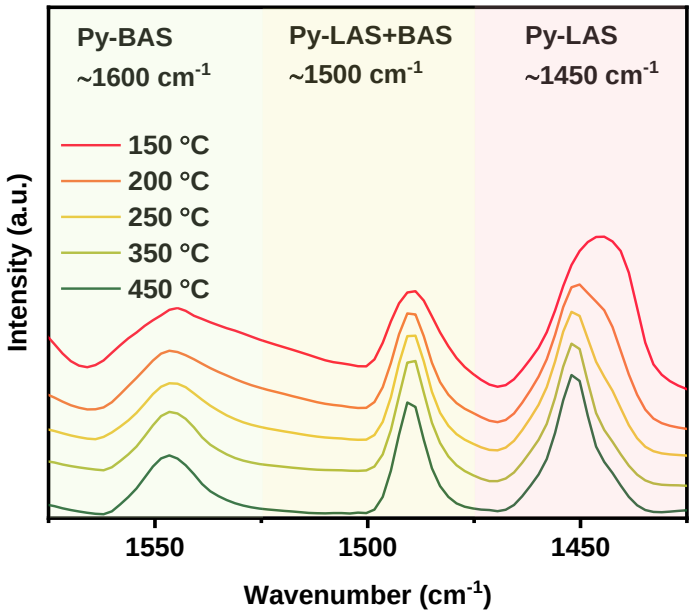

Figure 5.8. Py-FTIR spectra of Cu/Ga-Z.

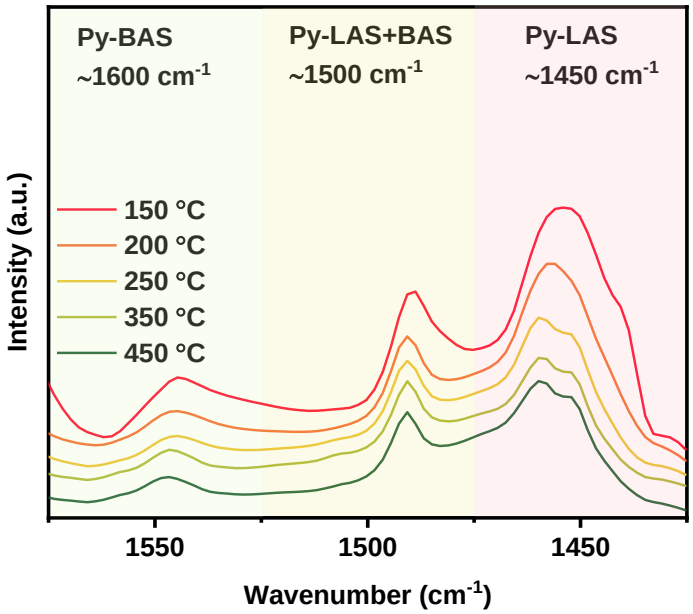

Figure 5.9. Py-FTIR spectra of Cu/B-Z.

We further employed extended X-ray absorption fine structure spectroscopy (EXAFS) to complement the above structural findings. In the wavelet transform (WT) analysis on the EXAFS data (**Figure 5.11a–5.11f**), only a strong lobe centered at k ≈ 5 $Å^{-1}$ (smaller than 10) and R ~ 1.5 Å was observed, which corresponds to the oxygen atoms surrounding the metal centers. The absence of lobes at higher k-space at the second shell or even third shell suggests the lack of metal or metal oxide aggregates in the samples, the peak located at around 2.5 Å can be attributed to the nearby Si or O atom from the zeolite framework because of the location at low k-range. The average bond lengths of M–O in the first shell were calculated to be ~2.0 Å, with an average coordination number of around 4 (see detailed quantitative analysis in **Figure 5.12** and **Tables 5.13** and **5.14**). This indicates that all the M species are well isolated within the zeolitic framework in the form of MO_4 tetrahedra. In addition, the X-ray absorption near edge spectroscopic results (XANES) revealed the oxidation states of the Fe and Cu species as +3 and +2, respectively (**Figure 5.11g** and **5.11h**).

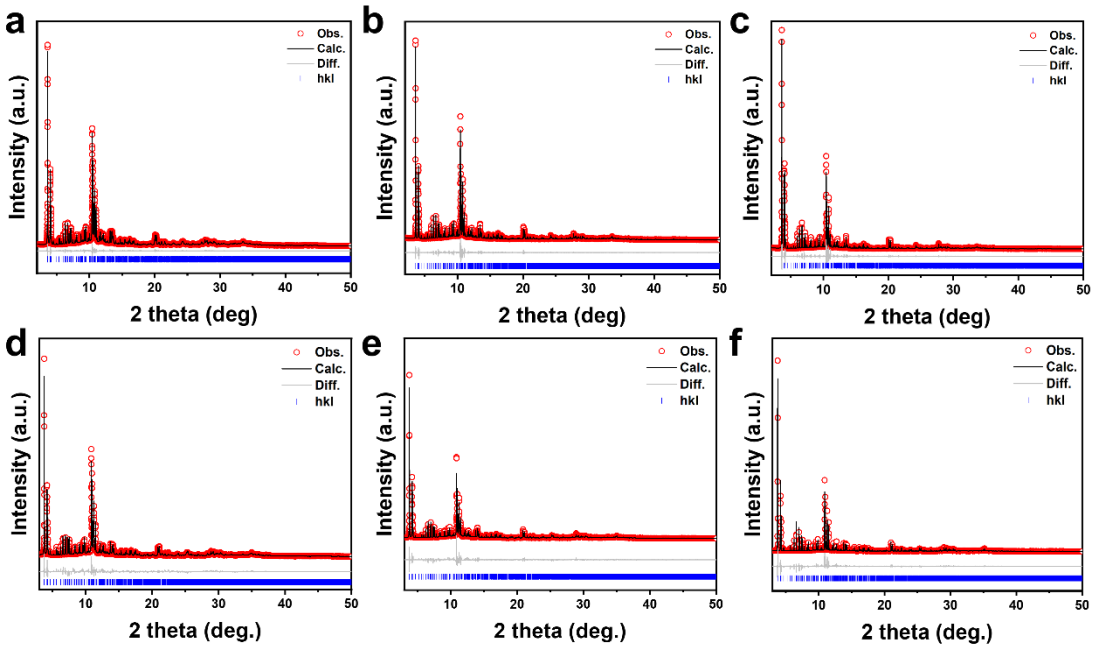

Figure 5.10. The Rietveld refinement profiles of high-resolution synchrotron PXRD of (a) Fe/Al-Z, (b) Fe/Ga-Z, (c) Fe/B-Z, (d) Cu/Al-Z, (e) Cu/Ga-Z, and (f) Cu/B-Z. The structural and atomic parameters are summarized in **Tables 5.13–5.18**.

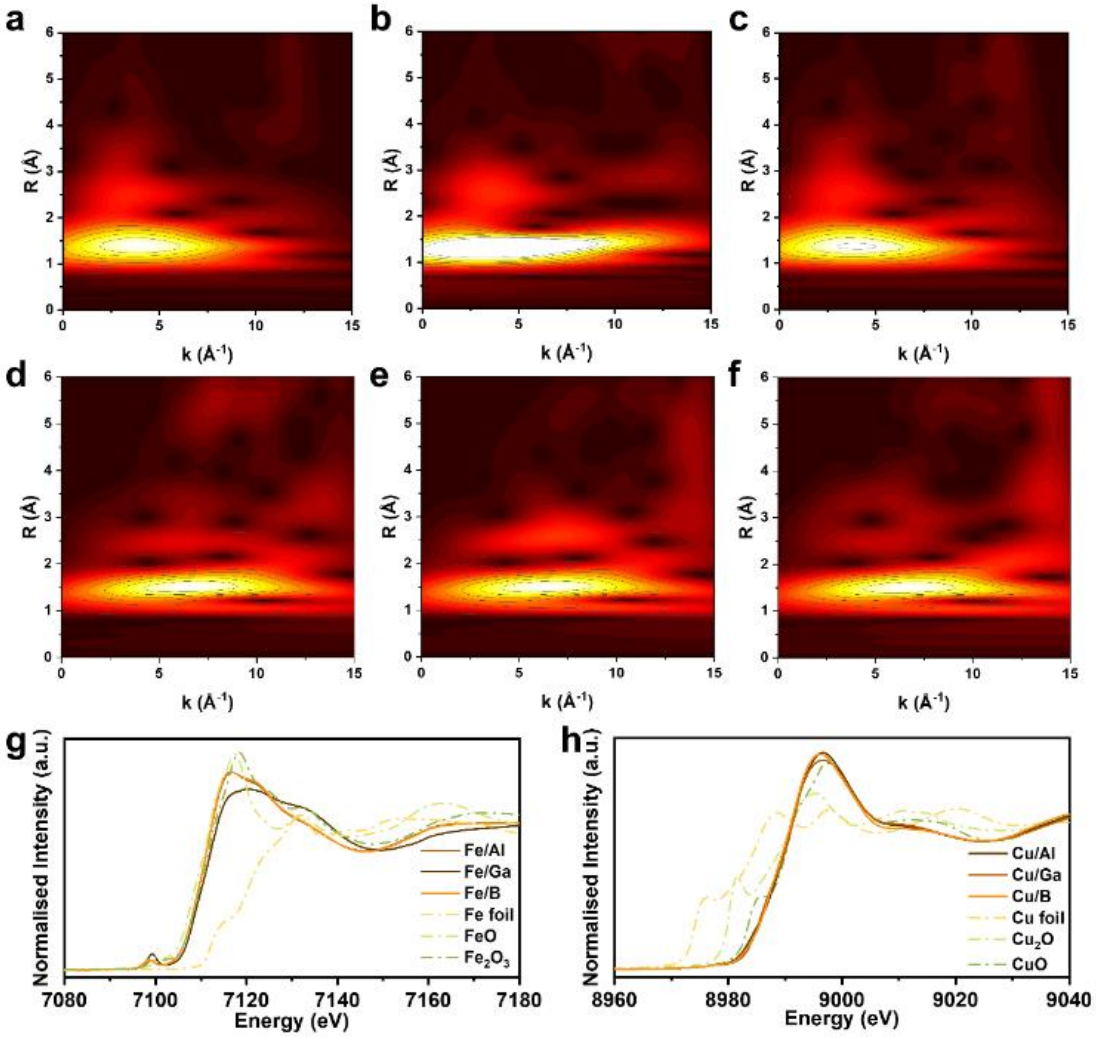

Figure 5.11. k^3 weighted Fe K-edge WT-EXAFS of (**a**) Fe/Al-Z, (**b**) Fe/Ga-Z, and (**c**) Fe/B-Z. k^3 weighted Cu K-edge WT-EXAFS of (**d**) Cu/Al-Z, (**e**) Cu/Ga-Z, and (**f**) Cu/B-Z. The structural and atomic parameters are summarized in **Tables S5.13–5.18**. (**g**) Fe K-edge XANES analysis of Fe/X-Z. (**h**) Cu K-edge XANES analysis of Cu/X-Z.

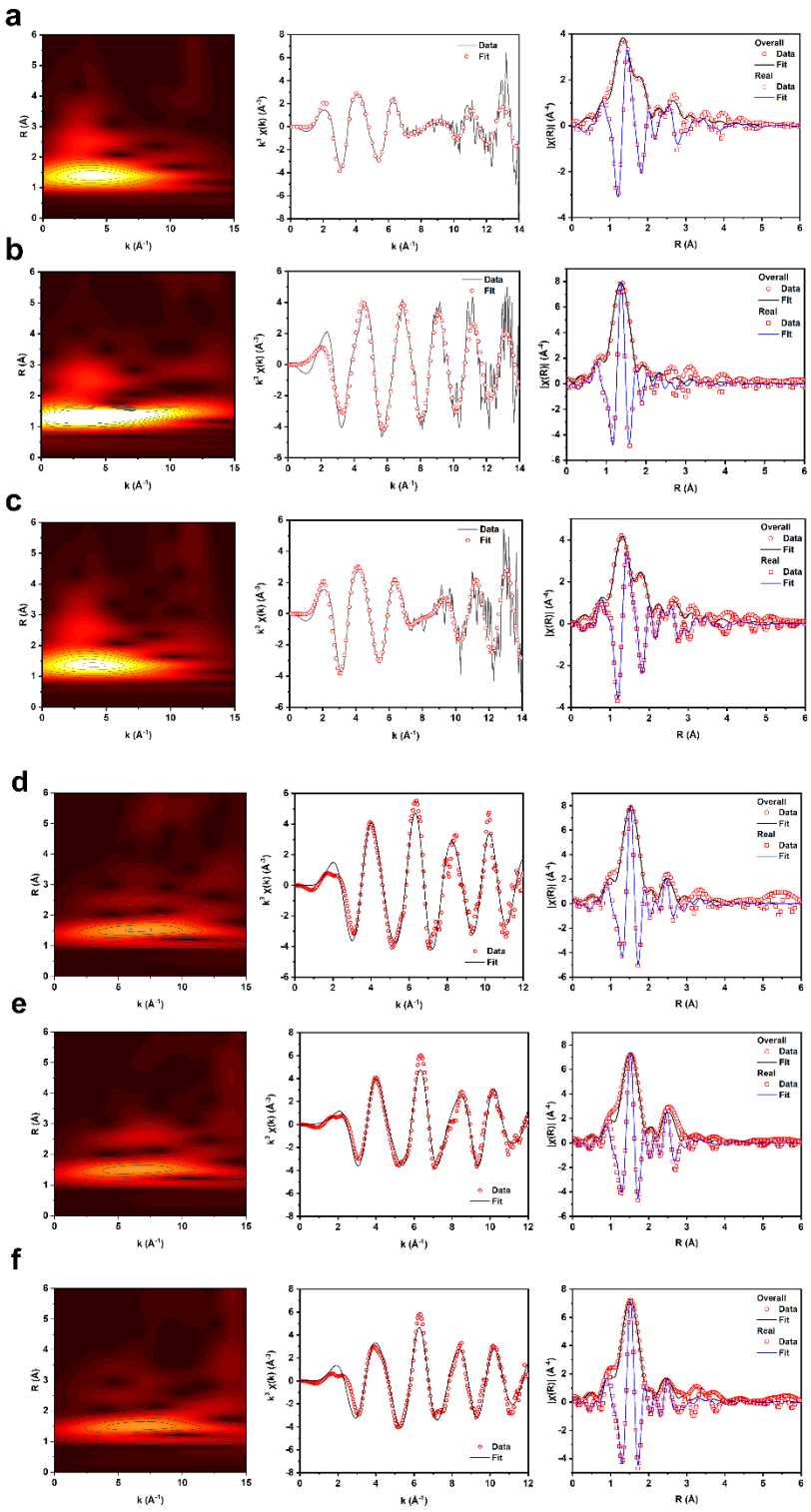

Figure 5.12. Wavelet transform for k^3 weighted EXAFS signal of (a) Fe/Al-Z, (b) Fe/Ga-Z, (c) Fe/B-Z, (d) Cu/Al-Z, (e) Cu/Ga-Z, and (f) Cu/B-Z, and the corresponding Fe and Cu K-edge EXAFS (red) and fitting profile (black) in k^3 weighted k-space and R-space.

Accordingly, the separation between the metal sites and the BASs can be obtained (**Figure 5.13a–5.13f)**. It is apparent that the separations are comparable among Fe/X-Z (at ~6.0 Å) and among Cu/X-Z (at ~6.3 Å). We made multiple attempts to ensure that comparable metal···BAS separation for a fair and systematic investigation of their synergistic cooperativity.

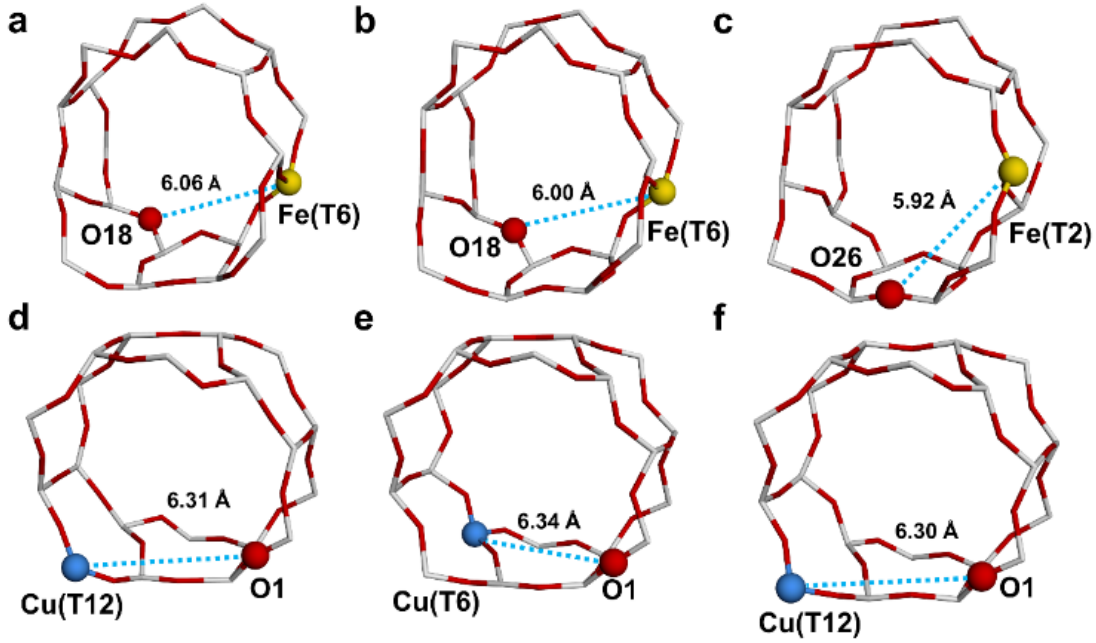

Figure 5.13. The Rietveld refined crystal structure of high-resolution synchrotron PXRD of (**a**) Fe/Al-Z, (**b**) Fe/Ga-Z, (**c**) Fe/B-Z, (**d**) Cu/Al-Z, (**e**) Cu/Ga-Z, and (**f**) Cu/B-Z. The same style and color scheme are adopted in **Figure 5.2**.

Our characterizations have shown that the metal-doped zeolites feature well-controlled concentrations and distribution of metal sites and BASs. The major differences between the samples can be accordingly narrowed down to the BAS strength and the metal site property. Accordingly, we have selected two well-studied zeolite-catalyzed reactions as model systems: the oxidation of 4-chlorostyrene with hydrogen peroxide and the decarboxylation of gamma-valerolactone (GVL), to investigate the dynamic synergism between BASs and metal sites pertaining to their catalytic properties.

In the oxidation reaction of 4-chlorostyrene with hydrogen peroxide over metal-doped zeolites, it is widely believed that the zeolitic BASs can facilitate the adsorption of 4-chlorostyrene, while the metal sites undergo a redox reaction to cleave H_2O_2 [31–34]. To confirm the role of BASs, we conducted control experiments by poisoning the BASs with Na^+. The Na^+-poisoned sample showed a significant decrease in conversion rate (to less than 15%), showing the adsorptive function of BASs (**Table 5.21**). We subsequently examined the

impact on the conversion rate with different combinations of Brønsted acidity and metal sites. Interestingly, Fe/X-Z and Cu/X-Z exhibited contrasting trends in conversion with changes in Brønsted acidity (**Figure 5.14a**, with the selectivity of 4-chlorobenzaldedye product remaining relatively constant at ~80%). Fe/X-Z demonstrated the highest conversion rate when Brønsted acidity was the weakest over Fe/B-Z, whereas Cu/X-Z exhibited the lowest conversion rate when Brønsted acidity was the weakest over Cu/B-Z. We have also collected catalysis data at different reaction temperatures (50, 70, and 90 °C) to extrapolate the apparent activation energy for the reaction (**Table 5.21**). Similar to the conversion rate data, the activation energy over Fe/B-Z (at 49.5 kJ mol^{-1}) is the lowest among the three Fe/X-Z samples (between 49.5 to 87.7 kJ mol^{-1}) whereas that over Cu/Al-Z (at 50.1 kJ mol^{-1}) is the lowest among Cu/X-Z (between 50.1 to 84.4 kJ mol^{-1}). The yield of benzaldehyde product increases with a decrease in the BAS/LAS ratio and strong/weak acid ratio, reflecting its high correlation with Brønsted acidity (**Figure 5.14b–5.14c**). The correlation of the BAS/LAS ratio and strong/weak acid ratio pertaining to the catalytic performance over Fe/X-Z is summarized in **Figure 5.14d**.

It is intriguing to observe such a contrast in trend with different metal sites as this trend should be consistent if both Fe/X-Z and Cu/X-Z systems exhibit similar synergistic cooperativity. The current observation suggests that the synergism of the metal sites and the BASs are inherently different over the Fe/X-Z and Cu/X-Z systems, which may indicate that different reaction mechanisms are involved. Analyzing the difference in the adsorbate structures of the reaction substrates enables valuable insights to directly reveal the host-guest interaction and explain the trend in different catalysis. Within the Fe/X-Z system, the shortest interatomic distance between the zeolitic BAS and $C{=}C_{styrene}$ is 3.58(2) Å in Fe/Al-Z and decreases to 3.51(2) Å in Fe/B-Z, which agrees with the trend in Brønsted acidity (**Figure 5.14e** and **5.14f**). The interatomic distances between the Fe sites and $C{=}C_{styrene}$ were measured at > 4.5 Å, which infers minimal Fe···styrene adsorption interaction. Accordingly, it suggests that 4-chlorostyrene has a high potential to be directly adsorbed on the BASs without notable influence by the Fe sites. Upon adsorption, the charge distribution of $C{=}C_{styrene}$ will be substantially affected by the adsorption on the BASs. A stronger BAS will lead to greater polarization of the $C{=}C_{styrene}$.

Meanwhile, it is well-documented that Fe^{III} centers primarily generate ·OOH radicals in a Fenton-like pathway from H_2O_2 cleavage, whereas Cu^{II} primarily generates ·OH radicals [35–38]. Based on the inherent properties of styrene polarization and H_2O_2 cleavage, a proposed mechanistic explanation was

achieved as depicted in **Scheme 5.2**. The conversion towards the target benzaldehyde product is achieved through two different pathways: oxidative cleavage of $C=C_{styrene}$ bonds *via* a [2+2] cycloaddition pathway involving ·OOH, and a radical addition pathway involving ·OH [39,40]. The presence of a weak BAS increases the favorability of the [2+2] cycloaddition reaction between ·OOH and less polarized $C=C_{styrene}$ and *vice versa*, thus the Fe/B-Z exhibits the highest yield among the Fe/X-Z system. For OH addition over Cu/X-Z, more polarization of the $C=C_{styrene}$ bond promotes the radical addition reaction. Consequently, the yield of 4-chlorobenzaldehyde increases over Cu/X-Z along with zeolitic Brønsted acidity.

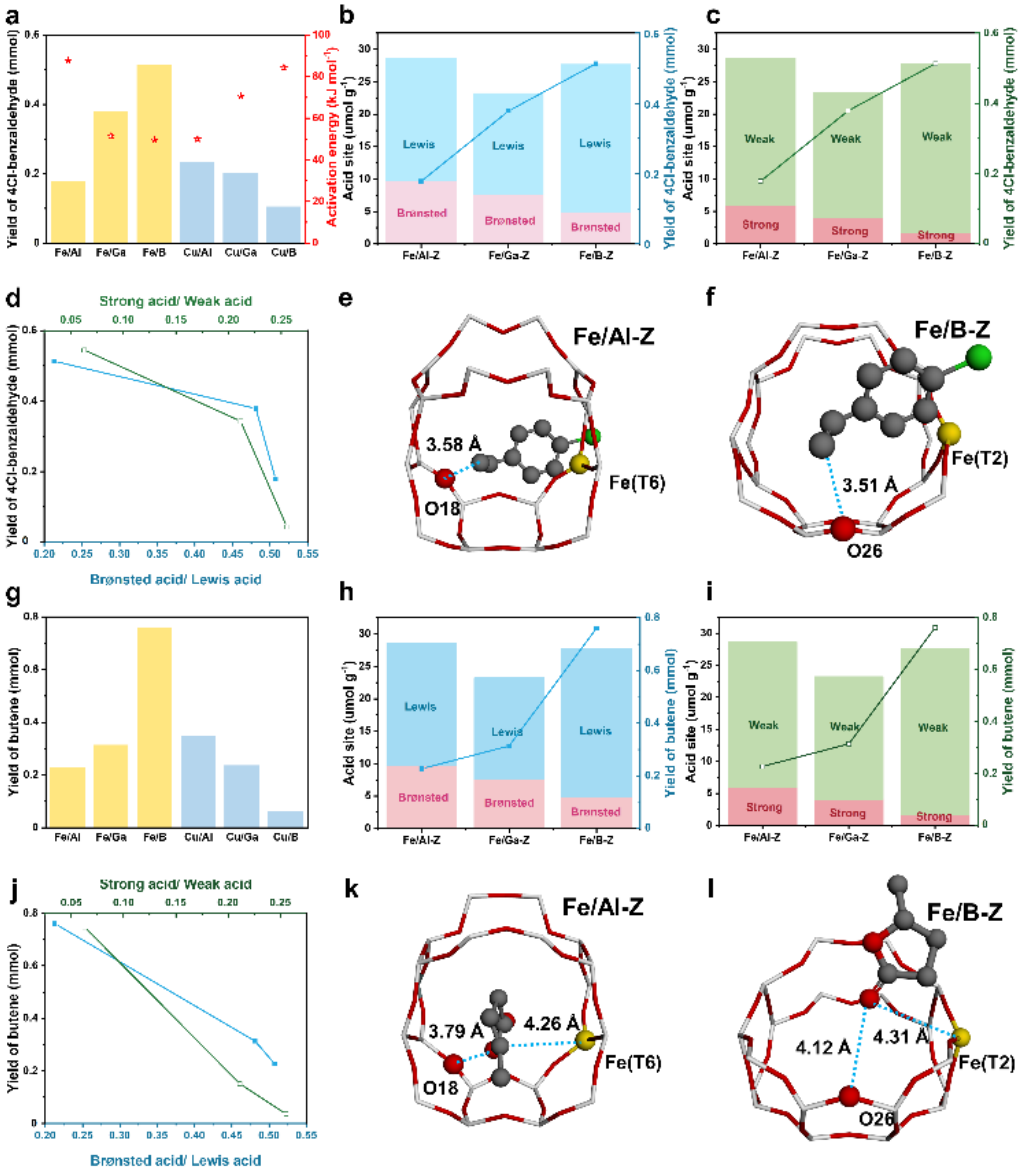

Figure 5.14. (**a**) Catalytic performance and activation energy of the oxidation of 4-chlorostyrene, the evaluation of the catalytic performance with respect to the quantities of (**b**) Brønsted/Lewis acid, (**c**) strong/weak acid, and (**d**) the BAS/LAS ratio and strong/weak acid ratio, and the Rietveld refined crystal structure of (**e**) Fe/Al-Z, and (**f**) Fe/B-Z. (**g**) Catalytic performance of the decarboxylation of GVL, the evaluation of the catalytic performance with respect to the quantities of (**h**) Brønsted/Lewis acid, (**i**) strong/weak acid, and (**j**) the BAS/LAS ratio and strong/weak acid ratio, and the Rietveld refined crystal structure of (**k**) Fe/Al-Z, and (**l**) Fe/B-Z. The structural and atomic parameters are summarized in **Tables 5.23–5.26** and **Figures 5.15–5.18**. The same style and color scheme are adopted in **Figure 5.2**.

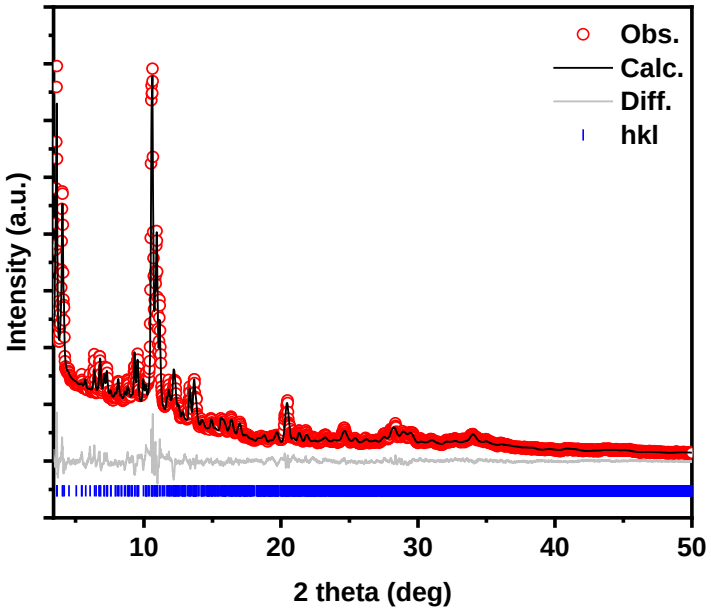

Figure 5.15. PXRD data and Rietveld refinement of 4-chlorostyrene pre-adsorbed on Fe/Al-Z.

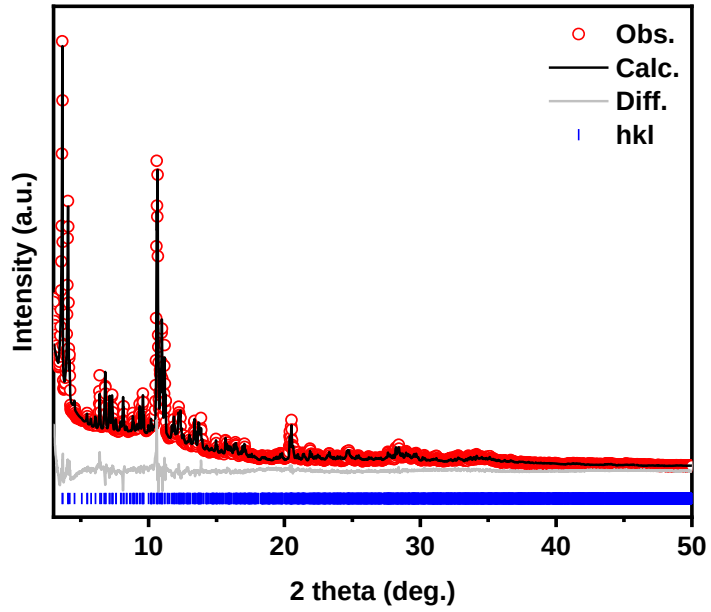

Figure 5.16. PXRD data and Rietveld refinement of 4-chlorostyrene pre-adsorbed on Fe/B-Z.

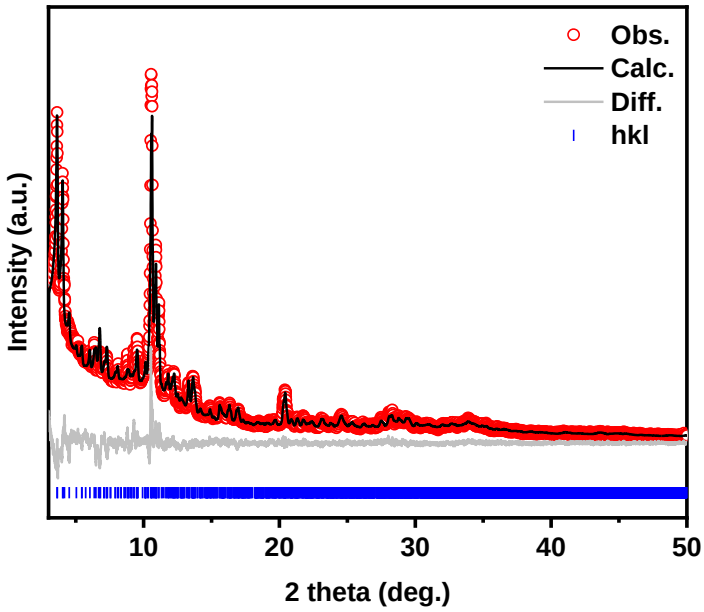

Figure 5.17. PXRD data and Rietveld refinement of GVL pre-adsorbed on Fe/Al-Z.

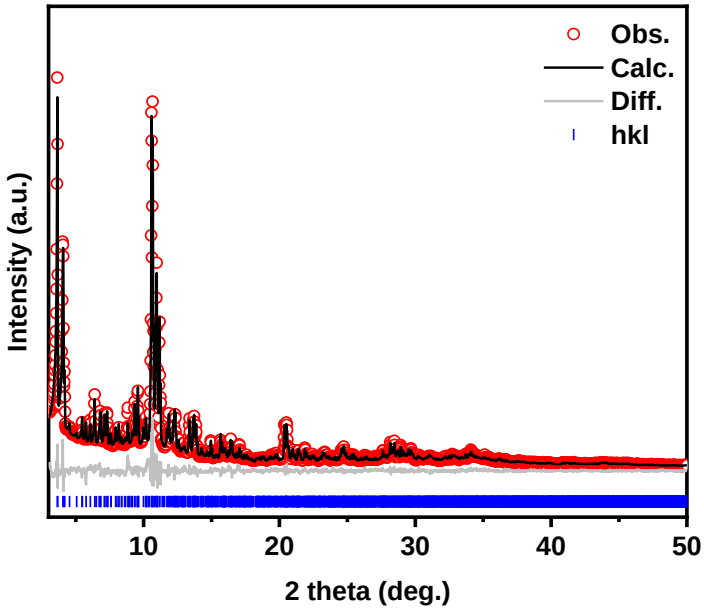

Figure 5.18. PXRD data and Rietveld refinement of GVL pre-adsorbed on Fe/B-Z.

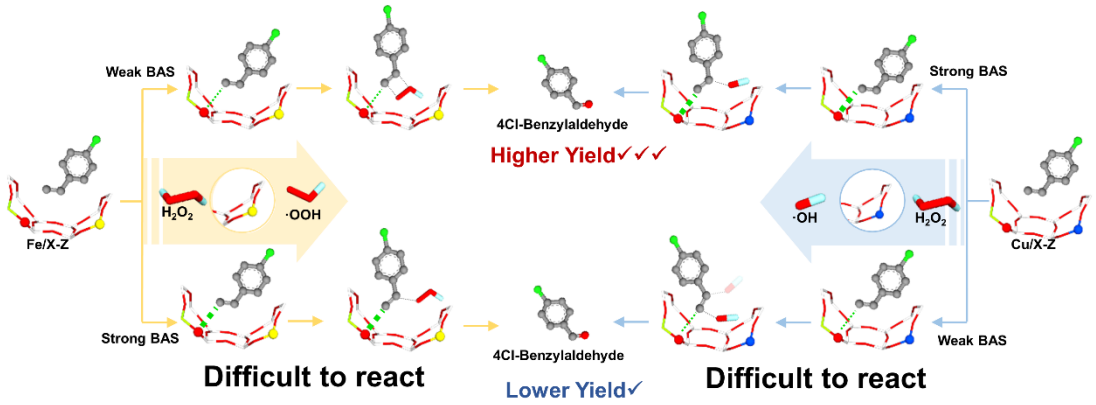

Scheme 5.2. Proposed reaction mechanism of the oxidation of 4-chlorostyrene over Fe/X-Z and Cu/X-Z with varying BAS strengths.

Another modelling system, the decarboxylation of biomass-derived GVL-producing butene at high conversion [41], or further dimerizing to form BTX aromatics [42], has been extensively investigated by utilizing metal-modified zeolites. Neighboring functional motifs have been engineered specifically to offer synergistic cooperativity to facilitate the decarboxylation process, as well as the potential tandem reaction(s) [14,43]. However, there is a lack of systematic studies to investigate how these neighboring motifs catalyze collaboratively. Based on our systematic investigation, we observed a similar trend as in the above styrene oxidation reaction (**Figure 5.14g**), where the yield of butene increases with a weaker Brønsted acidity over Fe/X-Z but decreases over Cu/X-Z. The yield decreases with Fe/X-Z with an increase in the BAS/LAS ratio and strong/weak ratio, also revealing its dependence on Brønsted acidity (**Figure 5.14h–5.14j**). We similarly analyzed their GVL adsorbate structures through the Rietveld refinement of PXRD data, revealing a 'bidentate' binding mode of GVL between the BAS and the metal site (**Figure 5.14k** and **5.14l**). This finding is in contrast to the adsorption by BAS alone in H-ZSM-5, where only 'monodentate' binding is present [41]. Furthermore, the adsorbed GVL molecules exhibit notably different interatomic distances, indicating variable host-guest interactions. These distinctions in interatomic distances further highlight the diverse nature of interactions between GVL and the metal-BAS pair.

The decarboxylation of GVL is typically a two-step process over various metal-modified zeolites [44,45]. In Step 1, GVL is adsorbed via a 'bidentate' mode by the metal-BAS pair. The ring-opening of the lactone group is hence facilitated, forming a protonated pentenoic acid intermediate. In Step 2, the intermediate first deprotonates, followed by decarboxylation to form butene product. We therefore make the following postulations over our M/X-Z systems. The Fe^{III} site

demonstrates stronger Lewis acidity than the Cu^{II} site. Even though the metal-Lewis acidity is weaker than a common BAS, the presence of Fe^{III} can better compensate for the weaker Brønsted acidity to promote the protonation of GVL when compared with that of Cu^{II}. This affects the lactone ring-opening step, thereby making the subsequent decarboxylation step (Step 2) rate-determining. On the other hand, the strength of the conjugate base of the zeolitic BASs plays a critical role in Step 2, with the weakest BASs displaying the strongest conjugate base behavior, facilitating the deprotonation of the protonated pentenoic acid intermediate. Hence, the synergistic cooperation of both Cu^{II} sites and BASs for the lactone ring-opening step, becomes necessary, making Step 1 rate-determining. Consequently, a higher yield is achieved with stronger BASs over Cu/X-Z, whereas a lower yield is achieved with weaker BASs over Fe/X-Z.

We conducted density functional theory (DFT) calculations in order to comprehend the distinct reaction trends exhibited in our model reactions. The projected density of states (PDOS) analysis investigated the electronic structures of the adsorption models, see **Figure 5.19a** and **5.19b**. In the case of GVL in zeolites, the Fe-3*d* band of Fe/X-Z demonstrates a prominent peak near E_V-0.2 eV (where E_V denotes 0 eV), featuring a *d*-band center at –0.231 (Al), –0.222 (Ga), and –0.236 eV (B). For Cu/X-Z, the *d*-band centers of the corresponding Cu-3*d* band are at 0.007 (Al), –0.002 (Ga), and –0.001 eV (B). For 4-chlorostyrene in zeolites, the Fe-3*d* band of Fe/X-Z demonstrates a dominant peak with a *d*-band center at –0.244 (Al), –0.267 (Ga), and –0.641 eV (B). For Cu/X-Z, the Cu-3*d* band has a *d*-band center at –0.199 eV (Al), –0.221 eV (Ga), and –0.203 eV (B), respectively (**Figure 5.19c** and **5.19d**). A negligible shift of PDOS was observed, indicating that the co-existence of BASs and doped metals does not significantly affect the electroactivity of the metal active sites.
To further elucidate the binding behaviors, we calculated the binding energies of the adsorbate species. As seen in **Figure 5.19e** and **5.19f**, the binding energies of both 4-chlorostyrene and GVL on both Fe/X-Z and Cu/X-Z increase with Brønsted acidity (governed by the X site); the corresponding PDOSs are presented in **Figures 5.20–5.23**). There is a clear disparity in the binding energy of 4-chlorostyrene and GVL on Cu/X-Z and Fe/X-Z, indicating there is a difference in the substrate binding activity between Fe/X-Z and Cu/X-Z, which agrees with our above experimental findings. Furthermore, we analyzed the variations in electronic distribution between the HOMO and LUMO of the substrates, as summarized in **Figures 5.24** and **5.25**. A difference extent of electron transfer between the substrate molecules and the zeolites is noticed. Our

calculations thus highlight the role of variations in acid strength associated with different X atoms (B, Al, Ga) influencing substrate binding during reactions.

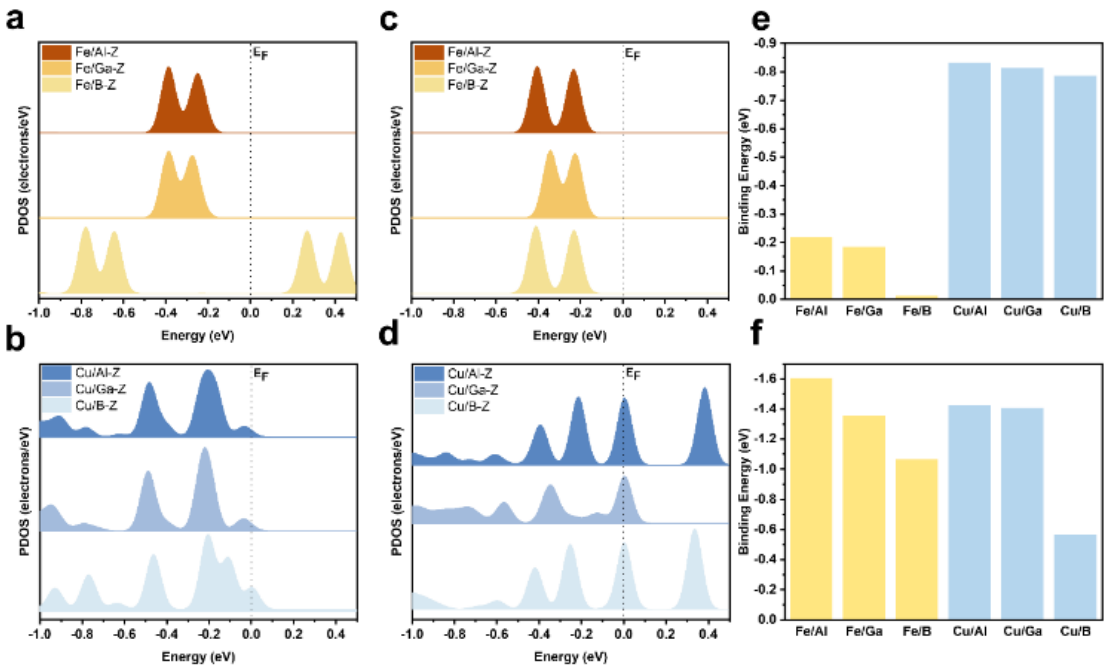

Figure 5.19. Projected density of states of the metal *d*-band center for Fe/X-Z and Cu/X-Z, with (**a**, **b**) 4-chlorostyrene and (**c**, **d**) GVL, respectively. Calculated binding energies for the labeled zeolite samples with (**e**) 4-chlorostyrene and (**f**) GVL molecular adsorption. Insets show the optimized crystal structures. The calculations were performed at the GGA/PBE level of theory.

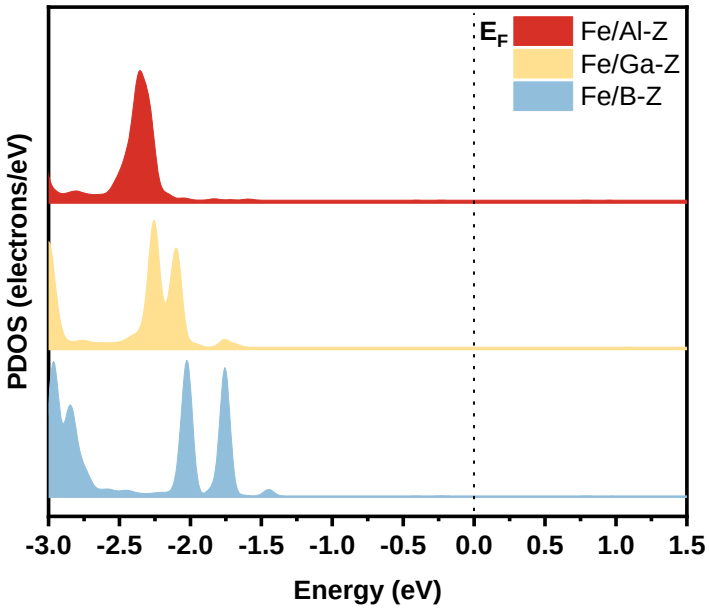

Figure 5.20. Projected density of states of substrate molecule orbitals for Fe/X-Z with pre-adsorbed GVL.

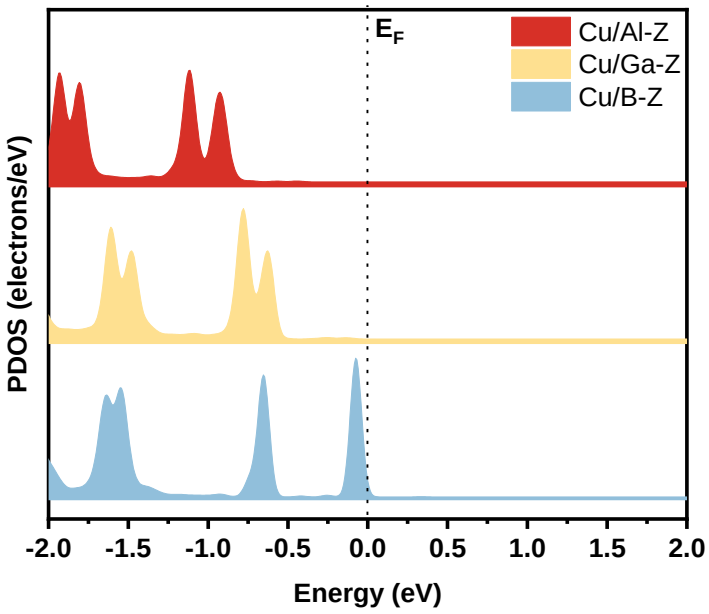

Figure 5.21. Projected density of states of substrate molecule orbitals for Cu/X-Z with pre-adsorbed GVL.

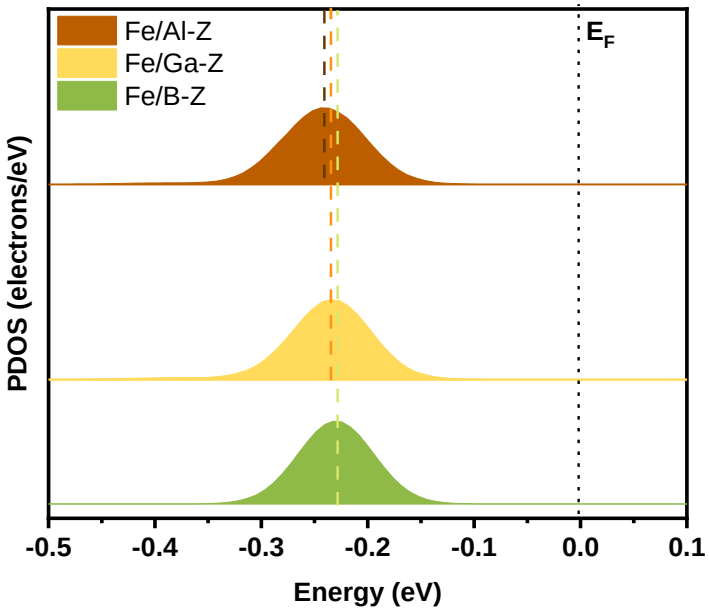

Figure 5.22. Projected density of states of substrate molecule orbitals for Fe/X-Z with pre-adsorbed 4-chlorostyrene.

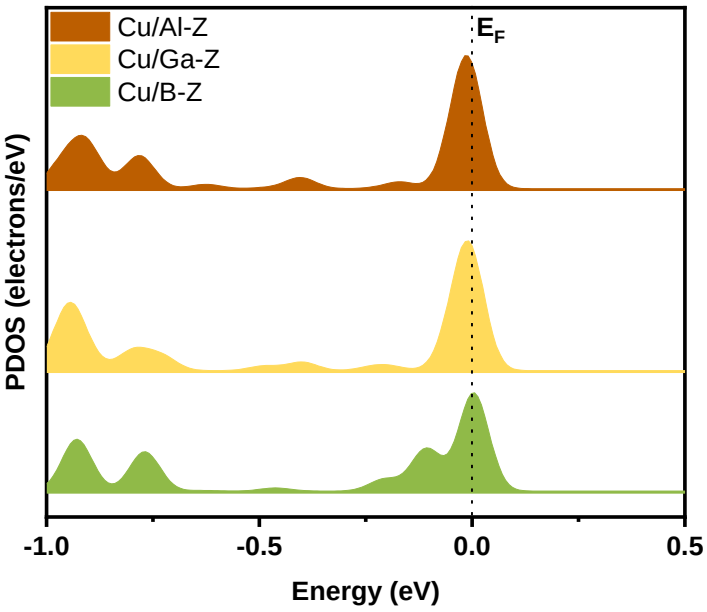

Figure 5.23. Projected density of states of substrate molecule orbitals for Cu/X-Z with pre-adsorbed 4-chlorostyrene.

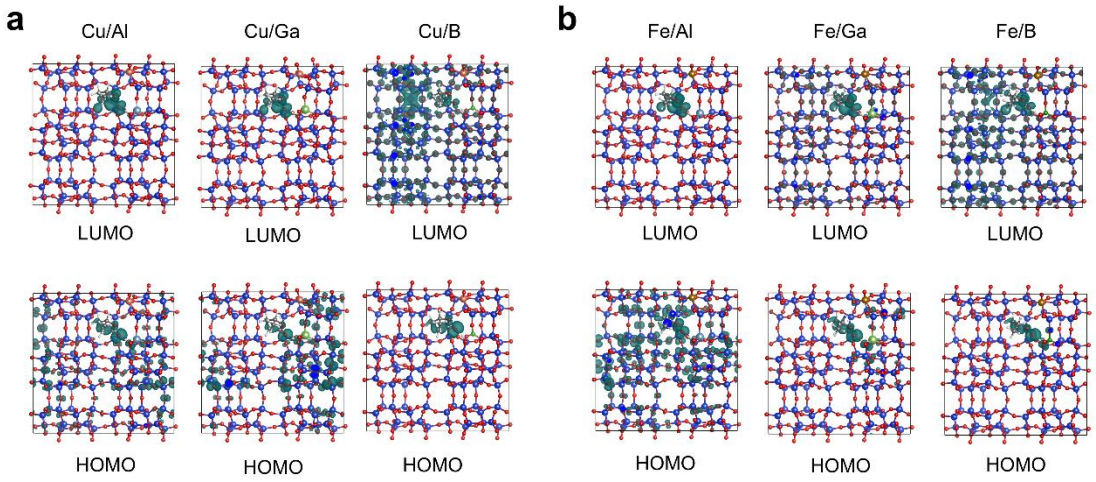

Figure 5.24. Electronic charge densities of LUMO and HOMO for (a) Cu/X-Z and (b) Fe/X-Z with pre-adsorbed GVL.

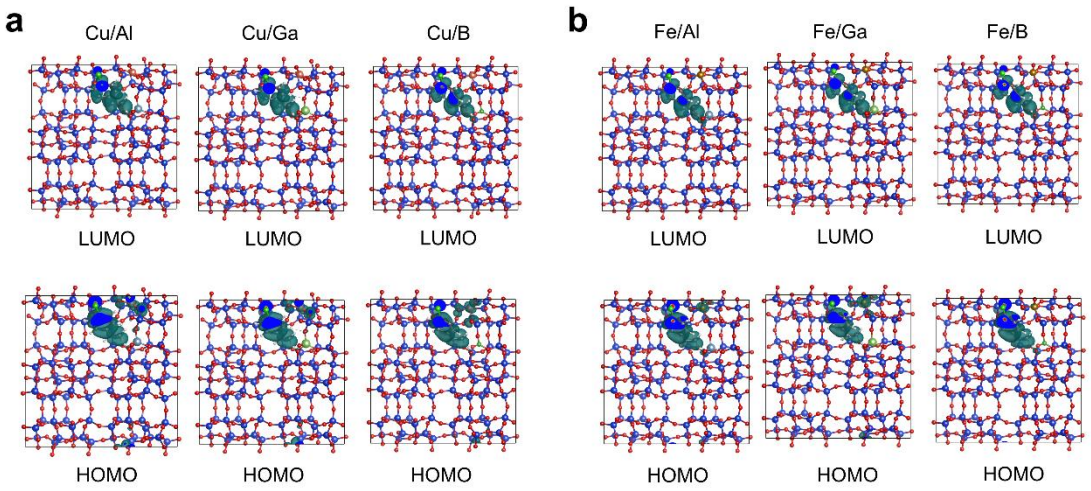

Figure 5.25. Electronic charge densities of LUMO and HOMO for (a) Cu/X-Z and (b) Fe/X-Z with pre-adsorbed 4-chlorostyrene.

5.4 Conclusion

In this study, we conducted a meticulous preparation of a highly controlled library of zeolite catalysts. This involved incorporating diverse combinations of Fe/Cu species and varying strengths of BAS. To systematically investigate the synergistic cooperativity in this system, we carefully controlled the concentrations and separation of the metal species and BASs. The physicochemical, structural, and atomic properties of the zeolite samples were characterized using a combination of spectroscopic and crystallographic techniques.

From a wide range of catalytic reactions, we specifically selected styrene oxidation and GVL decarboxylation as our model reactions to study the structure-reactivity correlations. These reactions were chosen due to their well-recognized involvement of multiple functional motifs, which contribute to enhanced catalytic performance. By deciphering the structure-reactivity correlations, we gained valuable insights for the design of 'next-generation' catalysts with more superior properties.

One key finding of our study is the importance of achieving a delicate balance between multiple functional motifs in an active site when they are involved in a catalytic reaction. This balance is crucial based on the intricate reaction mechanism and is essential for optimizing catalytic performance. Overall, our research provides valuable knowledge for the design and development of microenvironments, highlighting the significance of understanding the structure-reactivity correlations and the interplay of different functional motifs in a conventional 'active site'.

5.5 Reference

(1) Wun, C. K. T.; Wang, Z.; Kawaguchi, S.; Kobayashi, S.; Wu, T. S.; Chen, T.; Lin, C.; Tang, C. C.; Yin, J.; Lo, T. W. B.Investigating Synergistic Cooperativity of Metal-Brønsted Acid Site Pair in MFI-Type Zeolites by Synchrotron X-Ray Powder Diffraction. *J. Mater. Chem. A* **2024**, 25442–25448. https://doi.org/10.1039/d4ta04737k.

(2) vanDeelen, T. W.; Hernández Mejía, C.; deJong, K. P.Control of Metal-Support Interactions in Heterogeneous Catalysts to Enhance Activity and Selectivity. *Nat. Catal.* **2019**, *2* (11), 955–970. https://doi.org/10.1038/s41929-019-0364-x.

(3) Somorjai, G. A.; Kliewer, C. J.Reaction Selectivity in Heterogeneous Catalysis. *React. Kinet. Catal. Lett.* **2009**, *96* (2), 191–208. https://doi.org/10.1007/s11144-009-5531-7.

(4) Leenders, S. H. A. M.; Gramage-Doria, R.; DeBruin, B.; Reek, J. N. H.Transition Metal Catalysis in Confined Spaces. *Chem. Soc. Rev.* **2015**, *44* (2), 433–448. https://doi.org/10.1039/c4cs00192c.

(5) Yu, C.; He, J.Synergic Catalytic Effects in Confined Spaces. *Chem. Commun.* **2012**, *48* (41), 4933–4940. https://doi.org/10.1039/c2cc31585h.

(6) Hai, X.; Zheng, Y.; Yu, Q.; Guo, N.; Xi, S.; Zhao, X.; Mitchell, S.; Luo, X.; Tulus, V.; Wang, M.; Sheng, X.; Ren, L.; Long, X.; Li, J.; He, P.; Lin, H.; Cui, Y.; Peng, X.; Shi, J.; Wu, J.; Zhang, C.; Zou, R.; Guillén-Gosálbez, G.; Pérez-Ramírez, J.; Koh, M. J.; Zhu, Y.; Li, J.; Lu, J.Geminal-Atom Catalysis for Cross-Coupling. *Nature* **2023**, *622* (7984), 754–760. https://doi.org/10.1038/s41586-023-06529-z.

(7) He, T.; Santiago, A. R. P.; Kong, Y.; Ahsan, M. A.; Luque, R.; Du, A.; Pan, H.Atomically Dispersed Heteronuclear Dual-Atom Catalysts: A New Rising Star in Atomic Catalysis. *Small* **2022**, *18* (12).

(8) Kim, U. B.; Jung, D. J.; Jeon, H. J.; Rathwell, K.; Lee, S. G.Synergistic Dual Transition Metal Catalysis. *Chem. Rev.* **2020**, *120* (24), 13382–13433. https://doi.org/10.1021/acs.chemrev.0c00245.

(9) Zaera, F.Designing Sites in Heterogeneous Catalysis: Are We Reaching Selectivities Competitive with Those of Homogeneous Catalysts? *Chem. Rev.* **2021**.

(10) Poovan, F.; Chandrashekhar, V. G.; Natte, K.; Jagadeesh, R.V.Synergy between Homogeneous and Heterogeneous Catalysis. *Catal. Sci. Technol.* **2022**, *12* (22), 6623–6649. https://doi.org/10.1039/d2cy00232a.

(11) Liu, L.; Díaz, U.; Arenal, R.; Agostini, G.; Concepción, P.; Corma, A.Generation of Subnanometric Platinum with High Stability during Transformation of a 2D Zeolite into 3D. *Nat. Mater.* **2017**, *16* (1), 132–138.

(12) Fang, X.; Shang, Q.; Wang, Y.; Jiao, L.; Yao, T.; Li, Y.; Zhang, Q.; Luo, Y.; Jiang, H.-L.Single Pt Atoms Confined into a Metal-Organic Framework for Efficient Photocatalysis. *Adv. Mater.* **2018**, *30* (7), 1705112. https://doi.org/10.1002/adma.201705112.

(13) Jiao, L.; Wan, G.; Zhang, R.; Zhou, H.; Yu, S. H.; Jiang, H. L.From Metal–Organic

Frameworks to Single-Atom Fe Implanted N-Doped Porous Carbons: Efficient Oxygen Reduction in Both Alkaline and Acidic Media. *Angew. Chem. Int. Ed.* **2018**, *57* (28), 8525–8529. https://doi.org/10.1002/anie.201803262.

(14) Wang, X.; Chen, Z.; Zhao, X.; Yao, T.; Chen, W.; You, R.; Zhao, C.; Wu, G.; Wang, J.; Huang, W.; Yang, J.; Hong, X.; Wei, S.; Wu, Y.; Li, Y.Regulation of Coordination Number over Single Co Sites: Triggering the Efficient Electroreduction of CO 2. *Angew. Chem. Int. Ed.* **2018**, *130* (7), 1962–1966. https://doi.org/10.1002/ange.201712451.

(15) Wu, C.; Zhao, M.Incorporation of Molecular Catalysts in Metal–Organic Frameworks for Highly Efficient Heterogeneous Catalysis. *Advanced Materials*. Wiley Online Library 2017, p 1605446. https://doi.org/10.1002/adma.201605446.

(16) Zhang, Y.; Feng, X.; Yuan, S.; Zhou, J.; Wang, B.Challenges and Recent Advances in MOF-Polymer Composite Membranes for Gas Separation. *Inorg. Chem. Front.* **2016**, *3* (7), 896–909. https://doi.org/10.1039/c6qi00042h.

(17) Guo, N.; Li, L.; Marks, T. J.Bimetallic Catalysis for Styrene Homopolymerization and Ethylene− Styrene Copolymerization. Exceptional Comonomer Selectivity and Insertion Regiochemistry. *J. Am. Chem. Soc.* **2004**, *126* (21), 6542–6543.

(18) Xiao, P.; Osuga, R.; Wang, Y.; Kondo, J. N.; Yokoi, T.Bimetallic Fe-Cu/Beta Zeolite Catalysts for Direct Hydroxylation of Benzene to Phenol: Effect of the Sequence of Ion Exchange for Fe and Cu Cations. *Catal. Sci. Technol.* **2020**, *10* (20), 6977–6986. https://doi.org/10.1039/d0cy01216e.

(19) Zhang, W.; Chen, J.; Liu, R.; Wang, S.; Chen, L.; Li, K.Hydrodeoxygenation of Lignin-Derived Phenolic Monomers and Dimers to Alkane Fuels over Bifunctional Zeolite-Supported Metal Catalysts. *ACS Sustain. Chem. Eng.* **2014**, *2* (4), 683–691. https://doi.org/10.1021/sc400401n.

(20) Wang, Y.; Wang, G.; van derWal, L. I.; Cheng, K.; Zhang, Q.; deJong, K. P.; Wang, Y.Visualizing Element Migration over Bifunctional Metal-Zeolite Catalysts and Its Impact on Catalysis. *Angew. Chem. Int. Ed.* **2021**, *133* (32), 17876–17884. https://doi.org/10.1002/ange.202107264.

(21) Lo, B. T. W.; Ye, L.; Tsang, S. C. E.The Contribution of Synchrotron X-Ray Powder Diffraction to Modern Zeolite Applications: A Mini-Review and Prospects. *Chem* **2018**, *4* (8), 1778–1808. https://doi.org/10.1016/j.chempr.2018.04.018.

(22) Lin, W. C.; Wu, S.; Li, G.; Ho, P. L.; Ye, Y.; Zhao, P.; Day, S.; Tang, C.; Chen, W.; Zheng, A.; Lo, B. T. W.; Edman Tsang, S. C.Cooperative Catalytically Active Sites for Methanol Activation by Single Metal Ion-Doped H-ZSM-5. *Chem. Sci.* **2021**, *12* (1), 210–219. https://doi.org/10.1039/d0sc04058d.

(23) Topsøe, N. Y.; Pedersen, K.; Derouane, E. G.Infrared and Temperature-Programmed Desorption Study of the Acidic Properties of ZSM-5-Type Zeolites. *J. Catal.* **1981**, *70* (1), 41–52. https://doi.org/10.1016/0021-9517(81)90315-8.

(24) Hidalgo, C.V.; Itoh, H.; Hattori, T.; Niwa, M.; Murakami, Y.Measurement of the Acidity of Various Zeolites by Temperature-Programmed Desorption of Ammonia. *J. Catal.* **1984**, *85* (2), 362–369. https://doi.org/10.1016/0021-9517(84)90225-2.

(25) Jones, A. J.; Carr, R. T.; Zones, S. I.; Iglesia, E.Acid Strength and Solvation in Catalysis by MFI Zeolites and Effects of the Identity, Concentration and Location of Framework Heteroatoms. *J. Catal.* **2014**, *312*, 58–68. https://doi.org/10.1016/j.jcat.2014.01.007.

(26) Meng, L.; Zhu, X.; Mezari, B.; Pestman, R.; Wannapakdee, W.; Hensen, E. J. M.On the Role of Acidity in Bulk and Nanosheet [T]MFI (T=Al3+, Ga3+, Fe3+, B3+) Zeolites in the Methanol-to-Hydrocarbons Reaction. *ChemCatChem* **2017**, *9* (20), 3942–3954. https://doi.org/10.1002/cctc.201700916.

(27) Parry, E. P.An Infrared Study of Pyridine Adsorbed Solids. Characterisatization of Surface Acidity. *J. Catal.* **1963**, *2*, 371–379.

(28) Cardona-Martínez, N.; Dumesic, J. A.Acid Strength of Silica-Alumina and Silica Studied by Microcalorimetric Measurements of Pyridine Adsorption. *J. Catal.* **1990**, *125* (2), 427–444. https://doi.org/10.1016/0021-9517(90)90316-C.

(29) Ma, Y. K.; Rigolet, S.; Michelin, L.; Paillaud, J. L.; Mintova, S.; Khoerunnisa, F.; Daou, T. J.; Ng, E. P.Facile and Fast Determination of Si/Al Ratio of Zeolites Using FTIR Spectroscopy Technique. *Microporous Mesoporous Mater.* **2021**, *311* (August 2020), 110683. https://doi.org/10.1016/j.micromeso.2020.110683.

(30) Lo, B. T. W.; Ye, L.; Qu, J.; Sun, J.; Zheng, J.; Kong, D.; Murray, C. A.; Tang, C. C.; Tsang, S. C. E.Elucidation of Adsorbate Structures and Interactions on Brønsted Acid Sites in H-ZSM-5 by Synchrotron X-ray Powder Diffraction. *Angew. Chem. Int. Ed.* **2016**, *55* (20), 6085–6088. https://doi.org/10.1002/ange.201600487.

(31) Gonzalez-Olmos, R.; Holzer, F.; Kopinke, F. D.; Georgi, A.Indications of the Reactive Species in a Heterogeneous Fenton-like Reaction Using Fe-Containing Zeolites. *Appl. Catal. A Gen.* **2011**, *398* (1–2), 44–53. https://doi.org/10.1016/j.apcata.2011.03.005.

(32) He, J.; Yang, X.; Men, B.; Wang, D.Interfacial Mechanisms of Heterogeneous Fenton Reactions Catalyzed by Iron-Based Materials: A Review. *J. Environ. Sci. (China)* **2016**, *39*, 97–109. https://doi.org/10.1016/j.jes.2015.12.003.

(33) Zhang, M.; Wang, X.Preparation of a Gangue-Based X-Type Zeolite Molecular Sieve as a Multiphase Fenton Catalyst and Its Catalytic Performance. *ACS Omega* **2021**, *6* (28), 18414–18425. https://doi.org/10.1021/acsomega.1c02469.

(34) Lyu, L.; Zhang, L.; Hu, C.Enhanced Fenton-like Degradation of Pharmaceuticals over Framework Copper Species in Copper-Doped Mesoporous Silica Microspheres. *Chem. Eng. J.* **2015**, *274*, 298–306. https://doi.org/10.1016/j.cej.2015.03.137.

(35) Angi, A.; Sanli, D.; Erkey, C.; Birer, Ö.Catalytic Activity of Copper (II) Oxide Prepared via Ultrasound Assisted Fenton-like Reaction. *Ultrason. Sonochem.* **2014**, *21* (2), 854–859. https://doi.org/10.1016/j.ultsonch.2013.09.006.

(36) Mestivier, M.; Li, J. R.; Camy, A.; Frangville, C.; Mingotaud, C.; Benoît-Marquié, F.; Marty, J. D.Copper-Based Hybrid Polyion Complexes for Fenton-Like Reactions. *Chem. - Eur. J.* **2020**, *26* (62), 14152–14158. https://doi.org/10.1002/chem.202002362.

(37) Luo, Y.; Kustin, K.; Epstein, I. R.Kinetics and Mechanism of H2O2 Decomposition Catalyzed by Cu2+ in Alkaline Solution. *Inorg. Chem.* **1988**, *27* (14), 2489–2496. https://doi.org/10.1021/ic00287a023.

(38) Lee, H. J.; Lee, H.; Lee, C.Degradation of Diclofenac and Carbamazepine by the Copper(II)-Catalyzed Dark and Photo-Assisted Fenton-like Systems. *Chem. Eng. J.* **2014**, *245*, 258–264. https://doi.org/10.1016/j.cej.2014.02.037.

(39) Huang, K.; Guo, L. L.; Wu, D. F.Synthesis of Nanorod MOF Catalyst Containing Cu2+ and Its Selective Oxidation of Styrene. *Mater. Res. Express* **2019**, *6* (12).

(40) Liu, J.; Wang, Z.; Jian, P.; Jian, R.Highly Selective Oxidation of Styrene to Benzaldehyde over a Tailor-Made Cobalt Oxide Encapsulated Zeolite Catalyst. *J. Colloid Interface Sci.* **2018**, *517*, 144–154. https://doi.org/10.1016/j.jcis.2018.01.113.

(41) Lin, L.; Sheveleva, A. M.; daSilva, I.; Parlett, C. M. A.; Tang, Z.; Liu, Y.; Fan, M.; Han, X.; Carter, J. H.; Tuna, F.; McInnes, E. J. L.; Cheng, Y.; Daemen, L. L.; Rudić, S.; Ramirez-Cuesta, A. J.; Tang, C. C.; Yang, S.Quantitative Production of Butenes from Biomass-Derived γ-Valerolactone Catalysed by Hetero-Atomic MFI Zeolite. *Nat. Mater.* **2020**, *19* (1), 86–93. https://doi.org/10.1038/s41563-019-0562-6.

(42) Ye, L.; Song, Q.; Lo, B. T. W.; Zheng, J.; Kong, D.; Murray, C. A.; Tang, C. C.; Tsang, S. C. E.Decarboxylation of Lactones over Zn/ZSM-5: Elucidation of the Structure of the Active Site and Molecular Interactions. *Angew. Chem. Int. Ed.* **2017**, *56* (36), 10711–10716. https://doi.org/10.1002/anie.201704347.

(43) Zhao, Z.; Yang, C.; Sun, P.; Gao, G.; Liu, Q.; Huang, Z.; Li, F.Synergistic Catalysis for Promoting Ring-Opening Hydrogenation of Biomass-Derived Cyclic Oxygenates. *ACS Catal.* **2023**, *13* (8), 5170–5193. https://doi.org/10.1021/acscatal.3c00317.

(44) Bond, J. Q.; Wang, D.; Alonso, D. M.; Dumesic, J. A.Interconversion between γ-Valerolactone and Pentenoic Acid Combined with Decarboxylation to Form Butene over Silica/Alumina. *J. Catal.* **2011**, *281* (2), 290–299. https://doi.org/10.1016/j.jcat.2011.05.011.

(45) Wang, H.; Wu, Y.; Guo, S.; Dong, C.; Ding, M.γ-Valerolactone Converting to Butene via Ring-Opening and Decarboxylation Steps over Amorphous SiO2-Al2O3 Catalyst. *Mol. Catal.* **2020**, *497* (October).

5.6 Supplementary information for Chapter 5

Table 5.1. Crystallographic data of the synchrotron PXRD measurement of the zeolite samples labelled.

	Fe/Al-Z	Fe/Ga-Z	Fe/B-Z	Cu/Al-Z	Cu/Ga-Z	Cu/B-Z
X-ray energy (keV)	17.7	17.7	17.7	17	17	17
Beamline	Spring-8 BL02B2	Spring-8 BL02B2	Spring-8 BL02B2	Spring-8 BL02B2	Spring-8 BL02B2	Spring-8 BL02B2
Wavelength (Å) (synchrotron)	0.700261	0.700261	0.700261	0.729589	0.729589	0.729589
2θ – zero point (°)	0.00020	0.00020	0.00020	-0.00019	-0.00019	-0.00019
Space group	*Pnma*	*Pnma*	*Pnma*	*Pnma*	*Pnma*	*Pnma*
Crystal system	Orthorhombic	Orthorhombic	Orthorhombic	Orthorhombic	Orthorhombic	Orthorhombic
a (Å)	20.13162(15)	20.11702(17)	20.08193(27)	20.14844(16)	20.12378(21)	20.04048(11)
b (Å)	19.93828(16)	19.91554(19)	19.86314(31)	19.94904(16)	19.91965(24)	19.85013(10)
c (Å)	13.41994(14)	13.40324(15)	13.37000(22)	13.42828(14)	13.40730(18)	13.36017(7)
V (Å^3)	5386.63(8)	5369.89(9)	5333.16(14)	5397.39(8)	5374.43(11)	5314.76(5)
2θ range for refinement (°)	2-50	2-50	2-50	3-50	3-50	3-50
Detector	MYTHEN	MYTHEN	MYTHEN	MYTHEN	MYTHEN	MYTHEN
Number of parameters	27	27	29	27	27	27
Number of *hkl*s	5241	5246	5246	4648	4647	4580
Refinement methods	LeBail	LeBail	LeBail	LeBail	LeBail	LeBail
$R_{wp}/R_{exp}/R_p$ (%)	2.905/0.694/2.059	5.906/0.791/3.657	10.759/0.737/6.108	3.404/0.831/2.342	5.631/0.760/3.520	6.780/0.761/4.275
Gof	4.189	7.465	14.594	4.095	7.414	8.913

R_{wp}: weighted profile; R_{exp}: expected; R_p: profile; *gof:* goodness-of-fit.

Table 5.2. Summary of the acidity of the zeolite samples. Values were determined by combined NH_3-TPD and Py-FTIR results.

Catalyst	strong/weak acid ratio [a]	B/L acid ratio [b]
Fe/Al-Z	0.255	0.50
Fe/Ga-Z	0.211	0.481
Fe/B-Z	0.006	0.213
Cu/Al-Z	0.700	0.796
Cu/Ga-Z	0.437	0.664
Cu/B-Z	0.377	0.617

a. From NH_3-TPD
b. From Py-FTIR

Table 5.3. Crystallographic data of the synchrotron PXRD measurements of the pyridine pre-adsorbed zeolite samples.

	Py-Fe/Al-Z	**Py-Fe/Ga-Z**	**Py-Fe/B-Z**	**Py-Cu/Al-Z**	**Py-Cu/Ga-Z**	**Py-Cu/B-Z**
X-ray energy (keV)	17.7	17.7	17.7	17	17	17
Beamline	Spring-8 BL02B2	Spring-8 BL02B2	Spring-8 BL02B2	Spring-8 BL02B2	Spring-8 BL02B2	Spring-8 BL02B2
Wavelength (Å)	0.700261	0.700261	0.700261	0.729589	0.729589	0.729589
2θ – zero point (°)	0.00020	0.00020	0.00020	-0.00019	-0.00019	-0.00019
Space group	*Pnma*	*Pnma*	*Pnma*	*Pnma*	*Pnma*	*Pnma*
Crystal system	Orthorhombic	Orthorhombic	Orthorhombic	Orthorhombic	Orthorhombic	Orthorhombic
a (Å)	20.07500(32)	20.11925(10)	20.08267(24)	20.11861(20)	20.10727(13)	20.03008(10)
b (Å)	19.87873(27)	19.89772(10)	19.85981(29)	19.95147(20)	19.92729(14)	19.83891(10)
c (Å)	13.40706(22)	13.42167(9)	13.38353(23)	13.44488(19)	13.41986(12)	13.35547(8)
V (Å^3)	5350.30(14)	5373.06(5)	5337.86(14)	5396.72(11)	5377.12(7)	5307.13(5)
2θ range for refinement (°)	2-50	2-50	2-50	3-50	3-50	3-50
Detector	MYTHEN	MYTHEN	MYTHEN	MYTHEN	MYTHEN	MYTHEN
Number of parameters	28	24	24	27	27	27
Number of *hkl*s	5256	5249	5212	4644	4658	4576
Refinement methods	LeBail	LeBail	LeBail	LeBail	LeBail	LeBail
$R_{wp}/R_{exp}/R_p$ (%)	3.689/0.726/2.547	3.558/0.746/2.513	9.897/0.759/5.893	3.263/0.865/2.232	3.936/0.736/2.724	7.055/0.733/4.255
Gof	5.084	4.770	13.042	3.770	5.346	9.622

R_{wp}: weighted profile; R_{exp}: expected; R_p: profile; *gof:* goodness-of-fit.

Table 5.4. Atomic parameters of Py-Fe/Al-Z derived from synchrotron PXRD.

Species	Atom	x	y	z	SOF	B_{eq}	Wyckoff
Zeolite	O1	0.36489	0.05895	0.76052	1	1.3968	8d
framework	O2	0.30581	0.06876	0.92451	1	1.3968	8d
	O3	0.20497	0.05808	0.01484	1	1.3968	8d
	O4	0.08619	0.06535	0.92424	1	1.3968	8d
	O5	0.13149	0.04593	0.75060	1	1.3968	8d
	O6	0.25258	0.05714	0.72809	1	1.3968	8d
	O7	0.37456	0.85138	0.74921	1	1.3968	8d
	O8	0.28716	0.83291	0.91950	1	1.3968	8d
	O9	0.19531	0.84373	0.05442	1	1.3968	8d
	O10	0.06315	0.84501	0.93008	1	1.3968	8d
	O11	0.10665	0.84750	0.71981	1	1.3968	8d
	O12	0.23507	0.83455	0.75581	1	1.3968	8d
	O13	0.30894	0.94376	0.81333	1	1.3968	8d
	O14	0.06832	0.95430	0.81205	1	1.3968	8d
	O15	0.41385	0.13021	0.56598	1	1.3968	8d
	O16	0.42853	0.98767	0.58886	1	1.3968	8d
	O17	0.41367	0.87903	0.58130	1	1.3968	8d
	O18	0.17407	0.13535	0.60737	1	1.3968	8d
	O19	0.20533	-0.01364	0.62343	1	1.3968	8d
	O20	0.18998	0.85092	0.60966	1	1.3968	8d
	O21	0.99350	0.05423	0.79371	1	1.3968	8d
	O22	0.99546	0.85280	0.79006	1	1.3968	8d
	O23	0.40563	0.75000	0.65828	1	1.3968	4c
	O24	0.19533	0.75000	0.63190	1	1.3968	4c
	O25	0.29224	0.75000	0.06621	1	1.3968	4c
	O26	0.11226	0.75000	0.04182	1	1.3968	4c
	Si1	0.41588	0.06002	0.65566	1	0.6984	8d
	Si2	0.30885	0.02717	0.81515	1	0.6984	8d
	Si3	0.28282	0.06965	0.03070	1	0.6984	8d
	Si4	0.10963	0.05713	0.02639	1	0.6984	8d
	Si5	0.06686	0.03197	0.80184	1	0.6984	8d
	Si6	0.18062	0.06305	0.66747	1.46553	0.6984	8d
	Si7	0.42248	0.82219	0.67922	1	0.6984	8d
	Si8	0.31064	0.86594	0.80821	1	0.6984	8d
	Si9	0.26734	0.82841	0.03037	1	0.6984	8d
	Si10	0.11923	0.82804	0.03326	1	0.6984	8d
	Si11	0.07491	0.86887	0.82600	1	0.6984	8d
	Si12	0.18000	0.83054	0.69340	1	0.6984	8d
Pyridine1	C1	0.29611	0.25616	-0.12414	0.5574	8	8d
	C2	0.24489	0.26873	-0.05686	0.5574	8	8d
	C3	0.17946	0.25882	-0.08599	0.5574	8	8d
	C4	0.16463	0.23654	-0.18144	0.5574	8	8d
	C5	0.21586	0.22398	-0.24871	0.5574	8	8d
	C6	0.28128	0.23389	-0.21955	0.5574	8	8d
Pyridne2	C11	1.49595	1.06343	0.99928	0.8615	8	8d
	C12	1.52140	1.11003	1.06661	0.8615	8	8d
	C13	1.52747	1.17675	1.03839	0.8615	8	8d
	C14	1.50844	1.19743	0.94382	0.8615	8	8d
	C15	1.48300	1.15082	0.87651	0.8615	8	8d
	C16	1.47693	1.08410	0.90476	0.8615	8	8d

Table 5.5. Atomic parameters of Py-Fe/Ga-Z derived from synchrotron PXRD.

Species	Atom	x	y	z	SOF	B_{eq}	Wyckoff
Zeolite	O1	0.38268	0.03934	0.77104	1	2.1229	8d
framework	O2	0.31300	0.05796	0.92671	1	2.1229	8d
	O3	0.20511	0.05954	0.01852	1	2.1229	8d
	O4	0.09447	0.06888	0.92945	1	2.1229	8d
	O5	0.12441	0.04678	0.72699	1	2.1229	8d
	O6	0.24949	0.06889	0.75204	1	2.1229	8d
	O7	0.38450	0.84531	0.76885	1	2.1229	8d
	O8	0.30274	0.83968	0.91213	1	2.1229	8d
	O9	0.17806	0.84774	0.03699	1	2.1229	8d
	O10	0.08236	0.84801	0.92496	1	2.1229	8d
	O11	0.12400	0.84654	0.73464	1	2.1229	8d
	O12	0.24606	0.84447	0.78334	1	2.1229	8d
	O13	0.31719	0.94580	0.82964	1	2.1229	8d
	O14	0.07406	0.95174	0.81895	1	2.1229	8d
	O15	0.41565	0.12973	0.59613	1	2.1229	8d
	O16	0.40656	0.98884	0.59120	1	2.1229	8d
	O17	0.39583	0.85995	0.54944	1	2.1229	8d
	O18	0.19785	0.13575	0.63850	1	2.1229	8d
	O19	0.19555	-0.00584	0.60311	1	2.1229	8d
	O20	0.20627	0.85657	0.60028	1	2.1229	8d
	O21	1.00118	0.05020	0.79470	1	2.1229	8d
	O22	0.99382	0.84499	0.77493	1	2.1229	8d
	O23	0.42618	0.75000	0.66379	1	2.1229	4c
	O24	0.20461	0.75000	0.64077	1	2.1229	4c
	O25	0.28291	0.75000	0.07395	1	2.1229	4c
	O26	0.10080	0.75000	0.08383	1	2.1229	4c
	Si1	0.42004	0.05590	0.67607	1	1.0615	8d
	Si2	0.31375	0.03331	0.82453	1	1.0615	8d
	Si3	0.27790	0.05802	0.03514	1	1.0615	8d
	Si4	0.12600	0.06903	0.02551	1	1.0615	8d
	Si5	0.07350	0.03000	0.81142	1	1.0615	8d
	Si6	0.18643	0.05876	0.67353	1.3352	1.0615	8d
	Si7	0.42408	0.82079	0.67652	1	1.0615	8d
	Si8	0.31398	0.86789	0.82429	1	1.0615	8d
	Si9	0.27296	0.83727	0.02946	1	1.0615	8d
	Si10	0.11590	0.82225	0.04499	1	1.0615	8d
	Si11	0.07819	0.87413	0.80908	1	1.0615	8d
	Si12	0.19243	0.82855	0.69073	1	1.0615	8d
Pyridine1		0.03586	-0.26355	0.35748	0.5843	8	8d
		-0.03098	-0.24679	0.36829	0.5843	8	8d
		-0.04886	-0.19467	0.43145	0.5843	8	8d
		-0.00080	-0.15914	0.48387	0.5843	8	8d
		0.06603	-0.17591	0.47304	0.5843	8	8d
		0.08389	-0.22804	0.40988	0.5843	8	8d
Water1		0.34558	0.75163	0.37933	0.4580	8	8d
Water2		0.22994	0.18872	0.40248	0.0221	8	8d

Table 5.6. Atomic parameters of Py-Fe/B-Z derived from synchrotron PXRD.

Species	Atom	x	y	z	SOF	B_{eq}	Wyckoff
Zeolite	O1	0.37686	0.04813	0.75883	1	1.3739	8d
framework	O2	0.31082	0.05507	0.91713	1	1.3739	8d
	O3	0.20112	0.06355	0.00433	1	1.3739	8d
	O4	0.10336	0.06510	0.93051	1	1.3739	8d
	O5	0.11462	0.05350	0.71909	1	1.3739	8d
	O6	0.23998	0.07514	0.77006	1	1.3739	8d
	O7	0.38211	0.84393	0.78430	1	1.3739	8d
	O8	0.30744	0.82999	0.91451	1	1.3739	8d
	O9	0.18633	0.85661	0.04354	1	1.3739	8d
	O10	0.07853	0.85774	0.91971	1	1.3739	8d
	O11	0.12928	0.83790	0.73223	1	1.3739	8d
	O12	0.24089	0.85367	0.76425	1	1.3739	8d
	O13	0.31564	0.95104	0.81424	1	1.3739	8d
	O14	0.07100	0.94595	0.81238	1	1.3739	8d
	O15	0.41916	0.13031	0.60349	1	1.3739	8d
	O16	0.40138	1.00008	0.56399	1	1.3739	8d
	O17	0.39111	0.85156	0.53447	1	1.3739	8d
	O18	0.19802	0.13670	0.62161	1	1.3739	8d
	O19	0.19283	0.00538	0.59552	1	1.3739	8d
	O20	0.20297	0.86667	0.59320	1	1.3739	8d
	O21	0.99966	0.05396	0.78808	1	1.3739	8d
	O22	1.00021	0.86091	0.76028	1	1.3739	8d
	O23	0.43089	0.75000	0.67678	1	1.3739	4c
	O24	0.20800	0.75000	0.65755	1	1.3739	4c
	O25	0.27639	0.75000	0.06768	1	1.3739	4c
	O26	0.10781	0.75000	0.06329	1	1.3739	4c
	Si1	0.42603	0.04914	0.66672	1	0.6870	8d
	Si2	0.31552	0.03263	0.83019	1.2406	0.6870	8d
	Si3	0.27740	0.04952	0.03991	1	0.6870	8d
	Si4	0.12019	0.06579	0.03123	1	0.6870	8d
	Si5	0.07302	0.03374	0.81956	1	0.6870	8d
	Si6	0.18431	0.06092	0.66666	1	0.6870	8d
	Si7	0.42603	0.82580	0.66790	1	0.6870	8d
	Si8	0.31308	0.87107	0.81985	1	0.6870	8d
	Si9	0.26675	0.83436	0.03648	1	0.6870	8d
	Si10	0.11622	0.82232	0.03135	1	0.6870	8d
	Si11	0.07850	0.86881	0.80555	1	0.6870	8d
	Si12	0.19522	0.83413	0.68868	1	0.6870	8d
Pyridine1	C1	0.04470	-0.23737	0.30234	0.4561	8	8d
	C2	-0.02150	-0.25693	0.31341	0.4561	8	8d
	C3	-0.04038	-0.29362	0.39692	0.4561	8	8d
	C4	0.00606	-0.31097	0.46940	0.4561	8	8d
	C5	0.07226	-0.29141	0.45831	0.4561	8	8d
	C6	0.09112	-0.25472	0.37479	0.4561	8	8d

Table 5.7. Atomic parameters of Py-Cu/Al-Z derived from synchrotron PXRD.

Species	Atom	x	y	z	SOF	B_{eq}	Wyckoff
Zeolite	O1	0.37683	0.04816	0.74754	1	1.73028	8d
framework	O2	0.29809	0.05837	0.92673	1	1.73028	8d
	O3	0.21354	0.05358	0.04447	1	1.73028	8d
	O4	0.08659	0.05702	0.90951	1	1.73028	8d
	O5	0.11294	0.03731	0.72367	1	1.73028	8d
	O6	0.25456	0.05534	0.74653	1	1.73028	8d
	O7	0.37972	0.83551	0.76924	1	1.73028	8d
	O8	0.30661	0.85235	0.91195	1	1.73028	8d
	O9	0.21161	0.84457	0.01736	1	1.73028	8d
	O10	0.09950	0.84568	0.89937	1	1.73028	8d
	O11	0.12851	0.84325	0.73351	1	1.73028	8d
	O12	0.24376	0.85654	0.75179	1	1.73028	8d
	O13	0.29490	0.93761	0.82243	1	1.73028	8d
	O14	0.06969	0.94733	0.82745	1	1.73028	8d
	O15	0.40670	0.13603	0.60248	1	1.73028	8d
	O16	0.40599	0.99239	0.58265	1	1.73028	8d
	O17	0.39184	0.85596	0.56116	1	1.73028	8d
	O18	0.18491	0.13497	0.62303	1	1.73028	8d
	O19	0.18690	0.00013	0.60171	1	1.73028	8d
	O20	0.20119	0.86092	0.58828	1	1.73028	8d
	O21	0.99829	0.04366	0.79344	1	1.73028	8d
	O22	0.98284	0.84344	0.79409	1	1.73028	8d
	O23	0.42394	0.75000	0.63228	1	1.73028	4c
	O24	0.19235	0.75000	0.62993	1	1.73028	4c
	O25	0.29512	0.75000	0.06288	1	1.73028	4c
	O26	0.08843	0.75000	0.07474	1	1.73028	4c
	Si1	0.41990	0.05046	0.66656	1	0.86514	8d
	Si2	0.30985	0.03005	0.82155	1	0.86514	8d
	Si3	0.28108	0.06204	0.03101	1	0.86514	8d
	Si4	0.12670	0.06599	0.01801	1	0.86514	8d
	Si5	0.07896	0.03510	0.80796	1	0.86514	8d
	Si6	0.18143	0.05175	0.67912	1	0.86514	8d
	Si7	0.42141	0.82333	0.67058	1	0.86514	8d
	Si8	0.31151	0.87186	0.81409	1	0.86514	8d
	Si9	0.28364	0.82978	0.01591	1	0.86514	8d
	Si10	0.12084	0.82212	0.03599	1	0.86514	8d
	Si11	0.06746	0.86416	0.81743	1	0.86514	8d
	Si12	0.18891	0.82671	0.66548	1.2588	0.86514	8d
Pyridine1	C1	0.43910	-0.61872	-0.10331	0.7707	8	8d
	C2	0.45177	-0.68734	-0.10663	0.7707	8	8d
	C3	0.49518	-0.71558	-0.03825	0.7707	8	8d
	C4	0.52603	-0.67611	0.03329	0.7707	8	8d
	C5	0.51335	-0.60750	0.03659	0.7707	8	8d
	C6	0.46994	-0.57927	-0.03179	0.7707	8	8d
Water1	O1	0.11394	0.25040	0.85654	1.0405	8	8d
Water2	O2	0.12562	0.22440	0.59923	0.4039	8	8d

Table 5.8. Atomic parameters of Py-Cu/Ga-Z derived from synchrotron PXRD.

Species	Atom	x	y	z	SOF	B_{eq}	Wyckoff
Zeolite	O1	0.37115	0.05338	0.73877	1	1.73028	8d
framework	O2	0.29811	0.06846	0.91865	1	1.73028	8d
	O3	0.20658	0.05291	0.02585	1	1.73028	8d
	O4	0.09055	0.06139	0.91139	1	1.73028	8d
	O5	0.11633	0.06366	0.71292	1	1.73028	8d
	O6	0.24231	0.06636	0.75527	1	1.73028	8d
	O7	0.37792	0.82977	0.76290	1	1.73028	8d
	O8	0.31106	0.84951	0.90643	1	1.73028	8d
	O9	0.19279	0.84983	0.01429	1	1.73028	8d
	O10	0.09498	0.84282	0.92890	1	1.73028	8d
	O11	0.10994	0.84340	0.71516	1	1.73028	8d
	O12	0.24678	0.86012	0.74223	1	1.73028	8d
	O13	0.30036	0.94221	0.80679	1	1.73028	8d
	O14	0.06981	0.95310	0.82639	1	1.73028	8d
	O15	0.41049	0.11876	0.59935	1	1.73028	8d
	O16	0.41309	0.99160	0.60043	1	1.73028	8d
	O17	0.40538	0.87180	0.56497	1	1.73028	8d
	O18	0.19275	0.13100	0.61485	1	1.73028	8d
	O19	0.19208	0.00555	0.58138	1	1.73028	8d
	O20	0.19447	0.86146	0.57770	1	1.73028	8d
	O21	0.99912	0.05077	0.77639	1	1.73028	8d
	O22	1.00011	0.84962	0.79174	1	1.73028	8d
	O23	0.41884	0.75000	0.66564	1	1.73028	4c
	O24	0.18917	0.75000	0.64342	1	1.73028	4c
	O25	0.28740	0.75000	0.05324	1	1.73028	4c
	O26	0.10720	0.75000	0.06186	1	1.73028	4c
	Si1	0.42528	0.05528	0.66165	1	0.86514	8d
	Si2	0.30748	0.03036	0.81113	1	0.86514	8d
	Si3	0.28124	0.05841	0.02461	1	0.86514	8d
	Si4	0.12326	0.06258	0.01881	1	0.86514	8d
	Si5	0.07288	0.02706	0.80679	1	0.86514	8d
	Si6	0.18729	0.06060	0.67089	1.3346	0.86514	8d
	Si7	0.42449	0.82800	0.66878	1	0.86514	8d
	Si8	0.30633	0.87313	0.80566	1	0.86514	8d
	Si9	0.27574	0.83032	0.01955	1	0.86514	8d
	Si10	0.11869	0.82598	0.03602	1	0.86514	8d
	Si11	0.07019	0.86645	0.81723	1	0.86514	8d
	Si12	0.18497	0.82688	0.67716	1	0.86514	8d
Pyridine1	C1	0.05862	0.73253	-0.66085	0.4879	8	8d
	C2	0.08377	0.67720	-0.60975	0.4879	8	8d
	C3	0.04579	0.64725	-0.53577	0.4879	8	8d
	C4	-0.01694	0.67190	-0.51229	0.4879	8	8d
	C5	-0.04207	0.72723	-0.56340	0.4879	8	8d
	C6	-0.00408	0.75717	-0.63737	0.4879	8	8d
Water1	O1	-0.00702	0.03260	0.43392	0.4575	8	8d
Water2	O2	0.10580	0.26810	0.85863	0.5791	8	8d

Table 5.9. Atomic parameters of Py-Cu/B-Z derived from synchrotron PXRD.

Species	Atom	x	y	z	SOF	B_{eq}	Wyckoff
Zeolite	O1	0.37508	0.06038	0.75351	1	2.2312	8d
framework	O2	0.30733	0.05869	0.92335	1	2.2312	8d
	O3	0.20230	0.05912	0.02514	1	2.2312	8d
	O4	0.09469	0.06431	0.91276	1	2.2312	8d
	O5	0.11415	0.05582	0.72545	1	2.2312	8d
	O6	0.24312	0.04591	0.74803	1	2.2312	8d
	O7	0.37226	0.84182	0.76217	1	2.2312	8d
	O8	0.30750	0.84712	0.92267	1	2.2312	8d
	O9	0.19684	0.84769	0.02825	1	2.2312	8d
	O10	0.08685	0.83435	0.92849	1	2.2312	8d
	O11	0.11645	0.84412	0.72622	1	2.2312	8d
	O12	0.24474	0.84269	0.76831	1	2.2312	8d
	O13	0.31583	0.95031	0.81533	1	2.2312	8d
	O14	0.08271	0.94847	0.82126	1	2.2312	8d
	O15	0.41965	0.13151	0.60694	1	2.2312	8d
	O16	0.41241	0.99690	0.58170	1	2.2312	8d
	O17	0.39948	0.86931	0.57510	1	2.2312	8d
	O18	0.19420	0.13006	0.61971	1	2.2312	8d
	O19	0.19092	0.00208	0.58938	1	2.2312	8d
	O20	0.19728	0.86770	0.58179	1	2.2312	8d
	O21	0.99691	0.04943	0.79070	1	2.2312	8d
	O22	0.99689	0.85216	0.78442	1	2.2312	8d
	O23	0.42376	0.75000	0.65543	1	2.2312	4c
	O24	0.19367	0.75000	0.64587	1	2.2312	4c
	O25	0.28429	0.75000	0.06250	1	2.2312	4c
	O26	0.10859	0.75000	0.05833	1	2.2312	4c
	Si1	0.42321	0.05822	0.66328	1	1.1156	8d
	Si2	0.30949	0.02954	0.81041	1	1.1156	8d
	Si3	0.27936	0.06171	0.03265	1	1.1156	8d
	Si4	0.12076	0.06316	0.02537	1	1.1156	8d
	Si5	0.07167	0.02922	0.81379	1	1.1156	8d
	Si6	0.18663	0.05912	0.67035	1	1.1156	8d
	Si7	0.42420	0.82784	0.67272	1	1.1156	8d
	Si8	0.30723	0.86909	0.81622	1	1.1156	8d
	Si9	0.27286	0.82842	0.03087	1	1.1156	8d
	Si10	0.11989	0.82699	0.03182	1	1.1156	8d
	Si11	0.07201	0.87121	0.81751	1	1.1156	8d
	Si12	0.18796	0.82687	0.68439	1.0842	1.1156	8d
Pyridine1	C1	-0.04342	-0.22608	0.45025	0.3862	8	8d
	C2	-0.01757	-0.16891	0.49685	0.3862	8	8d
	C3	0.04681	-0.14797	0.47449	0.3862	8	8d
	C4	0.08561	-0.18343	0.40621	0.3862	8	8d
	C5	0.05975	-0.24060	0.35962	0.3862	8	8d
	C6	-0.00464	-0.26153	0.38200	0.3862	8	8d
Water1	O1	-0.00422	0.02992	0.44724	0.2060	8	8d

Table 5.10. Element content of the zeolite samples.

Sample	Si (Atom%)	M (Fe, Cu) (Atomic %)	X (Al. Ga, B) (Atomic %)	Si:M	Si:X
Fe/Al-Z	88.20	1.92	9.88	1: 0.021	1: 0.112
Fe/Ga-Z	93.41	2.09	4.51	1: 0.022	1: 0.048
Fe/B-Z	96.82	1.45	1.73	1: 0.015	1: 0.018
Cu/Al-Z	91.79	1.23	6.98	1: 0.013	1: 0.076
Cu/Ga-Z	93.19	0.94	5.87	1: 0.010	1: 0.063
Cu/B-Z	95.48	0.84	3.68	1: 0.009	1: 0.038

Table 5.11. Occupancies of different T sites for Fe/X-Z by Rietveld refinement.

Occupancies	Fe/Al-Z	Fe/Ga-Z	Fe/B-Z
T1	1.3364	1.1594	0.9679
T2	1.2157	1.2235	**1.2786**
T3	1.1597	1.1788	1.1410
T4	0.8413	0.9102	0.6391
T5	0.9910	1.1033	1.0068
T6	**1.4610**	**1.3352**	1.2703
T7	0.6662	0.7214	0.6399
T8	1.1055	1.0372	1.2354
T9	1.1902	1.1406	1.2216
T10	0.9400	0.8666	0.8288
T11	0.7569	0.8250	0.9490
T12	0.9840	0.9800	1.0955

Table 5.12. Occupancies of different T sites for Cu/X-Z by Rietveld refinement.

Occupancies	Cu/Al-Z	Cu/Ga-Z	Cu/B-Z
T1	1.0790	1.1871	1.0000
T2	1.1216	1.0289	1.0483
T3	1.0290	1.0604	1.0010
T4	1.0002	1.0002	1.0003
T5	1.1109	1.1277	1.0148
T6	1.1861	**1.2906**	1.0617
T7	1.0574	1.0001	1.0098
T8	1.1698	1.0457	1.0389
T9	1.1310	1.1031	1.0461
T10	1.0514	1.0088	1.0070
T11	1.0263	1.0000	1.0005
T12	**1.2701**	1.1170	**1.0800**

Table 5.13. Fitting parameters for Fe K-edge EXAFS for the sample labelled.

Sample	Path	C.N.	R/Å	σ^2	ΔE	R-factor	k-range/Å^{-1}
Fe/Al	Fe–O	1.32 (8)	1.873(10)	0.0009(90)	-0.5 (4)	0.009	3-11
Fe/Al	Fe–O	3.06 (8)	2.059 (5)	0.0062(51)	-0.5 (4)	0.009	3-11
Fe/Al	Fe–O	4.44 (41)	3.001(13)	0.0210(86)	-0.5 (4)	0.009	3-11
Fe/Ga	Fe–O	3.01 (11)	1.825 (8)	0.0027(15)	-9.1 (5)	0.004	3-11
Fe/B	Fe–O	2.01 (6)	1.872(31)	0.0016(16)	-2.2 (3)	0.003	3-11
Fe/B	Fe–O	2.40 (5)	2.059 (4)	0.0022(27)	-2.2 (3)	0.003	3-11
Fe/B	Fe–O	4.88 (39)	2.974 (11)	0.0260(86)	-2.2 (3)	0.003	3-11

C.N. is the average coordination number around the central atoms. R and σ^2 are the average path length (Å) and the Debye factor (Å^2), respectively. The ΔE_0 values of the first shell are constrained to share the same value in the fitting models. The s_0^2 was fixed as 0.9 for all fitting.

Table 5.14. Fitting parameters for Cu K-edge EXAFS for the sample labeled.

Sample	Path	C.N.	R/Å	σ^2	ΔE	R-factor	k-range/Å^{-1}
Cu/Al	Cu–N/O	3.3(1)	1.959(7)	0.027(1)	-0.8(4)	0.008	3-11
Cu/Al	Cu–N/O	1.7(4)	2.864(21)	0.005	-0.8(4)	0.008	3-11
Cu/Ga	Cu–N/O	3.0(2)	1.950(10)	0.003(2)	-1.1(5)	0.020	3-11
Cu/Ga	Cu–N/O	1.6(4)	2.932(24)	0.002	-1.1(5)	0.020	3-11
Cu/B	Cu–N/O	3.3(1)	1.952(7)	0.003(1)	-2.3(3)	0.006	3-11
Cu/B	Cu–N/O	2.4(3)	2.846(14)	0.008(6)	-2.3(3)	0.006	3-11

C.N. is the average coordination number around the central atoms. R and σ^2 are the average path length (Å) and the Debye factor (Å^2), respectively. The ΔE_0 values of the first shell are constrained to share the same value in the fitting models. The s_0^2 was fixed as 0.9 for all fitting.

Table 5.15. Atomic parameters of Fe/Al-Z derived from synchrotron PXRD.

Species	Atom	x	y	z	SOF	B_{eq}	Wyckoff
Zeolite framework	O1	0.37995	0.06505	0.77466	1	1.2	8d
	O2	0.29840	0.06294	0.93825	1	1.2	8d
	O3	0.20062	0.05667	0.01049	1	1.2	8d
	O4	0.09196	0.04483	0.91863	1	1.2	8d
	O5	0.11423	0.05946	0.74148	1	1.2	8d
	O6	0.25062	0.06483	0.74034	1	1.2	8d
	O7	0.41931	0.84891	0.73863	1	1.2	8d
	O8	0.31426	0.84127	0.93028	1	1.2	8d
	O9	0.16434	0.83846	0.02039	1	1.2	8d
	O10	0.11745	0.87118	0.92897	1	1.2	8d
	O11	0.11951	0.85409	0.74143	1	1.2	8d
	O12	0.27462	0.85547	0.77080	1	1.2	8d
	O13	0.31258	0.99712	0.80324	1	1.2	8d
	O14	0.07323	0.87609	0.80518	1	1.2	8d
	O15	0.40009	0.25031	0.60888	1	1.2	8d
	O16	0.40615	0.97417	0.59746	1	1.2	8d
	O17	0.39894	0.88471	0.57718	1	1.2	8d
	O18	0.19543	0.13149	0.62111	1	1.2	8d
	O19	0.18527	-0.00006	0.57673	1	1.2	8d
	O20	0.19536	0.85570	0.58349	1	1.2	8d
	O21	1.00277	0.06246	0.79792	1	1.2	8d
	O22	0.99991	0.84253	0.79040	1	1.2	8d
	O23	0.42805	0.75000	0.67261	1	1.2	4c
	O24	0.19073	0.75000	0.63547	1	1.2	4c
	O25	0.32987	0.75000	0.05097	1	1.2	4c
	O26	0.11494	0.75000	0.04384	1	1.2	4c
	Si1	0.42871	0.06027	0.65935	1	0.6	8d
	Si2	0.31207	0.03855	0.81976	1	0.6	8d
	Si3	0.27885	0.05952	0.03252	1	0.6	8d
	Si4	0.12157	0.06155	0.04353	1	0.6	8d
	Si5	0.06426	0.03098	0.81211	1	0.6	8d
	Si6	0.19647	0.06422	0.67826	1.46553*	0.6	8d
	Si7	0.42832	0.82882	0.67608	1	0.6	8d
	Si8	0.31083	0.86841	0.82170	1	0.6	8d
	Si9	0.29063	0.82889	0.03312	1	0.6	8d
	Si10	0.11895	0.82988	0.03223	1	0.6	8d
	Si11	0.07387	0.86996	0.81198	1	0.6	8d
	Si12	0.18908	0.82651	0.67832	1	0.6	8d

Table 5.16. Atomic parameters of Fe/Ga-Z derived from synchrotron PXRD.

Species	Atom	x	y	z	SOF	B_{eq}	Wyckoff
Zeolite framework	O1	0.38133	0.05960	0.76617	1	1.4398	8d
	O2	0.30580	0.06053	0.91424	1	1.4398	8d
	O3	0.19432	0.06084	0.01228	1	1.4398	8d
	O4	0.09846	0.06169	0.91886	1	1.4398	8d
	O5	0.11918	0.05443	0.71804	1	1.4398	8d
	O6	0.25548	0.04437	0.75660	1	1.4398	8d
	O7	0.39208	0.84730	0.78530	1	1.4398	8d
	O8	0.30764	0.84096	0.91430	1	1.4398	8d
	O9	0.19398	0.84655	0.02954	1	1.4398	8d
	O10	0.08007	0.85374	0.92174	1	1.4398	8d
	O11	0.11128	0.84363	0.73470	1	1.4398	8d
	O12	0.22848	0.83628	0.76170	1	1.4398	8d
	O13	0.31080	0.93679	0.82497	1	1.4398	8d
	O14	0.07270	0.93017	0.81185	1	1.4398	8d
	O15	0.41660	0.13504	0.58744	1	1.4398	8d
	O16	0.40266	0.99628	0.56227	1	1.4398	8d
	O17	0.40404	0.86416	0.57133	1	1.4398	8d
	O18	0.19309	0.14498	0.62759	1	1.4398	8d
	O19	0.19514	-0.01980	0.61480	1	1.4398	8d
	O20	0.19471	0.85979	0.59974	1	1.4398	8d
	O21	1.00748	0.04953	0.78963	1	1.4398	8d
	O22	1.00359	0.85114	0.75091	1	1.4398	8d
	O23	0.42003	0.75000	0.65462	1	1.4398	4c
	O24	0.19853	0.75000	0.63479	1	1.4398	4c
	O25	0.29195	0.75000	0.08286	1	1.4398	4c
	O26	0.10733	0.75000	0.07404	1	1.4398	4c
	Si1	0.42315	0.05762	0.67142	1	0.7199	8d
	Si2	0.31296	0.03522	0.82653	1	0.7199	8d
	Si3	0.28049	0.06251	0.03372	1	0.7199	8d
	Si4	0.12151	0.06057	0.03645	1	0.7199	8d
	Si5	0.07382	0.02748	0.81817	1	0.7199	8d
	Si6	0.19081	0.06168	0.67409	1.3352*	0.7199	8d
	Si7	0.42749	0.83008	0.69250	1	0.7199	8d
	Si8	0.30938	0.86737	0.82959	1	0.7199	8d
	Si9	0.27677	0.82878	0.04337	1	0.7199	8d
	Si10	0.11663	0.81993	0.03769	1	0.7199	8d
	Si11	0.07222	0.86890	0.80191	1	0.7199	8d
	Si12	0.18079	0.82814	0.67462	1	0.7199	8d

Table 5.17. Atomic parameters of Fe/B-Z derived from synchrotron PXRD.

Species	Atom	x	y	z	SOF	B_{eq}	Wyckoff
Zeolite	O1	0.36796	0.05042	0.74038	1	0.9609	8d
framework	O2	0.30322	0.06319	0.92658	1	0.9609	8d
	O3	0.20163	0.05992	0.01475	1	0.9609	8d
	O4	0.09144	0.03945	0.90694	1	0.9609	8d
	O5	0.12457	0.07261	0.74069	1	0.9609	8d
	O6	0.22629	0.06964	0.77696	1	0.9609	8d
	O7	0.39382	0.83980	0.77672	1	0.9609	8d
	O8	0.31058	0.83573	0.93479	1	0.9609	8d
	O9	0.18804	0.84068	-0.00241	1	0.9609	8d
	O10	0.11011	0.84887	0.90099	1	0.9609	8d
	O11	0.12777	0.84581	0.73324	1	0.9609	8d
	O12	0.25737	0.84408	0.76581	1	0.9609	8d
	O13	0.30304	0.93787	0.81241	1	0.9609	8d
	O14	0.08562	0.95326	0.82506	1	0.9609	8d
	O15	0.41559	0.13509	0.64600	1	0.9609	8d
	O16	0.40494	0.98840	0.58940	1	0.9609	8d
	O17	0.39952	0.86555	0.55371	1	0.9609	8d
	O18	0.18533	0.12592	0.61261	1	0.9609	8d
	O19	0.18412	0.03370	0.58815	1	0.9609	8d
	O20	0.20354	0.85679	0.59221	1	0.9609	8d
	O21	0.99431	0.04966	0.77471	1	0.9609	8d
	O22	0.99423	0.84906	0.78463	1	0.9609	8d
	O23	0.42449	0.75000	0.70717	1	0.9609	4c
	O24	0.20688	0.75000	0.67519	1	0.9609	4c
	O25	0.27058	0.75000	0.01086	1	0.9609	4c
	O26	0.10459	0.75000	0.06982	1	0.9609	4c
	Si1	0.41936	0.05714	0.67305	1	0.4804	8d
	Si2	0.30802	0.02944	0.82280	1.2406*	0.4804	8d
	Si3	0.28244	0.05460	0.04556	1	0.4804	8d
	Si4	0.11743	0.06626	0.03184	1	0.4804	8d
	Si5	0.07212	0.03750	0.81429	1	0.4804	8d
	Si6	0.18327	0.04427	0.68045	1	0.4804	8d
	Si7	0.42237	0.82315	0.66708	1	0.4804	8d
	Si8	0.31068	0.87140	0.82534	1	0.4804	8d
	Si9	0.27739	0.83304	0.02539	1	0.4804	8d
	Si10	0.11548	0.82555	0.04495	1	0.4804	8d
	Si11	0.07427	0.86774	0.81369	1	0.4804	8d
	Si12	0.19103	0.82381	0.67879	1	0.4804	8d
Water1	O1	0.48146	0.36773	0.45202	0.5452	7	8d

Table 5.18. Atomic parameters of Cu/Al-Z derived from synchrotron PXRD.

Species	Atom	x	y	z	SOF	Beq	Wyckoff
Zeolite	O1	0.38292	0.05969	0.76470	1	1.2	8d
framework	O2	0.30991	0.06035	0.91453	1	1.2	8d
	O3	0.19925	0.04396	0.02637	1	1.2	8d
	O4	0.09250	0.05904	0.93912	1	1.2	8d
	O5	0.11301	0.06095	0.69945	1	1.2	8d
	O6	0.24093	0.04684	0.75345	1	1.2	8d
	O7	0.39521	0.85010	0.77988	1	1.2	8d
	O8	0.31640	0.84709	0.89548	1	1.2	8d
	O9	0.19990	0.84678	0.04076	1	1.2	8d
	O10	0.09168	0.83705	0.93887	1	1.2	8d
	O11	0.10799	0.84922	0.73094	1	1.2	8d
	O12	0.23713	0.86111	0.78160	1	1.2	8d
	O13	0.31313	0.93952	0.80765	1	1.2	8d
	O14	0.07981	0.93925	0.83211	1	1.2	8d
	O15	0.42831	0.15378	0.63664	1	1.2	8d
	O16	0.39939	1.00792	0.57081	1	1.2	8d
	O17	0.39321	0.86854	0.54115	1	1.2	8d
	O18	0.18847	0.14147	0.61464	1	1.2	8d
	O19	0.19712	-0.00808	0.60575	1	1.2	8d
	O20	0.20133	0.86754	0.59088	1	1.2	8d
	O21	1.00052	0.06068	0.75599	1	1.2	8d
	O22	1.00213	0.84925	0.79446	1	1.2	8d
	O23	0.41989	0.75000	0.66265	1	1.2	4c
	O24	0.19451	0.75000	0.60233	1	1.2	4c
	O25	0.30322	0.75000	0.09781	1	1.2	4c
	O26	0.08779	0.75000	0.08809	1	1.2	4c
	Si1	0.42525	0.05959	0.68484	1	0.6	8d
	Si2	0.31354	0.03220	0.82342	1	0.6	8d
	Si3	0.27579	0.06253	0.02584	1	0.6	8d
	Si4	0.12404	0.05455	0.01350	1	0.6	8d
	Si5	0.07146	0.03555	0.81274	1	0.6	8d
	Si6	0.19149	0.06400	0.67078	1	0.6	8d
	Si7	0.42616	0.83196	0.66609	1	0.6	8d
	Si8	0.31359	0.86384	0.82773	1	0.6	8d
	Si9	0.28994	0.81987	0.02762	1	0.6	8d
	Si10	0.12176	0.81615	0.04350	1	0.6	8d
	Si11	0.06907	0.86692	0.80583	1	0.6	8d
	Si12	0.18408	0.82669	0.68732	1.2588*	0.6	8d
Water1	O1	0.50920	0.25123	-0.13938	0.4171	8	8d
Water2	O2	0.50697	-0.02271	-0.06333	0.3971	8	8d
Water3	O3	-0.50826	0.16454	-0.04125	0.7816	8	8d
Water4	O4	-0.73969	0.24463	-0.10154	0.6393	8	8d
Water5	O5	-0.52583	-0.21553	-0.06154	0.4389	8	8d

Table 5.19. Atomic parameters of Cu/Ga-Z derived from synchrotron PXRD.

Species	Atom	x	y	z	SOF	B_{eq}	Wyckoff
Zeolite	O1	0.37457	0.05369	0.77299	1	1.73028	8d
framework	O2	0.30270	0.06622	0.91221	1	1.73028	8d
	O3	0.20333	0.05209	0.01384	1	1.73028	8d
	O4	0.09571	0.06158	0.92047	1	1.73028	8d
	O5	0.11842	0.05225	0.71586	1	1.73028	8d
	O6	0.24506	0.05807	0.75603	1	1.73028	8d
	O7	0.39861	0.84194	0.78950	1	1.73028	8d
	O8	0.31507	0.84758	0.90637	1	1.73028	8d
	O9	0.18333	0.84471	0.02910	1	1.73028	8d
	O10	0.08878	0.85064	0.90931	1	1.73028	8d
	O11	0.10683	0.84985	0.74288	1	1.73028	8d
	O12	0.23777	0.84202	0.75938	1	1.73028	8d
	O13	0.30892	0.93744	0.82488	1	1.73028	8d
	O14	0.07227	0.93686	0.82515	1	1.73028	8d
	O15	0.41537	0.14335	0.62519	1	1.73028	8d
	O16	0.39892	0.98777	0.56410	1	1.73028	8d
	O17	0.40016	0.86953	0.56708	1	1.73028	8d
	O18	0.19322	0.15115	0.62909	1	1.73028	8d
	O19	0.20424	-0.01749	0.61817	1	1.73028	8d
	O20	0.19680	0.85901	0.59980	1	1.73028	8d
	O21	1.00655	0.05534	0.77681	1	1.73028	8d
	O22	1.00098	0.85193	0.75080	1	1.73028	8d
	O23	0.42186	0.75000	0.63774	1	1.73028	4c
	O24	0.18365	0.75000	0.61364	1	1.73028	4c
	O25	0.29574	0.75000	0.07985	1	1.73028	4c
	O26	0.09478	0.75000	0.10587	1	1.73028	4c
	Si1	0.42149	0.05327	0.66977	1	0.86514	8d
	Si2	0.31209	0.03267	0.83037	1	0.86514	8d
	Si3	0.27907	0.06183	0.03274	1	0.86514	8d
	Si4	0.11874	0.05807	0.03030	1	0.86514	8d
	Si5	0.07391	0.02963	0.82086	1	0.86514	8d
	Si6	0.19348	0.06171	0.66472	1.3346*	0.86514	8d
	Si7	0.43022	0.82861	0.68293	1	0.86514	8d
	Si8	0.31121	0.86714	0.82330	1	0.86514	8d
	Si9	0.27795	0.82692	0.03767	1	0.86514	8d
	Si10	0.11834	0.81607	0.03232	1	0.86514	8d
	Si11	0.07271	0.86383	0.81411	1	0.86514	8d
	Si12	0.18731	0.82692	0.67519	1	0.86514	8d
Water1	O1	0.35314	0.23586	-0.12051	0.3406	8	8d
Water2	O2	0.48732	0.49544	0.06707	0.4175	8	8d
Water3	O3	0.61909	0.30742	0.56819	0.5779	8	8d
Water4	O5	0.51675	0.28235	0.90390	0.6172	8	8d

Table 5.20. Atomic parameters of Cu/B-Z derived from synchrotron PXRD.

Species	Atom	x	y	z	SOF	B_{eq}	Wyckoff
Zeolite	O1	0.37439	0.06183	0.75485	1	1.73028	8d
framework	O2	0.30843	0.06014	0.92019	1	1.73028	8d
	O3	0.19967	0.06045	0.03227	1	1.73028	8d
	O4	0.09096	0.06092	0.91501	1	1.73028	8d
	O5	0.11881	0.05304	0.72666	1	1.73028	8d
	O6	0.24172	0.04834	0.73954	1	1.73028	8d
	O7	0.37975	0.84450	0.76134	1	1.73028	8d
	O8	0.31314	0.84467	0.91851	1	1.73028	8d
	O9	0.19003	0.84636	0.02615	1	1.73028	8d
	O10	0.09219	0.83758	0.93354	1	1.73028	8d
	O11	0.11418	0.84383	0.73161	1	1.73028	8d
	O12	0.24904	0.85774	0.77817	1	1.73028	8d
	O13	0.31183	0.96003	0.81917	1	1.73028	8d
	O14	0.07785	0.94729	0.82187	1	1.73028	8d
	O15	0.42134	0.12905	0.61701	1	1.73028	8d
	O16	0.40273	0.99599	0.57894	1	1.73028	8d
	O17	0.40140	0.87114	0.57054	1	1.73028	8d
	O18	0.19283	0.12880	0.61905	1	1.73028	8d
	O19	0.19170	-0.00143	0.59485	1	1.73028	8d
	O20	0.19928	0.86818	0.57730	1	1.73028	8d
	O21	0.99872	0.04775	0.79441	1	1.73028	8d
	O22	0.99952	0.84781	0.78421	1	1.73028	8d
	O23	0.42804	0.75000	0.65033	1	1.73028	4c
	O24	0.19182	0.75000	0.64219	1	1.73028	4c
	O25	0.28222	0.75000	0.07094	1	1.73028	4c
	O26	0.09929	0.75000	0.08109	1	1.73028	4c
	Si1	0.42599	0.05721	0.66306	1	0.86514	8d
	Si2	0.30768	0.02957	0.81107	1	0.86514	8d
	Si3	0.27727	0.06332	0.02911	1	0.86514	8d
	Si4	0.12257	0.06249	0.02250	1	0.86514	8d
	Si5	0.06984	0.03118	0.81126	1	0.86514	8d
	Si6	0.18793	0.06159	0.67112	1	0.86514	8d
	Si7	0.42398	0.82858	0.67892	1	0.86514	8d
	Si8	0.31146	0.86726	0.81668	1	0.86514	8d
	Si9	0.27839	0.82553	0.03141	1	0.86514	8d
	Si10	0.12425	0.82453	0.03381	1	0.86514	8d
	Si11	0.07494	0.86972	0.81423	1	0.86514	8d
	Si12	0.18733	0.82701	0.68146	1.1842*	0.86514	8d
Water1	O5	0.49092	0.30494	-0.07982	0.4289	8	8d

Table 5.21. Catalytic performance of 4-chlorostyrene of the zeolite sample labelled.

Catalyst	Reaction temp. (°C)	Conv.$_{(4Cl\text{-}styrene)}$ (%)	Sel.$_{(4Cl\text{-}benzaldehyde)}$ (%)	Activation energy (kJ)
Fe/Al-Z	50	7.2	54.1	87.685
	70	35.0	74.7	
	90	24.1	74.0	
Fe/Ga-Z	50	6.9	67.5	51.578
	70	33.6	71.5	
	90	51.6	73.4	
Fe/B-Z	50	9.3	74.5	49.533
	70	57.4	75.4	
	90	65.3	78.6	
Cu/Al-Z	50	No reaction	-	50.060
	70	36.9	57.8	
	90	30.3	76.6	
	110	73.0	75.6	
Cu/Ga-Z	50	No reaction	-	70.744
	70	10.6	37.0	
	90	23.6	85.5	
	110	78.6	65.9	
Cu/B-Z	50	No reaction	-	84.369
	70	9.6	67.3	
	90	13.3	78.3	
	110	61.5	72.9	
Na-Fe/Al-Z	70	16.3	76.0	-
Na-Fe/Ga-Z	70	12.7	62.0	-
Na-Fe/B-Z	70	15.2	71.5	-
H-ZSM-5	70	14.7	55.1	-
Na-ZSM-5	70	No reaction	-	-

Table 5.22. Crystallographic data of the synchrotron PXRD measurement of the 4-chlorostrene (4Cl-sty) and GVL pre-adsorbed zeolite sample labelled.

	4Cl-sty-Fe/Al-Z	**4Cl-sty-Fe/B-Z**	**GVL-Fe/Al-Z**	**GVL-Fe/B-Z**
Diffractometer	Rigaku SmartLab	Rigaku SmartLab	Rigaku SmartLab	Rigaku SmartLab
Wavelength (Å)	0.7093	0.7093	0.7093	0.7093
2θ – zero point (°)	-0.00557(17)	-0.00817(16)	-0.00154(28)-	-0.00335
Space group	*Pnma*	*Pnma*	*Pnma*	*Pnma*
Crystal system	Orthorhombic	Orthorhombic	Orthorhombic	Orthorhombic
a (Å)	20.11775(58)	20.01241(48)	20.12910(72)	20.04154(30)
b (Å)	19.92743(53)	19.88942(54)	19.95968(86)	19.86729(33)
c (Å)	13.40824(40)	13.36641(37)	13.44821(56)	13.37965(25)
V (Å^3)	5375.30(27)	5320.29(24)	5403.09(38)	5327.39(15)
2θ range for refinement (°)	3-50	3-50	3-50	3-50
Detector	D/tex Ultra 250-HE	D/tex Ultra 250-HE	D/tex Ultra 250-HE	D/tex Ultra 250-HE
Number of parameters	24	24	24	24
Number of *hkl*s	5036	8187	5073	4986
Refinement methods	LeBail	LeBail	LeBail	LeBail
$R_{wp}/R_{exp}/R_p$ (%)	2.329/2.828/1.791	4.467/3.051/3.239	4.073/6.008/3.012	4.253/6.069/3.290
Gof	0.824	1.464	0.678	0.701

R_{wp}: weighted profile; R_{exp}: expected; R_p: profile; *gof:* goodness-of-fit.

Table 5.23. Atomic parameters of 4Cl-sty-Fe/Al-Z derived from PXRD.

Species	Atom	x	y	z	SOF	B_{eq}	Wyckoff
Zeolite	O1	0.38399	0.05878	0.76741	1	0.1941	8d
framework	O2	0.28158	0.05573	0.93411	1	0.1941	8d
	O3	0.18726	0.04622	0.02763	1	0.1941	8d
	O4	0.0833	0.0704	0.9258	1	0.1941	8d
	O5	0.11522	0.04014	0.71712	1	0.1941	8d
	O6	0.25712	0.03818	0.74286	1	0.1941	8d
	O7	0.37293	0.84347	0.76652	1	0.1941	8d
	O8	0.31422	0.83556	0.93155	1	0.1941	8d
	O9	0.20253	0.84841	-0.01042	1	0.1941	8d
	O10	0.08887	0.83149	0.91674	1	0.1941	8d
	O11	0.12424	0.844	0.73922	1	0.1941	8d
	O12	0.22386	0.84756	0.77626	1	0.1941	8d
	O13	0.3093	0.94395	0.8213	1	0.1941	8d
	O14	0.0881	0.95694	0.80367	1	0.1941	8d
	O15	0.4167	0.13068	0.60315	1	0.1941	8d
	O16	0.41828	0.99026	0.59621	1	0.1941	8d
	O17	0.40663	0.87397	0.59093	1	0.1941	8d
	O18	0.1878	0.11457	0.61751	1	0.1941	8d
	O19	0.23153	0.0079	0.61313	1	0.1941	8d
	O20	0.19795	0.84274	0.58141	1	0.1941	8d
	O21	0.9988	0.05178	0.78692	1	0.1941	8d
	O22	0.99935	0.83687	0.77263	1	0.1941	8d
	O23	0.43513	0.75	0.62121	1	0.1941	4c
	O24	0.20272	0.75	0.62301	1	0.1941	4c
	O25	0.313	0.75	0.04502	1	0.1941	4c
	O26	0.09524	0.75	0.0782	1	0.1941	4c
	Si1	0.42606	0.06764	0.66273	1	0.097	8d
	Si2	0.32293	0.03747	0.83325	1	0.097	8d
	Si3	0.26831	0.0716	0.03174	1	0.097	8d
	Si4	0.12128	0.07527	0.02309	1	0.097	8d
	Si5	0.07129	0.02925	0.81017	1	0.097	8d
	Si6	0.18292	0.05472	0.68203	1.46553	0.097	8d
	Si7	0.433	0.82948	0.6832	1	0.097	8d
	Si8	0.31414	0.86191	0.82342	1	0.097	8d
	Si9	0.27583	0.84036	0.04001	1	0.097	8d
	Si10	0.11537	0.82756	0.04262	1	0.097	8d
	Si11	0.07958	0.86622	0.81762	1	0.097	8d
	Si12	0.1933	0.83018	0.67705	1	0.097	8d
4-Cl-sty	Cl1	0.42768	-0.02431	-0.04426	0.8511	8	8d
	C2	0.44962	0.068549	-0.02199	0.8511	8	8d
	C3	0.498821	0.086401	0.04602	0.8511	8	8d
	C4	0.514738	0.152872	0.062259	0.8511	8	8d
	C5	0.481573	0.20371	0.010441	0.8511	8	8d
	C6	0.432138	0.185687	-0.05789	0.8511	8	8d
	C7	0.416608	0.119063	-0.07356	0.8511	8	8d
	C8	0.496921	0.268667	0.026017	0.8511	8	8d
	C9	0.544947	0.295024	-0.03224	0.8511	8	8d
Water1	O1	0.11817	0.2492	0.839868	0.9011	8	8d
Water2	O1	-0.08561	0.73743	1.020655	0.1874	8	8d

Table 5.24. Atomic parameters of 4Cl-sty-Fe/B-Z derived from PXRD.

Species	Atom	x	y	z	SOF	B_{eq}	Wyckoff
Zeolite	O1	0.37846	0.04456	0.7543	1	0.6848	8d
framework	O2	0.30255	0.05825	0.92132	1	0.6848	8d
	O3	0.19771	0.06239	0.03627	1	0.6848	8d
	O4	0.09774	0.06008	0.90918	1	0.6848	8d
	O5	0.11632	0.0525	0.73301	1	0.6848	8d
	O6	0.25356	0.04071	0.73525	1	0.6848	8d
	O7	0.37667	0.8333	0.76649	1	0.6848	8d
	O8	0.31233	0.84136	0.91544	1	0.6848	8d
	O9	0.19782	0.84948	0.03346	1	0.6848	8d
	O10	0.09304	0.83247	0.91558	1	0.6848	8d
	O11	0.11448	0.84535	0.74292	1	0.6848	8d
	O12	0.2269	0.84348	0.74855	1	0.6848	8d
	O13	0.31314	0.94349	0.81784	1	0.6848	8d
	O14	0.083	0.94816	0.81488	1	0.6848	8d
	O15	0.42729	0.12889	0.59605	1	0.6848	8d
	O16	0.41533	0.9871	0.58405	1	0.6848	8d
	O17	0.39958	0.86522	0.56047	1	0.6848	8d
	O18	0.18625	0.12612	0.60881	1	0.6848	8d
	O19	0.19668	0.008	0.5778	1	0.6848	8d
	O20	0.19989	0.87331	0.57849	1	0.6848	8d
	O21	0.99577	0.04711	0.79585	1	0.6848	8d
	O22	0.99936	0.85809	0.79922	1	0.6848	8d
	O23	0.42216	0.75	0.6502	1	0.6848	4c
	O24	0.18939	0.75	0.65863	1	0.6848	4c
	O25	0.28173	0.75	0.04457	1	0.6848	4c
	O26	0.09582	0.75	0.05746	1	0.6848	4c
	Si1	0.42525	0.05682	0.6514	1	0.3424	8d
	Si2	0.31554	0.0252	0.82444	1.2406	0.3424	8d
	Si3	0.27542	0.06648	0.02767	1	0.3424	8d
	Si4	0.123	0.06121	0.01425	1	0.3424	8d
	Si5	0.0693	0.02965	0.79928	1	0.3424	8d
	Si6	0.18213	0.06262	0.66263	1	0.3424	8d
	Si7	0.42143	0.82977	0.67589	1	0.3424	8d
	Si8	0.30501	0.87318	0.8045	1	0.3424	8d
	Si9	0.27615	0.82871	0.02818	1	0.3424	8d
	Si10	0.12053	0.8229	0.03505	1	0.3424	8d
	Si11	0.06846	0.86274	0.81932	1	0.3424	8d
	Si12	0.18557	0.82948	0.66918	1	0.3424	8d
4-Cl-sty	Cl1	-0.06098	0.5132	0.45773	0.4062	8	8d
	C2	-0.07135	0.424641	0.513972	0.4062	8	8d
	C3	-0.04573	0.368587	0.465033	0.4062	8	8d
	C4	-0.05303	0.305011	0.505011	0.4062	8	8d
	C5	-0.08644	0.295725	0.595812	0.4062	8	8d
	C6	-0.11217	0.35211	0.644907	0.4062	8	8d
	C7	-0.10459	0.415465	0.604272	0.4062	8	8d
	C8	-0.0937	0.233775	0.635156	0.4062	8	8d
	C9	-0.04498	0.212526	0.697187	0.4062	8	8d
Water1	O1	0.453865	0.746407	0.205945	0.7854	8	8d
Water2	O1	0.106236	0.24761	0.878777	0.9006	8	8d
Water3	O1	0.598411	0.607566	0.400832	0.4697	8	8d

Table 5.25. Atomic parameters of GVL-Fe/Al-Z derived from PXRD.

Species	Atom	x	y	z	SOF	B_{eq}	Wyckoff
Zeolite	O1	0.39307	0.05508	0.75835	1	0.0783	8d
framework	O2	0.30006	0.05278	0.9248	1	0.0783	8d
	O3	0.19555	0.06785	0.03664	1	0.0783	8d
	O4	0.09335	0.06499	0.92963	1	0.0783	8d
	O5	0.1077	0.05233	0.73747	1	0.0783	8d
	O6	0.25159	0.03222	0.75088	1	0.0783	8d
	O7	0.37149	0.8291	0.75601	1	0.0783	8d
	O8	0.31226	0.83354	0.93241	1	0.0783	8d
	O9	0.18104	0.84347	0.02251	1	0.0783	8d
	O10	0.09732	0.84165	0.92837	1	0.0783	8d
	O11	0.11863	0.84584	0.74045	1	0.0783	8d
	O12	0.22675	0.83588	0.74783	1	0.0783	8d
	O13	0.31746	0.94589	0.81134	1	0.0783	8d
	O14	0.07893	0.96925	0.8524	1	0.0783	8d
	O15	0.41833	0.13184	0.60776	1	0.0783	8d
	O16	0.40526	0.9989	0.5674	1	0.0783	8d
	O17	0.39508	0.85595	0.55118	1	0.0783	8d
	O18	0.19649	0.12847	0.59526	1	0.0783	8d
	O19	0.20624	-0.00915	0.57762	1	0.0783	8d
	O20	0.1995	0.86953	0.58716	1	0.0783	8d
	O21	0.99816	0.06328	0.79917	1	0.0783	8d
	O22	1.00053	0.84426	0.76162	1	0.0783	8d
	O23	0.43516	0.75	0.66466	1	0.0783	4c
	O24	0.19814	0.75	0.6766	1	0.0783	4c
	O25	0.29264	0.75	0.06819	1	0.0783	4c
	O26	0.10279	0.75	0.07787	1	0.0783	4c
	Si1	0.42263	0.06215	0.65924	1	0.0391	8d
	Si2	0.31424	0.02616	0.81001	1	0.0391	8d
	Si3	0.27196	0.06216	0.03914	1	0.0391	8d
	Si4	0.11708	0.07182	0.02464	1	0.0391	8d
	Si5	0.07281	0.03726	0.82548	1	0.0391	8d
	Si6	0.18078	0.05318	0.68277	1.46553	0.0391	8d
	Si7	0.42254	0.83121	0.66751	1	0.0391	8d
	Si8	0.31033	0.85628	0.80372	1	0.0391	8d
	Si9	0.27183	0.8257	0.02391	1	0.0391	8d
	Si10	0.12367	0.83036	0.02057	1	0.0391	8d
	Si11	0.06119	0.87702	0.81605	1	0.0391	8d
	Si12	0.18274	0.82418	0.65791	1	0.0391	8d
GVL1	O1	-0.23101	-0.25501	0.20205	0.4062	8	8d
	C2	-0.28835	-0.25249	0.169251	0.4062	8	8d
	C3	-0.30461	-0.26493	0.062113	0.4062	8	8d
	C4	-0.37816	-0.28321	0.075302	0.4062	8	8d
	C5	-0.39424	-0.23823	0.163103	0.4062	8	8d
	C6	-0.45596	-0.26036	0.222006	0.4062	8	8d
	O7	-0.33719	-0.22493	0.225266	0.4062	8	8d

Table 5.26. Atomic parameters of GVL-Fe/B-Z derived from PXRD.

Species	Atom	x	y	z	SOF	Beq	Wyckoff
Zeolite	O1	0.3767	0.05686	0.75479	1	0.887	8d
framework	O2	0.30619	0.05106	0.93662	1	0.887	8d
	O3	0.20404	0.0635	0.03351	1	0.887	8d
	O4	0.09899	0.05903	0.90753	1	0.887	8d
	O5	0.11556	0.04714	0.72618	1	0.887	8d
	O6	0.24291	0.0406	0.74579	1	0.887	8d
	O7	0.37887	0.83434	0.76967	1	0.887	8d
	O8	0.30478	0.83507	0.91662	1	0.887	8d
	O9	0.20903	0.84221	0.02826	1	0.887	8d
	O10	0.08594	0.83661	0.91963	1	0.887	8d
	O11	0.12537	0.83796	0.73282	1	0.887	8d
	O12	0.23988	0.84741	0.77008	1	0.887	8d
	O13	0.31517	0.93993	0.81996	1	0.887	8d
	O14	0.0811	0.94061	0.82238	1	0.887	8d
	O15	0.41755	0.13087	0.60403	1	0.887	8d
	O16	0.40589	0.9998	0.57135	1	0.887	8d
	O17	0.38962	0.85873	0.57453	1	0.887	8d
	O18	0.20098	0.11991	0.63244	1	0.887	8d
	O19	0.19218	0.00993	0.60727	1	0.887	8d
	O20	0.20698	0.8583	0.60123	1	0.887	8d
	O21	0.9902	0.04613	0.79892	1	0.887	8d
	O22	0.98764	0.8525	0.78882	1	0.887	8d
	O23	0.43218	0.75	0.64883	1	0.887	4c
	O24	0.18441	0.75	0.65766	1	0.887	4c
	O25	0.28109	0.75	0.05715	1	0.887	4c
	O26	0.09823	0.75	0.06307	1	0.887	4c
	Si1	0.42281	0.06252	0.66092	1	0.4435	8d
	Si2	0.3094	0.02423	0.82168	1	0.4435	8d
	Si3	0.27533	0.06012	0.03387	1	0.4435	8d
	Si4	0.12119	0.06761	0.01499	1	0.4435	8d
	Si5	0.06856	0.02724	0.80209	1	0.4435	8d
	Si6	0.18494	0.05095	0.6706	1.46553	0.4435	8d
	Si7	0.41951	0.82336	0.67547	1	0.4435	8d
	Si8	0.30499	0.87383	0.80578	1	0.4435	8d
	Si9	0.27572	0.82787	0.04124	1	0.4435	8d
	Si10	0.12292	0.83469	0.04091	1	0.4435	8d
	Si11	0.07247	0.87495	0.80975	1	0.4435	8d
	Si12	0.19067	0.82734	0.67882	1	0.4435	8d
GVL1	O1	0.08929	-0.28655	0.36562	0.7346	8	8d
	C2	0.051614	-0.32146	0.417244	0.7346	8	8d
	C3	0.041815	-0.39536	0.399448	0.7346	8	8d
	C4	0.016477	-0.41427	0.503944	0.7346	8	8d
	C5	-0.02031	-0.34952	0.529036	0.7346	8	8d
	C6	-0.03127	-0.33879	0.641701	0.7346	8	8d
	O7	0.007312	-0.29126	0.4793	0.7346	8	8d
Water1	O1	0.105131	0.2509	0.827066	0.5881	8	8d

Chapter 6 Conclusion and Outlook

This thesis presents a comprehensive demonstration of diverse strategies for introducing active species into porous materials to achieve the rational design of bifunctional catalysts. Through the introduction of distinct active species into the porous material, two main categories of bifunctional catalysts have been identified: bimetallic catalysts and metal/non-metal catalysts embedded within the porous matrices of zeolites and metal-organic frameworks (MOFs). By employing state-of-the-art characterization techniques, it becomes possible to elucidate the properties and positioning of the active species. Furthermore, the investigation of the structure-activity relationship between the bifunctional catalysts and the reactants has been conducted using various probe reactions.

In Chapter 3, we present the preparation of atomic dispersed 3d metal bimetallic dual-atom catalysts. Through the utilization of a di-basic imidazole linker, a linker-bridged 3d bimetallic dual atom can be assembled within the zeolite support. The structure of the bimetallic cluster has been confirmed through Rietveld refinement of the RXRD pattern, in combination with various characterization techniques, including XAFS, MALDI-TOF-TOF-MS, and XPS. With the assistance of the probe superoxide dismutation reaction, three distinct synergistic advantages have been unveiled: (1) neighboring bimetallic active motifs, (2) a tertiary structure encompassing the zeolite support, and (3) the local coordination environment. These findings provide valuable insights into a reliable approach for the precise engineering of novel bimetallic catalysts.

In Chapter 4, we extend the concept of ligand-mediated bimetallic clusters localized within porous materials, as discussed in Chapter 3, to MOF materials. We present the preparation of Cu-Fe dual-atom catalysts (DACs) on the Zr_6O_4 secondary building unit (SBU) of UiO-66-NH_2. In contrast to the approaches described in Chapter 3, an additional activation step is employed to form a Cu-oxo-Fe bimetallic cluster on the SBU of UiO-66-NH_2. The presence of the oxo-bridge within the Cu-Fe DACs promotes the selective oxidation of styrene, resulting in a selectivity of over 92% towards benzaldehyde. The significant results obtained from the probe reaction indicate that supported bimetallic dual-atom catalysts (DACs) represent a promising class of materials for the activation of small molecules, despite the challenges associated with their synthesis.

Chapter 5 provides a comprehensive investigation of the systematic studies conducted to prepare a bifunctional metal/Brønsted acid zeolite catalyst via a one-pot hydrothermal synthesis. The Lewis acidity, Brønsted acidity, and the precise positioning of the active species are confirmed through Rietveld refinement using probe molecules, as well as information derived from various characterization techniques, including XAFS, Py-FT-IR, NH_3-TPD, and XPS. By employing two probe reactions, namely styrene oxidation and GVL decarboxylation, we confirm the optimal combination of acid strength from different acid sites and unveil the synergistic cooperativity between the two active species.

In conclusion, this thesis presents a comprehensive and systematic study of achieving a rational design of bifunctional catalysts utilizing various porous materials. Through the application of diverse characterization techniques, we have successfully revealed the geometric and electronic structural information of the active species. Furthermore, the structure-activity relationship has been elucidated, providing valuable insights into the catalyst's performance. The findings of this thesis highlight the possibility of tailoring the active species of heterogeneous catalysts for specific applications, emphasizing the potential for customized catalytic systems.